

https://dspace.org/

A Computational Fluid Dynamic Study on the Relief of Intraocular Pressure in the Human Eye in Glaucoma Surgery

Basson, Nicol

2025
University of the Witwatersrand, Johannesburg
https://hdl.handle.net/10539/50036
Basson, Nicol. (2025). A Computational Fluid Dynamic Study on the Relief of Intraocular Pressure in the Human Eye in Glaucoma Surgery. [PhD thesis, University of the Witwatersrand, Johannesburg]. WIReDSpace. https://hdl.handle.net/10539/50036

Downloaded from a DSpace repository. https://dspace.org/

A COMPUTATIONAL FLUID DYNAMIC STUDY ON THE RELIEF OF INTRAOCULAR PRESSURE IN THE HUMAN EYE IN GLAUCOMA SURGERY

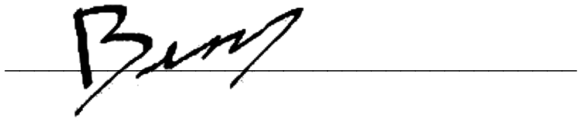
Nicol Basson

A dissertation submitted to the Faculty of Engineering & the Built Environment, University of the Witwatersrand, in partial fulfilment of the requirements for the degree of Doctor of Philosophy in Engineering.

Johannesburg, 2025

Declaration

I declare that this thesis is my own work. It is being submitted for the Degree of Doctor of Philosophy at the University of the Witwatersrand, Johannesburg. It has not been submitted before for any degree or examination at any other University.



(Signature of candidate)

21 day of May 20 25 at Somerset West

AI Assistance Disclaimer

In the preparation of this thesis, I have made use of artificial intelligence (AI) tools, specifically OpenAI's ChatGPT, to support aspects of this thesis, including literature exploration, structural planning, and improving clarity and coherence of the written content. All content was critically reviewed and edited by me, and I take full responsibility for the final work.

Abstract

This study investigates the immediate post-operative outcomes of glaucoma filtration surgeries using computational fluid dynamics (CFD). Three surgical procedures, namely trabeculectomy, non-penetrating deep sclerectomy (NPDS), and modified NPDS (mNPDS) were simulated across 3D eye models to evaluate intraocular pressure (IOP) reduction and flow dynamics. Results were analysed for both unsutured conditions, where surgical incisions were open to atmosphere, and sutured conditions, where flow resistance was introduced. Key parameters such as velocity patterns, recirculation zones, and wall shear stress (WSS) were compared to clinical and experimental studies.

Initial simulations were performed on an idealised eye geometry, demonstrating that CFD effectively replicated clinical trends in IOP reduction and surgical outcomes. Trabeculectomy and mNPDS were shown to achieve appropriate post-operative IOP levels, with mNPDS more closely aligning with physiologically balanced aqueous humour flow. NPDS was less effective, highlighting its sensitivity to surgical techniques. While the use of an idealised model provided valuable insights, it limited the study's ability to capture anatomical variability.

To address this limitation, ethnic-representative models were developed for European and African eyes based on biometric data. These models revealed differences in flow dynamics, influenced by variations in anterior chamber parameters. The African eye models exhibited lower velocities near the corneal wall, indicating potential nutrient deficiencies. These findings emphasize the importance of ethnicity-specific anatomy in surgical planning, particularly as glaucoma tends to present earlier in African populations, when anterior chamber depths (ACDs) are typically larger. Conversely, the European eye models demonstrated more balanced flow patterns, aligning more closely with normal flow conditions.

Despite its promising results, the study acknowledges the limitations in the accuracy of biometry data, particularly due to variability in measurement techniques and the influence of factors like age and surgical timing. These variables may cause discrepancies between simulated and clinical outcomes, particularly as anterior chamber parameters change significantly over a patient’s lifetime. Additionally, while the models relied on ethnic averages, real-world geometries exhibit greater variability, underscoring the need for patient-specific approaches to glaucoma surgery.

This study is the first to compare glaucoma surgical treatments using CFD and the first to incorporate ethnic-representative anterior chamber models. The findings highlight CFD's potential as a virtual tool for evaluating surgical techniques, offering a cost-effective and time-efficient method for assessing outcomes prior to clinical trials. Future work should focus on refining patient-specific geometries, integrating finite element models for tissue biomechanics, and validating CFD results with clinical data. By improving our understanding of how surgical interventions influence aqueous humour dynamics, this study lays the groundwork for optimizing glaucoma treatments and improving long-term patient outcomes.

Research Outputs

The research represented in this thesis has resulted in the following research outputs, including work conducted by students' related research projects that extended the scope of this initial PhD work:

1. **Journal article**: N. Basson, P.H. Geoghegan, S.E. Williams and W.H. Ho, A Computational Fluid Dynamic Analysis of Glaucoma Filtration Surgeries and Immediate Postoperative Intraocular Pressure, Journal of Glaucoma *(submitted)*.
2. **Journal article**: N. Basson, B. Mashele, S.E. Williams, P.H. Geoghegan, & W.H. Ho, A Review of Ethnic, Sex, and Age-Related Variations in Ocular Anterior Segment Geometries *(in preparation)*.
3. **Journal article**: N. Basson, C.H. Peng, P.H. Geoghegan, T. van der Lecq, D. Steven, S.E. Williams, A.E. Lim and W.H. Ho, A computational fluid dynamics investigation of endothelial cell damage from glaucoma drainage devices. Scientific Reports 14, 3777 (2024). https://www.nature.com/articles/s41598-023-50491-9.
4. **Peer-reviewed conference proceeding**: N. Basson, F. Alimahomed, P.H. Geoghegan, S.E. Williams and W.H. Ho, "An aqueous humour fluid dynamic study for normal and glaucomatous eye conditions", 44th International Engineering in Medicine and Biology Conference, Glasgow, United Kingdom, 4p, 11 – 15 Jul 2022, 10.1109/EMBC48229.2022.9871009.
5. **Presentation**: N. Basson, F. Alimahomed, P.H. Geoghegan, S.E. Williams and W.H. Ho, "A Computational Fluid Dynamic Study of Aqueous Humour Flow for Glaucomatous Conditions", 2nd International Symposium in Biomedical Engineering Innovation, Johannesburg, South Africa, 23 – 24 Nov 2021.
6. **Presentation**: N. Basson, W.H. Ho, P.H. Geoghegan, S.E. Williams and F. Alimahomed, "A Computational Study of Glaucomatous Aqueous Humour Dynamics in the Human Eye", 12th SACAM Conference, Cape Town, South Africa, 29 Nov – 1 Dec 2021.
7. **Poster**: N. Basson, S.E. Williams, P.H. Geoghegan and W.H. Ho, "A computational comparison of three glaucoma filtration surgeries", 10th World Glaucoma Congress, Rome, Italy, 1p, 28 Jun – 1 Jul 2023, https://research.utwente.nl/en/publications/a-computational-comparison-of-three-glaucoma-filtration-surgeries.
8. **Abstract and presentation**: N. Basson, P.H. Geoghegan, S.E. Williams, and W.H. Ho "Exploring Ethnic Diversity in Glaucoma Surgery Efficacy Using Computational Fluid Dynamics", Virtual Physiological Human Conference, Stuttgart, Germany, 4-6 September 2024

Acknowledgements

First and foremost, my deepest appreciation goes to my knowledgeable supervisors – Prof. Weihua Ho, Dr. Patrick Geoghegan, and Prof. Susan Williams – for providing me with the opportunity to learn from them, network through them, and always being available to guide me through this monumental research project.

Further, I would like to express my gratitude to everyone who helped me acquire data for this project, including Dr. Craig Dean Anderson at Chris Hani Baragwanath St John Eye Hospital, Dr. Peggy Mohlabi and Dr. Genevieve Ephraim for granting me access to their resources at Netcare Sunninghill Hospital, as well as to Dr. Ryan Hamilton-Hoskins at Execuspecs Woodmead for kindly sharing optometry records that enriched this study

I am also grateful to the School of Mechanical, Industrial & Aeronautical Engineering at the University of the Witwatersrand for their generous partial funding of this research, and to NRF Thuthuka for their additional financial support, which was instrumental in the completion of this work. I am deeply appreciative of my colleagues at Wits as well as the University of Twente for their encouragement and for providing the space and support necessary to complete this thesis while balancing work commitments.

I would like to extend my appreciation to my fellow postgraduate students at the University of the Witwatersrand, Aston University, and the University of Cape Town, who assisted and extended my own work.

Special thanks are owed to Matthew Wensor, Grant Frisken, Trevor Anderson, and Andrew Waterson at Cylite Optics for their support in obtaining patient-specific images, and to James Wolffson at Aston University for allowing me to use his facilities for scanning.

Finally, I am very grateful to my husband, along with other family members and friends, for their unwavering encouragement and support throughout my studies.

Contents

Declaration i

Abstract ii

Research Outputs iii

Acknowledgements iv

Contents v

List of Figures viii

List of Tables xvi

List of Symbols xvii

Nomenclature xviii

1 Introduction 1

1.1 Background 1

1.1.1 Anatomy of the Eye 1

1.1.2 Glaucoma 4

1.1.3 Trabeculectomy 5

1.1.4 Non-Penetrating Deep Sclerectomy (NPDS) 7

1.1.5 Glaucoma Filtration Post-Surgical Complications 8

1.1.6 Using *in silico* Methods to Study Glaucoma Treatments 9

1.2 Problem Statement 10

1.3 Identified Gaps 11

1.4 Hypothesis 11

1.5 Objectives 12

1.6 Research Aim 12

1.7 Assumptions and Limitations 13

1.8 Ethical Clearance 13

1.9 Structure of this Thesis 13

2 Literature Review 16

2.1 Introduction 16

2.2 Glaucoma Prevalence and Outcomes for Different Ethnicities 16

2.3 Safety and Efficacy of Trabeculectomy vs Deep Sclerectomy 17
2.4 Scleral Flap Suturing to Control IOP 18
2.5 The Potential Clinical Implications of Biofluid Flow Changes 20
2.6 Computational Models to Study Aqueous Humour Dynamics 21
2.7 Summary 23
3 Theoretical Framework 24
3.1 Ocular Fluid Dynamics 24
3.2 Assumptions & Governing Equations 25
3.3 The Trabecular Meshwork 27
3.4 Material & Fluid Properties 29
3.5 Q-Criterion and λ2-Criterion 30
3.6 Optical Coherence Tomography 31
4 Idealised Model 33
4.1 Trabeculectomy, NPDS, & mNPDS 39
4.2 Mesh Independence Study 43
4.3 Model Validation 46
4.3.1 Validation Based on Previous Computational Studies 46
4.3.2 Validation Based on Experimental Studies 49
4.4 Additional Study on Glaucoma Drainage Devices 51
4.5 Results & Discussion 51
4.5.1 Comparison with Clinical Studies Comparison 59
4.6 Summary 60
5 Demographic-Representative Models 62
5.1 Creation of Demographic-Specific Geometries 62
5.2 Fluent Setup 70
5.3 Mesh Independence Study 73
5.4 Results & Discussion 74
5.4.1 Normal Flow 75
5.4.2 Post-Surgical Flow 83

5.4.3 Wall Shear Stress 106
5.4.4 Vorticity & Q-Criterion 119
5.4.5 Uniformity Index 126
5.4.6 Parametric Study on Suturing Tightness 128
5.4.7 Unsteady Considerations 130
5.5 Summary 131
6 Reconstructed OCT Model 136
6.1 Methodology 136
6.2 Results & Discussion 142
6.3 Summary 152
7 Conclusion & Recommendations 154
7.1 Conclusions 154
7.2 Recommendations for Future Research 157
8 References 159
Appendix A. In-Vitro Experimental Setup ..... A
8.1.1 Dye Injection Setup ..... B
8.1.2 Particle Image Velocimetry Setup ..... D
Appendix B. GDD as Glaucoma Treatment Study ..... G
Appendix C. Anterior Chamber Raw Parameter Data ..... J
Appendix D. Extract from Statistical Analysis Study ..... B
Appendix E. Unsutured Surgical Results ..... A

List of Figures

Figure 1 Diagram illustrating the anterior and posterior segments of the human eye (adapted from Clker-Free-Vector-Images via Pixabay) 1
Figure 2 Human eye anatomy infographic (Designed by Freepik) 3
Figure 3 Production of aqueous humour in the eye (created by Dr Susan Williams using Vector Works) 4
Figure 4 Aqueous humour pathway flow following trabeculectomy procedure (created by Dr Susan Williams using Vector Works) 6
Figure 5 Flowchart to visually represent the thesis structure 15
Figure 6 Cutaway view of the three layers of the trabecular meshwork (inspired by [131]) 27
Figure 7 Frontal view of eye and its resulting axial image using OCT 32
Figure 8 Flow domain representation (green) and flow direction (red arrows) for normal and glaucomatous eye conditions. 33
Figure 9 Flow region of the anterior chamber in an idealised eye model for normal and glaucomatous eye conditions. 34
Figure 10 Defined fluid flow zones of the eye anterior segment 38
Figure 11 Flow domain representation (dark green), the new addition to the flow domain, namely the Kelly punch surgical site (light green), and flow direction (red arrows) for trabeculectomy conditions. 41
Figure 12 Flow domain representation (dark green), the new addition to the flow domain, namely the deep scleral flap surgical site (light green), and flow direction (red arrows) for NPDS conditions. 42
Figure 13 Flow region of the anterior chamber in an idealised eye model for (a) trabeculectomy and (b) NPDS and mNPDS. 43
Figure 14 Resulting mesh for the anterior chamber eye model (cross-sectional view on the XZ-plane) 44
Figure 15 Mesh independence study results of number of cells vs volume-average pressure (IOP) for the trabeculectomy model (left) and NPDS model (right). 45
Figure 16 Idealised model velocity pathline results for normal conditions when the model is oriented in the (a) upright and (b) supine position. 47
Figure 17 Velocity pathline results from the Villmarin et al. study oriented in the (a) upright and (b) supine position [124] 47
Figure 18 Idealised model WSS results for normal conditions when the model is oriented in the (a) supine and (b) upright position 48
Figure 19 WSS results from the Villamarin et al. study oriented in the (a) supine and (b) upright position [124] 49

Figure 20 (a) CFD simulation on the xy-plane comparison for experimental dye visualization with temperature gradient at (b) 30 seconds, (c) 60 seconds, (d) 90 seconds [146]. 50
Figure 21 Velocity flow results from the Wang et al. PIV study (extracted from [140]) 51
Figure 22 Idealised model IOP results for normal conditions (left) and glaucomatous conditions (right). 52
Figure 23 Comparison of idealised model IOP results vs TM permeability as calculated using Darcy's law and extracted from the CFD software (published in [155]). 53
Figure 24 Comparison of idealised model IOP for normal and glaucomatous conditions, as well as unsutured NPDS, mNPDS, and trabeculectomy conditions. 54
Figure 25 Comparison of idealised model velocity pathline results for normal and glaucomatous conditions, as well as unsutured NPDS, mNPDS, and trabeculectomy conditions. 55
Figure 26 Zoomed in illustration of normal (left) and glaucomatous (right) superior outlet sections. 55
Figure 27 Comparison of idealised model IOP results for normal and glaucomatous conditions, as well as sutured NPDS, mNPDS, and trabeculectomy conditions. 56
Figure 28 Comparison of idealised model velocity pathline results for normal and glaucomatous conditions, as well as sutured NPDS, mNPDS, and trabeculectomy conditions. 57
Figure 29 Zoomed in illustration idealised model velocity pathline result at the cornea-iris angle near the surgical site for normal and glaucomatous conditions, as well as sutured NPDS, mNPDS, and trabeculectomy conditions. 58
Figure 30 Anterior chamber parameter definitions including White-To-White (WTW) length, Anterior Chamber Depth (ACD), Anterior Chamber Angle (ACA), Lens Vault (LV), Pupil Diameter (PD), Trabecular Meshwork Length (TML), and Trabecular Meshwork Height (TMH). 63
Figure 31 Graphic representation of the anterior chamber parameters as created in Autodesk Inventor with a close-up graphic representation of the eye structure parameters at the ACA 67
Figure 32 3D model of the European-representative anterior chamber as a result of the defined ethnic geometry parameters including the anterior chamber (green), TM (blue), and Schlemm's canal with collector channels (yellow) 68
Figure 33 Velocity vector results at the outlet of the anterior chamber of the European eye for a single uniform collector channel (top) and 26 separate cylindrical outlet channels (bottom) 69
Figure 34 3D model of the European-representative anterior chamber and trabeculectomy procedure including the anterior chamber with the iridectomy incision (green), TM (blue), Schlemm's canal with collector channels (yellow), and Kelly punch sclerostomy incision (pink) 72
Figure 35 3D model of the European-representative anterior chamber and NPDS/mNPDS procedure including the anterior chamber with the iridectomy incision (green), TM (blue), Schlemm's canal with collector channels (yellow), and the deep scleral flap incision (pink) 73
Figure 36 IOP results under normal conditions for the European-representative eye (left) and the African representative eye (right) 75

Figure 37 Velocity pathline results under normal conditions for the supine European-representative eye (top) and the supine African-representative eye (bottom) 77
Figure 38 Velocity vector results under normal conditions for the supine European-representative eye (top) and the supine African-representative eye (bottom) 77
Figure 39 Velocity magnitude and streamline contours for normal supine orientation for the European model (top) and African model (bottom) 78
Figure 40 Velocity pathline results under normal conditions for the upright European-representative eye (left) and the upright African-representative eye (right) 79
Figure 41 Velocity vector results under normal conditions for the upright European-representative eye (left) and the upright African-representative eye (right) 80
Figure 42 Velocity magnitude and streamline contours for normal upright orientation for the European model (left) and African model (right) 81
Figure 43 Normalized stagnation point position versus average anterior chamber velocity for normal upright eye models 81
Figure 44 Q-criterion results under normal conditions for the supine European-representative eye (left) and the supine African-representative eye (right) 82
Figure 45 Q-criterion results under normal conditions for the upright European-representative eye (top) and the upright African-representative eye (bottom) 83
Figure 46 IOP results under trabeculectomy conditions for the supine unsutured European-representative eye (left) and supine unsutured African representative eye (right) 84
Figure 47 IOP results under trabeculectomy conditions for the upright sutured European-representative eye (left) and the upright sutured African representative eye (right) 85
Figure 48 IOP results under NPDS conditions for the supine unsutured European-representative eye (left) and the supine unsutured African representative eye (right) 86
Figure 49 IOP results under NPDS conditions for the upright sutured European-representative eye (left) and the upright sutured African representative eye (right) 87
Figure 50 IOP results under mNPDS conditions for the supine unsutured European-representative eye (top) and the supine unsutured African-representative eye (bottom) 88
Figure 51 IOP results under mNPDS conditions for the upright sutured European-representative eye (left) and the upright sutured African-representative eye (right) 89
Figure 52 Inset velocity pathline results under normal for the supine sutured European-representative eye (top) and the supine sutured African representative eye (bottom) 90
Figure 53 Inset velocity pathline results under normal for the upright sutured European-representative eye (top) and the supine sutured African representative eye (bottom) 91
Figure 54 Velocity pathline results under trabeculectomy conditions for the supine sutured European-representative eye (top) and the supine sutured African representative eye (bottom), with the flow concentration circled in red 92

Figure 55 Inset velocity pathline results under trabeculectomy conditions for the supine sutured European-representative eye (top) and the supine sutured African representative eye (bottom), with the black arrow indicating the entrance flow from the iridectomy site..... 93
Figure 56 Velocity magnitude and streamline contours for trabeculectomy supine orientation for the European model (top) and African model (bottom)..... 94
Figure 57 Sclerostomy top view of velocity magnitude contours at the outlets under trabeculectomy conditions for the supine sutured European-representative eye (top) and the supine sutured African representative eye (bottom)..... 95
Figure 58 Velocity pathline results under trabeculectomy conditions for the upright sutured European-representative eye (left) and the upright sutured African representative eye (right), with the flow concentration circled in red..... 96
Figure 59 Inset velocity vector results under trabeculectomy conditions for the upright sutured European-representative eye (top) and the upright sutured African representative eye (bottom), with out-of-plane flow circled in red..... 97
Figure 60 Velocity magnitude and streamline contours for trabeculectomy supine orientation for the European model (top) and African model (bottom)..... 98
Figure 61 Top view of velocity magnitude contours at the outlets under trabeculectomy conditions for the upright sutured European-representative eye (top) and the upright sutured African-representative eye (bottom)..... 99
Figure 62 Velocity pathline results under NPDS conditions for the supine sutured European-representative eye (top) and the supine sutured African-representative eye (bottom)..... 100
Figure 63 Inset velocity pathline results under NPDS conditions for the supine sutured European-representative eye (top) and the supine sutured African-representative eye (bottom)..... 101
Figure 64 Velocity pathline results under NPDS conditions for the upright sutured European-representative eye (left) and the upright sutured African-representative eye (right)..... 102
Figure 65 Inset velocity pathline results under NPDS conditions for the upright sutured European-representative eye (top) and the upright sutured African-representative eye (bottom)..... 103
Figure 66 Velocity pathline results under mNPDS conditions for the supine sutured European-representative eye (top) and the supine sutured African-representative eye (bottom)..... 104
Figure 67 Velocity magnitude and streamline contours for mNPDS supine orientation for the European model (top) and African model (bottom)..... 105
Figure 68 Velocity pathline results under mNPDS conditions for the upright sutured European-representative eye (left) and the upright sutured African-representative eye (right)..... 106
Figure 69 WSS results under normal conditions for the supine European-representative eye (left) and the supine African-representative eye (right)..... 107
Figure 70 WSS results under normal conditions for the upright European-representative eye (left) and the upright African-representative eye (right)..... 108

Figure 71 WSS results under trabeculectomy conditions for the upright unsutured European-representative eye (left) and the upright unsutured African representative eye (right)..... 109
Figure 72 WSS results under trabeculectomy conditions for the supine sutured European-representative eye at the periphery (top left), supine sutured African-representative eye at the periphery (top right), supine sutured European-representative eye at the anterior chamber walls (bottom left), and the supine sutured African-representative eye at the anterior chamber walls (bottom right)..... 110
Figure 73 WSS results under trabeculectomy conditions for the upright sutured European-representative eye at the periphery (top left), upright sutured African-representative eye at the periphery (top right), upright sutured European-representative eye at the anterior chamber walls (bottom left), and the upright sutured African-representative eye at the anterior chamber walls (bottom right)..... 111
Figure 74 Close-up view of the WSS for the trabeculectomy surgical site WSS results supine sutured European-representative eye (left) and the supine sutured African-representative eye (right), with the dashed line indicating where the sclerostomy punch tool would be applied 112
Figure 75 Close-up view of the adjusted WSS scale for the trabeculectomy surgical site WSS results supine sutured European-representative eye (left) and the supine sutured African-representative eye (right), with the WSS resulting from the iridectomy entrance flow circled in red 113
Figure 76 Side view of the adjusted WSS scale for the trabeculectomy surgical site WSS results supine sutured European-representative eye (left) and the supine sutured African-representative eye (right), along with the velocity pathlines resulting from the iridectomy inflow 113
Figure 77 WSS results under NPDS conditions for the supine sutured European-representative eye around the periphery (top left), the supine sutured African-representative eye around the periphery (top right), supine sutured European-representative eye at the anterior chamber walls (bottom left), and the supine sutured African-representative eye at the anterior chamber walls (bottom right) 114
Figure 78 WSS results under NPDS conditions for the upright sutured European-representative eye around the periphery (top left), the upright sutured African-representative eye around the periphery (top right), upright sutured European-representative eye at the anterior chamber walls (bottom left), and the upright sutured African-representative eye at the anterior chamber walls (bottom right) 115
Figure 79 Side view of the adjusted scale for the NPDS surgical site WSS results for supine sutured European-representative eye (left) and the supine sutured African-representative eye (right), along with the velocity contours 116
Figure 80 WSS results under mNPDS conditions for the supine sutured European-representative eye around the periphery (top left), the supine sutured African-representative eye around the periphery (top right), supine sutured European-representative eye at the anterior chamber walls (bottom left), and the supine sutured African-representative eye at the anterior chamber walls (bottom right) 117
Figure 81 WSS results under mNPDS conditions for the upright sutured European-representative eye around the periphery (top left), the upright sutured African-representative eye around the periphery (top

right), upright sutured European-representative eye at the anterior chamber walls (bottom left), and the upright sutured African-representative eye at the anterior chamber walls (bottom right) 118
Figure 82 Adjusted scale for the mNPDS surgical site WSS results for supine sutured European-representative eye (left) and the supine sutured African-representative eye (right) 119
Figure 83 $Q > 0$ results under normal conditions for the supine European-representative eye (top) and the supine African-representative eye (bottom) 120
Figure 84 $Q > 0$ results under normal conditions for the upright European-representative eye (left) and the upright African-representative eye (right) 121
Figure 85 $Q > 0$ results under trabeculectomy conditions for the supine sutured European-representative eye (left) and the supine sutured African representative eye (right) 122
Figure 86 $Q > 0$ results under trabeculectomy conditions for the upright sutured European-representative eye (top) and the upright sutured African representative eye (bottom) 122
Figure 87 $Q > 0$ results under NPDS conditions for the upright supine European-representative eye (left) and the supine sutured African-representative eye (right) 123
Figure 88 $Q > 0$ results under NPDS conditions for the upright sutured European-representative eye (top) and the upright sutured African-representative eye (bottom) 124
Figure 89 $Q < 0$ results under mNPDS conditions for the supine sutured European-representative eye (left) and the supine sutured African-representative eye (right) 125
Figure 90 $Q < 0$ results under mNPDS conditions for the upright sutured European-representative eye (top) and the upright sutured African-representative eye (bottom) 126
Figure 91 IOP results for all models based on suture pressure tightness, with a target IOP of 10 mmHg indicated by the dashed line 129
Figure 92 Mass flow rate plot results for unsteady unsutured trabeculectomy simulation 130
Figure 93 Visualization of the anterior segment of a patient's eye using ITK-SNAP displaying the sagittal view (top left), the axial view (bottom left), the coronal view (bottom right), and a 3D rendering of the segmented structure (top right). 137
Figure 94 Segmented anterior segment of the patient's eye using ITK-SNAP with the ROI highlighted in green displaying the sagittal view (top left), the axial view (bottom left), the coronal view (bottom right), and a 3D rendering of the segmented structure (top right). 138
Figure 95 3D model of segmented and reconstructed patient-specific eye as (a) isometric view and (b) front view. 139
Figure 96 Mirrored patient-specific model from OCT scans as (a) isometric view and (b) front view. 139
Figure 97 Final OCT-reconstructed model from OCT scans as (a) isometric view and (b) front view. 140

Figure 98 Final dimension-based model based on OCT scan parameters as (a) isometric view and (b) front view. 141
Figure 99 Pre-surgical velocity pathline results for (a) OCT-reconstructed model in supine position, (b) dimension-based model in supine positions, (c) OCT-reconstructed model in upright position, and (d) dimension-based model in upright positions. 144
Figure 100 WSS contour results on the iris for the OCT-reconstructed model (left) and dimension-based model (right) in the supine orientation 145
Figure 101 Inset pre-surgical velocity pathline results for OCT-reconstructed model in upright position (top) and dimension-based model in upright position (bottom), with the out-of-plane flow circled in red 146
Figure 102 Post-trabeculectomy velocity pathline results for (a) OCT-reconstructed model in supine position, (b) dimension-based model in supine positions, (c) OCT-reconstructed model in upright position, and (d) dimension-based model in upright positions, with the flow disturbances circled in red 147
Figure 103 Inset post-trabeculectomy velocity pathline results for OCT-reconstructed model in supine position, (left) and the dimension-based model in supine position (right) 148
Figure 104 Inset post-trabeculectomy velocity pathline results for OCT-reconstructed model in upright position (top) and the dimension-based model in upright position (bottom) 149
Figure 105 Comparison on WSS contours under supine trabeculectomy conditions for the OCT-reconstructed model (left) and the dimension-based model (right) 150
Figure 106 Comparison on velocity contours and streamlines under supine trabeculectomy conditions for the OCT-reconstructed model (top) and the dimension-based model (bottom) 151
Figure 107 Schematic representation of the in-vitro flow setup, showing the key components and flow paths [146]. ..... B
Figure 108 (a) CFD simulation on the xy-plane comparison for experimental dye visualization without temperature gradient at (b) 30 seconds, (c) 60 seconds, (d) 90 seconds [146]. C
Figure 109 (a) CFD simulation on the xy-plane comparison for experimental dye visualization with temperature gradient at (b) 30 seconds, (c) 60 seconds, (d) 90 seconds [146]. ..... D
Figure 110 (a) CFD simulation on the yz-plane (PIV window outlined in black) comparison for (b) particle visualization without temperature gradient [146]. ..... E
Figure 111 (a) CFD simulation on the yz-plane (PIV window outlined in black) comparison for (b) particle visualization with temperature gradient [146]. ..... F
Figure 112 Diagram illustrating measurements in mm of the idealised anterior chamber of the eye, showing the placement of a glaucoma drainage device (published in [148]). ..... G
Figure 113 Results of Cohen's D analysis [168] ..... B
Figure 114 Cohen's D effect arranged per ethnicity [168] C

Figure 115 Velocity pathline results under trabeculectomy conditions for the supine unsutured European-representative eye (left) and the supine unsutured African representative eye (right) ..... A
Figure 116 Velocity vector results under trabeculectomy conditions for the supine unsutured European-representative eye (left) and the supine unsutured African representative eye (right)..... B
Figure 117 Velocity pathline results under NPDS conditions for the supine unsutured European-representative eye (left) and the supine unsutured African-representative eye (right) ..... B
Figure 118 Velocity vector results under NPDS conditions for the supine unsutured European-representative eye (left) and the supine unsutured African representative eye (right)..... C
Figure 119 Velocity pathline results under mNPDS conditions for the supine unsutured European-representative eye (left) and the supine unsutured African-representative eye (right) ..... D
Figure 120 Velocity vector results under mNPDS conditions for the supine unsutured European-representative eye (left) and the supine unsutured African representative eye (right)..... E

List of Tables

Table 1 Fluid property values for water [135] 30
Table 2 Material property values for general eye structures [136] 30
Table 3 Summary of Reynolds number calculations 35
Table 4 Summary of Richardson number calculations 36
Table 5 Parameters to define the porous zone in Ansys Fluent for idealised models. 37
Table 6 Summary of IOP results for a variety of conditions including model orientation. 59
Table 7 Summary of number of biometric studies and total sample sizes 64
Table 8 Ocular geometries selected to represent European and African males over the age of 50 based on literature. 66
Table 9 List of models discussed in chapter 5 70
Table 10 Parameters to define the porous zone in Ansys Fluent for demographic-representative models. 71
Table 11 Mesh independence study results for ethnic-representative eye models 74
Table 12 UI-value calculations for all upright models 128
Table 13 Summary of main European-representative model results in the upright position 132
Table 14 Summary of main African-representative model results in the upright position 133
Table 15 Anterior chamber geometry parameters for dimension-based model based on OCT scan data 141
Table 16 Permeability parameter and calculation results for OCT-reconstructed and dimension-based models 142
Table 17 Error analysis of central rotational flow magnitudes based on maximum central velocity . 151
Table 18 UI-values and error% results for all OCT-reconstructed and dimension-based models 152

List of Symbols

Symbol	Description	SI Unit
A	Cross-sectional area	m^2
C_0	Constant in pressure gradient source term	-
D_{ID}	Hydraulic diameter	m
g	Gravitational acceleration vector	m/s^2
n	Sample size	-
λ_2	Lambda2-criterion	-
p	Fluid pressure	Pa
Q	Volumetric flow rate	m^3/s
Q	Q-criterion	-
S	Vorticity tensor	s^{-1}
S_i	Pressure gradient over the porous medium	Pa/m
T	Fluid temperature	K
T_{ref}	Reference temperature	K
u	Fluid velocity vector	m/s
v	Fluid velocity vector	m/s
z	Vertical height	m
α	Permeability of the porous medium	m^2
β	Thermal expansion coefficient	K^{-1}
μ	Dynamic viscosity of the fluid	Pa·s
ρ	Fluid density	kg/m^3
Ω	Rate of strain tensor	s^{-1}
ω	Vorticity	s^{-1}

Nomenclature

Abbreviation	Description
ACD	Anterior Chamber Depth
ACA	Anterior Chamber Angle
AGV	Ahmed Glaucoma Valve
CAD	Computer-Aided Design
CFD	Computational Fluid Dynamics
CCT	Central Corneal Thickness
ECD	Endothelial Cell Damage
FDM	Finite Difference Method
FEM	Finite Element Method
FVM	Finite Volume Method
GDD	Glaucoma Drainage Device
IOP	Intraocular Pressure
JCT	Juxtacanalicular Tissue
KP	Kelly Punch
LV	Lens Vault
MIGS	Minimal Invasive Glaucoma Surgery
mNPDS	Modified Non-Penetrating Deep Sclerectomy
NPDS	Non-Penetrating Deep Sclerectomy
OCT	Optical Coherence Tomography
ODR	Ocular Decompression Retinopathy
PIV	Particle Image Velocimetry
POAG	Primary Open Angle Glaucoma
Post-IOP	Post-operative Intraocular Pressure
Pre-IOP	Pre-operative Intraocular Pressure
SCR	Schlemm's Canal Radius
TM	Trabecular Meshwork
UI	Uniformity Index
WTW	White-To-White

1 Introduction

1.1 Background

1.1.1 Anatomy of the Eye

The human eye serves as the primary organ for vision. Despite its small size, measuring approximately 24 mm in diameter [1], the eye boasts a sophisticated anatomical structure composed of various interconnected components that collaborate to transform light into vision. Broadly categorized into two main segments, namely the anterior and posterior, which forms the eye's intricate design essential for its functions.

The anterior segment encompasses five main components: the sclera, cornea, iris, lens, and ciliary body (Figure 1). The sclera, recognized as the "white part" of the eye, provides structural support to the surrounding tissues. The extra-ocular muscles attached to the sclera facilitate eye movement.

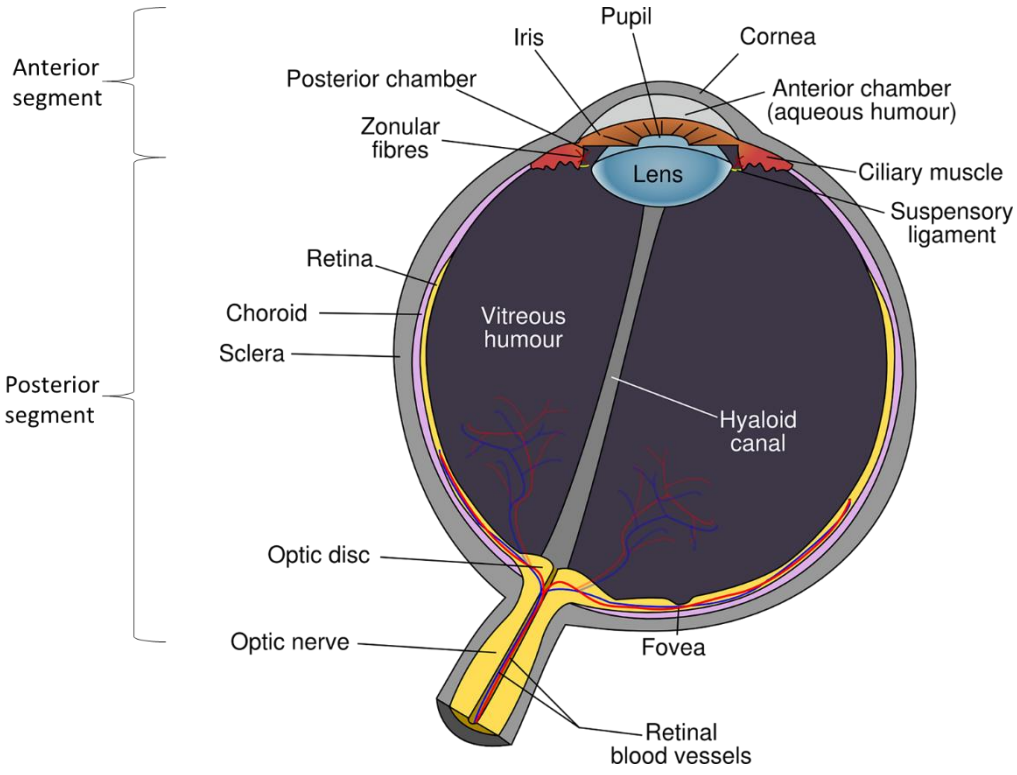


Figure 1 Diagram illustrating the anterior and posterior segments of the human eye (adapted from Clker-Free-Vector-Images via Pixabay)

Situated in the forefront of the eye, the cornea acts as the initial entry point for light, directing its passage to the lens. The iris, the circular-coloured portion, is a diaphragm that regulates the amount of light entering the eye through its centre, the pupil, by means of pupillary muscles. The ciliary body lies behind the iris. It functions to stabilize the lens and alter its shape by means of the zonules that attach to the ciliary body and the ciliary muscle within the ciliary body. The ciliary body also, importantly,

produces aqueous humour. Aqueous humour is a transparent, watery fluid with vital functions in nourishing the anterior segment of the eye and maintaining structural integrity by creating intraocular pressure (IOP).

The structures of the anterior segment create two continuous aqueous humour containing chambers connected by the pupil, the anterior and posterior chambers. The anterior chamber is located between the cornea and iris, whereas the posterior chamber lies behind the iris, contains the lens and is separated from the posterior segment of the eye by the hyaloid face that marks the anterior boundary of the vitreous body (Figure 2). The posterior segment of the eye consists of the retina, the choroid, the posterior sclera and the optic nerve. The retina is a transparent, specialised neural tissue that converts light signals into neuro-electrical impulses. It is supported by the vascular choroid and the posterior sclera. The posterior segment is primarily occupied by vitreous humour, a stable, clear and gelatinous fluid that plays a pivotal role in maintaining the eye's shape and transmitting light to the retina. Unlike aqueous humour, vitreous humour is not continually produced and replaced but remains constant and is thus not responsible for intra-ocular pressure. Positioned at the back of the posterior segment are the optic disc and optic nerve. The optic nerve transmits the electrical pulses from the retina to the visual cortex of the brain. Any damage to the optic nerve poses a significant risk of partial or complete vision loss, underscoring its critical role in ocular function.

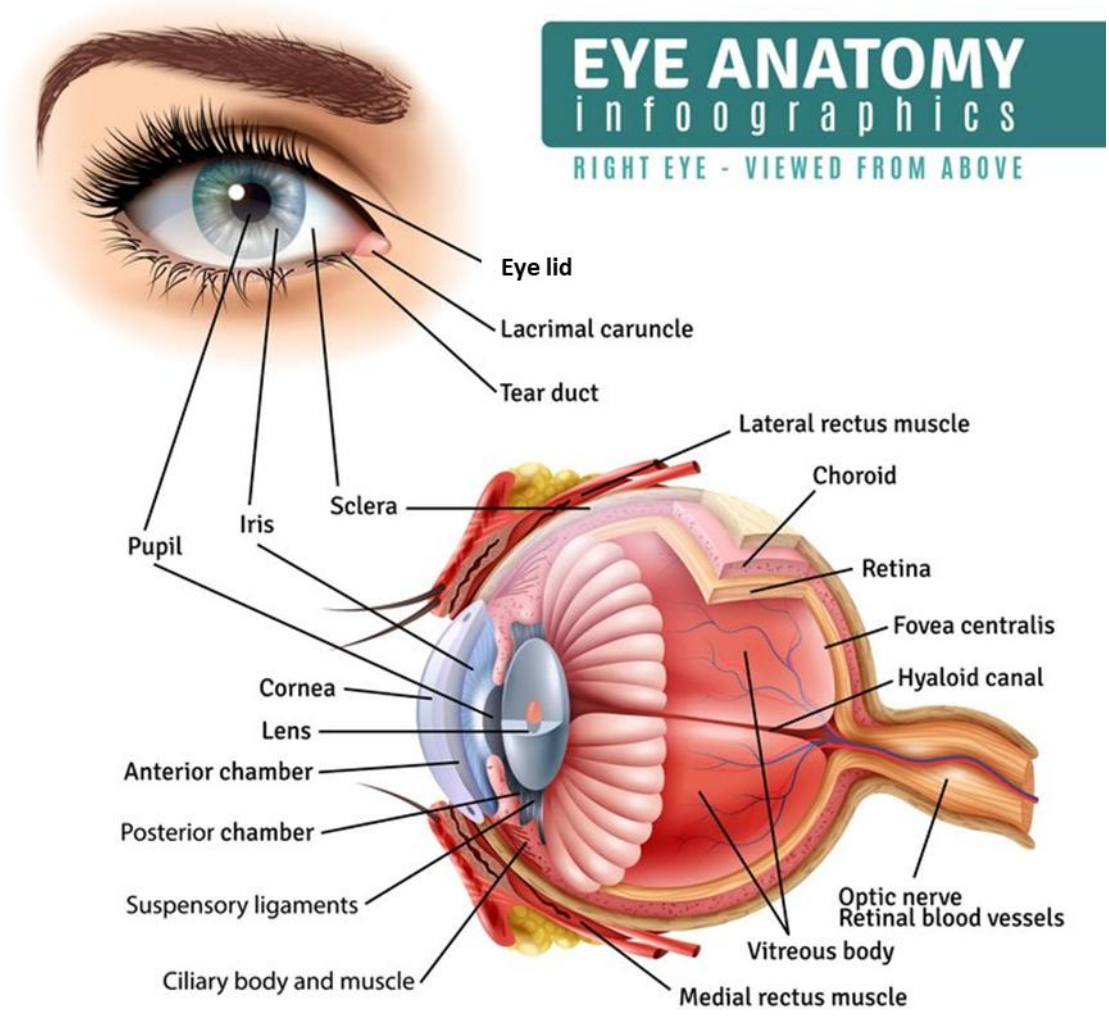


Figure 2 Human eye anatomy infographic (Designed by Freepik)

In the posterior chamber, aqueous humour is consistently produced by the ciliary body at an approximate rate of 2.5 ml/min [2]. To sustain a normal IOP (The average IOP produced by the eye is approximately 15 mmHg [3]), this aqueous humour flows from the posterior chamber, circulates around the lens, and traverses through the pupil to reach the anterior chamber. The primary drainage pathway for aqueous humour to exit the eye is through the trabecular meshwork (TM), a porous tissue structure housed in the "angle" of the eye, that occurs at the intersection of iris and cornea (Figure 3). The rate of drainage is crucial; if it diminishes, it results in an elevated IOP. Once through the TM, aqueous humour enters the Schlemm's canal, a circular vessel that delivers aqueous humour to the venous drainage pathways of the eye. An alternative pathway for aqueous to leave the eye is across the iris base through what is known as the uveoscleral pathway. Flow through the uveoscleral pathway is constant.

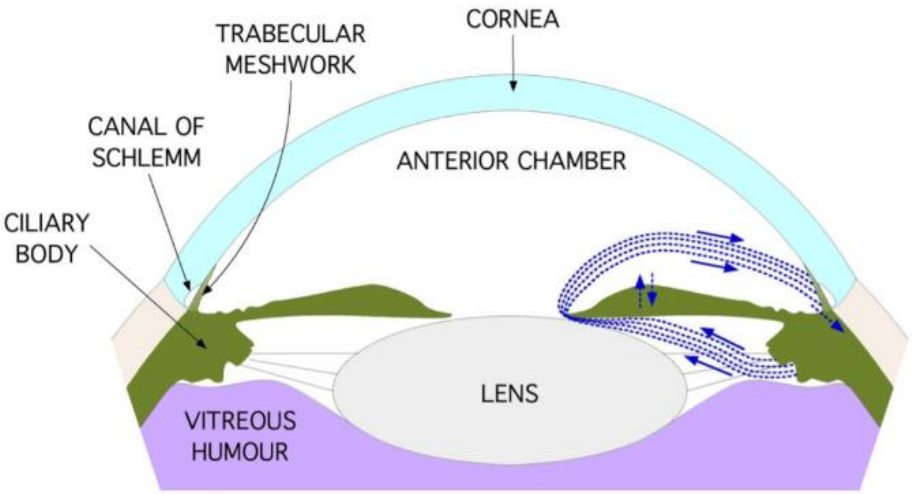


Figure 3 Production of aqueous humour in the eye (created by Dr Susan Williams using Vector Works)

1.1.2 Glaucoma

Glaucoma encompasses a range of disorders characterised by a specific pattern of damage to the optic nerve. An elevated intra-ocular pressure (IOP) is the most important risk factor for glaucoma, and it is also currently the only modifiable risk factor for the disease. Measuring the intra-ocular pressure is therefore an important investigation to perform on any patient with, or suspected of having, glaucoma. Normal IOP tends to vary from 12-22 mmHg (approximately 1.6-2.9 kPa) [4]. with an elevated IOP more likely to be associated with glaucoma development. It is postulated that an elevated IOP could cause mechanical damage to the nerve or to its vasculature, however the aetiology of glaucoma remains poorly understood. Not all individuals with an elevated IOP develop glaucoma (this is then known as ocular hypertension) and, conversely, glaucoma may develop in the presence of low IOPs (this is known as Low or Normal Tension Glaucoma (NTG)) [5,6]. Regardless of the presentation of glaucoma, lowering the IOP has been demonstrated to prevent progression of the disease whose natural history is one of progressive damage to the optic nerve culminating in irreversible visual loss [7,8].

Glaucoma is recognised as presenting with either an open-angle or a closed-angle. The distinction is made on gonioscopy which is performed using a specialised lens for visualisation of the drainage angle of the eye during slit lamp ocular examination. If the trabecular meshwork can be seen on gonioscopy, the glaucoma is designated ‘open-angle’. Both open- and closed-angle glaucoma are further described depending on whether the cause is ‘primary’ (isolated condition with no other ocular or systemic predisposition) or ‘secondary’ to another ocular or systemic condition. Primary open-angle glaucoma (POAG) is the most prevalent form of glaucoma [9].

By contrast, Primary Angle Closure is caused by an enlarged lens impeding flow of aqueous from the posterior chamber through the pupil to the anterior chamber. Aqueous accumulates behind the iris which narrows the drainage angle and interferes with aqueous reaching the trabecular meshwork. This can be

asymptomatic or cause a gradual elevation in IOP or intermittent IOP spikes or a dramatic sudden IOP elevation when the angle is completely closed.

Glaucoma is currently the leading cause of irreversible blindness worldwide [10]. In addition to an elevated IOP, other risk associations for glaucoma include age, familial predisposition, and ethnic background, particularly among individuals of Asian, Hispanic, or African descent [11]. Notably, individuals of African descent face a fivefold higher risk of developing glaucoma compared to those of European descent, and the condition tends to manifest earlier and progress more rapidly in this demographic.

Approximately 30% of blindness in Africa is attributed to glaucoma, highlighting its considerable impact on visual health. The precise reasons for the disproportionate prevalence of glaucoma among individuals of African ethnicity remain undetermined, although several factors have been linked. These include anatomical and geometrical variations in the eye, such as thinner corneas, larger optic nerves [12,13], and specific ocular anatomical features like the height of the TM [14]. The intricate interplay of these factors underscores the multifaceted nature of glaucoma and emphasizes the need for tailored approaches to understanding and addressing the condition within diverse populations.

The management of glaucoma encompasses a diverse array of approaches tailored to reduce the IOP, ranging from drug therapies to laser procedures and surgical interventions or a combination of these treatments. Among the surgical procedures, trabeculectomy has long held the status of the gold standard for reducing IOP surgically by bypassing the trabecular meshwork. Recognised for its efficacy, this surgical intervention has traditionally been a cornerstone in glaucoma treatment.

However, in recent years, the landscape of glaucoma surgeries has witnessed the emergence of alternative procedures challenging the dominance of trabeculectomy. New surgical approaches and innovations have prompted a re-evaluation of treatment strategies to enhance efficacy, reduce invasiveness, and improve patient outcomes. The evolving field of glaucoma management reflects a dynamic and progressive endeavour to explore and refine surgical alternatives, signalling a paradigm shift in the development of optimal therapeutic interventions.

1.1.3 Trabeculectomy

Trabeculectomy is a well-established and invasive filtering surgical procedure that stands as a key intervention for treating glaucoma, particularly POAG.

The procedure is as follows[1]:

[1] See video: https://www.youtube.com/watch?v=uVOzlNl__6c&t=16s

The conjunctiva is incised and reflected from the sclera along with the tenons capsule (the fibrous tissue deep to the conjunctiva) exposing the subconjunctival space and the underlying sclera. Subsequently, a scleral flap is cut to approximately 50% of scleral thickness, usually in a triangular, trapezoidal, or rectangular shape with dimensions ranging from 3 mm to 4 mm [15]. At this stage, it is usual to augment the procedure with the addition of an anti-fibrotic agent (for example mitomycin-C) to prevent scarring. Next, a puncture/sclerostomy is meticulously crafted underneath this flap using a punch tool, e.g., a Kelly Punch, to penetrate the anterior chamber through the TM, facilitating the drainage of accumulated aqueous humour to bypass the trabecular meshwork and exit the eye. Creation of this opening into the anterior chamber usually results in immediate decompression of the eye with consequent iris tissue prolapse from the eye. This is managed with a peripheral iridectomy (partial removal of the peripheral iris tissue, typically a triangular shape). This step is important in providing direct flow of aqueous from the posterior chamber to the sclerostomy site, as illustrated in Figure 4. Following this, the scleral flap is sutured closed (although not water-tight) to create a guarded fistula from the anterior chamber to the subconjunctival space. The tightness of the suturing (which can be modified with releasable and/or adjustable sutures), has been shown to impact intraocular pressure (IOP) control and hypotony prevention [16]. The conjunctival wound is then closed to create a water-tight 'bleb' where aqueous humour from the anterior chamber can accumulate and ultimately be resorbed into the venous circulation of the eye.

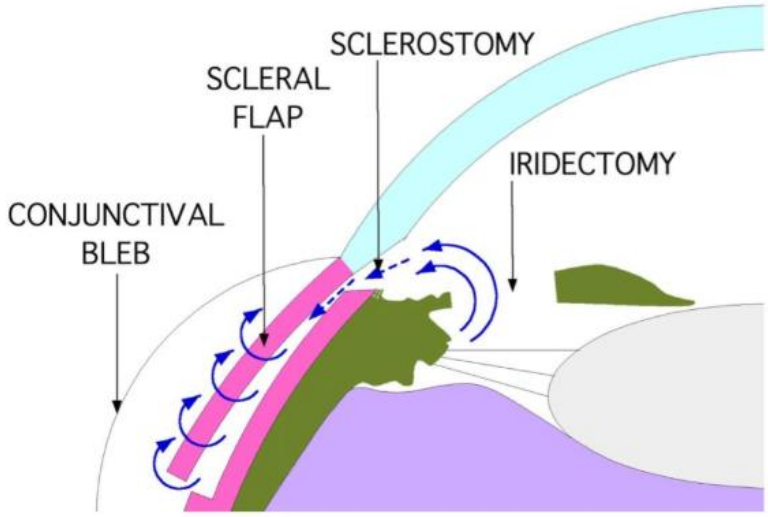


Figure 4 Aqueous humour pathway flow following trabeculectomy procedure (created by Dr Susan Williams using Vector Works)

Having been successfully performed since 1968, trabeculectomy has earned its reputation as the most effective surgical means of lowering IOP in glaucoma patients. Its efficacy extends across ethnicities, proving effective for both African and European populations [17]. Contemporary studies continue to advocate for trabeculectomy as the primary surgical consideration for glaucoma patients [18]. A notable 20-year follow-up study in 2011 indicated a success rate of approximately 60% without additional

medication and an impressive 90% with supplemental medication [19]. However, the procedure is not without its challenges, especially for high-risk patients with elevated IOP, prior ocular surgeries, or concurrent ocular diseases. Post-operative complications include elevated IOP, hypotony, and scarring or episcleral fibrosis [20–23].

In response to the significant risk of complications, modifications have been introduced to enhance the safety profile of trabeculectomy. A common alternative involves the incorporation of drainage device implants to manage IOP over the long term and prevent scarring-induced IOP elevation [24]. The necessity of such alternatives remains debated, with some studies highlighting improved safety and efficacy profiles, while others show marginal differences [25–27]. Long-term effects of these modifications continue to undergo investigation.

Despite its historical prominence, trabeculectomy has witnessed a decline in usage in recent years, yielding ground to newer surgical techniques. The ongoing discourse around modifications and the emergence of alternative procedures contributes to the evolving landscape of glaucoma surgical interventions.

1.1.4 Non-Penetrating Deep Sclerectomy (NPDS)

In recent years, non-penetrating deep sclerectomy (NPDS) has emerged as a noteworthy glaucoma surgical procedure, gaining prominence for its considered non-invasive nature and frequent application in treating POAG [28].

NPDS is also a filtering procedure, that, in common with trabeculectomy, diverts fluid from the anterior chamber of the eye to a sub-conjunctival drainage bleb. The procedure therefore begins the same way as a trabeculectomy with a conjunctival incision and conjunctival and Tenon's reflection. The scleral flap is also similar, although it is a bit larger and typically parabolic or square with approximate 4 x 4 mm dimensions and it extends further anteriorly into the cornea [29]. Mitomycin-C is likewise an important addition to the surgery. At this point the surgical procedures of trabeculectomy and NPDS diverge, with a deep sclerectomy being constructed within the site of the scleral flap. This dissection is continued anteriorly until the canal of Schlemm is revealed and deroofed. The deroofed canal of Schlemm has a lower resistance to outflow than the remainder of the trabecular meshwork and allows passage of fluid to percolate from the anterior chamber without completely decompressing the eye. The anterior chamber therefore never collapses, and the iris does not prolapse from the wound and no iridectomy is required. The deep scleral flap is entirely removed leaving behind a potential space where fluid may collect deep to the superficial scleral flap in a "scleral lake". The superficial flap is sutured closed to create a fistula as with a trabeculectomy. The conjunctival wound is closed to create a filtering bleb in the same way as with a trabeculectomy.

Considered a safer alternative to trabeculectomy, NPDS has faced some scepticism regarding its effectiveness in reducing IOP [30–32]. A 2006 study suggested that while NPDS is successful in short-term IOP reduction without post-operative complications, long-term sustainability of low IOP is questionable [33]. However, more recent research in 2018 provided conflicting results, showing a long-term qualified success rate exceeding 70% for patients with steroid-induced glaucoma [25].

Like trabeculectomy, modifications have been proposed for NPDS to enhance its efficacy. Certain modifications have demonstrated effectiveness comparable to trabeculectomy, coupled with increased safety in both short-term [12,34] and long-term scenarios. A notable letter to the editor in Acta Ophthalmologica recently advocated for the heightened use of deep sclerectomy as the preferred method over trabeculectomy [35], underscoring the evolving landscape and ongoing discourse in the realm of glaucoma surgical interventions.

1.1.5 Glaucoma Filtration Post-Surgical Complications

Aqueous humour plays a pivotal role in maintaining IOP and providing essential nutrients to avascular ocular tissues such as the cornea and lens. Any alteration in aqueous humour dynamics, whether due to natural causes or surgical interventions, can lead to a range of clinical complications, many of which are relevant to glaucoma surgery.

There are several complications that could occur following any glaucoma filtration surgery, though they may be more common in some procedures than others. Glaucoma filtration surgeries such as trabeculectomy and NPDS aim to reduce IOP by facilitating the drainage of aqueous humour, either by creating new outflow pathways or modifying existing ones. However, these procedures can significantly alter the natural flow of aqueous humour, leading to complications such as hypotony and/or bleb failure, all of which are related to changes in fluid dynamics.

Hypotony is a potential consequence of glaucoma surgery which arises from the surgeries' objective to drain excess fluid from the eye [36]. This post-surgical risk is associated with the excessive drainage of aqueous humour. Hypotony is characterized by an extreme decrease in IOP, often falling below 5 mmHg, although an eye may still be considered hypotonous if the IOP drops below 10 mmHg [37,38]. While hypotony may resolve spontaneously, intervention, such as additional scleral flap suturing following filtration surgery, may be necessary. To mitigate this risk of all complications related to hyptony, optimal suturing techniques of the scleral flap incision have been proposed for better IOP control [39].

Additionally, glaucoma surgery, particularly procedures like trabeculectomy and drainage device implantations, can result in corneal endothelial cell loss. This loss may be mild in some cases but can lead to corneal decompensation, especially if there are pre-existing conditions affecting the cornea [40].

Complications like Descemet's membrane detachment and localized corneal oedema have also been reported in non-penetrating surgeries.

Bleb failure following glaucoma surgery refers to the scarring of the filtering bleb that is created during the surgery to drain aqueous humour. This failure can result in suboptimal IOP control, leading to disease progression or the need for additional treatment or surgery [41]. The bleb is the small fluid-filled blister formed on the scleral surface where the aqueous humour drains out of the anterior chamber.

Aqueous misdirection, also known as malignant glaucoma, is a severe form of secondary angle-closure glaucoma, which can occur after ocular surgery, particularly following filtering procedures such as trabeculectomy. Shallow anterior chambers have been linked to aqueous misdirection [42]. The exact mechanism is still debated, but it typically involves anterior displacement of the lens-iris diaphragm, leading to aqueous humour being directed posteriorly behind the lens into the sub-hyaloid space where it causes the lens to be further displaced anteriorly with shallowing of the anterior chamber. This condition often requires careful management due to its poor response to conventional treatments. Surgical intervention may be necessary in severe cases [43,44].

The exact mechanisms causing these complications are still unclear. This thesis aims to relate changes in aqueous humour dynamics to discover potential links.

1.1.6 Using *in silico* Methods to Study Glaucoma Treatments

CFD is an *in silico* numerical method used to study the behaviour of fluids. CFD numerically analyses fluid flow by solving the Navier-Stokes equations, which are the fundamental equations that describe how velocity, pressure, and viscosity interact to determine fluid motion. A more detailed mathematical treatment of these equations is provided in section 3.2. The complexity of such a computational model can depend on many factors such as fluid type (Newtonian or non-Newtonian), flow type (laminar or turbulent) or the flow domain. CFD allows for the detailed simulation of fluid flow within complex anatomical structures, making it an ideal tool for understanding how surgical modifications and disease states affect aqueous humour dynamics.

Although conventionally used for industrial engineering-type flows, CFD has been utilized since the late 2000's to characterize aqueous humour flow in the human eye [45–48]. Since then, other CFD studies have been conducted to study the outcomes of ocular treatments [49–51], however these studies have been limited to normal and glaucomatous flow. Thus far, none of these models have been used to study the aqueous humour dynamic changes with glaucoma treatments in detail. The literature available on the present methods employed to study aqueous humour dynamics will be discussed in more detail in section 2.6.

CFD can model how different surgical techniques, such as trabeculectomy or NPDS, alter the flow of aqueous humour through the anterior chamber and outflow pathways like the TM. By simulating

changes in the flow rate, resistance, and velocity post-surgery, it is possible to predict the impact on IOP regulation and the risk of complications such as hypotony.

Changes in aqueous humour flow can also alter the shear stress experienced by tissues in the anterior segment. CFD will allow for the analysis of the mechanical forces exerted by altered flow patterns on these tissues. This could improve our understanding of how these forces contribute to possible fibrosis or scarring, which can lead to surgical failure or long-term complications such as bleb failure. CFD can also predict areas of increased shear stress that may contribute to endothelial cell loss.

CFD is also valuable in modelling how flow disturbances affect nutrient distribution within the eye. Post-surgical flow alterations can lead to uneven distribution of nutrients, which is critical for tissue healing and avoiding complications like corneal decompensation or fibrosis. By simulating these flow patterns, CFD can help predict areas of nutrient deprivation and guide post-operative care to improve healing outcomes.

It is important to note that CFD models cannot capture long-term effects such as bleb evolution over time, scarring around the surgical site, or tissue remodelling in response to wall shear stress (WSS) [52]. Long-term outcomes may diverge from the early fluid dynamic conditions modelled. However, short-term benchmarks can be established for evaluating the effectiveness of surgical interventions in restoring aqueous humour dynamics. For example, higher WSS near the surgical site early which could indicate a risk for fibrosis, and poor circulation or asymmetric flow may predict nutrient delivery deficits and localized tissue health issues. These are discussed in more detail in section 2.5.

1.2 Problem Statement

Glaucoma particularly impacts individuals of African descent and poses a significant risk of irreversible blindness. POAG stands out as the most common form of this condition, extensively investigated through both *in vivo* and *in vitro* methods. However, these studies are often subjected to unknown factors such as underlying diseases and prior surgeries, making it challenging to discern the independent impact of physical factors on surgical outcomes.

There is an ongoing discourse that surrounds the optimal approach to treat POAG, with trabeculectomy historically considered a gold standard, albeit not without associated risks. The emergence of safer and less invasive procedures, such as NPDS, has sparked debates over whether they should be prioritized over traditional methods. Both surgical interventions carry inherent risks, and despite extensive research, patient-specific risk factors remain inadequately quantified.

Very little is still understood about aqueous humour flow, especially as it relates to post-surgical outcomes, and there is a need for new/improved methods to improve this understanding [53,54]. It is also unclear how anatomical differences affect the flow and how it relates to the potential success of filtration surgeries, although correlations have been suggested [55,56].

A critical research gap exists in comprehending the dynamics of aqueous humour flow for these filtration procedures through *in silico* methods. This innovative approach could provide valuable insights into the efficacy and safety profiles of trabeculectomy and NPDS. By employing computational simulations, it is possible to elucidate the nuanced behaviours of aqueous humour flow, shedding light on potential modifications to address patient-specific risk factors. This study will enhance our understanding of glaucoma surgical interventions, paving the way for more tailored and effective approaches in the quest to preserve vision and mitigate risks associated with this debilitating condition.

1.3 Identified Gaps

The following gaps in research have been identified and will be addressed throughout the course of this thesis:

- There is currently no universal standard to measure and explain the effectiveness of different procedures. This study will be the first attempt at directly studying the efficacy and safety of competing glaucoma surgical procedures using *in silico* methods.
- There are many contradictory studies regarding the comparable efficacy and safety between trabeculectomy and NPDS. Most studies are retrospective *in vivo* studies, either using human participants or animal eyes. This can cause difficulty in studying surgical modifications as not all related properties can be held constant. An *in silico* CFD study, however, can achieve this.
- Though the outcome of different filtration surgeries may be similar, the post-surgical complications may vary greatly. The reason for this is still unclear and may be related to changes aqueous humour dynamics.

1.4 Hypothesis

The study posits a hypothesis that employing CFD to scrutinize different glaucoma surgical procedures can yield quantitative and qualitative insights into patient- and ethnic-specific considerations. In line with this hypothesis, the study formulates the following research questions:

- Does NPDS have the potential to be as effective in reducing IOP as trabeculectomy?
- Can computational models of the anterior chamber, whether generalized, ethnically representative, or patient-specific, enhance our understanding of aqueous humour dynamics following glaucoma filtration surgeries?
- Can these models provide insights into clinical implications such as IOP regulation, nutrient distribution, and risk of complications?
- Can the results from the above studies be used to recommend surgical methods for most effective and safe results depending on patient eye geometry?

1.5 Objectives

The primary aim of this study is to evaluate the immediate post-operative outcomes of different glaucoma filtration surgeries (trabeculectomy and NPDS) using CFD, with special focus placed on ethnic variation of the anterior segment.

This study will comprise of the following main objectives:

- Characterize and compare the flow behaviour of aqueous humour in the eye directly following trabeculectomy and NPDS procedures. This addresses the aim by quantifying post-operative flow alterations across procedures.
- Compare the efficacy in reducing IOP of the two procedures using results from CFD on an idealised model. This directly supports the aim by providing a reference condition for evaluating surgical modifications.
- Evaluate how anatomical differences between European and African eye geometries influence aqueous humour dynamics following glaucoma filtration surgeries. This fulfils the aim of assessing how patient anatomy influences surgical outcomes and potential complication risks.

1.6 Research Aim

Glaucoma encompasses various optic nerve disorders primarily associated with elevated IOP. The management of the disease focuses on IOP reduction through medications, laser treatments, implants, or surgeries. Trabeculectomy is currently considered as the gold standard of filtration surgeries. However, various other options exist, including NPDS – a less invasive filtration surgery. This study will mainly focus on trabeculectomy and NPDS.

While quantitative data resulting from this study will be discussed, a large focus will be on qualitative findings. Currently, there is a lack of quantitative clinical data related to clinical implications like nutrient distribution and potential complications. What is known is how certain flow alterations may influence these implications. Thus, while precise numerical comparisons to clinical outcomes is not yet feasible, the patterns and trends identified in the simulations are still highly valuable. These qualitative insights can guide understanding of fluid dynamics in the eye and its implications post-surgery.

This study advances the understanding of aqueous humour dynamics, particularly in the post-surgical context, where many mechanisms remain poorly understood. By focusing on the behaviour of aqueous humour after different glaucoma surgical procedures, the goal is to understand how specific changes in flow patterns could explain post-surgical complications such as nutrient deficiencies and other post-surgical complications. These insights are particularly valuable because they address knowledge gaps in the field, helping to clarify why certain complications may occur in some patients or ethnic groups and not others.

This approach enhances the clinical relevance of CFD without overextending its scope into unvalidated or purely theoretical territory. In short, the study is about connecting computational findings to clinical

practice and offering insights into how surgical decisions may need to be tailored based on factors like ethnicity or anatomy.

1.7 Assumptions and Limitations

In delineating the scope of this study, certain parameters and considerations have been defined.

This study will focus exclusively on fully developed eye geometries, aligning with the higher susceptibility of mature eyes to glaucoma. Thus, paediatric eye geometries will not be considered within the scope of this research. Additionally, as this study is the first of its kind, adult eyes will form the initial study since data for adult eyes are easier to access.

The study will narrow its focus to eye geometries of African and European descent for initial investigations. The developed methodology holds the potential for subsequent application to other ethnicities, including Hispanic, Asian, and beyond.

While various surgical procedures exist for glaucoma treatment, this research will specifically concentrate on trabeculectomy and NPDS. This deliberate choice aims to juxtapose an invasive approach with a non-invasive alternative. POAG, being the most prevalent form, will be the primary focus of the computational model.

Geometrical models for this study will assume that the eye has not undergone any previous surgeries or experienced additional eye-related diseases, aside from POAG. This assumption facilitates the isolation of risk factors, enabling an in-depth exploration of their individual impacts on aqueous humour flow. Consideration of other influencing factors, such as cataracts and eye medication, may be incorporated in subsequent research studies.

Flow-related results obtained from the study will primarily reflect early post-operative outcomes. Long-term analyses may be limited due to factors like scarring and other bio-features beyond the study's current scope. However, the qualitative extension of results may provide insights suggestive of potential links with long-term effects. Fluid dynamic metrics such as flow patterns, IOP, and WSS are reasonable proxies for evaluating surgical success.

1.8 Ethical Clearance

The following ethical clearance certificates were obtained to gather data for this study:

- Non-medical ethical clearance for survey of ophthalmologists (HRECNM20).
- Medical ethical clearance for enrolment of research participants to provide OCT scans and access to readily available database of OCT scans (M210520).

1.9 Structure of this Thesis

The thesis is structured as follows (Figure 5):

Chapter 2: A literature study of previous research conducted on glaucoma, specifically looking at trabeculectomy and NPDS, and how these surgical procedures have been modified to improve safety and efficacy. Emphasis is also placed on how glaucoma affects people of African descent in developing countries, including the cost-effectiveness of surgeries. Additionally, previous studies of anatomical systems using CFD and *in vitro* experiments are discussed.

Chapter 3: A chapter on theory that defines the key terms and terminology, as well as the necessary scientific formulae that were used throughout this project. The material properties of the eye tissues and the fluid properties of aqueous humour are defined. The creation of the computational model and the relevancy of Navier-Stokes in CFD is also discussed.

Chapter 4: This chapter explains the methodology, results, and discussion for simulating idealised geometry data and validating this against existing literature and in-vitro experiments. This section also includes the initial comparison between the outcomes of trabeculectomy, NPDS, and mNPDS on the idealised geometry.

Chapter 5: This chapter explains methodology, results, and discussion for simulating demographic-representative geometry and comparing the outcomes between trabeculectomy, NPDS, and mNPDS on the idealised geometry. This chapter includes a more detailed analysis of the resulting flow behaviour and wall shear stresses and what it could clinically indicate for patient-specific care.

Chapter 6: This chapter explains methodology, results, and discussion for simulating patient-specific geometry reconstructed from OCT scans. This chapter includes a discussion on whether detailed patient-specific scans are required for a more thorough understanding of patient-specific flow.

Chapter 7: Some final conclusions are drawn based on the results and recommendations are given to assist with any future studies to be performed.

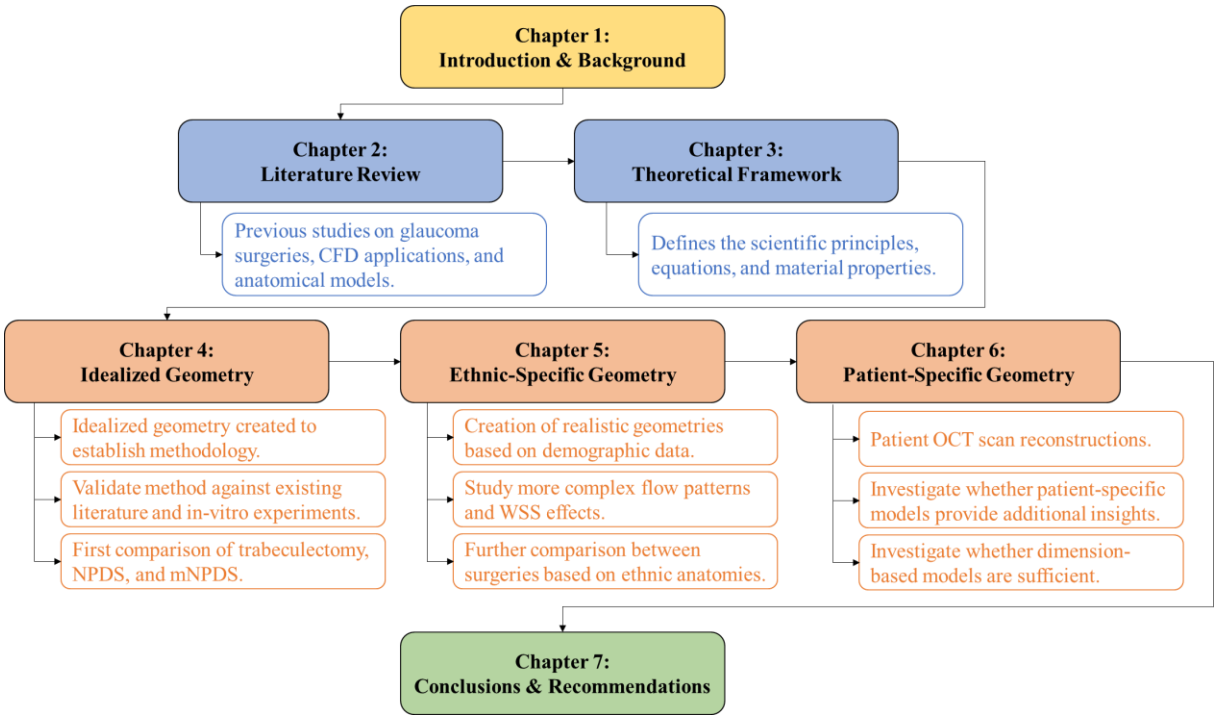


Figure 5 Flowchart to visually represent the thesis structure

2 Literature Review

2.1 Introduction

In this section, a literature review is performed to better understand the medical research that has been conducted by experts in the industry to improve treatments for glaucoma. The efficacy, safety, associated risks and cost-effectiveness of various treatments are discussed. This study also investigates research conducted *in silico* regarding general biomedical applications and, more specifically, applications to the human eye to assist in formulating the methodology for this project.

2.2 Glaucoma Prevalence and Outcomes for Different Ethnicities

It is well-established in literature that glaucoma is more prevalent in specific ethnicities [34]. People of African descent are at the highest risk of developing glaucoma and the success rates for their surgical treatments are generally lower [57,58].

There are many risk factors associated with the onset of glaucoma. Some of these risk factors can be associated with all ethnicities, including being male and being over the age of 50. There are direct relationships between glaucoma development and comorbidities such as hypertension diabetes and obesity [59]. An individual's risk may also increase due to lifestyle choices such as smoking, high alcohol consumption and steroid use. More specific to people of African descent, there seems to be a correlation between darker skin pigmentation and higher IOP [59]. Genetics may also play a role, though not many studies have been conducted to establish the index variants for people of African descent [60,61]. Those that have recently been conducted primarily aimed to determine the relationship between POAG and central corneal thickness (CCT) [62,63]. Though still not entirely conclusive, thinner CCT, as found in African populations, does seem to be a risk factor for glaucoma [64]. The study for this thesis will focus more on the geometrical eye structure together with the effect of pre-operative aqueous flow behaviour and its relationship to glaucoma in different ethnicities, rather than biological factors.

Many studies have been conducted regarding the relationship between race and glaucoma, specifically relating to anatomical and geometrical differences of the eye. A study conducted in 2003 suggested that the rim area of the optic disc was less pronounced in African people and suggested its relationship to the earlier development of glaucoma [65]. In 2015, another study noted that people of African descent tend to have shorter TM heights [66]. Since the TM is vital for the effective outflow of aqueous humour, the study suggests that the height could be a risk factor. Several other studies also suggest that there may be a relationship between the anterior chamber shape and the potential outcome of glaucoma surgeries [67–69].

A literature review conducted in 2016 stated from evidence that trabeculectomy is not as effective in treating African glaucoma than it is for their European counterparts, and that there is "a need for data on the efficacy of minimally invasive glaucoma surgery (MIGS) in Black populations" [57]. Factors such as variations in wound healing responses and fibrosis can influence the success rates of glaucoma surgeries in the African population [70]. There also seems to be a higher incidence of postoperative complications, including scarring and bleb failure, among African patients.

Overall, the findings underscore the importance of personalized treatment approaches in glaucoma management.

2.3 Safety and Efficacy of Trabeculectomy vs Deep Sclerectomy

Trabeculectomy is still the surgery of choice to treat glaucoma among a majority of ophthalmologists due its reputation for high efficacy. However, post-surgical complications can be frequent. Over-filtration causing hypotony, or under filtration causing a further increase in IOP, are both possibilities for any glaucoma filtration surgery, which could result in failure of the treatment. NPDS has emerged as a safer alternative procedure.

Glaucoma filtration surgery is generally assumed to be successful if the IOP remains between 6 and 21 mmHg [71] or at least a 20% reduction in IOP [14]. The efficacy of NPDS compared with trabeculectomy has been extensively debated [72,73]. This may be a reflection on surgical difficulties or technique [21]. In the following section, the literature comparing trabeculectomy and NPDS will be explored.

This long-term retrospective study of 201 eyes with POAG found that both NPDS and trabeculectomy achieved comparable success rates at 24 months [74]. NPDS was also associated with fewer postoperative complications compared to trabeculectomy, suggesting a more favourable safety profile. However, a randomized paired-eye study on POAG found that trabeculectomy achieved significantly lower IOP at major follow-up points (up to 18 months) and had a higher complete success rate compared to NPDS [75]. While both procedures indicated a reduction in IOP post-operatively, trabeculectomy had a higher probability of achieving success.

In a one-year prospective study, NPDS was modified using a shunt in an effort to improve its efficacy. The results showed that, with this modification, NPDS decreased IOP as effectively as trabeculectomy and fewer complications were experienced overall [27,71,76]. Other studies have demonstrated similar findings, supporting the hypothesis that NPDS with modifications can match trabeculectomy in efficacy [27,71,77,78].

In contrast to the above studies, NPDS without modification has been suggested an effective alternative to trabeculectomy and that trabeculectomy should rather be considered for patients that present with higher IOP [31]. A retrospective study in patients with Fuchs' heterochromic uveitis compared

trabeculectomy and NPDS, but outcomes in this cohort may not be generalizable to POAG, since intraocular inflammation can disproportionately disadvantage penetrating procedures [79]. However, another retrospective study in an adult POAG population with a follow-up period of 60 months came to a similar conclusion, with NPDS having more favourable outcomes across surgeons of varying experience [14].

In some prospective studies, NPDS has been found to be as efficient in lowering IOP with similar success rates and less complications [30,80,81]. A study in primary congenital glaucoma noted that NPDS was found to have comparable safety and efficacy to combined trabeculotomy–trabeculectomy in primary congenital glaucoma [29] , where scleral thinning is generally observed in clinical practice, potentially making NPDS advantageous. One 24-month prospective study found that NPDS allowed for better IOP control and demonstrated a lower rate of postoperative complications, such as fewer instances of choroidal detachment, late bleb fibrosis, visual field deterioration, and cataract progression [23].

The safety profiles of trabeculectomy and NPDS differ significantly due to the invasive nature of trabeculectomy. Specifically, thinner corneas and shallow anterior chambers seem to be a risk factor for hypotony and bleb failure [42,82]. A failed trabeculectomy may require additional surgeries, which could decrease IOP in the short-term, but cause irreversible eye damage in the long-term.

NPDS, as a minimally invasive procedure, is generally associated with fewer severe complications [30,80,81], while trabeculectomy has been known to result in more post-operative complications, and IOP outcomes can also be influenced by surgical factors such as scleral flap edge apposition [22,83].

While NPDS shows promise as a safer alternative to trabeculectomy, particularly with modifications, its long-term efficacy relative to trabeculectomy remains under scrutiny. Most studies referenced are *in vivo* clinical studies, but additional data is available. One mathematical model assessing aqueous humour outflow concluded that NPDS allows for higher outflow via natural pathways than trabeculectomy, which could contribute to its safety and efficacy profile [84].

While studies show that trabeculectomy often has a higher success rate, NPDS with modifications can achieve comparable IOP reductions with fewer complications. Retrospective and prospective studies have generally demonstrated similar long-term efficacy between the two procedures, with NPDS offering a better safety profile, particularly for patients at higher risk of complications. However, further research is needed to clarify their relative efficacy and long-term outcomes.

2.4 Scleral Flap Suturing to Control IOP

The scleral flap is a critical component of glaucoma filtration surgery, providing resistance that ultimately determines IOP after aqueous humour drainage. Several variables influence the effectiveness

of the scleral flap, including its size, shape, thickness, and suture tension. This section reviews the findings from various studies on the impact of these variables on IOP regulation.

The scleral flap in glaucoma filtration surgery has been the subject of many studies to determine whether the size and shape of the flap has a significant effect on IOP. One such study also found that minor changes in flap size (4x4 mm vs 3x2 mm) did not have a significant effect on IOP before suturing [85]. Numerical and physical modelling studies demonstrated that flap size impacts IOP minimally. While larger surface areas may reduce resistance slightly, the shorter dimension of the flap was found to be the primary factor affecting pressure differences across the flap [86]. Larger scleral flaps have been associated with greater pressure drops, especially when combined with reduced suture numbers [39].

The shape of the scleral flap, whether triangular, rectangular, circular, or semi-circular, has been examined for its impact on aqueous outflow. A study comparing triangular and rectangular flaps found no significant difference in IOP reduction before suturing but noted that thinner flaps resulted in larger pressure drops [87]. An experimental study observed that circular and semi-circular flaps had a more significant impact on IOP, resulting in up to a 39% increase in aqueous outflow compared to rectangular flaps [88]. While the flap shape influences initial aqueous flow and pressure drops, most clinical studies suggest that the long-term effects of flap shape on IOP are minimal [87].

The thickness of the scleral flap may also impact IOP outcomes. It has been suggested that the scleral flap should not be thinner than half the scleral thickness, which could lead to hypotony [83]. Consistent with these findings, an experimental and numerical study found that thinner scleral flaps result in larger pressure drops [39].

Scleral flap suturing, which determines the outflow resistance, is another crucial factor influencing IOP regulation. An *in vitro* study conducted in 2008 used six human donor eyes to study the effect of scleral flap tightness on IOP regulation following a trabeculectomy procedure [38]. The donor eyes had not undergone any previous ocular surgeries and IOP was regulated by means of constant infusion to remain between 23 and 30 mmHg for the duration of the experiment. The experiment had the donor eyes undergo the rectangular flap trabeculectomy procedure, after which the scleral flaps were tightly sutured to increase outflow resistance and the IOP was recorded after equilibrium was reached. An increased IOP was linked to increased suture tension (tighter suturing of the scleral flap). Adjusting suture tension postoperatively is a common strategy to fine-tune IOP and prevent complications such as hypotony or excessive pressure.

While the studies above primarily pertain to trabeculectomy, there is limited research on the impact of scleral flap manipulation in non-invasive surgeries like NPDS. One prospective clinical study was conducted in 2017 to examine the effects of sutureless deep sclerectomy for POAG [24]. After following up with a small participant group of 6 patients after a six-month period, it was found that IOP significantly decreased for all patients without any complications. These results suggest that sutureless

techniques may provide effective pressure control, though further studies are required to confirm long-term efficacy. However, more studies are required to determine the long-term effects.

It is important to note that the early postoperative period is indicative of the ultimate success or failure of the surgery [89,90]. Postoperative events such as inflammation, wound healing, and fibrosis/scarring in the subconjunctival space can significantly affect long-term outcomes.

The scleral flap's size, shape, thickness, and suture tension are key variables influencing IOP outcomes in glaucoma filtration surgery. While flap manipulation appears to have limited long-term impact on IOP, flap thickness and suture tension seem to be a more important for early postoperative outcomes. Further research is needed to extend these findings to non-invasive procedures like NPDS and explore the potential for sutureless techniques to improve surgical outcomes.

2.5 The Potential Clinical Implications of Biofluid Flow Changes

Aqueous humour carries essential nutrients, such as glucose, ascorbate, amino acids, and electrolytes, to the avascular tissues of the eye [45,91]. Alterations in aqueous humour flow caused by surgical interventions can lead to uneven distribution of these nutrients, especially near surgical sites where flow may become irregular or stagnated.

Nutrient imbalances in other tissues, like the heart or muscles, can lead to cellular dysfunction and impaired tissue repair. Similarly, nutrient deficiencies in the eye may result in delayed healing or contribute to inflammation. Studies on nutrient delivery in tissues with altered blood flow show that localized deficiencies can exacerbate injury and slow tissue recovery [92–94]. In the context of the eye, aqueous humour flow disturbances could deprive the corneal endothelium or lens of essential nutrients, leading to corneal decompensation, which is considered a serious post-surgical complication [95]. Uneven nutrient distribution has also been linked to the post-surgical complication of cataract formation [96,97], which is more likely to occur after trabeculectomy than NPDS [98,99].

In patients undergoing trabeculectomy, inadequate nutrient delivery due to flow alterations could promote fibrosis, reducing the long-term success of the surgery [100]. Similarly, in NPDS where the JCT is altered, a disruption in nutrient distribution can negatively impact the function of remaining tissues, leading to complications such as bleb failure or elevated IOP.

Battista et al. produced a study on trabeculated embryonic ventricles, providing insights into how small alterations in tissue morphology, such as in the TM, can drastically affect bulk flow and tissue structure [101]. Using *in vivo* models of intracardial haemodynamic structures, the study demonstrated that subtle changes in trabecular structure, such as flow steadiness, can result in significant vortex formation and alterations in shear stress distributions. When extrapolated to the eye, these findings highlight the potential effects of changes at the TM on aqueous flow. Vortex formation and irregular flow near surgical sites can increase shear stress on surrounding tissues. This, in turn, can lead to tissue

remodelling or fibrotic scarring, especially if the normal flow patterns are altered for extended periods. Additionally, small flow perturbations can lead to downstream effects in terms of fluid velocity and the distribution of mechanical stresses. In the eye, this could manifest as increased tissue stiffness or altered extracellular matrix deposition in the TM.

Flow changes in the eye are further evidenced by an *in vitro* investigation by Wiedenmann et al. on how interstitial fluid flow influences fibrosis, particularly in the context of glaucoma surgery [102]. The findings suggests that even small deviations from normal flow conditions in aqueous humour dynamics can contribute to fibrosis. The greatest risk of fibrosis occurs at low continuous flow rates of approximately 150 µL/h. This scarring could obstruct the surgical drainage pathways, reducing the success rate of procedures like trabeculectomy or other interventions aimed at lowering IOP. This has significant implications for glaucoma surgeries, as postoperative fluid dynamics might contribute to scarring and surgical failure.

A study by Pederson et al. discusses how fluid flow pathways through the TM and into Schlemm's canal are influenced by hydrodynamic resistance [103]. In filtration surgeries such as trabeculectomy, where new drainage channels are created, the direction of flow can have a significant impact on how effectively aqueous humour is drained from the eye. If flow is unevenly distributed or encounters areas of high resistance, this can lead to suboptimal IOP reduction, a critical factor for successful surgical outcomes. The study further highlights how shear stress in Schlemm’s canal can influence tissue remodelling and outflow capacity. This is particularly relevant in post-surgical scenarios, where the direction and velocity of aqueous humour flow might alter the mechanical forces exerted on tissues, potentially affecting the long-term success of filtration surgery. If the flow direction is such that shear stress is concentrated in certain areas, this may lead to localized scarring or even failure of the filtration site.

One imaging study also suggests that minor anatomical changes in the Schlemms’ canal, such as narrowing or alterations in the inner wall, can have significant effects on aqueous humour outflow [53]. These changes directly influence the resistance of the outflow pathway, which in turn affects IOP regulation. It may then be possible to apply this concept to other anterior chamber parameters for studying the outcomes of filtration surgery.

The comparison of aqueous humour flow under various conditions can reveal critical insights into the implications of altered aqueous humour dynamics.

2.6 Computational Models to Study Aqueous Humour Dynamics

The use of numerical and computational models to study anatomical systems has gained more traction in recent years as a means to better understand biofluidic flows and their effects [104]. The purpose of these types of studies is mainly to assist in clinical applications such as drug delivery, diagnosis,

prognosis, and treatments. The use of *in silico* methods is common in hemodynamic studies that apply to the femoral arteries, cerebral arteries, carotid arteries, etc. to gain a better understanding of blood flow and how it affects specific diseases [105–108]. Computational models have also been used to study aqueous humour dynamics and its effects on eye movement, drug delivery and ocular diseases like glaucoma [47,49,109–111].

Aqueous humour dynamics is arguably the most important factor when studying glaucoma as it directly impacts IOP. Therefore, a comprehensive understanding of aqueous humour flow, including its related mechanisms like the ciliary body, the TM and the uveoscleral body, is critical for the present study. It has been stated that a better understanding of aqueous humour outflow and its pathways could lead to enhanced patient-specific treatments [16].

Aqueous humour is modelled as a Newtonian fluid due to its fluid properties closely resembling the fluid properties of water [112]. Aqueous humour is produced in the ciliary body through a series of mechanisms namely diffusion, ultrafiltration and active secretion [45]. As mentioned in section 1.1.1, aqueous humour is produced at a constant rate of approximately 2.5 ml/min. Aqueous humour exits through uveoscleral body at approximately the same rate to maintain a constant IOP. The outflow of aqueous humour may change with age, and, in a healthy eye, the ciliary body will reduce production to leave the IOP unchanged.

The TM is a triangular-shaped porous tissue [113]. From the TM into the Schlemm's canal, aqueous humour is transported through natural convection. A study using a mathematical model of the TM and Schlemm's canal found that the distribution of aqueous humour outflow through these channels could strongly affect IOP [114]. This distribution has also been linked to changes in WSS in the Schlemm's canal [115].

In previous computational studies, the TM is generally modelled as a porous medium consisting of parallel capillary tubes with variable permeability [112]. Porosity and permeability have been shown to directly influence eye IOP distribution [116]. Several CFD models have been developed to study aqueous humour dynamics. Clinical observations and predictions may be possible using CFD in ophthalmology [117].

These types of models have mainly been used to study the outcome of trabeculectomy and its modifications, including how aqueous humour outflow is affected by drainage devices and other implants [24,118–120]. These studies have suggested that the type and position of an implant can affect the aqueous humour outflow [50]. Novel implants and even IOP measuring technology have been developed from such models [121–123].

One of the earliest 3D CFD models developed in 2016 reconstructed the model using microphotographs of healthy eyes [124]. The boundary conditions were then manipulated to simulate glaucoma conditions for further study. In 2016, an idealised geometry of the anterior segment was modelled in CFD to study

how the iris interacted with changes in aqueous humour flow [125]. The model was validated using a 3D-printed phantom and particle image velocimetry (PIV). The study was able to establish a relationship between IOP and iris deformation. Other studies have used numerical models to study the effect of age and IOP on corneal thickness [126]. PIV methods, together with 3D-printed models, have been successfully applied to study anatomical systems, which can be used to validate the *in silico* models. One such study concluded that 3D-printed models "reduces the complexity, time and effort required" to study flow visualization simulations [127,128].

Though many computational models have been developed to study aqueous humour dynamics and how it may improve surgical techniques, none have been used to compare the outcome of two competing glaucoma surgical techniques. The only mathematical model found that has been used to compare trabeculectomy with NPDS was conducted in 2009, though CFD was not utilized [84]. The study found that NPDS allows for more outflow of aqueous humour at high pre-IOP.

2.7 Summary

POAG is a common disease that is more prevalent in the African ethnicity than any other ethnicity. Trabeculectomy is the current gold standard for treating POAG and no other surgical procedure has been shown to be more effective for treating glaucoma. However, NPDS may present as a safer alternative and can be just as effective with the appropriate modifications. The size and shape of the scleral flap does apparently not have a significant effect on decreasing IOP, however altering the tightness of scleral flap suturing may offer better IOP control following filtration surgery. A CFD model presents the opportunity to study the effects of these surgeries and their modifications on anatomical variations that occur with different ethnicities *in silico*. This study could give an indication of the possible success of the pressure relief following filtration surgeries on different eye geometries subjected to different pre-IOP.

3 Theoretical Framework

3.1 Ocular Fluid Dynamics

CFD is a branch of fluid mechanics that leverages numerical methods and algorithms to analyse and simulate the behaviour of fluid flows. The primary goal of CFD is to understand and predict the intricate details of fluid motion in various environments by solving the governing equations of fluid motion.

At its core, CFD involves solving the Navier-Stokes partial differential equations, which describe the motion of fluids based on conservation laws of mass, momentum, and energy. However, solving these equations analytically is often nearly impossible due to their complexity in real-world scenarios, leading to the adoption of numerical methods. To address this challenge, CFD employs numerical methods to discretize the fluid domain and solve the governing equations approximately.

Several numerical methods can be employed to discretize and solve the Navier-Stokes equations, the most common being the Finite Difference Method (FDM), Finite Element Method (FEM), and Finite Volume Method (FVM). Each method has its unique approach to breaking down the fluid domain, handling discretization, and solving the fluid flow problem.

FDM involves discretizing the fluid domain into a grid of points and approximating the derivatives of the Navier-Stokes equations using differences between function values at these grid points. The method is relatively simple and efficient but is limited by its reliance on structured grids, making it less flexible for complex geometries.

FEM subdivides the fluid domain into small elements, which form an unstructured mesh. Each element is associated with interpolation functions that approximate the solution across the element. FEM is highly versatile and is well-suited to complex geometries and multiphysics problems. However, it can be computationally intensive and is not as commonly used for fluid flow problems in CFD as FVM.

FVM is most commonly used in CFD to discretize the fluid domain into smaller control volumes (or cells) and integrates the governing equations over each control volume. This method ensures the conservation of mass, momentum, and energy across the boundaries of each control volume, making it particularly well-suited for fluid dynamics problems. In FVM, the fluxes of quantities are calculated at the faces of each control volume, and the values at the cells' centres are interpolated between the control volume faces. This method's flexibility is especially useful in handling unstructured meshes.

Since the human eye is an organ that can be considered as a complex system, FVM-based CFD simulations is an appropriate tool for modelling and analysing aqueous humour flow within the eye. By simulating the fluid dynamics, the impact of various factors, such as changes in the geometry of the eye, the structure of drainage pathways, and the influence of diseases on fluid flow can be investigated.

This information could aid in identifying potential risk factors and designing interventions for better management of ocular conditions.

3.2 Assumptions & Governing Equations

Creating a comprehensive eye model for CFD involves making several assumptions to simplify the complex biological reality. The following assumptions are necessary to streamline the mathematical representation of ocular fluid dynamics and facilitate numerical simulations:

- **Incompressibility**: The aqueous humour is treated as incompressible, since the density variations in ocular fluids due to pressure changes are typically small.
- **Steady-state flow**: The eye model assumes steady-state fluid flow, since most physiological processes in the eye occur on a timescale where transient effects are minimal.
- **Newtonian fluid behaviour**: The ocular fluid behaves as a Newtonian fluid. Aqueous humour primarily consists of water, with dissolved salts, proteins, and other small molecules. While the fluid used for CFD might not perfectly represent the rheological properties of biological fluids, it simplifies the equations and is a reasonable approximation for many scenarios. The viscosity of the aqueous humour is low and does not vary significantly with changes in shear rate, which is in line with the majority of aqueous humour modelling studies adopting a Newtonian assumption [125,129].
- **Rigid tissue structures**: In the present models, the surrounding eye tissues like the cornea are considered rigid. These tissues are relatively stiff and have high tensile strength. The cornea is a tough, collagen-rich structure that maintains the shape of the anterior part of the eye and withstands intraocular pressure. This simplifies the simulation by avoiding the need to model the deformable nature of tissues. While this assumption may not be completely accurate, the effects of tissue deformation may be secondary to the primary focus of fluid dynamics.
- **Absence of eye movement**: Eye movements such as saccades can induce transient flow effects However, these were not included since the focus was on steady-state post-operative outcomes under upright and supine conditions.

The fundamental equations governing fluid flow in the eye model of this study are based on the incompressible Navier-Stokes equations and the Boussinesq approximation to address temperature-induced density variations. In the eye, there can be small but significant temperature gradients, particularly between the warmer tissue structures (approximately 37°C) and the cooler aqueous humour produced (approximately 35°C) [124]. These temperature differences can lead to slight variations in the density of the aqueous humour. Even small density variations due to temperature can lead to buoyancy-driven flow within the anterior chamber of the eye [130]. The Boussinesq approximation is used to capture these effects without needing to solve for full compressible fluid equations, which would be computationally expensive and unnecessary given the small magnitude of the density changes.

The incompressible Navier-Stokes equation describes the conservation of momentum, accounting for pressure, viscous forces, and gravitational effects:

$$\rho(v \cdot \nabla v) = -\nabla p + \mu \cdot \nabla^2 v + \rho g \quad 3.1$$

Where:

- ρ is the fluid density,
- v is the fluid velocity vector,
- p is the fluid pressure,
- μ is the dynamic viscosity of the fluid, and
- g is the gravitational acceleration vector.

The Boussinesq approximation simplifies the density term, assuming it remains close to the reference density (ρ_0). Therefore, the density is replaced with the reference density ($\rho = \rho_0$) in all terms of the governing equations, except for the buoyancy term, which considers temperature-induced density variations:

$$\rho = \rho_0[1 - \beta(T - T_{ref})] \quad 3.2$$

Where:

- T is the fluid temperature,
- β is the thermal expansion coefficient, and
- T_{ref} is the reference temperature.

The only place where the temperature-dependent term is retained is in the buoyancy term ($\rho g\beta(T-T_{ref})$) in eq. 3.1. This term represents the density difference caused by temperature variations, and it is typically much smaller than the reference density. Therefore, the Boussinesq approximation allows for the inclusion of the significant effect of temperature on buoyancy while maintaining the simplicity of treating the fluid as incompressible in most other aspects.

In essence, the Boussinesq approximation acknowledges the compressibility effects due to temperature variations but retains the convenience of an incompressible fluid assumption for the majority of the fluid flow equations.

The combined equation incorporates the effects of incompressible flow and buoyancy due to temperature changes. It captures the complexity of fluid dynamics in the eye, where variations in temperature play a role in the overall behaviour of aqueous humour flow:

$$\rho v \cdot \nabla v = -\nabla p + \mu \cdot \nabla^2 v + \rho_0 g\beta(T - T_{ref}) \quad 3.3$$

3.3 The Trabecular Meshwork

The TM is the part of the ocular drainage system that plays a crucial role in regulating IOP. Situated in the angle between the iris and the cornea, the TM serves as the primary outflow pathway for aqueous humour from the anterior chamber of the eye. Its intricate architecture and specialized cellular composition facilitate the controlled drainage of aqueous humour, ensuring a balance between production and outflow, which is vital for ocular homeostasis.

The TM comprises multiple layers, namely the uveal meshwork, corneoscleral meshwork, and juxtacanalicular tissue (JCT), as depicted in Figure 6. Each layer is distinguished by its anatomical location and cellular composition.

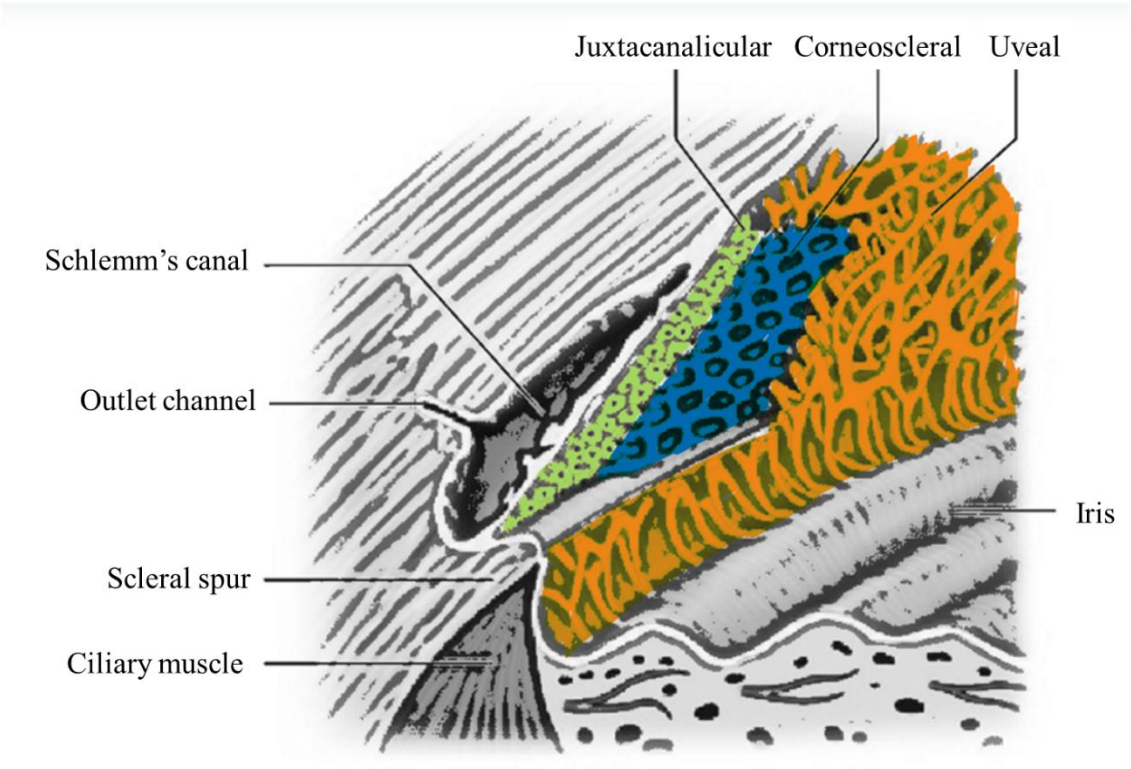


Figure 6 Cutaway view of the three layers of the trabecular meshwork (inspired by [131])

The uveal meshwork consists of fenestrated trabecular beams lined by endothelial cells. These beams form a sieve-like structure that permits the passage of aqueous humour into the Schlemm's canal. The corneoscleral meshwork is characterized by thicker trabecular beams interspersed with extracellular matrix components. This region provides structural support to the TM and facilitates the transmission of aqueous humour from the uveal meshwork. The JCT, which comprises densely packed extracellular matrix and a network of cells, including fibroblasts and endothelial cells, modulates the main resistance to aqueous humour drainage [132], which can be approximated as 90% of the TM resistance, influencing overall IOP levels.

The exact outflow distribution varies between individuals, but this complexity cannot yet be modelled in detail. Therefore, simplified outlet distribution will be imposed, which is sufficient for relative comparisons between surgical models. While the TM comprises distinct layers, these layers are anatomically and functionally interconnected. The porous structure of the TM allows for the passage of aqueous humour across its entire span, facilitating fluid flow from the anterior chamber to Schlemm's canal. Recent image-based CFD modelling has demonstrated that the velocity distribution throughout the TM structure is highly heterogeneous[133]. Thus, the TM can be modelled as a single porous region, which preserves the continuity and interconnectedness of its constituent layers, reflecting the physiological process of aqueous outflow. Additionally, simulating the flow through individual layers of the TM separately would entail a significant increase in computational complexity and resource requirements.

The concept of homogenization is commonly employed in CFD to model complex porous media as effective homogeneous structures. By treating the TM as a homogenized porous region, the intricate details of its microstructure and individual layers are encapsulated within the porous medium properties, such as permeability and porosity. This approach allows for the representation of heterogeneous structures within a simplified framework, while still capturing the essential fluid flow characteristics and pressure dynamics.

Darcy's law is a fundamental principle in porous media flow, describing the relationship between fluid velocity and pressure gradient in a porous medium. In the context of aqueous humour flow through the TM, Darcy's law provides a framework for quantifying the permeability of the trabecular meshwork and its connection to IOP variations.

Darcy's law can be expressed mathematically as:

$$Q = -\frac{\alpha A_c}{\mu}\frac{dp}{dx} \tag{3.4}$$

Where:

- Q is the volumetric flow rate,
- α is the permeability of the porous medium,
- A_c is the cross-sectional area through which the flow occurs, and
- $\frac{dp}{dx}$ is the pressure gradient over the porous medium.

Thus, the pressure gradient across the TM structure is influenced by the permeability of the TM, which in turn affects the IOP. As IOP varies, the pressure gradient across the trabecular changes, impacting the rate of aqueous humour outflow. To account for these variations, the permeability can be adjusted based on the prevailing IOP (normal and glaucomatous conditions).

In Ansys Fluent, the pressure gradient source term can also be represented as a power law of the velocity magnitude [134], expressed as:

$$S_i = -C_0|v|^{C_1} \quad 3.5$$

Where:

- S_i is equal to the pressure gradient over the porous medium,
- C_0 and C_1 are constants that govern the behaviour of the fluid (where $C_0 = 1$ for laminar flow), and
- v is the superficial velocity at the inlet of the porous region.

The constants C_0 and C_1 can be determined in this way and applied to a porous fluid zone in Ansys Fluent to simulate the outflow resistance through the TM.

3.4 Material & Fluid Properties

Material and fluid properties serve as fundamental inputs in computational simulations because they dictate how materials and fluids behave under various conditions. These properties are necessary for accurately modelling the physical processes that occur within the system being simulated. In CFD simulations, properties such as density, viscosity, and thermal conductivity govern the flow behaviour and heat transfer characteristics of the fluid. Similarly, a solid material was defined for the cornea, iris, and TM structures which allows for the setup of appropriate boundary conditions. For example, temperature conditions on the corneal and iris wall can be applied, which influence the convective flow within the anterior chamber due to the Boussinesq approximation. Additionally, since the TM is defined as a porous medium, the solid material imposes resistance to the flow of aqueous humour passing through it, based on the porosity and permeability values.

Aqueous humour is a clear, watery fluid that closely resembles water in terms of fluid properties. Since aqueous humour is also primarily composed of water, the fluid property values are suitable for modelling the behaviour of aqueous humour. The properties are provided in Table 1.

Table 1 Fluid property values for water [135]

Aqueous humour fluid property	Symbol	Unit	Value
Density (Boussinesq)	ρ_f	kg/m^3	1000
Specific heat capacity	c_f	J/(kg·K)	4182
Thermal conductivity	k_f	W/(m·K)	0.6
Viscosity	μ_f	kg/(m·s)	0.001
Thermal expansion coefficient	β_f	K^{-1}	0.0003

The material properties for the eye tissue are required as the solid medium that forms the porous structure of the TM, as well as the corneal wall of the anterior chamber. These properties are provided in Table 2.

Table 2 Material property values for general eye structures [136]

Eye tissue material property	Symbol	Unit	Value
Density	ρ_s	kg/m^3	1058
Specific heat capacity	c_s	J/(kg·K)	4178
Thermal conductivity	k_s	W/(m·K)	0.58

These fluid and material properties provide the necessary inputs for simulating the behaviour of aqueous humour and eye tissue in Ansys Fluent.

3.5 Q-Criterion and λ2-Criterion

In addition to the typical fluid dynamic analysis parameters, like pressure, velocity, and WSS, the vorticity of aqueous humour flow will also form part of the analysis in this study, specifically in section 5.4. The vorticity will be analysed using the parameters Q-criterion (Q) and λ_2-criterion (λ_2), which will attempt to quantify the flow behaviour and its potential clinical implications. Vorticity is a measure of local rotation in a fluid flow and is defined as the curl of the velocity field (u):

$$\omega = \nabla \times u \qquad 3.6$$

A high magnitude of vorticity indicates strong local rotation.

The Q-criterion measures the relative dominance of rotational effects over strain effects in the flow field. A higher Q-criterion value suggests stronger rotational motion, or more intense swirling or

vortices. Rotational regions can be detected where $Q > 0$, indicating an alteration in the aqueous humour flow and potential flow irregularities. Larger rotational regions could indicate increased flow recirculation in certain parts of the eye, which may imply inefficient flow transport, as vortices can trap fluid and slow down drainage. The Q-criterion is mathematically defined as:

$$Q = \frac{1}{2}(\|\Omega\|^2 - \|S\|^2) \tag{3.7}$$

Where:

- Ω is the antisymmetric part of the velocity gradient tensor (∇u), representing rotation, and
- S is the symmetric part of the velocity gradient tensor, representing strain.

The λ_2-criterion identifies vortex cores by locating regions of local pressure minima due to rotational motion in a reference frame. A value of $\lambda_2 < 0$ indicates stronger, more well-defined vortex core and can reveal areas of stagnation or persistent disturbances. Lower λ_2 values suggest that the vortices are more concentrated and intense, with stronger core dynamics. This indicates more localized disturbances in the flow, which could be due to sharp geometrical features. The matrix is given as:

$$M = S^2 + \Omega^2 \tag{3.8}$$

By analysing these vorticity parameters, an improved understanding of pathological changes in the eye can be developed. In turn, this may inform surgical intervention approaches and provide insights into how vortex dynamics influence IOP and aqueous humour drainage efficiency.

3.6 Optical Coherence Tomography

Optical coherence tomography (OCT) is a non-invasive imaging technique that provides high-resolution, cross-sectional images of biological tissues. OCT can also be described as a computer-aided instrument that is used to generate cross-sectional 2D images of the ocular structure. The average commercially available OCT has an axial resolution of approximately 10 μm [71]. OCT uses light waves directed at the frontal plane of the eye that are then reflected from various depths to reconstruct an axial image. These cross-sectional images (B-scans) provide detailed information about the internal structure of tissues. These images are typically displayed as grayscale or false-colour representations, with brighter regions indicating higher reflectivity. An example of such a scan is provided in Figure 7.

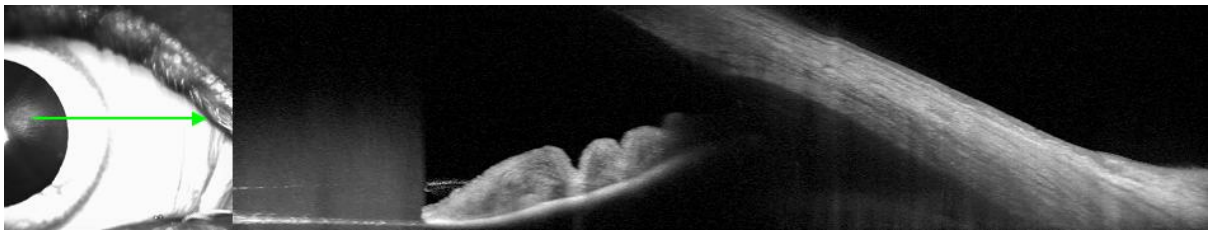


Figure 7 Frontal view of eye and its resulting axial image using OCT

OCT can be utilized to reconstruct 3D models of the anterior segment of the eye, including structures such as the cornea, anterior chamber, iris, and lens.

By raster scanning across the tissue, a series of B-scans are acquired at different lateral positions, covering the entire region of interest. The acquired B-scans can then be processed to align and register them spatially. Once aligned, the stack of B-scans is stacked together to form a volumetric dataset representing the anterior segment of the eye. Image processing techniques are applied to enhance contrast, reduce noise, and improve the quality of the volumetric dataset. Segmentation algorithms are then employed to delineate the boundaries of anatomical structures within the anterior segment, such as the cornea, iris, anterior chamber angle, and lens.

Using the segmented volumetric dataset, 3D models of the anterior segment are generated. Surface rendering algorithms convert the segmented boundaries into smooth, continuous surfaces, creating realistic representations of the anatomical features.

4 Idealised Model

The main objective of the section is to evaluate the immediate post-operative outcomes of various glaucoma filtration surgeries, namely NPDS, mNPDS, and trabeculectomy, on an idealised eye model using a commercial Ansys Fluent package for CFD simulations. This analysis aims to assess how each surgical procedure influences IOP reduction and general aqueous humour flow dynamics. By leveraging a 3D eye model with simplified geometry, the study seeks to simulate the effectiveness of these surgical interventions.

An idealised 3D model of the eye was developed from previous study at Aston University [137], which was later adapted for the work presented in this thesis. The 3D model of the eye was constructed using Autodesk Inventor®, a CAD software, due to its capability to handle complex geometries and provide detailed anatomical representations. The flow domain to be used for simulations is the anterior chamber, which includes key structures such as the pupil, corneal wall, iris wall, Schlemm's canal, TM, and collector channels (see Figure 3). A total of 26 outlets were included to correspond with the study from Villamarin et al. [124] for validation purposes.

The flow domain as it is extracted from the entire eye structure is depicted in Figure 8, which is superimposed onto a sketch of the other parts of the unmodelled eye for ease of reference. The model's primary goal was to replicate the anatomical features and the physiological flow conditions of the aqueous humour to ensure physiological relevance of the study.

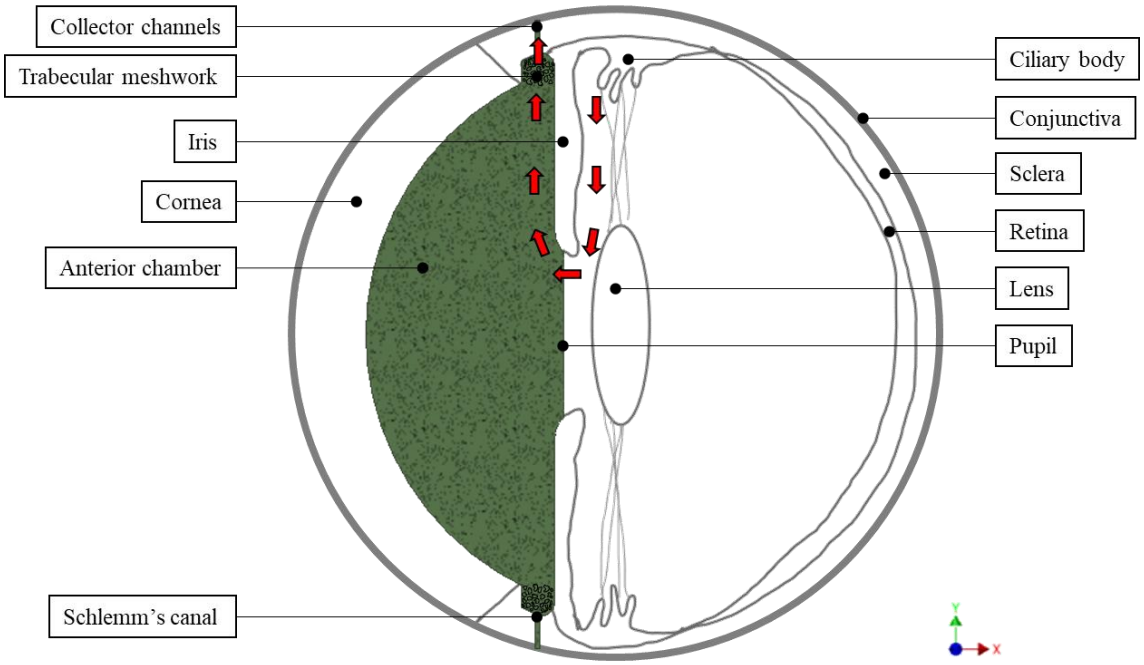


Figure 8 Flow domain representation (green) and flow direction (red arrows) for normal and glaucomatous eye conditions.

Adhering to the geometrical specifications observed in previous studies [124,138], the model included key components such as the pupil as the inlet of the aqueous humour flow to the flow domain to be studied and collector channels as the outlets, as shown in Figure 9. The flow domain was divided into four main bodies: the anterior segment (including the pupil and cornea), the trabecular meshwork, Schlemm's Canal, and the outlet channels. The length of the TM was modelled as an average length of 800 µm, with an average outlet diameter of 100 µm selected for the outlet channels [66].

Since this methodology will further be expanded to run more than 20 models later in section 5, the pupil was selected for the aqueous humour inflow to reduce computational complexity across multiple simulations. This simplification significantly reduces runtime while preserving physiological relevance, as the pupil naturally serves as the conduit between the posterior and anterior chambers. This assumption will be confirmed in the validation portion in section 4.3 of this thesis.

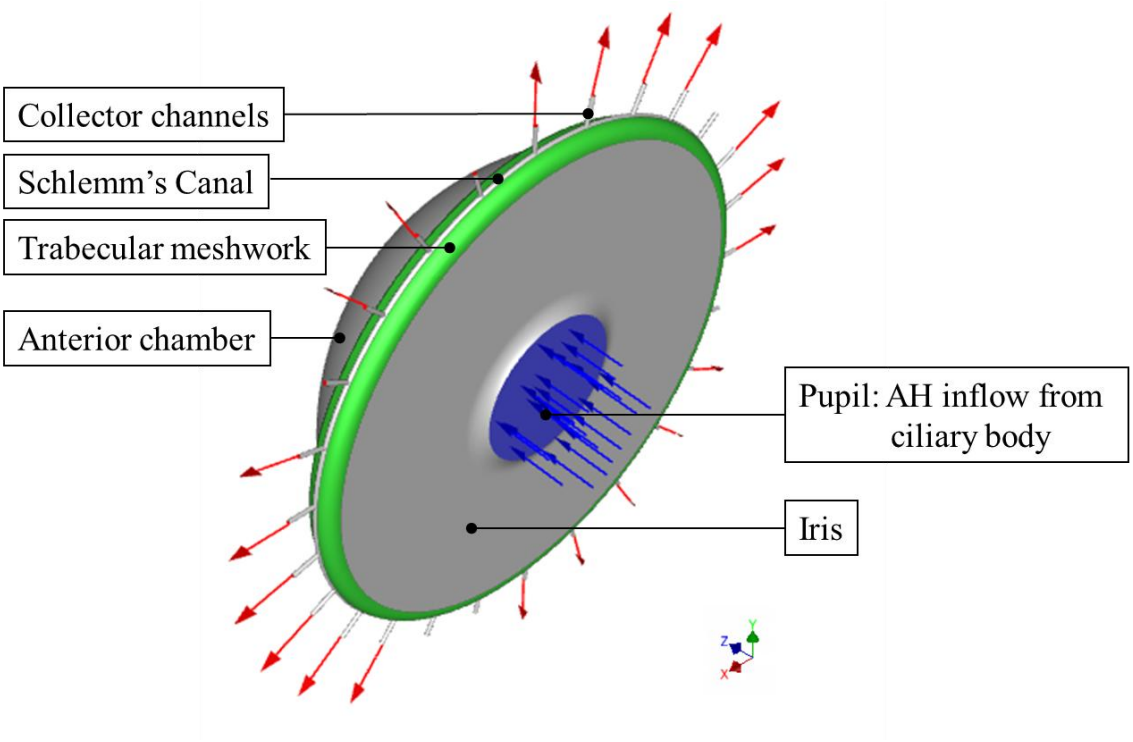


Figure 9 Flow region of the anterior chamber in an idealised eye model for normal and glaucomatous eye conditions.

The CFD simulations were conducted using Ansys Fluent 2021 R2. The aqueous humour was treated as an incompressible Newtonian fluid with properties as described in section 3.4. Steady-state laminar flow conditions were assumed throughout the simulations with non-slip, rigid walls.

The conditions for laminar flow were checked using the Reynolds number equation:

$$Re = \frac{\rho_f v D}{\mu_f} \tag{4.1}$$

Where:

- ρ_f is the fluid density for aqueous humour,
- v is the superficial velocity, and
- μ_f is the fluid dynamic viscosity for aqueous humour.

The superficial velocity is calculated as

$$v = \frac{\dot{m}}{\rho \cdot A_c} \tag{4.2}$$

Where:

- $\dot{m}$ is the mass flow rate at the pupil inlet (as produced by the ciliary body), and
- A_c is the cross-sectional area of flow, which can be measured using the measuring tool in Inventor.

For normal eye conditions, an inlet mass flow rate of 5E-08 kg/s was set at the pupil to replicate the average production of aqueous humour. A pressure outlet boundary was set to 7 mmHg at the end of each outlet channel to mimic typical outflow conditions [124]. The Reynolds number was calculated both at the pupil inlet and the collector channel outlets of the model. The results are summarised in Table 3. Since the result at the inlet and outlet conditions indicate a Reynolds number well below 2300, the assumption for laminar flow holds.

Table 3 Summary of Reynolds number calculations

Fluid/geometry property	**Symbol**	**Unit**	**Value (pupil inlet)**	**Value (collector channel outlet)**
Density	ρ_f	kg/m^3	1000	1000
Viscosity	μ_f	kg/(m·s)	1.00E-03	1.00E-03
Diameter	D	m	3.67E+00	1.00E-01
Cross-sectional area	A_c	m	1.06E+01	7.85E-03
Mass flow rate	$\dot{m}$	kg/s	5.00E-08	5.00E-08
Superficial velocity	v	m/s	4.73E-12	6.37E-09
Reynolds number	$\boldsymbol{Re}$	-	**1.74E-05**	**6.37E-04**

The fluid dynamics were governed by the Navier-Stokes equations for incompressible flow and the Boussinesq approximation to account for temperature variations within the eye as described in section 3.2. The importance of buoyancy-driven flow in the eye was verified using the densimetric Richardson number, calculated as:

$$Ri = \frac{g'(\partial \rho_f / \partial z)}{(\partial v / \partial z)^2} \quad 4.3$$

Where:

- g' is reduced gravity,
- z is the vertical height in the fluid flow system, and

The results are summarised in Table 4. The calculated Richardson number was based on the flow entering the pupil and resulted in a value in the order of 10^7. A Richardson number value >0.25 indicate that the viscous forces dominate, and turbulence is suppressed [139].

Table 4 Summary of Richardson number calculations

Fluid/geometry property	Symbol	Unit	Value
Density at ciliary body	ρ_i	kg/m^3	1000
Density at anterior chamber	ρ_o	kg/m^3	993.37
Change in density	$\Delta\rho = \rho_i - \rho_o$	kg/m^3	6.63
Gravitational acceleration	g	m/s^2	9.81
Characteristic length	L	m	4.40E-03
Iris diameter	D	m	3.67E-03
Iris area	A_c	m	1.06E-05
Mass flow rate	$\dot{m}$	kg/s	5.00E-08
Superficial velocity	v	m/s	4.73E-06
Richardson number	$\boldsymbol{Ri}$	**-**	**1.06E+07**

The TM was modelled as a porous medium using Darcy's law as described in section 3.3 to simulate resistance to aqueous humour outflow. The required parameters are provided in Table 5. Firstly, the change in pressure (Δp) over the TM was determined by selecting the desired IOP within the anterior chamber, which is 13.5 mmHg for normal flow and 27 mmHg for glaucomatous to correspond with Villamarin et al. [124]. The change is pressure is calculated as

$$\Delta p = IOP - p_o \quad 4.4$$

Where:

- IOP is the static pressure within the anterior chamber, and
- p_o is the outlet pressure boundary condition.

Next, the source term (S_i in eq. 3.5) can be calculated as

$$S_i = \Delta p / \Delta m \quad 4.5$$

Where:

- Δm is the equivalent height of the TM.

An equivalent height is used since the TM does not have a uniform height, which could cause some variations between the calculated permeability and the permeability required to reach the target IOP.

Finally, eq. 3.5 is used to determine the coefficient C_0 to fully define the porous TM zone in Fluent. Additionally, eq. 3.4 can be rearranged to determine the permeability of the TM. The viscous resistance, which can also be applied to the porous zone instead of the power law model, is $1/\alpha$. The various values from these calculations are summarised in Table 5. Many of the values are identical and so the ones that are different are highlighted for ease of reference. These are related to the targeted IOP and power law coefficients.

Table 5 Parameters to define the porous zone in Ansys Fluent for idealised models.

Parameter description	Symbol	Unit	Normal flow	Glaucomatous flow
Boundary conditions				
Target IOP	IOP	mmHg	13.5	27.0
Outlet pressure	p_o	mmHg	7.00	7.00
Change in pressure	Δp	mmHg	-6.50	-20.0
Inlet mass flow rate	$\dot{m}$	kg/s	5.00E-08	5.00E-08
Porous region properties				
Superficial velocity	v	Pa·s	1.71E-06	1.71E-06
Porous zone area	A	m^2	2.92E-05	2.92E-05
Equivalent TM height	Δm	m	6.76E-04	6.76E-04
Power law coefficients				
Source term = dp/dx	S_i	Pa/m	-1.28E+06	-3.94E+06
Pressure jump coefficient	C_0	-	7.49E+11	2.30E+12
Flow coefficient	C_1	-	1	1
TM permeability	α	m^2	1.34E-15	4.34E-16
Viscous resistance	C	m^{-2}	7.49E+14	2.30E+15

The simulation was configured to analyse the fluid flow using a 3D, double-precision, pressure-based, laminar model to correspond with the assumptions stated in section 3.2. The goal was to investigate the behaviour of aqueous humour flow through the trabecular meshwork and outlet pathways, incorporating heat transfer while neglecting factors such as solidification, radiation, and species transport. The

simulation was run in a steady state to observe the effects of aqueous humour flow under various boundary conditions.

The material properties used in the simulation included those for aqueous humour, both with and without the Boussinesq approximation, and corneal tissue, as described in section 3. The corneal tissue properties provided the necessary parameters for accurately simulating heat transfer within the model.

Four fluid zones were defined in the model as shown in Figure 10: the main anterior chamber flow (yellow), the TM (orange), the Schlemm's canal (blue), and the outlet channels (green). The anterior chamber flow zone represented the bulk flow of aqueous humour, treated as a standard fluid zone without any motion or porosity. The TM flow zone was treated as a porous medium to account for the resistance to aqueous outflow, using a power-law formulation for flow resistance. The outlet pathways zone handled the flow exiting the anterior chamber through the collector channels, also modelled as a fluid zone.

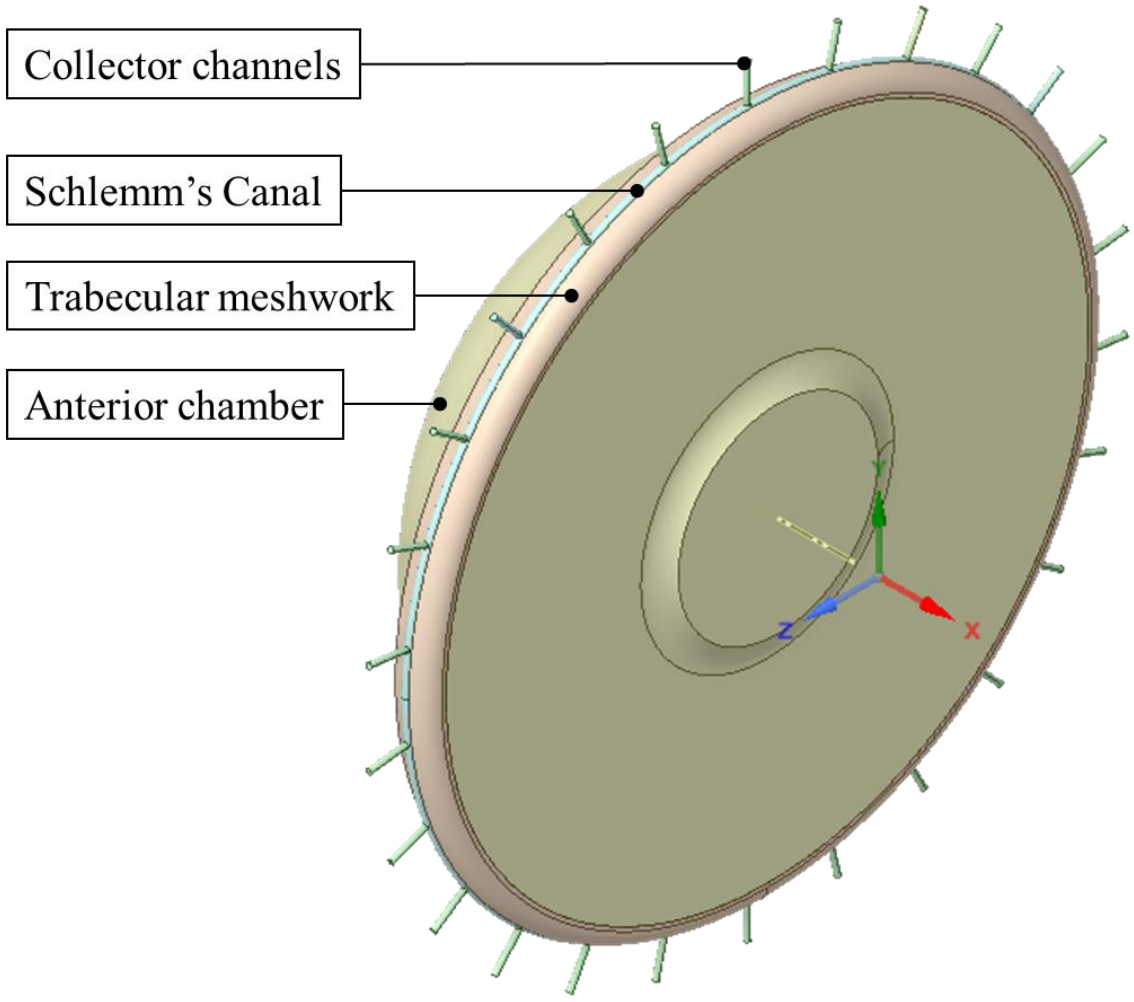


Figure 10 Defined fluid flow zones of the eye anterior segment

The boundary conditions were set to reflect the physiological environment of the anterior chamber and for later comparison with literature for validation [129,140]. At the inlet, a mass flow rate of 5e-08 kg/s was specified, representing the inflow of aqueous humour, with a temperature of 310.15 K to approximate body temperature. The walls of the model, including the TM and outlet pathway walls, were treated as stationary surfaces with no-slip boundary conditions. Temperature boundary conditions were applied to simulate thermal interaction between the fluid and the surrounding tissues. The outlet boundary was modelled as a pressure outlet with a gauge pressure of 7 mmHg, representing normal intraocular pressure at the collector channels. In the collector channels, the aqueous humour flow typically remains slow and steady. The drainage through the trabecular meshwork and into Schlemm's canal, then into the collector channels, is primarily pressure-driven and does not involve significant velocity changes. Thus, a static pressure boundary is sufficient for this outlet. The corneal wall was maintained at a constant temperature of 307.15 K [124].

The solver settings were configured to ensure accurate flow and thermal results. Pressure-velocity coupling was handled using the SIMPLE algorithm, which is effective for low-speed incompressible flows like those found in the anterior chamber [141]. Second-order discretization schemes were applied to both pressure and momentum to enhance accuracy, while second-order upwind schemes were used for energy calculations. Under-relaxation factors were set to 0.3 for pressure and 0.7 for momentum, with an energy factor of 1.0, ensuring stable and convergent solutions throughout the simulation process.

4.1 Trabeculectomy, NPDS, & mNPDS

The idealised model was used to simulate three glaucoma filtration surgeries: trabeculectomy, non-penetrating deep sclerectomy (NPDS), and a modified NPDS (mNPDS) with JCT meshwork removal as described in section 1.1.3 and 1.1.4. Each surgical procedure was modelled by altering the geometry and boundary conditions accordingly.

After filtration surgery, the surgical incision introduces a new, low-resistance drainage pathway for the aqueous humour. The incision is the Kelly punch for trabeculectomy, the scleral flap for NPDS, and the scleral flap with additional JCT membrane peel for mNPDS. This pathway can exhibit higher flow velocities compared to the TM and collector channels, especially if the pressure gradient between the anterior chamber and the incision is large. Higher velocities can lead to high WSS, which could have clinical implications and will be discussed in the following sections.

The solver should account for any increase in flow velocity and the associated dynamic pressure as aqueous humour drains through the incision. Thus, a total pressure boundary was applied to the incision outlets on all of the subsequent surgical simulation models.

The trabeculectomy model included a 0.8 mm Kelly punch incision through the TM to create a drainage pathway for aqueous humour. An iridectomy is commonly performed to allow some of the aqueous humour to bypass the flow path around the iris and drain directly through the Kelly punch incision. This involves cutting a section of the iris no smaller than 2 mm [142]. For ease of simulation, the iridectomy was modelled as a circular incision with a hydraulic diameter calculated using the formula for the diameter of an equivalent circle from an equilateral triangle with a side length of 2.2 mm:

$$D_{ID} = \frac{a}{\sqrt{3}} \tag{4.6}$$

Where:

- a is the side length of the equilateral triangle.

The resulting hydraulic diameter was 1.27 mm. The resulting flow domain is depicted in Figure 11, which shows the same anterior segment as described Figure 8. However, the Kelly punch sclerostomy has been added to the flow domain to represent the surgical incision made during a trabeculectomy (highlighted in a lighter shade of green). Additionally, the iridectomy (triangular incision made in the iris) has also been added to the anterior chamber, which forms a new flow pathway for the aqueous humour.

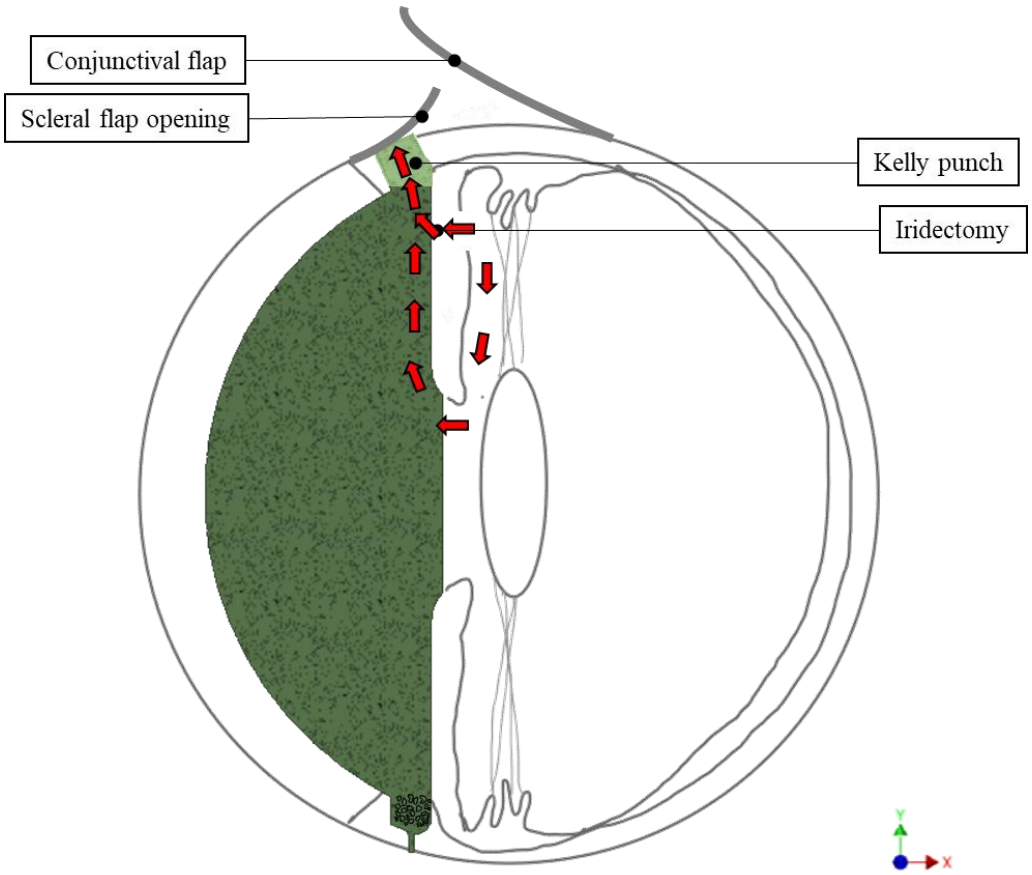


Figure 11 Flow domain representation (dark green), the new addition to the flow domain, namely the Kelly punch surgical site (light green), and flow direction (red arrows) for trabeculectomy conditions.

The trabeculectomy procedure results in two inlets namely the pupil and the iridectomy. The total inflow is kept constant at 5E-08 kg/s like with the normal and glaucomatous models. The mass flow rates are automatically divided according to area ratio by Ansys Fluent and checked once the solution had converged.

NPDS is a surgical procedure to lower IOP in glaucoma patients. NPDS involves a 4x4 mm excision of deep scleral tissue to create a scleral lake and deroofing Schlemm's Canal to expose the JCT meshwork. The superficial scleral flap remains in situ, allowing aqueous humour to drain from the sides.

The NPDS involves creating a flap depth to 50% thickness of the superficial scleral flap and extending the excision into the peripheral cornea. The scleral lake allows for the collection of aqueous humour, facilitating its drainage. At the anterior extent of the sclerectomy, the Schlemm’s canal is deroofed, exposing the JCT.

To model NPDS, the existing model was modified by scleral flap. The flow domain is illustrated in Figure 12, which shows the same anterior segment as described Figure 6. However, the deep scleral flap has been added to the flow domain to represent the surgical incision made during a NPDS procedure (highlighted in a lighter shade of green). The blue circle shows a zoomed-in version of the surgical site

to more clearly show where the deroofing of the Schlemm's canal is modelled between the scleral flap and the TM.

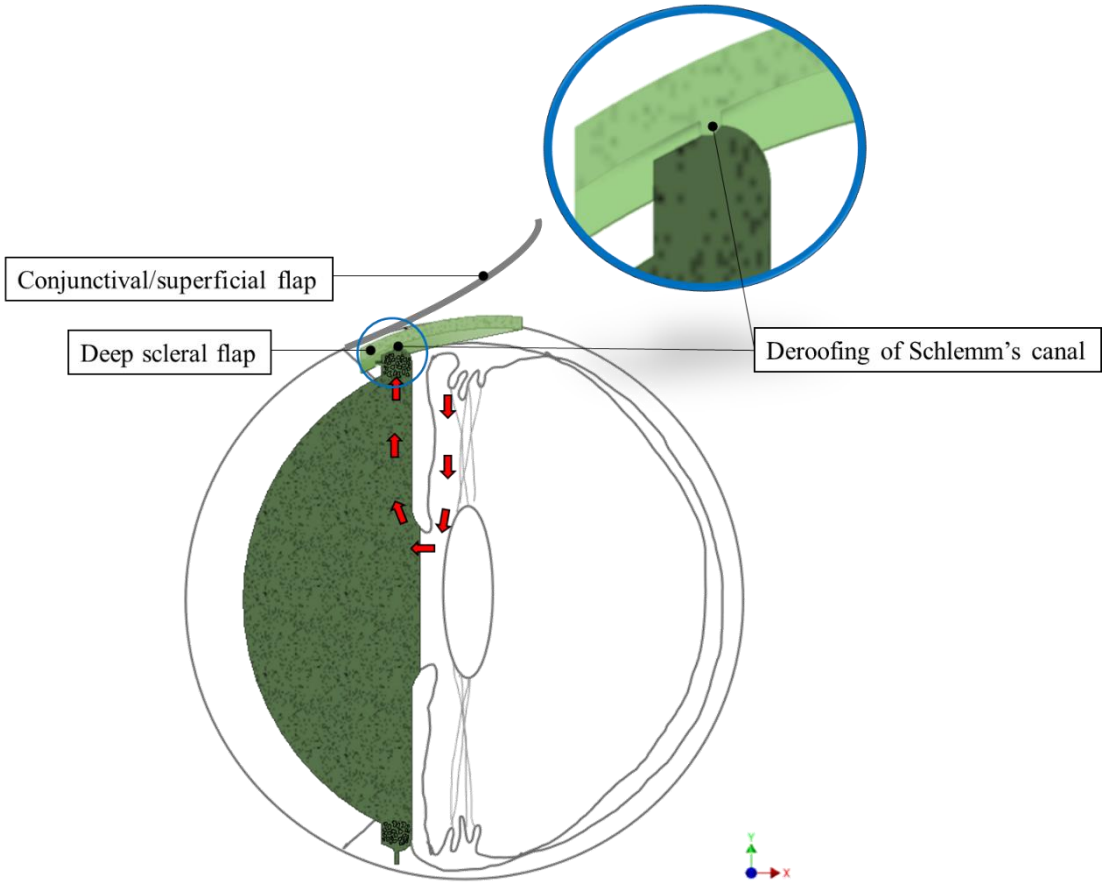


Figure 12 Flow domain representation (dark green), the new addition to the flow domain, namely the deep scleral flap surgical site (light green), and flow direction (red arrows) for NPDS conditions.

The mNPDS includes an additional step of removing a section of the JCT meshwork. This procedure involves an incision made at the edge of the deroofed Schlemm's canal area to a depth of 20 μm [143], and the juxtacanalicular membrane is detached and extracted along the length of the deroofed area. Thus, the 3D model was modified by removing the area representing the JCT directly under the deroofing of the Schlemm's canal.

For all cases, the same inlet mass flow rate, outlet channel pressure, and TM permeability were applied. The surgeries were simulated as "undergoing surgery" by creating incisions open to the atmosphere in setting the incision total outlet pressures at 0 mmHg. This was followed by suturing, or "after surgery", to restore tension to the anterior chamber by setting the scleral flap boundary at 7 mmHg to simulate postoperative conditions, which will restore tension to the anterior chamber by creating resistance to flow. No clinical data were found that expressly indicate the pressure resistance of eye sutures. Since the exact outlet pressure resulting from sutures is not known, a value of 7 mmHg was selected under the assumption that the suture pressure should be close to the original outlet pressure of the collector

channels before the operation [129]. However, this may vary depending on suture tightness and surgical technique, which will further be investigate in 5.4.5. Both were simulated using separate steady state simulations. The simulations setups are depicted in Figure 13.

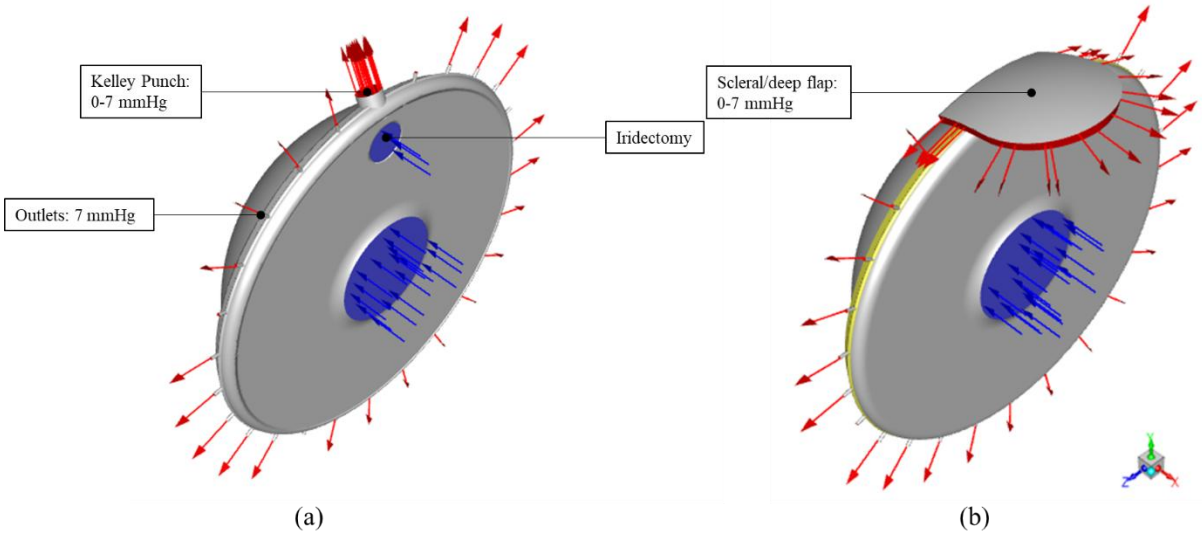


Figure 13 Flow region of the anterior chamber in an idealised eye model for (a) trabeculectomy and (b) NPDS and mNPDS.

4.2 Mesh Independence Study

The model for normal and glaucomatous flow was previously checked for mesh refinement by Alimahomed [137]. Due to the complex geometry, a tetrahedral mesh was chosen to ensure accuracy with fewer elements. The cornea was divided into 0.09 mm cells, along with a smooth transition inflation mesh on the boundaries of the anterior chamber. The inflation mesh included five layers with a growth factor of 1.3 for smooth transition into the bulk flow. This type of unstructured mesh in the bulk regions of the anterior chamber allow for flexibility and adaptability to complex geometries [144]. The mesh size was selected to adequately resolve bulk flow in the anterior chamber while maintaining computational efficiency, while also accounting for the smaller outlet structures, resulting in a total of 4,755,738 elements. The mesh's average skewness (acceptable values at <0.33) and aspect ratio (acceptable values at <5) yielded acceptable values of 0.214 and 2.113, respectively [144,145]. The mesh is illustrated in Figure 14.

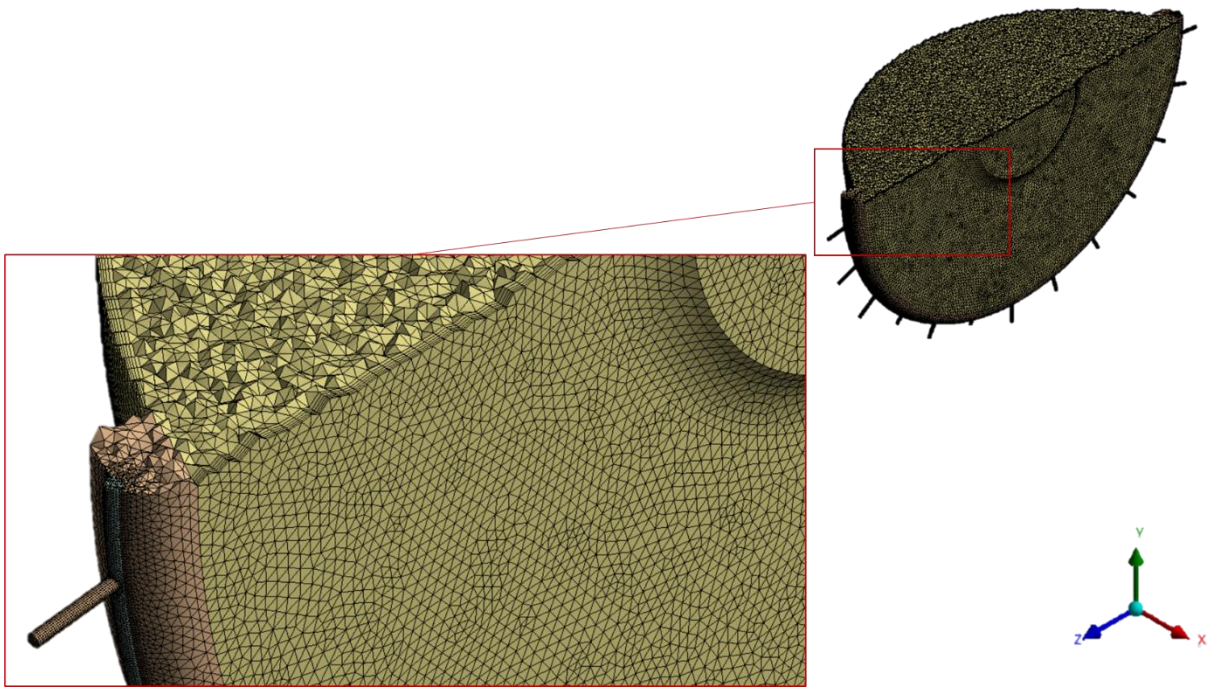


Figure 14 Resulting mesh for the anterior chamber eye model (cross-sectional view on the XZ-plane)

Further mesh independence studies were performed on the trabeculectomy and NPDS models. Similar to the normal eye model, a tetrahedral mesh was chosen to accommodate the complex geometry of the eye.

In all cases, body sizing with a smooth transitioning inflation mesh was used. To ensure the mesh's effect on the results was minimal, IOP was selected as the key parameter as the mesh independence study was performed as this is an integral parameter in eye health. The mesh was considered sufficient when the IOP value differed by less than 1%, as demonstrated in Figure 15 for both the trabeculectomy and NPDS models.

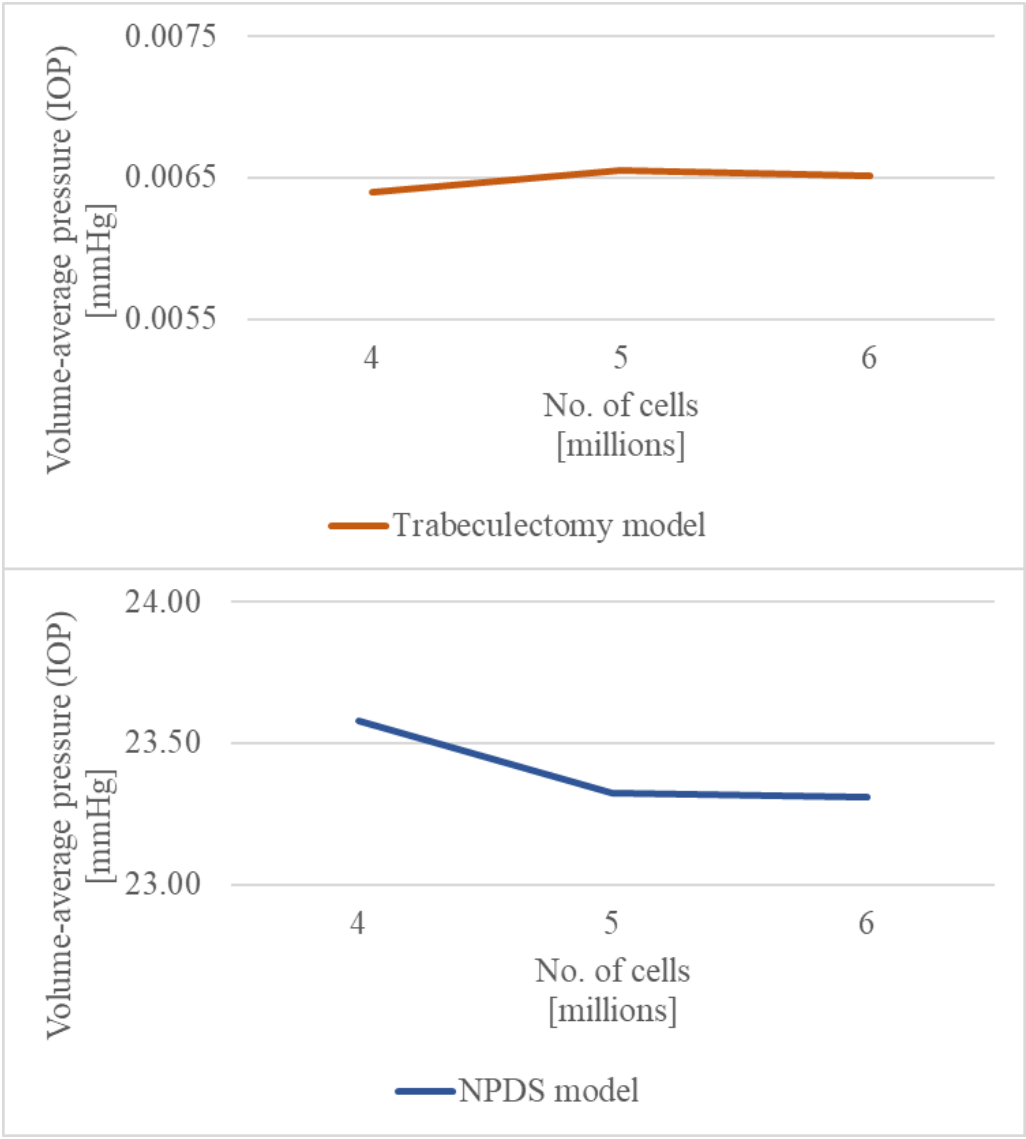


Figure 15 Mesh independence study results of number of cells vs volume-average pressure (IOP) for the trabeculectomy model (left) and NPDS model (right).

For both models, the same mesh element size used for the normal model was found to be sufficient. In general, an average skewness value that is less than 0.33 is recommended, while aspect ratios larger than 5 should be avoided in the bulk flow [145]. The mesh used for the trabeculectomy model comprised 4,645,559 cells and had acceptable average mesh skewness and aspect ratio values of 0.22 and 1.87, respectively. For the non-penetrating deep sclerectomy (NPDS) models, the mesh contained 4,956,830 cells, with an average skewness of 0.21 and an aspect ratio of 2.11, both deemed acceptable.

The present study did not compute local grid convergence index values due to the strong global convergence already demonstrated. Future studies could incorporate this analysis for additional rigor. However, the flow features were checked across coarse, medium, and fine meshes, and no significant qualitative differences in recirculation zones, velocity profiles, or WSS distributions were observed. This supports the <1% quantitative convergence reported.

4.3 Model Validation

4.3.1 Validation Based on Previous Computational Studies

The idealised model's validity was verified through analytical equations and validated against previous studies. The permeability values for the trabecular meshwork were calculated using Darcy's law and then applied to the CFD model to simulate different IOP conditions. The results from these simulations were compared to the established values in the Villamarin et al. study [124] for validation purposes.

To achieve a normal IOP of 13.5 mmHg, Darcy's law was applied to calculate the permeability value that corresponds to this IOP, which was then assigned to the porous zone in the model. The resulting permeability value was found to be 1.33E-15 m^2, closely matching the value reported by Villamarin et al., which was 1.5E-15 m^2 for achieving the same IOP. This permeability was then incorporated into the computational model, yielding an IOP of 13.51 mmHg.

Under glaucomatous conditions, Darcy's law produced a permeability value of 4.34E-16 m^2 to reach an IOP of 27 mmHg. The study by Villamarin et al. reported a similar value of 5E-16 m^2, supporting the accuracy of the current results. The discrepancies between the permeability values in this study and previous work are likely due to variations in the eye model geometry, as the reference study did not fully detail its model geometry.

Further comparison was done between the velocity fields from the idealised eye simulation (Figure 16) and the Villamarin et al. results (Figure 17). Although the present model does not include the posterior chamber, inflow was applied at the pupil to reduce computational load across a large simulation set. While this assumption might exclude some localized dynamics at the posterior chamber, comparison against the Villamarin et al. results confirmed that this assumption maintains the fidelity of anterior chamber dynamics, making it a valid and efficient modelling choice.

For the idealised eye simulation, the velocity magnitude peaks at approximately 0.48 mm/s, as indicated by the colour scale. The highest velocities are located near the exit of the collector channels and exhibit a circular pattern around the centre in both the upright and supine conditions. In the upright condition (Figure 16a), the fluid forms a clear vortex structure with a high concentration of velocity in the middle. Similarly, in the supine position (Figure 16b), two vortices form symmetrically around the centre, with a lower velocity in the peripheral regions.

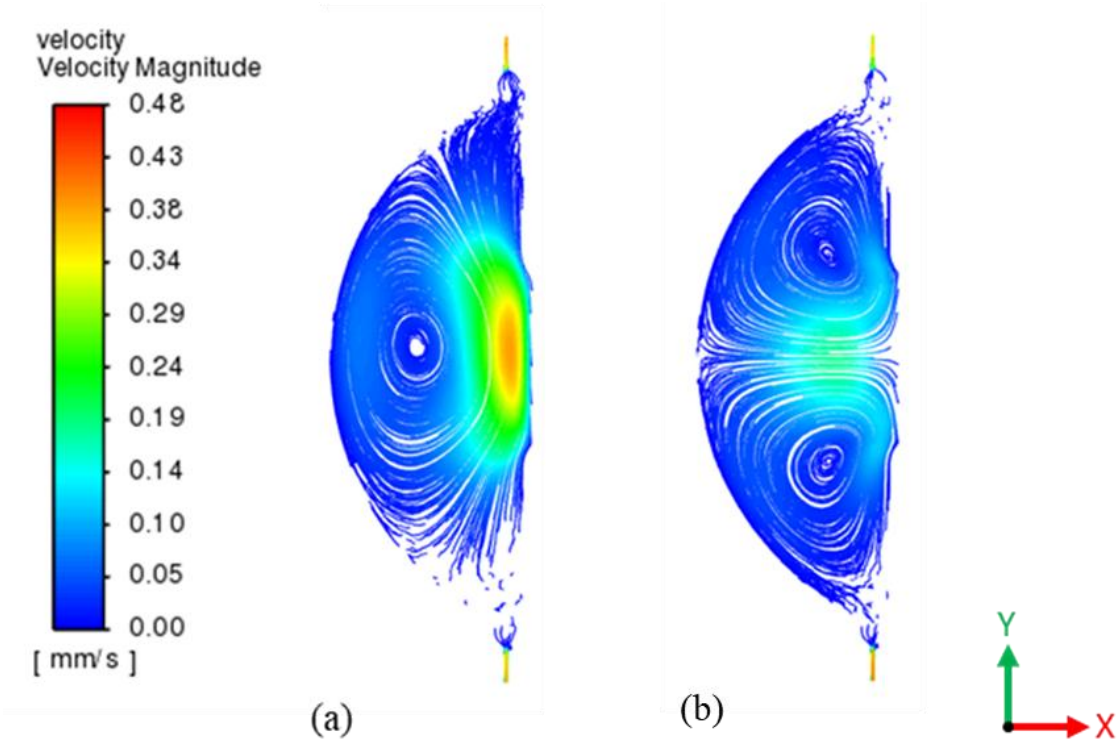


Figure 16 Idealised model velocity pathline results for normal conditions when the model is oriented in the (a) upright and (b) supine position.

The velocity magnitude in the Villamarin et al. simulations reach up to 5.0E-04 m/s (0.5 mm/s) in the upright condition (Figure 17C), similar to the idealised eye simulation results. In the supine condition (Figure 17A), the peak velocity increases to approximately 1.2E-04 m/s (0.12 mm/s). The idealised model results predict higher velocities in this condition, which could be a result of geometrical differences since the exact geometry parameters were not provided by the Villamarin et al. study.

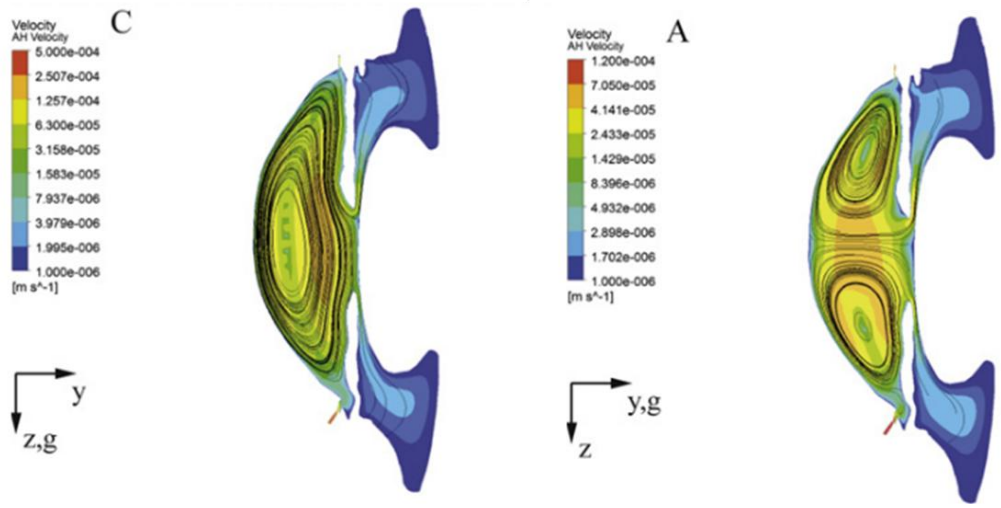


Figure 17 Velocity pathline results from the Villmarin et al. study oriented in the (a) upright and (b) supine position [124]

Both the idealised eye simulation and Villamarin et al.'s study demonstrate similar overall trends in the velocity field, particularly in the presence of vortex structures and the impact of gravity on flow patterns in the anterior chamber. Despite some slight discrepancies, the similar vortex behaviour and the alignment of velocity magnitudes is consistent with the known behaviour of aqueous humour flow, supporting the validity of the results.

The WSS distributions between the idealised simulation (Figure 18) and the results from Villamarin et al. (Figure 19) were also compared. Both the upright and supine conditions show a relatively smooth, symmetrical distribution of WSS across the cornea. The peak WSS is concentrated near the centre in both cases, particularly in the upright position (Figure 18a and Figure 19A). The WSS patterns are also radial and concentric under upright conditions, with a strong central focus of high stress, gradually decreasing toward the periphery.

In the supine position (Figure 18b), the distribution has some regions of higher stress concentrated toward the centre but spread more horizontally. In the Villamarin et al. study, the WSS distribution becomes more heterogeneous (Figure 19B), showing elevated WSS in horizontal bands along the mid-periphery, and lower WSS near the centre and outer edges.

Both the idealised CFD model and Villamarin et al.'s results show that WSS is highest in the central corneal region under upright conditions and that the WSS becomes more horizontally distributed when in the supine position. This trend validates that the initial simulation captures the gravitational influence on fluid dynamics within the eye, as Villamarin et al.'s study also identified this shift.

For the idealised eye simulation, the maximum WSS values range from 3.6E-04 to 4.0E-04 Pa. The overall scale shows a relatively confined peak of high WSS at the centre of the cornea, with most of the peripheral regions experiencing much lower WSS.

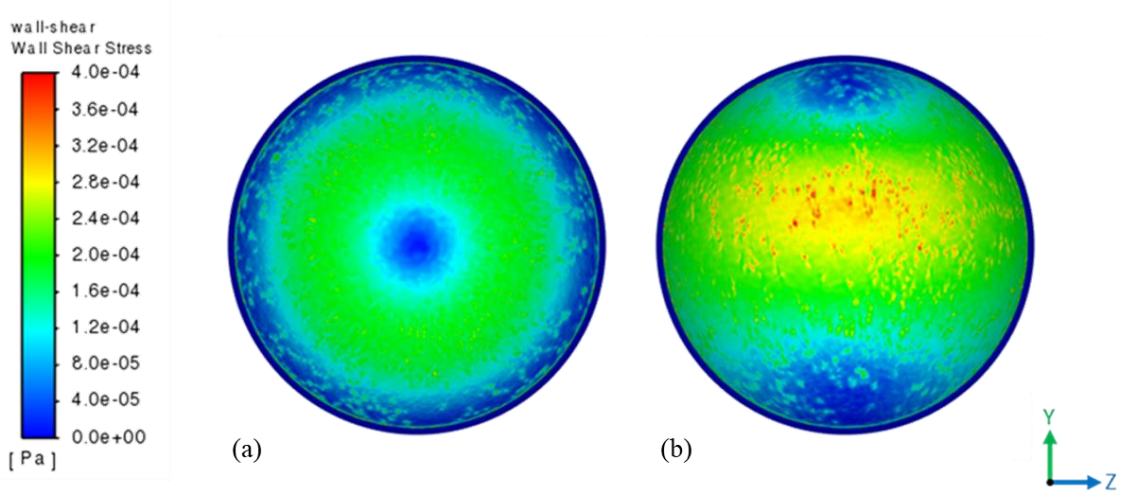


Figure 18 Idealised model WSS results for normal conditions when the model is oriented in the (a) supine and (b) upright position

The Villamarin et al. simulation shows a slightly wider range of WSS, with the peak values reaching up to 5.5E-04 to 6.5E-04 Pa, particularly in the supine condition. This suggests a somewhat higher WSS, especially in the horizontal bands observed in the supine configuration.

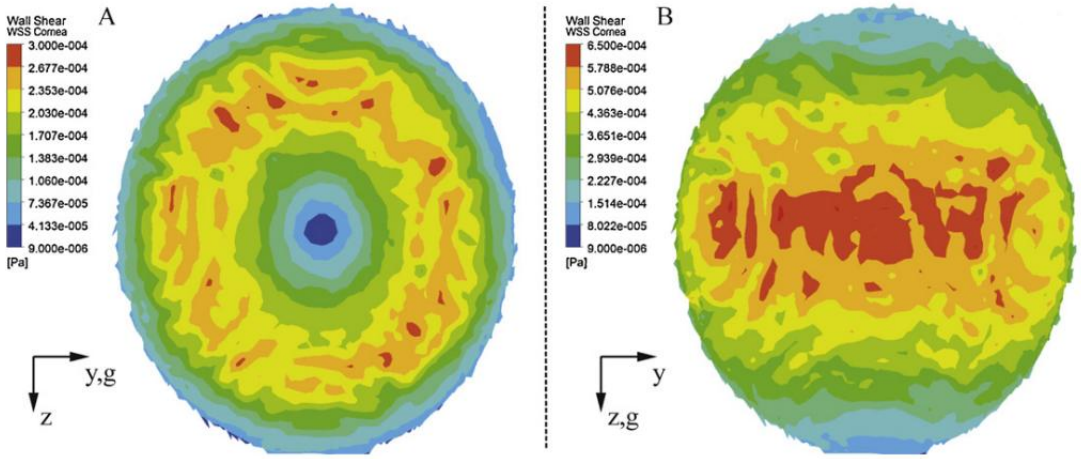


Figure 19 WSS results from the Villamarin et al. study oriented in the (a) supine and (b) upright position [124]

While the overall WSS patterns are similar, Villamarin et al.'s model seems to predict a higher magnitude of WSS and more distinct banding in the supine condition. This may be due to differences in the specific eye geometry, mesh resolution, or the fluid flow parameters used in their study compared to this study. However, the consistency in outcomes reinforces the validity of the current model's results.

4.3.2 Validation Based on Experimental Studies

A student project (by E.J.H. van der Vinne at the University of Twente supervised by me) attempted experimental flow visualisation as well as preliminary particle image velocimetry (PIV) setups to qualitatively compare the CFD model with in-vitro results. The study is detailed in Appendix A, and will be briefly summarised in this section.

In van der Vinne's experiment, two dye visualisation experiments were performed, namely without a temperature gradient and with a temperature gradient. The dye visualisation without a temperature gradient showed a concentrated flow dispersing outward symmetrically. The experimental data and CFD results align closely here, but the presence of buoyancy-driven effects became more pronounced when the temperature gradient was introduced, which disrupted symmetry and induced floating behaviour, as shown in Figure 20. While this qualitative comparison highlights asymmetry, it validates that temperature affects flow patterns.

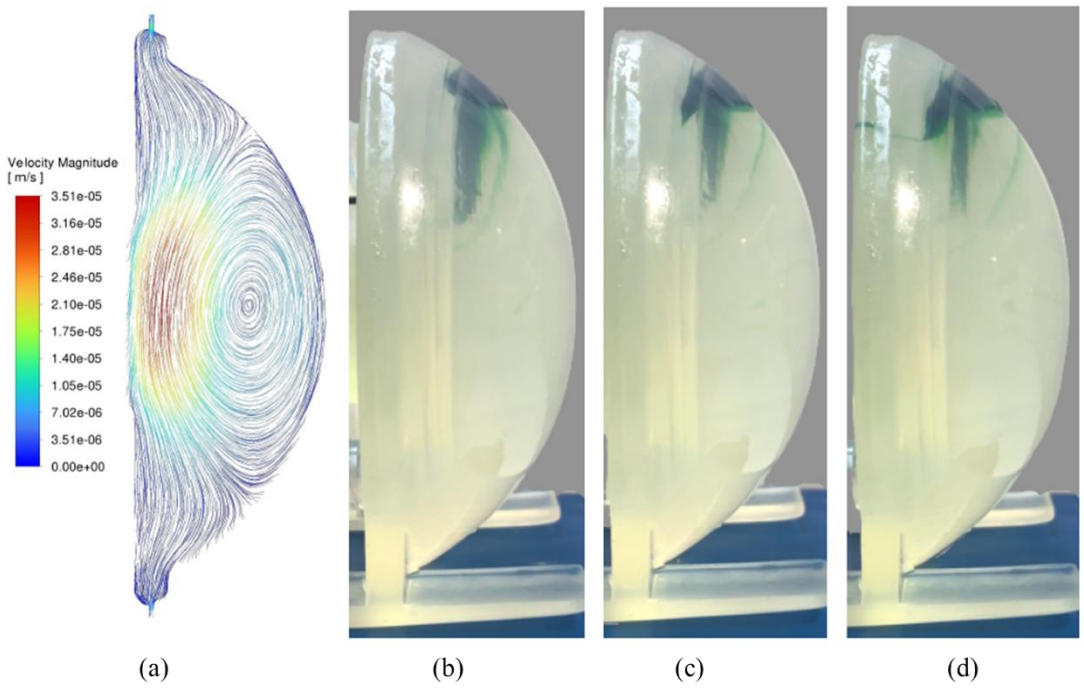


Figure 20 (a) CFD simulation on the xy-plane comparison for experimental dye visualization with temperature gradient at (b) 30 seconds, (c) 60 seconds, (d) 90 seconds [146].

Due to the way the flow phantom for van der Vinne's experiments were printed, only upright positions could be studied. A PIV study by Wang et al. [140] focuses on aqueous humour flow dynamics in supine conditions, which will be discussed for further validation.

The study highlights the formation of symmetrical vortices in the anterior chamber in the supine position, particularly at low differential pressures. At higher pressures, these vortices become more pronounced, and the positions of the vortices and velocity maxima change, which mirrors the behaviour of the simulation results. The study also found that velocity vectors and streamlines in the supine position tend to concentrate near the corneal endothelium and iris epithelium when the differential pressure increases (Figure 21). The velocity magnitudes in Wang's study peaked at approximately 0.201 mm/s, which can be compared with the velocity magnitudes from the simulations (which peak at approximately 0.480 mm/s in Figure 16).

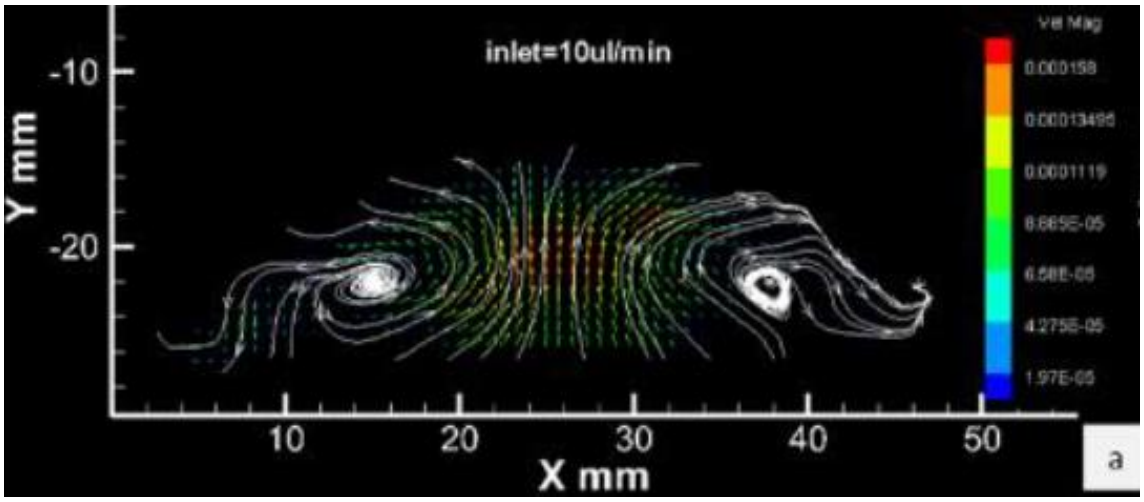


Figure 21 Velocity flow results from the Wang et al. PIV study (extracted from [140])

4.4 Additional Study on Glaucoma Drainage Devices

A separate student project (at the University of Witwatersrand supervised by me) also stemmed from the work described thus far to test glaucoma drainage devices (GDD's) as a treatment option. This study focused on the anterior chamber and the role of GDDs, which divert aqueous humour flow to reduce IOP, but can cause trauma to internal ocular structures, leading to endothelial cell damage (ECD) and potential corneal decompensation [147]. It found that GDD positions have a direct impact on disturbances to flow and can induce WSS on significant regions of the cornea above the threshold for ECD.

Details of the work has been published [148] and more details on the study is provided in Appendix B.

While mechanical damage during GDD insertion is immediate, continued ECD may result from altered aqueous humour flow affecting endothelial cell survival [149]. Clinical studies have linked specific GDD tube parameters with ECD [150–154].

The main findings of this study emphasize the importance of optimizing tube-cornea parameters to reduce corneal damage and stabilize post-operative IOP. While the model assumes consistent fluid outflow, clinical complications such as transient hypertensive phases or bleb encapsulation could lead to acute IOP spikes and WSS increases, contributing to ECD. Notably, clinical studies indicate significant ECD changes only after six months post-surgery, suggesting that transient IOP fluctuations may have limited long-term effects. The study highlights the critical need for precise GDD placement to minimize risks, improve IOP control, and ensure better long-term outcomes for glaucoma patients.

4.5 Results & Discussion

The results are derived from the CFD simulations of both the normal and glaucomatous eye conditions, as well as the different glaucoma filtration surgeries. The results were extracted based on the outcomes

of the residuals of each simulation. Residuals represent the differences between observed data and the model's predictions. The primary purpose of analysing residuals in this context is to verify the convergence of the models. In the context of this thesis, model convergence refers to the point at which iterative optimization algorithms cease to make significant adjustments to parameter estimates. This is typically achieved when residuals exhibit patterns indicative of no further improvements being possible by the model. Model convergence is a critical aspect in ensuring that the optimization algorithms used during model fitting have reached a stable solution. These offer a quantitative and visual means to confirm that the model has minimized prediction errors appropriately, leading to robust conclusions.

Generally, residuals for continuity and energy equations are considered converged when they fall below a set threshold, often between 10E-3 to 10E-6. However, residuals alone may not provide a complete picture; therefore, additional variables such as average-volume IOP and mass flow rate was also monitored, which had to reach steady values to ensure physical convergence.

Figure 22 displays IOP outcomes for (a) normal and (b) glaucomatous conditions (XY-planar view). Additionally, the velocity flow field and WSS for normal conditions are depicted in Figure 16 and Figure 18. Simulations were performed with two different orientations: upright (with gravity acting in the -y direction) and supine (with gravity in the x direction). These results align with findings from previous research [129], indicating that the employed methodology can further be used reliably to simulate surgical simulations.

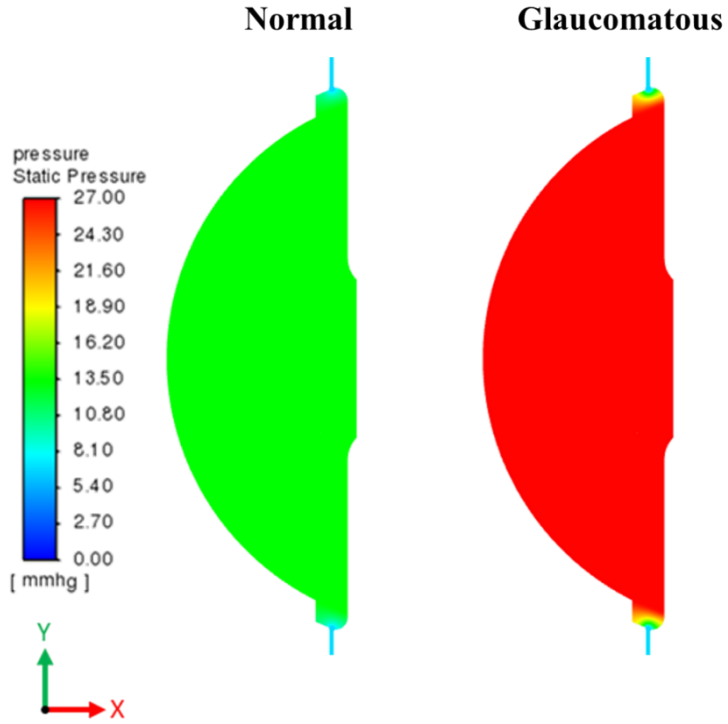


Figure 22 Idealised model IOP results for normal conditions (left) and glaucomatous conditions (right).

The relationship between IOP and TM permeability was also plotted, showing that lower permeability values correspond to higher IOPs. The results from the CFD model followed the trendline of Darcy's Law, verifying the simulations (Figure 23).

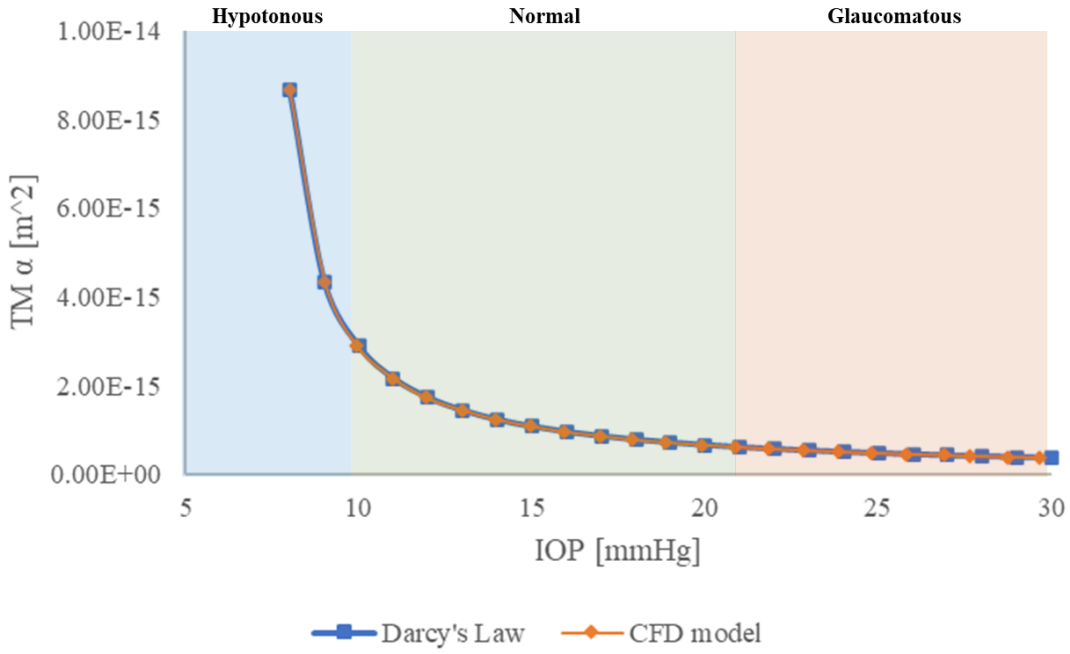


Figure 23 Comparison of idealised model IOP results vs TM permeability as calculated using Darcy's law and extracted from the CFD software (published in [155]).

The CFD model results closely followed the trend predicted by Darcy's law, validating the Fluent simulations. Minor discrepancies can be attributed to the non-uniformity of the trabecular meshwork, as Darcy's law assumes flow through a perfectly uniform medium. As expected, a lower permeability results in a higher IOP. For the specific eye geometry in this study, a permeability of 6E-16 m² or lower poses a risk for glaucoma development. However, this threshold can vary depending on changes in eye geometry, particularly the length of the trabecular meshwork.

Conversely, if the permeability becomes too high, there is a risk of hypotony (IOP < 10 mmHg), where the flow of aqueous humour is insufficient to maintain the eye's structure. In this model, a permeability of 3E-15 m² or higher indicates the risk of hypotony.

For glaucomatous eyes, filtration surgeries may be used to lower the IOP. A successful surgery would reduce the IOP to between 10 mmHg and 21 mmHg. If the IOP remains above 21 mmHg, glaucoma persists, while values below 10 mmHg suggest hypotony. The model developed in this study could be used to simulate and evaluate the success of glaucoma filtration surgeries, offering insights for personalized patient treatments.

In the CFD simulations for each surgical case, the post-operative IOP (post-IOP) before and after suturing was analysed. For all cases, a glaucomatous pre-IOP of 27 mmHg was set. The pre-suture IOP results are summarized in Figure 24.

For the NPDS procedure, the IOP decreased to 20 mmHg once the deep flap is created and Schlemm's canal is deroofed. Although the outlet area is enlarged to allow more outflow, no measures are taken to reduce TM resistance, leading to a moderate reduction in IOP. For mNPDS, which involves peeling the top JCT layer of the TM, the IOP decreases to 3.3 mmHg before suturing. In this case, the outflow area is expanded, similar to the NPDS procedure, but with the added membrane peel step, which also reduces TM resistance. For trabeculectomy, the post-IOP prior to suturing was 0.003 mmHg. This extremely low value is expected because the Kelly punch removes a full section of the TM, significantly decreasing aqueous outflow resistance.

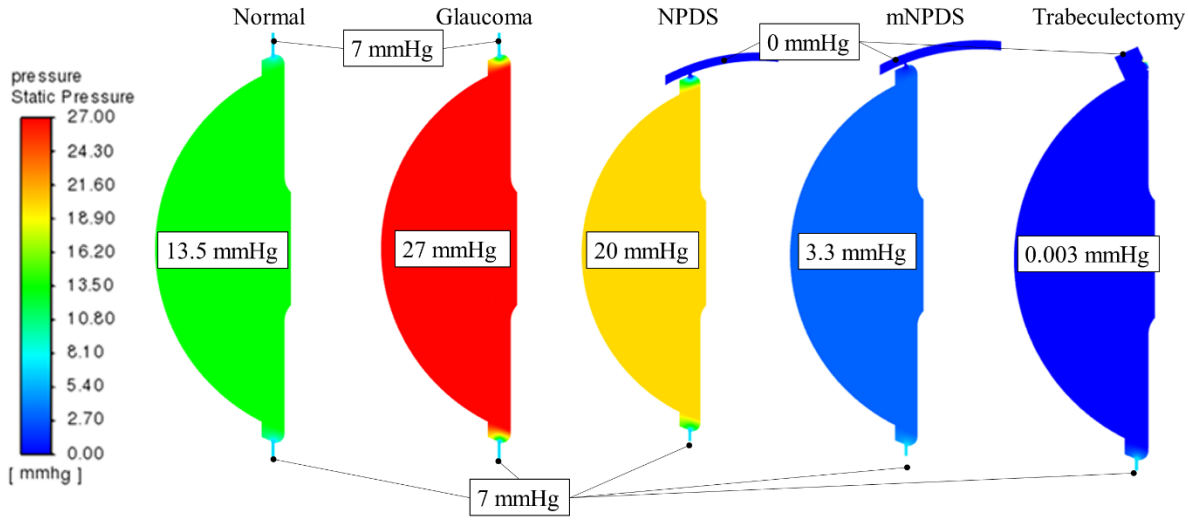


Figure 24 Comparison of idealised model IOP for normal and glaucomatous conditions, as well as unsutured NPDS, mNPDS, and trabeculectomy conditions.

Figure 25 shows the steady-state simulation results in the upright position based on the flow pathlines before suturing has taken place. In the normal flow simulation, the pathlines appear smooth with a balanced distribution across the anterior segment. Based on previous studies (discussed in section 4.3.1) the velocity is within physiological ranges (maximum velocity of ~0.48 mm/s), with a gradual gradient from high to low velocities as aqueous humour moves from the posterior chamber, through the TM, and into the drainage pathways. There is a slight stagnation zone at the inferior section of each model. This is likely due to the natural convection effects resulting from the heat of the cornea redirecting flow away from the inferior region of the model.

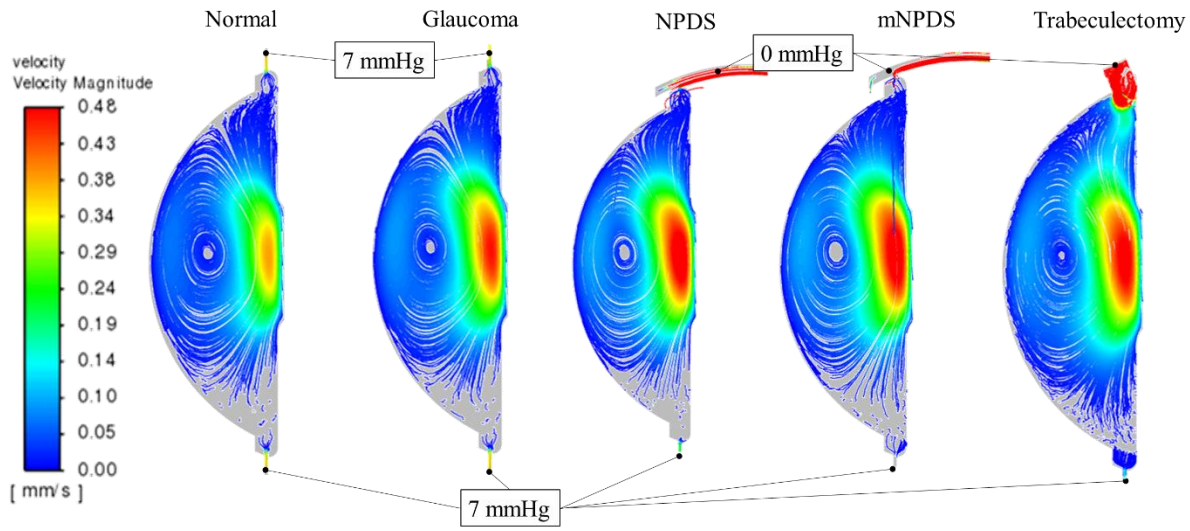


Figure 25 Comparison of idealised model velocity pathline results for normal and glaucomatous conditions, as well as unsutured NPDS, mNPDS, and trabeculectomy conditions.

The glaucomatous flow pattern shows alterations with increased resistance, which reflects a reduction in aqueous humour outflow capacity, leading to elevated IOP. The flow pathlines appear more congested, evidenced by the decreased velocity through the TM (depicted in Figure 26) and the increased velocity near the pupil. The reduced outflow can disrupt nutrient distribution, particularly to the corneal endothelium and lens, potentially accelerating cellular damage and contributing to complications such as corneal decompensation or cataract formation [45,91,95,156]. Increased velocity at the oulet can cause fibrosis and stiffening of the tissues over time [100,101].

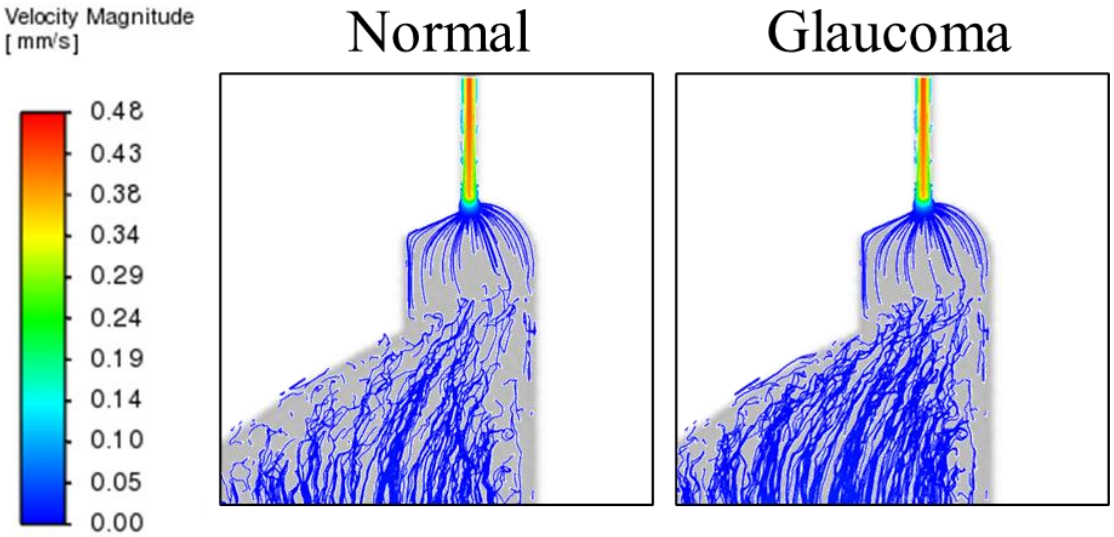


Figure 26 Zoomed in illustration of normal (left) and glaucomatous (right) superior outlet sections.

In the unsutured NPDS setup, the flow pathlines indicate a significant increase in velocity around the surgical site, which corresponds with the increased outlet area produced from the scleral flap generated.

Despite the increased velocity at the TM, there is still an indication of high outflow resistance demonstrated by the high velocity near the pupil.

The mNPDS model aims to further reduce outflow resistance by removing a section of the TM, resulting in even higher velocities and more rapid drainage through the TM. The pathlines show increased flow, with indications of a potential vortex or localized high-speed outflow near the surgical site.

The trabeculectomy simulation displays the most dramatic change in flow dynamics. There is a very high-velocity outflow near the filtration site, as well as flow irregularities near the incision site. The IOP has decreased to close to 0 mmHg, indicating a complete lack of pressure regulation. Clinically, this underscores the importance of controlled suturing in glaucoma filtration procedures to ensure that the outflow rate is appropriately regulated, avoiding drastic drops in IOP while maintaining effective drainage. Poorly regulated suturing could lead to insufficient drainage, causing the surgery to fail in managing glaucoma.

A suture pressure of 7 mmHg was applied to the surgical area to stabilize outflow (Figure 27), though suture tension can be adjusted based on expert opinion. Once the pressure is applied, IOP increases as the aqueous outflow area becomes restricted. The final IOP after trabeculectomy was 7 mmHg, marking a 74.1% reduction. The post-IOP for NPDS was 22 mmHg, indicating a 13.3% reduction from the glaucomatous 27 mmHg. Since the steady-state IOP remained above 21 mmHg, the NPDS procedure would be considered unsuccessful. This aligns with studies suggesting NPDS is often ineffective [157]. However, with the membrane peel included (mNPDS), the IOP fell to 6.98 mmHg, comparable to trabeculectomy at 7 mmHg.

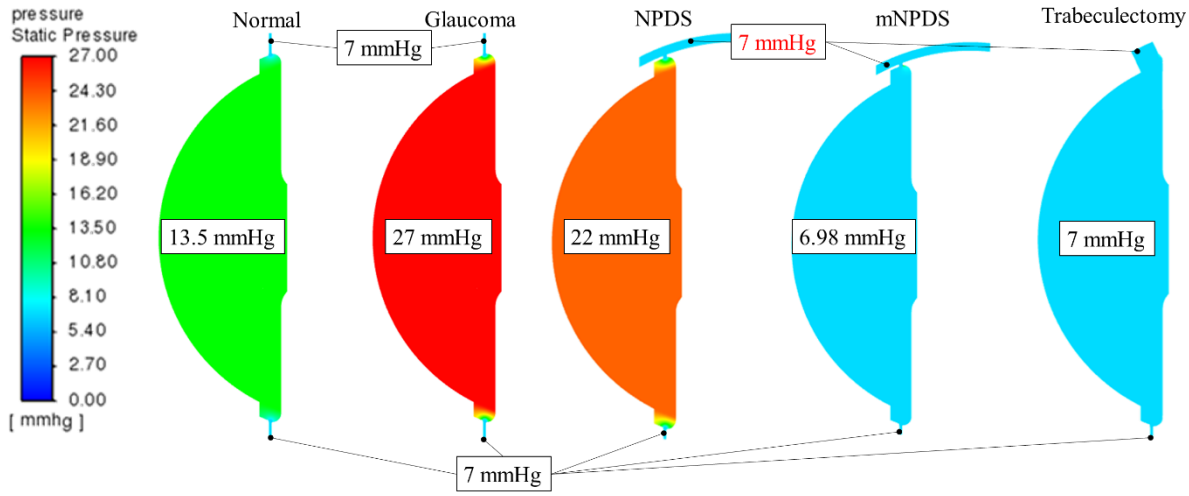


Figure 27 Comparison of idealised model IOP results for normal and glaucomatous conditions, as well as sutured NPDS, mNPDS, and trabeculectomy conditions.

Figure 28 shows the steady-state simulation results in the upright position based on the flow pathlines after suturing has taken place.

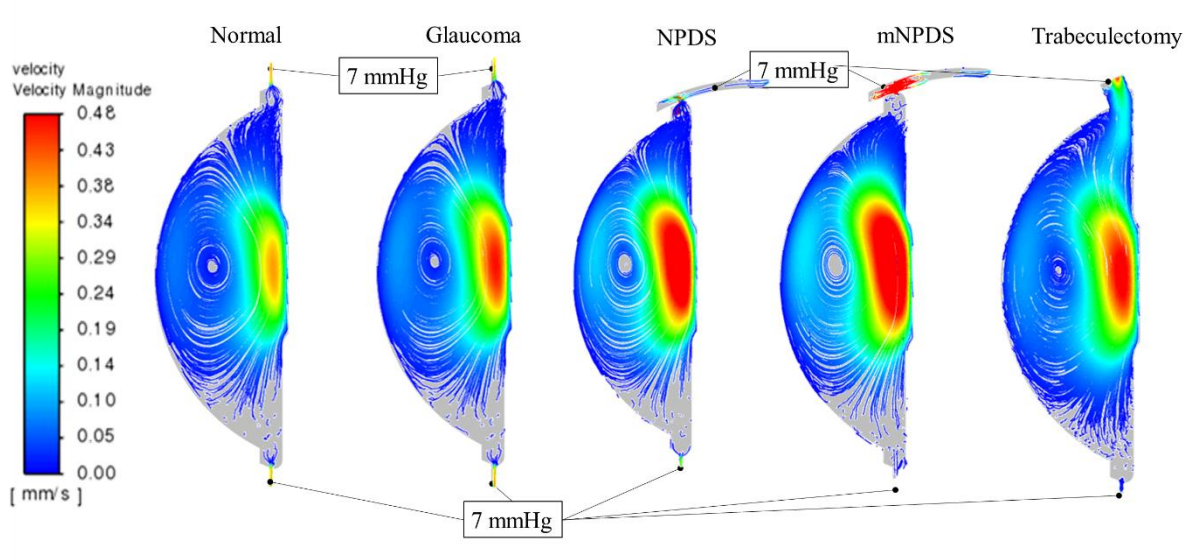


Figure 28 Comparison of idealised model velocity pathline results for normal and glaucomatous conditions, as well as sutured NPDS, mNPDS, and trabeculectomy conditions.

In NPDS, the flow pathlines indicate improved outflow compared to glaucomatous flow, bringing the flow patterns closer to those observed under normal, healthy conditions. This is indicated by the higher velocity at the surgical site. However, there still a large amount of resistance remaining in the pathway as no part of the TM was excised. Clinically, NPDS shows a lower velocity at the surgical site, which should minimize the risk of scarring and fibrosis, helping to maintain long-term outflow efficiency [102]. However, if resistance remains too high, there may still be a risk of insufficient IOP control and progression of glaucoma-related damage.

The mNPDS simulation shows a significant reduction in resistance compared to standard NPDS and a high velocity outflow. Clinically, mNPDS could offer a better balance between lowering IOP effectively and minimizing the risk of complications associated with excessive drainage.

In the trabeculectomy simulation, there is an accelerated flow region within the anterior chamber near the surgical site with more pronounced changes in flow when compared to normal flow conditions (see Figure 29). For normal, glaucomatous, NPDS, and mNPDS conditions, recirculation occurs near the surgical site shown by the flow separation/divergence. For trabeculectomy, however, the iridectomy seemed to cause a flow alteration that shifts the point of recirculation upwards. While successful in terms of IOP reduction, the irregular flow patterns near the filtration site suggests potential over-drainage, which could increase the risk of hypotony, particularly if the filtration site does not adequately self-regulate. The irregular flow pattern also poses a risk for fibrosis and scarring around the filtration site, which may lead to bleb failure over time, reducing the long-term efficacy of the surgery [100,101].

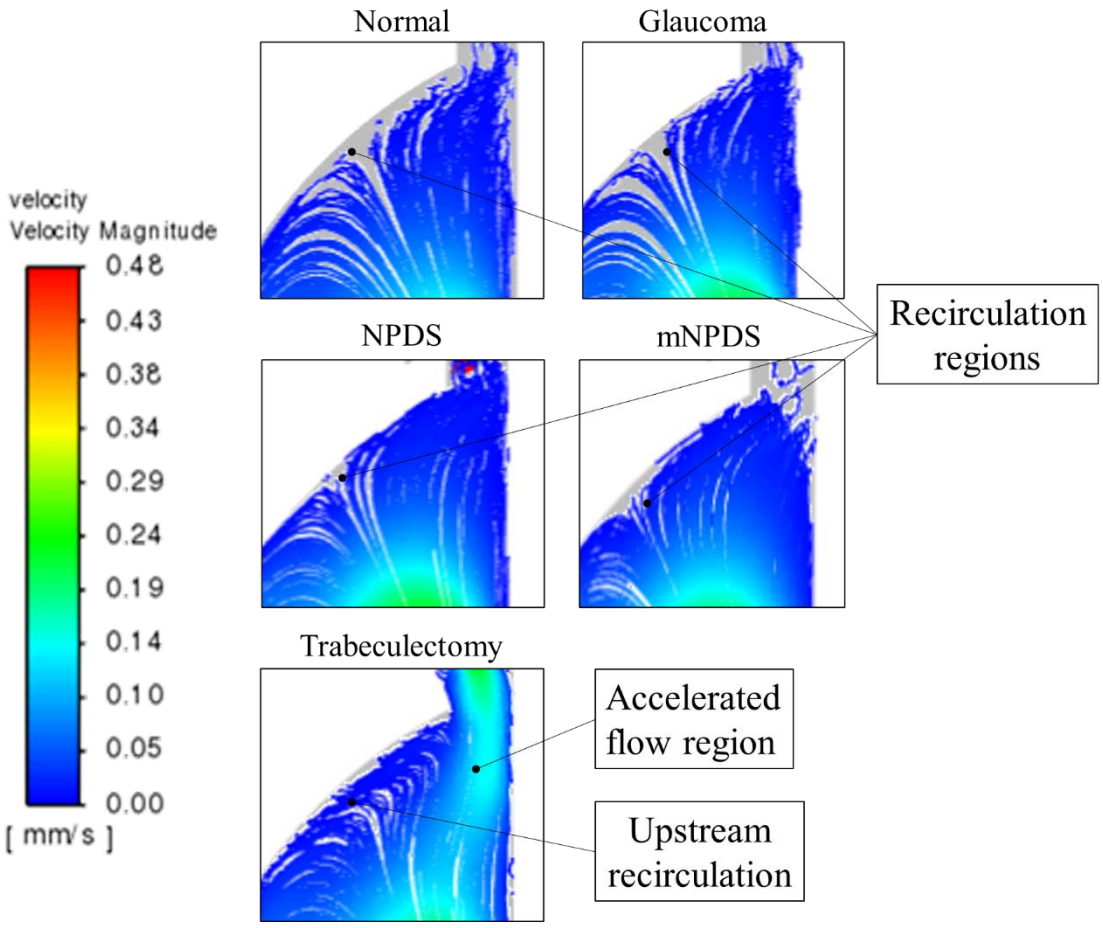


Figure 29 Zoomed in illustration idealised model velocity pathline result at the cornea-iris angle near the surgical site for normal and glaucomatous conditions, as well as sutured NPDS, mNPDS, and trabeculectomy conditions.

The post-IOP results of the models are summarised in Table 6. Not all of the models were simulated in each position as this would result in an unnecessarily large number of models. However, each scenario (normal, glaucomatous, NPDS, mNPDS, and trabeculectomy) was subjected to various suturing conditions (either unsutured or sutured), as well as various patient orientations (upright or supine). Interestingly, it is noted that NPDS and mNPDS procedure seem to observe slight changes in IOP when changing the orientation. This may suggest that these procedures are somehow unique in terms of how their outflow systems interact with gravity.

In a healthy eye, the outflow through the TM is primarily driven by pressure differentials. The effect of gravity is minimal because the flow resistance is high, and the system maintains its function regardless of orientation. Similarly, in a glaucomatous eye, increased resistance in the TM is primarily localized and is pressure-dependent. Thus, the flow remains restricted in both upright and supine positions, resulting in no IOP change with orientation. In a trabeculectomy, the newly created drainage route often bypasses the TM entirely. Like normal or glaucomatous outflow, trabeculectomy drainage tends to be

less dependent on gravity, as the flow is driven by pressure differences and the structure of the drainage pathway.

Both NPDS and mNPDS procedures involve the creation of a scleral flap as a new drainage pathway. This creates a subtler outflow change than a full trabeculectomy because it preserves part of the TM and does not fully penetrate the anterior chamber. This subtler modification could result in small variabilities in outflow depending on orientation since the flap may behave differently depending on how fluid accumulates near the drainage site or how pressure is distributed across the flap.

Table 6 Summary of IOP results for a variety of conditions including model orientation.

Scenario	**Orientation**	**Pre-IOP [mmHg]**	**Suture-IOP [mmHg]**	**Post-IOP [mmHg]**
Normal flow	Upright	13.5	-	-
Normal flow	Supine	13.5	-	-
Glaucomatous flow	Upright	27	-	-
Glaucomatous flow	Supine	27	-	-
Trabeculectomy (not sutured)	Upright	27	0	0.007
Trabeculectomy (not sutured)	Supine	27	0	0.007
Trabeculectomy (sutured)	Upright	27	7	7.00
NPDS (not sutured)	Upright	27	0	22.56
NPDS (not sutured)	Supine	27	0	20.43
NPDS (sutured)	Upright	27	7	24.69
mNPDS (not sutured)	Upright	27	0	4.46
mNPDS (not sutured)	Supine	27	0	3.08
mNPDS (sutured)	Upright	27	7	6.98

4.5.1 Comparison with Clinical Studies Comparison

Clinical studies have consistently demonstrated the efficacy of trabeculectomy in lowering IOP. For instance, Pantalon et al. [158] reported a significant reduction in IOP post-trabeculectomy, with an average reduction from 27 mmHg pre-operatively to approximately 7 mmHg post-operatively, similar to the CFD results presented here which also indicated a reduction to approximately 7 mmHg.

Studies on NPDS have shown mixed results. Lusthaus et al. [159] reported that NPDS could achieve a post-IOP reduction, but the efficacy varied widely. Some studies suggested that NPDS alone resulted in a post-IOP of approximately 20 mmHg, which aligns with the CFD findings indicating an IOP of

23.4 mmHg post-NPDS. This highlights the limited effectiveness of NPDS compared to trabeculectomy.

The introduction of the membrane peel in mNPDS has been shown to significantly improve outcomes. Clinical studies, such as those by Coroneo et al. [95], have reported that mNPDS could achieve post-IOP reductions comparable to trabeculectomy. For example, one study indicated a reduction from 27 mmHg pre-operatively to approximately 7-8 mmHg post-operatively, which matches the CFD simulation results showing a reduction to approximately 6.98 mmHg.

The alignment between CFD results and clinical study outcomes supports the use of CFD as a reliable tool for evaluating glaucoma surgical procedures, without the limitations of performing clinical analysis. The simulations provide valuable insights into the immediate post-operative effects of different surgeries, which can guide clinical decision-making and improve patient outcomes.

The verification process underscores the potential of CFD simulations to serve as a preliminary evaluation tool before clinical trials. This can expedite the development and assessment of new surgical techniques, reducing the reliance on costly and time-consuming clinical studies.

4.6 Summary

In this study, a 3D eye model with idealised geometry was developed. The model was employed to simulate both healthy and glaucomatous conditions. The findings were verified using analytical equations and compared with previous studies as well as experimental visualisation for validation. The model was then further developed to simulate aqueous humour dynamics of NPDS, mNPDS, and trabeculectomy procedures.

The success of these procedures depends on achieving adequate IOP reduction without causing low-pressure complications and undesirable flow features. NPDS and mNPDS were shown to be less likely to disrupt nutrient delivery compared to trabeculectomy, as their smoother flow patterns minimize the risk of nutrient stagnation and deprivation.

The surgical simulation results in this study also align closely with clinical findings, reinforcing the CFD model's value for studying glaucoma surgeries. The post-IOP values from trabeculectomy and mNPDS in the simulations are comparable to those observed in clinical studies, confirming the need for the membrane peel in NPDS procedures. Despite some numerical differences, both clinical and CFD studies predict a similar IOP reduction for all three procedures. This consistency demonstrates the model's capability to provide insights into the immediate post-operative effectiveness of glaucoma surgeries.

This study highlights the potential of CFD as a cost-effective and time-efficient tool for predicting the outcomes of glaucoma surgeries, providing valuable insights before clinical trials. Using a 3D model

with idealised eye geometry, CFD simulations evaluated the immediate post-operative IOP outcomes of three surgical techniques: trabeculectomy, NPDS, and mNPDS. The results demonstrated that trabeculectomy and mNPDS achieved effective IOP reduction, while NPDS without the membrane peel was less successful, underscoring the importance of the peel in contemporary surgical practices. The ability of CFD to control variables like suture tightness and outflow resistance allowed for precise comparisons without patient-specific variability, reinforcing its utility in optimizing surgical strategies.

However, limitations of CFD models, such as reliance on uniform geometries and estimated parameters for TM resistance and suture tightness, highlight the need for careful interpretation of results. Differences in patient-specific anatomy and surgical conditions may introduce discrepancies between simulated and clinical outcomes. Incorporating diverse geometries and combining CFD with finite element analysis could enhance the clinical relevance of these models, enabling better predictions of corneal biomechanics and post-operative scarring. Despite these challenges, this study underscores CFD's promise as a preliminary tool for assessing surgical outcomes and optimizing techniques, laying the groundwork for further validation through clinical trials and model refinements.

.

5 Demographic-Representative Models

Once the methodology was established on an idealised geometry, the work was further expanded to estimate the surgical outcomes for people of different ethnicities. From the discussion in section 2.2, European and African ethnicities were selected. Due to a lack of access to sufficient biometric data and OCT scans to reconstruct patient-specific geometries, the demographic-specific models were designed by adapting the established methodology and incorporating anatomical variations documented in literature.

The main objective of this section is to assess the immediate post-operative outcomes of glaucoma filtration surgeries (NPDS, mNPDS, trabeculectomy) across ethnically representative eye models, specifically focusing on European and Sub-Saharan African ethnicities, with a focus on understanding the variations in aqueous humour dynamics due to anatomical differences among ethnic groups. By incorporating average anterior chamber geometries typical of different ethnicities, this study aims to provide a more comprehensive analysis of IOP reduction, flow direction changes, and wall shear stresses. These parameters will be used to evaluate the potential clinical implications of surgical techniques in a demographically diverse population, specifically examining how ethnicity-related anatomical variations influence the efficacy and safety of glaucoma surgeries.

This ethnic-focused CFD study aims to deepen insights into surgical outcomes for diverse populations, potentially aiding in the personalisation of glaucoma treatment strategies by anticipating the unique risks, such as altered nutrient delivery, hypotony, and fibrosis susceptibility, for specific ethnic groups.

5.1 Creation of Demographic-Specific Geometries

This section outlines the methodology used to justify the ocular geometries selected to represent the anterior segments for people of European and Sub-Saharan African descent. The idealised eye discussed in chapter 4 was based on a previous master's student's work, that was slightly adapted as required. For this section, an all-new geometry was created to incorporate more detailed anatomical features and capture the ethnic differences of the anterior segment as much as possible.

Given the anatomical differences that might influence the susceptibility to glaucoma and the efficacy of surgical interventions (section 2.2), creating representative 3D models of the anterior segment of the eye for different ethnic groups could shed light on the reasons behind this disparity. The focus for the geometry (Figure 30) was on the:

- White-to-white (WTW) length: the horizontal diameter of the cornea and was used to determine the overall size of the model's corneal section.
- Anterior chamber depth (ACD): the distance between the corneal endothelium and the anterior lens surface.

- Anterior chamber angle (ACA): the angle between the cornea and the iris at the periphery of the anterior chamber.
- Anterior lens vault (LV): the height of the lens in relation to the corneal plane.
- Pupil diameter (PD): the horizontal diameter of the pupil.
- TM length (TML): the horizontal distance of the TM along the boundary of the anterior chamber.
- TM height (TMH): the vertical thickness of the TM.

By gathering and analysing data on these parameters for European and Sub-Saharan African populations, this section aims to simulate glaucoma and filtration surgery scenarios to explore why certain procedures may yield better outcomes in one ethnicity compared to another.

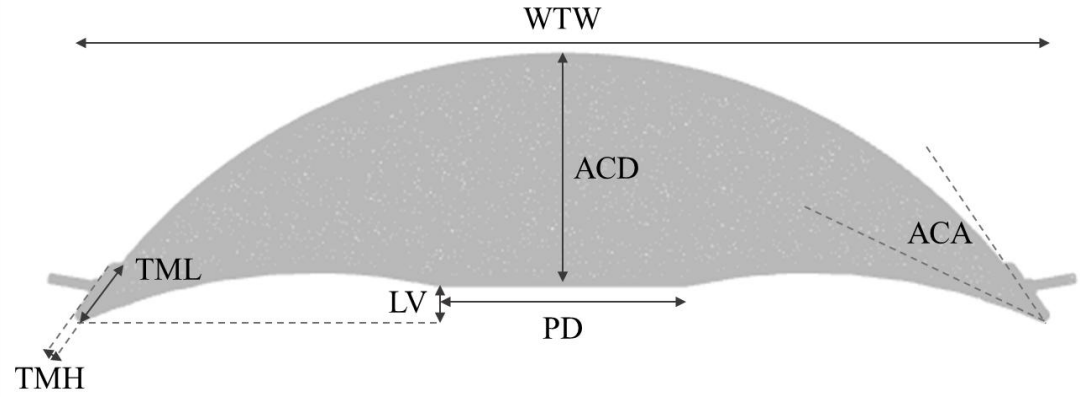


Figure 30 Anterior chamber parameter definitions including White-To-White (WTW) length, Anterior Chamber Depth (ACD), Anterior Chamber Angle (ACA), Lens Vault (LV), Pupil Diameter (PD), Trabecular Meshwork Length (TML), and Trabecular Meshwork Height (TMH).

A comprehensive review of existing literature was conducted to gather data on the geometric parameters of the anterior segment of the eye. The focus was on peer-reviewed studies, clinical trials, and review papers that measured the anterior segment parameters as previously described. The search was refined to focus on the European and Sub-Saharan African populations and included only those studies that provided detailed biometric data of the anterior segment of the eye. A specific exclusion criterion was applied to avoid North African populations due to their genetic diversity [160], which might introduce confounding factors in the comparison of Sub-Saharan African populations. For ease of reference, the Sub-Saharan African group will hereafter simply be referred to as the African group.

The following inclusion criteria were defined:

- Studies that provided specific biometric data for adults (age 18+), particularly focusing on the parameters of interest.
- Studies with populations over 40 years of age, given the higher risk of glaucoma in older adults.
- Studies that grouped data by ethnicity (European and Sub-Saharan African).

The following exclusion criteria were defined:

- Any studies exclusively involving participants under the age of 18 were excluded to ensure that all data reflected adult eye anatomy.
- North African populations were excluded due to their complex ethnic identification.

Once the relevant studies were identified, the data were extracted and compiled into a dataset. The parameters of interest were recorded for both European and African populations, including the sample sizes, mean values, and standard deviations where available. Multiple peer-reviewed studies were gathered, and a statistical analysis was conducted to develop models representing ocular geometries characteristic of individuals of European and African descent [161–167]. A summary of the raw data from multiple studies is provided in Appendix A . These models will be employed to investigate variations in aqueous humour dynamics associated with differing eye geometries.

These studies suggest that there can also be wide variances between age and gender. For example, ACD tends to significantly decrease with age, and males tend to have larger WTW lengths than females. Thus, the same methodology demonstrated here could be extended to explore differences across other demographic variables, such as age or gender, to further understand their influence on aqueous humour dynamics.

A total of 21 studies fit the inclusion and exclusion criteria mentioned above. Of these studies, 11 had biometric data on European eyes and 13 had biometric data on African eyes (four of the studies had data on both ethnicities). Table 7 provides a summary of the number of studies and total sample size across all studies associated with each geometric eye parameter.

Table 7 Summary of number of biometric studies and total sample sizes

	European		**African**	
	Number of studies	**Total sample size**	**Number of studies**	**Total sample size**
WTW	5	1329	3	1480
ACD	7	5209	9	7504
ACA	2	3094	2	4763
LV	3	558	2	204
PD	6	1288	3	318

Once the data were identified, collected, and recorded, a bachelor's student at the University of Cape Town (supervised by me) conducted a statistical analysis to explore the significance of biometric variations in the anterior chamber parameters among different ethnic groups [168]. Specifically, Cohen's D value was employed to quantify the effect sizes, which is a statistical measure used to quantify the effect size, or the magnitude of the difference between two groups. It is commonly used in fields such as psychology, education, and medicine to evaluate the practical significance of research

findings, rather than relying solely on statistical significance (p-values) [169]. Cohen's D provides a standardized way to assess how much one group's mean value differs from another in terms of the variability (or spread) within the data.

The formula for Cohen's D depends on whether the two groups being compared have equal sample sizes and variances. The resulting Cohen's D value expresses the difference between two groups' mean in terms of standard deviation units. Traditional guidelines classify effect sizes as small (0.20), medium (0.50), and large (0.80), but updated estimates recommend thresholds of 0.15, 0.40, and 0.75, respectively, to reflect more realistic benchmarks in gerontology research [169]. An extract of the results can be found in Appendix D.

The statistical analysis identified significant differences in parameters like ACA, ACD, and WTW. The African group exhibited shallower ACD, which can be associated with an increased risk of angle-closure glaucoma and elevated IOP (although African populations have a much lower incidence of angle closure disease [170]). Europeans showed slightly larger WTW corneal diameters, which, while not directly linked to disease risk, may influence surgical outcomes. These findings underscore the importance of ethnicity-specific assessments in clinical practice, particularly for glaucoma screening and management in populations at greater risk.

To create the models for each ethnicity and ensure a robust comparison, a weighted average was calculated for each biometric parameter to account for differences in sample size across studies. This method provided a more accurate representation of each parameter for each population, ensuring that larger studies had a proportional influence on the final values. The weighted average for each parameter was calculated using the following formula:

$$Weighted\ average = \frac{\sum(n \times \bar{X})}{\sum(n)} \tag{5.2}$$

Where:

- n is the sample size referring to the number of participants in each study, and
- $\bar{X}$ is the mean value of the parameter (e.g., ACD, WTW) reported in the study.

Once these calculations were completed, the biometric values could be translated into 3D models representing the anterior segments of European and African eyes. The biometric data were used to define the key anatomical features in CAD software.

For TM length, only one study was found that reported on the TM length between different ethnicities. The study reported values of 851 ± 131 μm for European males and 771 ± 118 μm for African males [66]. For TM thickness, both European and African males seem to have a consistent value of 103.9 ± 11.1 μm.

The final selected geometry for each ethnicity is presented in Table 8.

Table 8 Ocular geometries selected to represent European and African males over the age of 50 based on literature.

	European Eye	**African Eye**
WTW [mm]	11.96	11.58
ACD [mm]	2.85	2.70
ACA [deg]	32.45	36.6
LV [mm]	0.533	0.365
PD [mm]	4.06	3.86
TML [mm]	0.851	0.771
TMH [mm]	0.104	0.104

The demographic-specific models were constructed using the same CAD software, Autodesk Inventor®, as used for the idealised model. The key structures and flow domains were adapted to reflect the anatomical variations specific to each demographic. The flow domains included the anterior chamber, pupil, corneal wall, iris wall, Schlemm's canal, TM, and collector channels.

The anterior chamber as shown in Figure 31 was created using the parameters described in Table 8. The WTW total horizontal diameter of the cornea. The ACD is the vertical distance from the posterior surface of the cornea to the anterior surface of the lens. The ACA is the angle formed between the cornea and the iris, which helps to define the sloping of the corneal dome and the interface with the iris, contributing to the shape of the anterior chamber when revolved. The LV is the protrusion of the lens above the plane of the iris. When revolved, this protrusion will help shape the posterior segment of the anterior chamber. The PD is the size of the pupil, which is necessary to define how wide the pupil will be once the 3D shape is generated.

After fully defining the anterior chamber shape, the TM length and height is added at the end of the WTW length as a rectangular shape, shown in the red inset frame in Figure 31. The Schlemm's canal was added as a half-circular channel located near the base of the TM for which a radius (SCR) was specified.

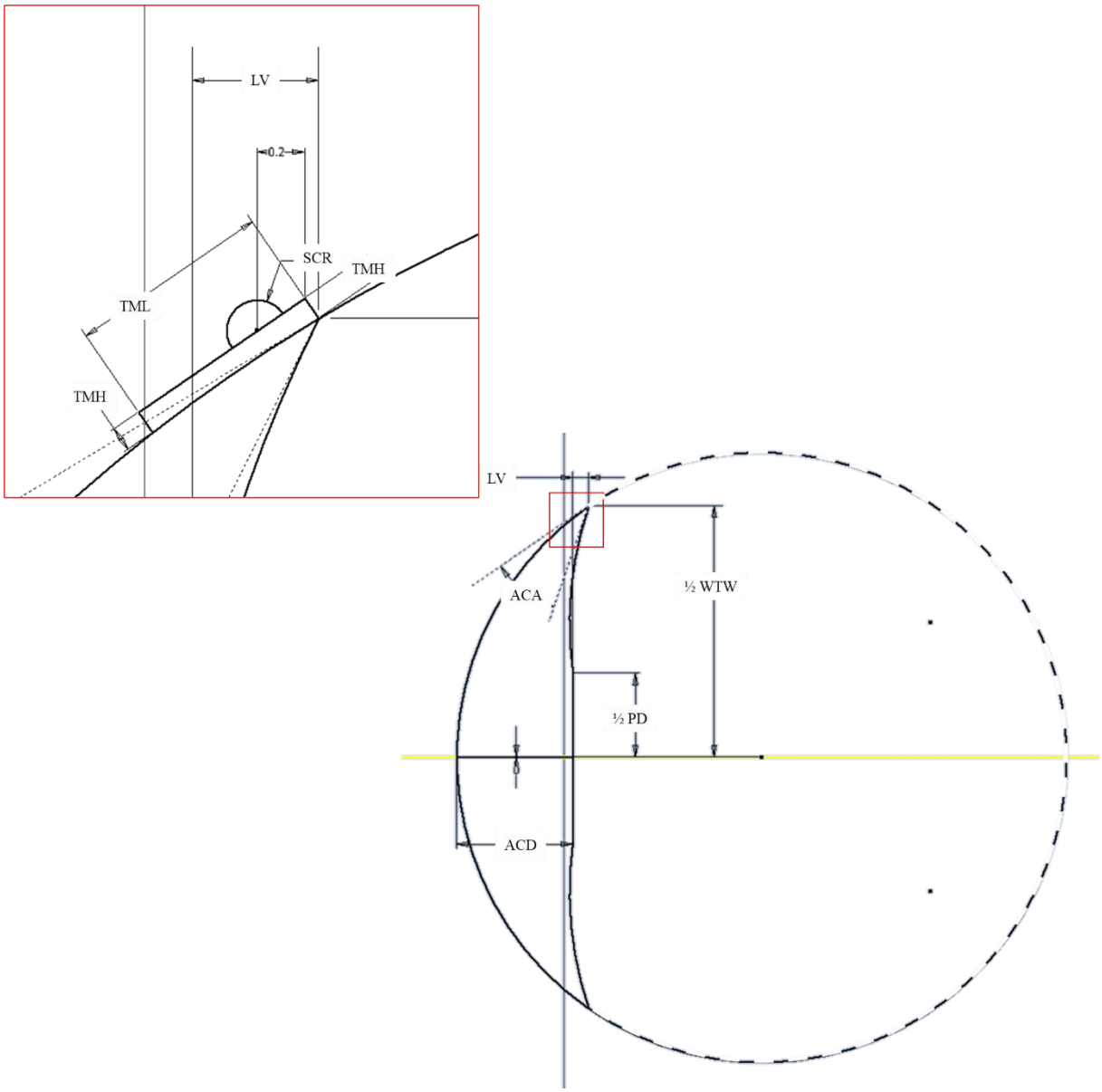


Figure 31 Graphic representation of the anterior chamber parameters as created in Autodesk Inventor with a close-up graphic representation of the eye structure parameters at the ACA

Finally, an outlet channel was added to the top of the eye and a circular pattern was created around the vertical centreline to produce a total of 26 outlets. The final 3D model of an ethnic-representative anterior segment is depicted in Figure 32. The anterior chamber resulting from the parameters described in Table 8 is depicted in green. The TM with its height and length as described in Table 8 is depicted in blue. Finally, the Schlemm's canal with the individual collector channels are depicted in yellow.

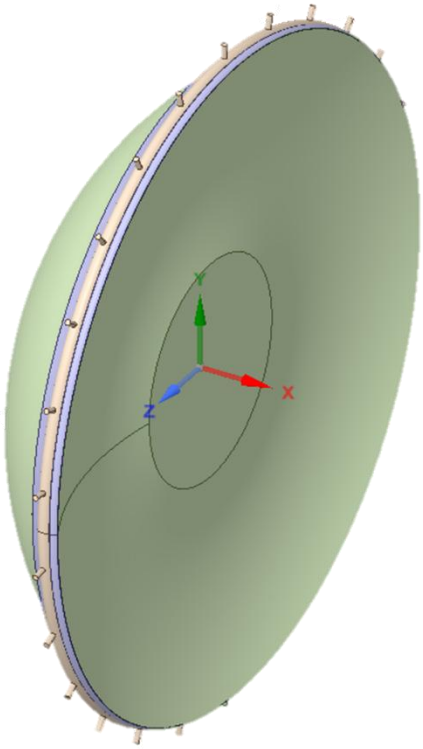


Figure 32 3D model of the European-representative anterior chamber as a result of the defined ethnic geometry parameters including the anterior chamber (green), TM (blue), and Schlemm's canal with collector channels (yellow)

A single uniform outlet in the shape of a ring was also considered to simplify the model by treating all the collector channels as a single unified outflow path instead of the 26 individual collector channels around the Schlemm's canal. However, the 26 individual collector channels more closely reflect the actual anatomy of the eye, where aqueous humour drains from Schlemm's Canal into multiple distinct channels. As an example of the difference between the uniform outlet and the separate collector channels, Figure 33 displays the velocity vector results from the European eye model under normal flow conditions. Specifically, the flow through the TM, Schlemm's canal, and collector channels are displayed.

The uniform outlet model shows a more uniform distribution and less localized variability. This simplification might limit the model's ability to predict localized flow resistance. The separate outlet model velocity vectors localized variations and directional behaviour near each outlet, which reflect the real-life resistance and localized outflow characteristics.

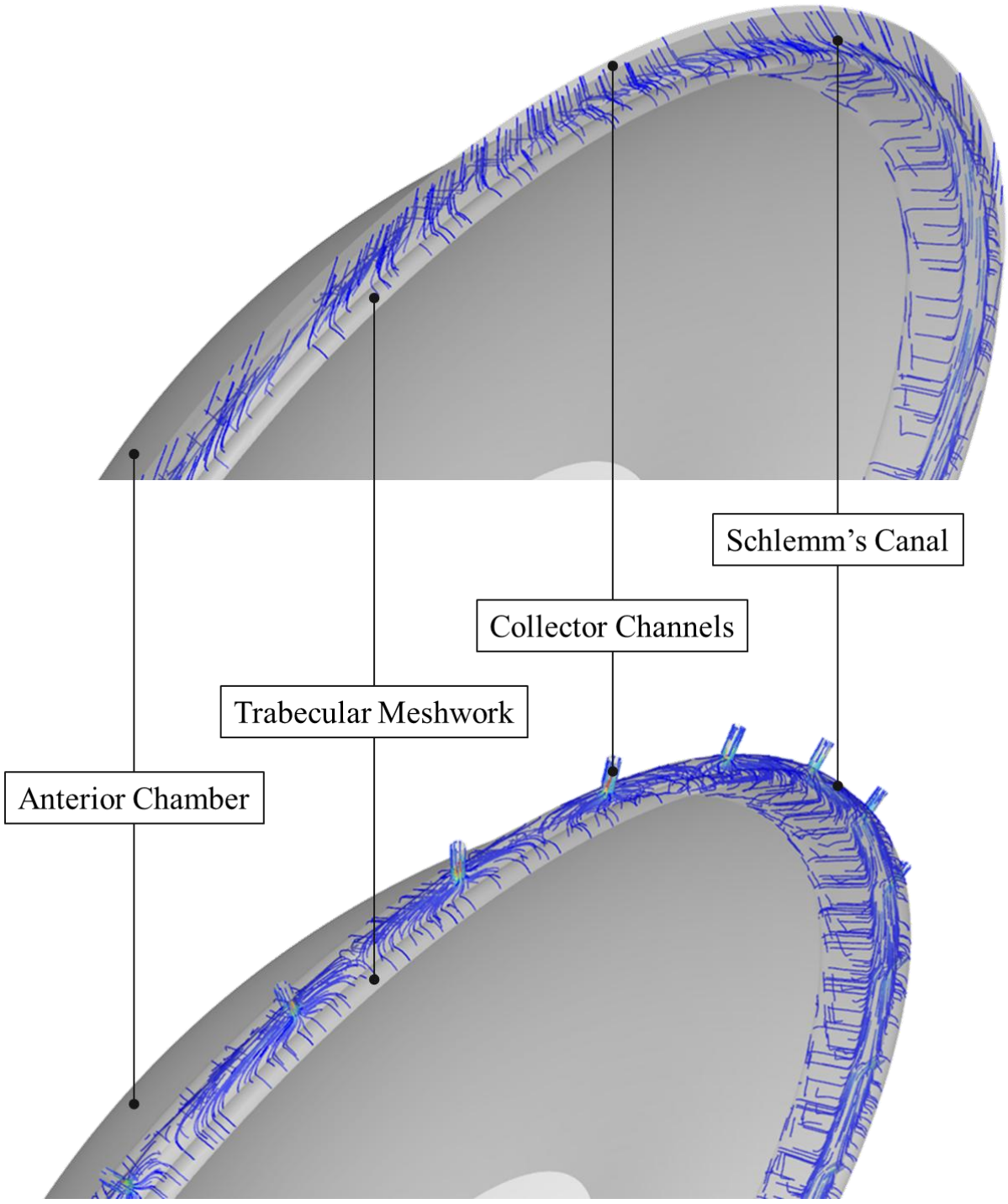


Figure 33 Velocity vector results at the outlet of the anterior chamber of the European eye for a single uniform collector channel (top) and 26 separate cylindrical outlet channels (bottom)

It was also observed that post-surgical simulations benefit from modelling the individual collector channels, especially since the procedure modifies the flow distribution across the TM and Schlemm's canal. By using individual outlets, more accurate assessment can be done on how the post-surgical modifications impact flow into the collector channels.

5.2 Fluent Setup

The CFD simulations for the ethnic-representative models were set up in a manner similar to that described in section 4, including the scenarios for normal flow, trabeculectomy, NPDS, and mNPDS. A list of all the models that will be discussed in this section is provided in Table 9.

Table 9 List of models discussed in chapter 5

		Scenario	**Sutured/unsutured**	**Orientation**
European model	1	Normal condition	-	Supine
	2	Normal condition	-	Upright
	3	Trabeculectomy	Unsutured	Supine
	4	Trabeculectomy	Sutured	Supine
	5	Trabeculectomy	Sutured	Upright
	6	NPDS	Unsutured	Supine
	7	NPDS	Sutured	Supine
	8	NPDS	Sutured	Upright
	9	mNPDS	Unsutured	Supine
	10	mNPDS	Sutured	Supine
	11	mNPDS	Sutured	Upright
African model	12	Normal condition	-	Supine
	13	Normal condition	-	Upright
	14	Trabeculectomy	Unsutured	Supine
	15	Trabeculectomy	Sutured	Supine
	16	Trabeculectomy	Sutured	Upright
	17	NPDS	Unsutured	Supine
	18	NPDS	Sutured	Supine
	19	NPDS	Sutured	Upright
	20	mNPDS	Unsutured	Supine
	21	mNPDS	Sutured	Supine
	22	mNPDS	Sutured	Upright

The aqueous humour flow was conducted using Ansys Fluent, treating the fluid as incompressible and Newtonian, with properties similar to water. The model assumed steady-state laminar flow with non-slip rigid walls. A mass flow rate was applied at the pupil inlet to represent aqueous humour production, while pressure outlets were set to physiological values to replicate IOP. The TM was modelled as a porous medium using Darcy's law to simulate resistance to outflow (Table 10), with parameters adjusted to match desired IOP conditions for both normal and glaucomatous eyes. Many of the values are identical and so the ones that are different are highlighted for ease of reference. These are related to the porous region and power law coefficients. The simulations used a 3D pressure-based laminar model to study fluid behaviour across different zones. Boundary conditions and solver settings were chosen to ensure accurate simulation results, particularly focusing on velocity, pressure, and temperature interactions in the eye.

Table 10 Parameters to define the porous zone in Ansys Fluent for demographic-representative models.

			European eye		African eye	
Parameter description	**Symbol**	**Unit**	**Normal flow**	**Glaucomatous flow**	**Normal flow**	**Glaucomatous flow**
Boundary conditions						
Target IOP	IOP	mmHg	13.5	27.0	13.5	27
Outlet pressure	p_o	mmHg	7.00	7.00	7.00	7.00
Change in pressure	Δp	mmHg	-6.50	-20.0	-6.50	-20.0
Change in pressure	Δp	Pa	-867	-2666	-867	-2666
Inlet mass flow rate	$\dot{m}$	kg/s	5.00E-08	5.00E-08	5.00E-08	5.00E-08
Porous region properties						
Superficial velocity	v	Pa·s	2.45E-07	2.45E-07	1.86E-06	1.86E-06
Porous zone area	A	m^2	2.04E-04	2.04E-04	2.69E-05	2.69E-05
Equivalent TM height	Δm	m	2.15E-04	2.15E-04	2.15E-04	2.15E-04
Power law coefficients						
Source term = dp/dx	S_i	Pa/m	-5.56E+05	-1.71E+06	-4.02E+06	-1.24E+07
Pressure jump coefficient	C_0	-	2.27E+12	6.98E+12	2.17E+12	6.67E+12
Flow coefficient	C_1	-	1	1	1	1
TM permeability	α	m^2	4.41E-16	1.43E-16	4.61E-16	1.50E-16
Viscous resistance	C	m^{-2}	2.27E+15	6.98E+15	2.17E+15	6.67E+15

The normal, glaucomatous, and sutured surgical models were all orientated in the standing positions, since this is typically the orientation in which IOP is measured pre- and post-surgery. The unsutured

models were all oriented in the supine position, as this is typically the orientation of a patient during surgery.

The ethnic-representative trabeculectomy models were created similar to the idealised trabeculectomy models described in section 4.1. As an example, the European ethnic-representative anterior segment for a trabeculectomy procedure is depicted in Figure 34. The anterior chamber with the iridectomy incision is depicted in green. The TM is depicted in blue. The Schlemm's canal with the individual collector channels is depicted in yellow. Finally, the Kelly punch incision (sclerostomy) is depicted in pink as the main surgical site.

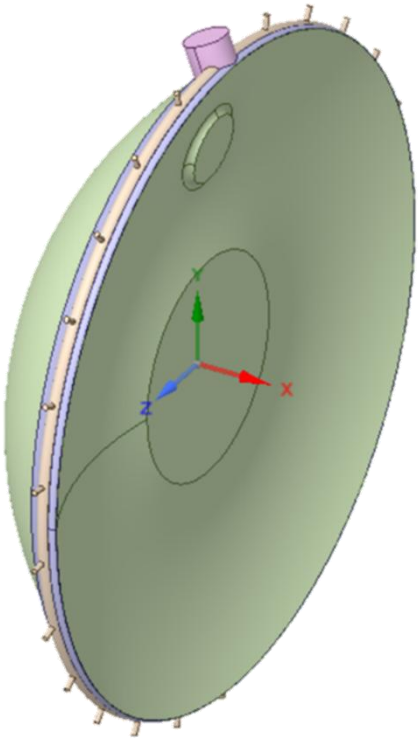


Figure 34 3D model of the European-representative anterior chamber and trabeculectomy procedure including the anterior chamber with the iridectomy incision (green), TM (blue), Schlemm's canal with collector channels (yellow), and Kelly punch sclerostomy incision (pink)

The ethnic-representative NPDS models were created in the same way as the idealised NPDS model described in section 4.1. A thin scleral flap is created by sketching a curved rectangular shape 4 mm in length over the anterior segment. This creates an approximate 4x4 mm flap shape as the new filtration area where aqueous humour drains into the subconjunctival space.

As an example, the European ethnic-representative anterior segment for a NPDS procedure is depicted in Figure 35. The anterior chamber is depicted in green. The TM is depicted in blue. The Schlemm's canal with the individual collector channels is depicted in yellow. Finally, the deep scleral flap incision (sclerostomy) is depicted in pink as the main surgical site.

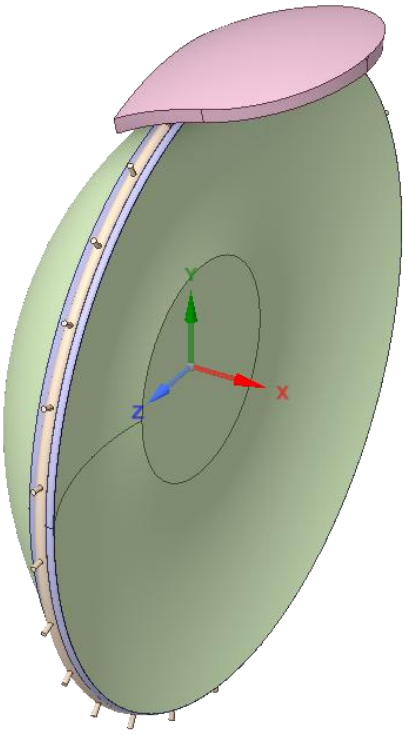


Figure 35 3D model of the European-representative anterior chamber and NPDS/mNPDS procedure including the anterior chamber with the iridectomy incision (green), TM (blue), Schlemm's canal with collector channels (yellow), and the deep scleral flap incision (pink)

5.3 Mesh Independence Study

Similar to the idealised model, a tetrahedral mesh was again chosen for its accuracy in handling complex geometries. Due to the geometrical similarities, it was speculated that similar body sizing and inflation could also be used for these ethnic-representative geometries. To ensure this, another mesh independence study was performed on the normal European eye geometry.

Body mesh element sizes ranging from 9.00E-4 to 5.00E-5 m were selected and the results from each analysed, which are provided in Table 11. IOP was once again selected as the key parameter for analysis, and the error between the current and previous mesh is calculated. Additionally, the number of nodes and elements are also tabulated, along with the average skewness as a measure of the mesh quality. These can be used to ensure an optimal mesh is selected while ensuring that the computational time is not unnecessarily increased.

Table 11 Mesh independence study results for ethnic-representative eye models

Body size [m]	IOP [Pa]	IOP [mmHg]	Error [%]	Number of nodes	Number of elements	Average skewness
0.0009	1800.0481	13.50		262610	1110085	0.290614773
0.0007	1800.1168	13.50	0.00%	263212	1110970	0.290484747
0.0005	1800.0795	13.50	0.00%	264821	1115888	0.289771091
0.0003	1800.1326	13.50	0.00%	276156	1155494	0.285634344
9.00E-05	**1799.6047**	**13.50**	**0.03%**	**713464**	**3118253**	**0.221597689**
7.00E-05	1799.6374	13.50	0.00%	1179626	5380435	0.206703811
5.00E-05	1799.1122	13.49	0.06%	2659592	12868623	0.197728106

The IOP values stabilize at 13.50 mmHg for all body sizes with insignificant error percentages compared to previous refinements. This suggests that refining the mesh further does not lead to significant improvements in accuracy, implying that the solution is mesh-independent at this point.

The average skewness improves significantly at a body size of 9.00E-05 m compared to larger element sizes, going from 0.2906 at 0.0009 m to 0.2216. This is a notable improvement in mesh quality and is well below the accepted average value of 0.33 [145]. At this body size of 9.00E-05 m, the mesh contains 713,464 nodes and 3,118,253 elements. These are significantly lower numbers compared to the finer mesh sizes (for example, the 5.00E-05 m body size contains 2,659,592 nodes and 12,868,623 elements). This means the computational cost at 9.00E-05 m will be far more manageable than at smaller body sizes, while still providing accurate results. Further refining the mesh drastically increases the number of elements, which translates to significantly more computational resources and time without offering noticeable improvements in the IOP results.

Thus, it can be confirmed that the mesh selected for the idealised eye can also be used for the ethnic-representative models moving forward, as it strikes a good balance between optimal mesh quality and computational time.

5.4 Results & Discussion

In this section, the velocity magnitudes, flow directions, WSS, and overall IOP reduction will be discussed to analyse the aqueous humour flow in two eye geometries – one representing a European-ethnic eye and the other an African-ethnic eye. The flow patterns will be depicted on the XY-plane of each model as this view showcases the flow field at the deepest ACD and consistently includes the surgical site. This view also corresponds well with other CFD studies, allowing for easy and direct comparison. By observing these flow characteristics and cross-examining it with the knowledge acquired from literature in section 2.5, conclusions can be drawn on how ethnic/anatomical variations in eye shape can lead to distinct fluid dynamics, with implications for IOP management, nutrient

distribution, and potentially varying surgical outcomes. This comparison provides a foundation for understanding how ethnic differences in eye anatomy might influence ocular health outcomes.

5.4.1 Normal Flow

Firstly, an analysis will be conducted on the normal aqueous flow dynamics for each eye model. These normal fluid dynamic conditions will be used as a baseline for what is considered a healthy eye. The fluid dynamic results of the surgical procedures will then be compared to these results.

The pressure map in Figure 36 shows the static pressure profile across the anterior segment for both the European (left) and African (right) eye models. The IOP distribution appears uniform within the anterior chamber across both the European and African eye models, with the majority of the anterior chamber showing pressure levels in the same range (13.5 mmHg). This suggests that the simulations are capturing a baseline steady-state pressure in each model, which is expected under normal physiological conditions. There is a minor pressure gradient near the TM in both models as the pressure decreases toward the drainage area.

These IOP results correspond with the permeability input for the TM as calculated from Darcy's law in Table 10 for normal flow conditions.

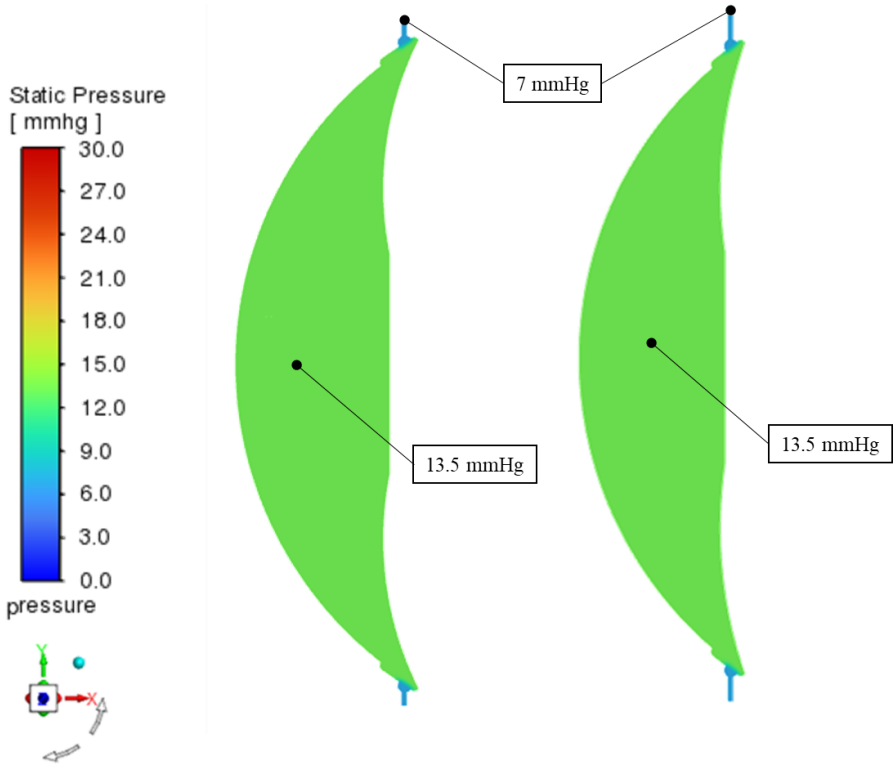


Figure 36 IOP results under normal conditions for the European-representative eye (left) and the African representative eye (right)

The velocity pathlines and vectors for normal flow conditions in the supine position are provided in Figure 37 and Figure 38, respectively, to reveal the general flow patterns and directions of aqueous

humour within the anterior chamber for each ethnic model, providing insights into potential differences in flow dynamics that could influence surgical outcomes.

In the supine position, both models exhibit distinct rotational formations in the anterior chamber, which is typical of aqueous humour circulation patterns as shown in section 4 of this thesis. These rotational recirculations suggest a cyclical flow that facilitates nutrient distribution to the cornea and lens by continuously circulating the aqueous humour. In both models, rotational circulations are centred symmetrically along the midline, indicative of stable flow structures. The rotational flow appear to be similarly positioned in both models, centred with the pupil, suggesting that the primary flow dynamics are preserved across the two anatomies.

Both models show maximum velocity magnitudes at the collector channel outlets of 0.47 mm/s. Close to the pupil, the maximum velocity for the European is 0.19 mm/s and 0.17 mm/s for the African eye model, which mainly provides nutrients to the lens (located behind the pupil). This could be due to the anatomical differences, particularly the ACD and ACA. The deeper ACD of the European model allows for the aqueous humour to maintain a longer flow path and larger vertical loop, which results in a higher flow velocity at the central anterior chamber. The slightly wider ACA in the African model allows for more distributed flow across the chamber. Additionally, there is a slight velocity elevation at the corneal wall (European: 0.07 mm/s, African: 0.06 mm/s), which is crucial for nutrient delivery to the corneal endothelium [46]. This pattern aligns with expected drainage flow dynamics, where the aqueous humour flows towards the drainage sites at the periphery, contributing to IOP regulation. While the overall range of velocities appears similar, the African model shows that the higher velocity streamlines are more confined to the central vortex region compared to the European model, circled in red in Figure 37. This suggests that the overall flow is more distributed in the European model.

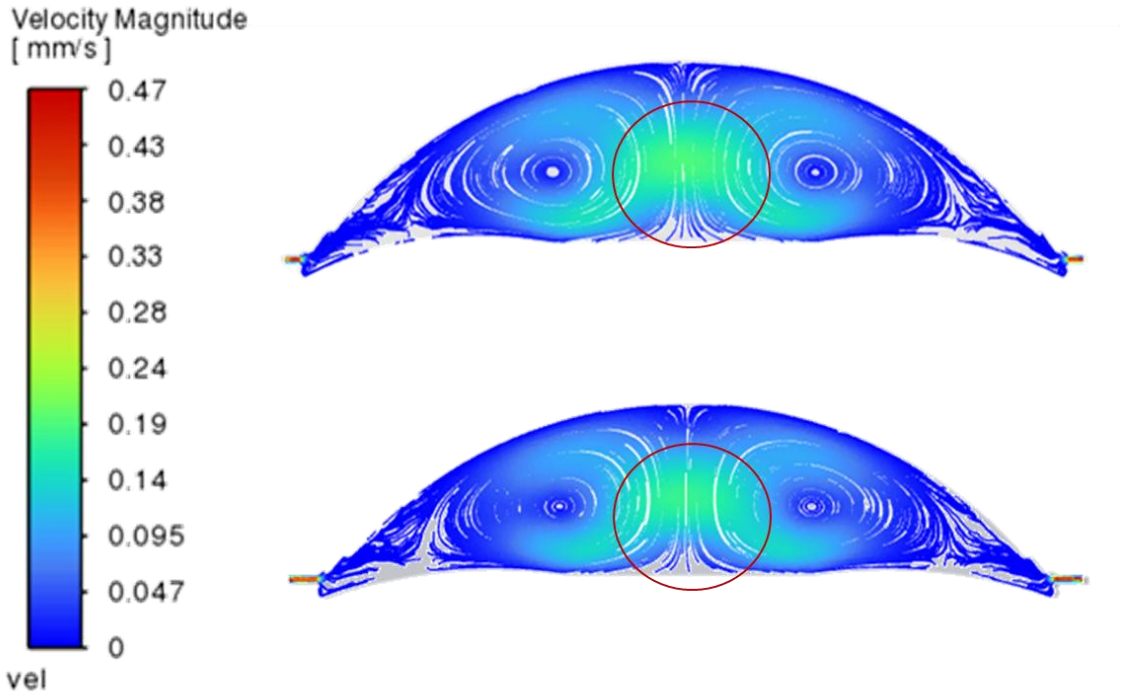


Figure 37 Velocity pathline results under normal conditions for the supine European-representative eye (top) and the supine African-representative eye (bottom)

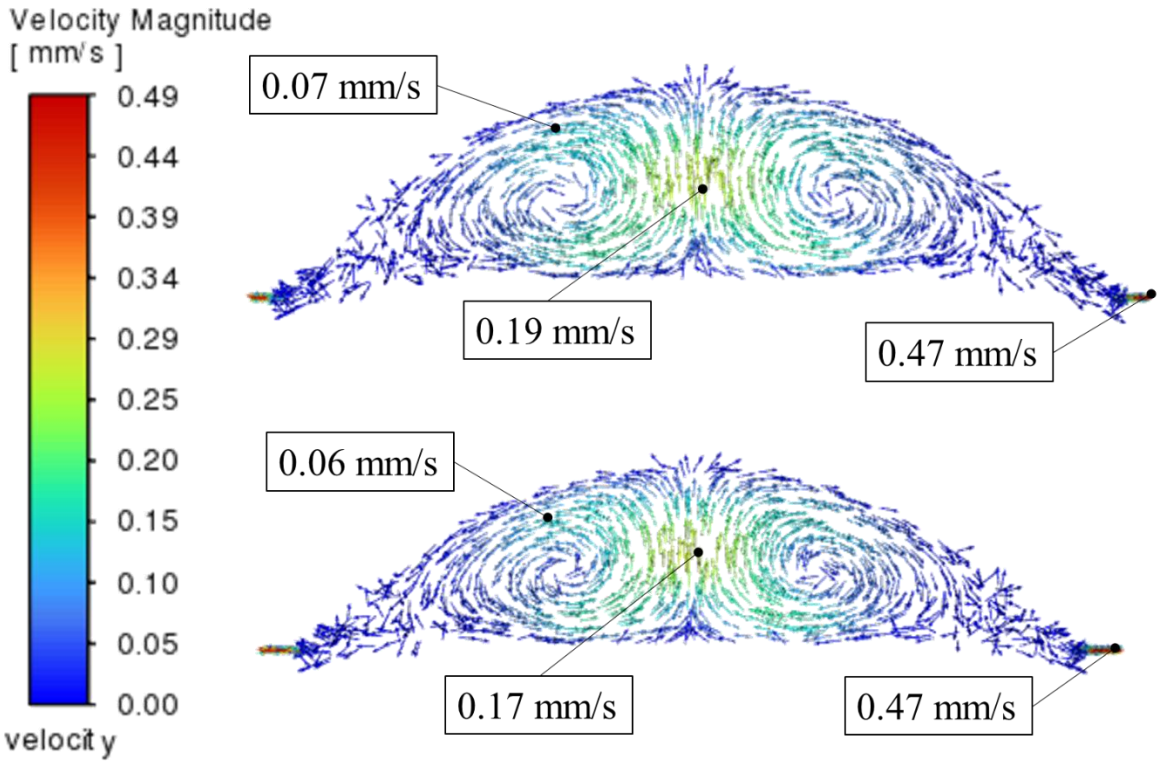


Figure 38 Velocity vector results under normal conditions for the supine European-representative eye (top) and the supine African-representative eye (bottom)

Figure 39 shows how the normal supine flow field has similar characteristics between both ethnic models, confirming the baseline physiological flow similarity. There are subtle distinctions, as previously discussed, in the recirculation spread and high-velocity zone distribution which offer early indicators of how anatomical differences might become amplified under post-surgical conditions.

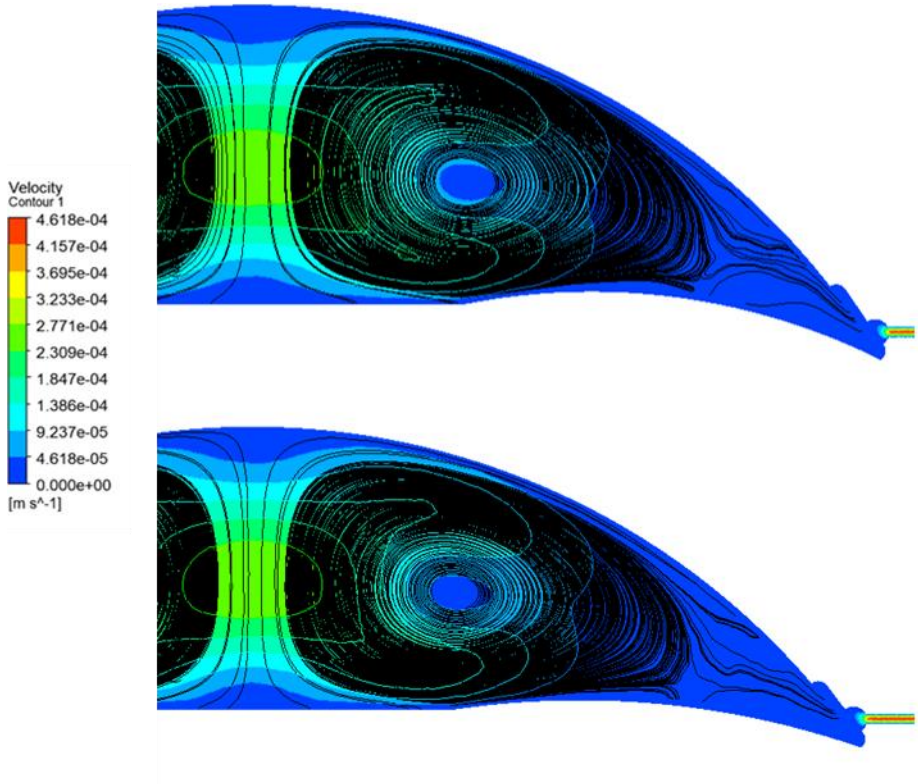


Figure 39 Velocity magnitude and streamline contours for normal supine orientation for the European model (top) and African model (bottom)

The velocity pathlines and vectors for normal flow conditions in the upright position are provided in Figure 40 and Figure 41, respectively. In the upright position for both models, the pathlines still display two prominent vortices in both models. Despite the shift in each vortex shape due to gravitational influence, the flow in both models remain relatively symmetrical in the central region of the anterior chamber. However, there does seem to be a difference between the superior and inferior sections of the anterior chamber, where the inferior section shows some flow stagnation (circled in green in Figure 40). This is likely due to the fact the gravity acts down towards this angle, working against the buoyancy forces, creating localized breaks as the direction of the fluid shifts, which could disrupt the continuity of the recirculation zones. This is expected as it is consistent with the results from section 4.5. In contrast, the superior region shows smooth continuous flow in both models.

The velocity field in the upright position indicate a higher velocity gradient near the pupil region (circled in red in Figure 40). In each model, the vectors show a clear circular pattern within the vortices, indicating strong recirculation zones, although this seems slightly stronger in the African model.

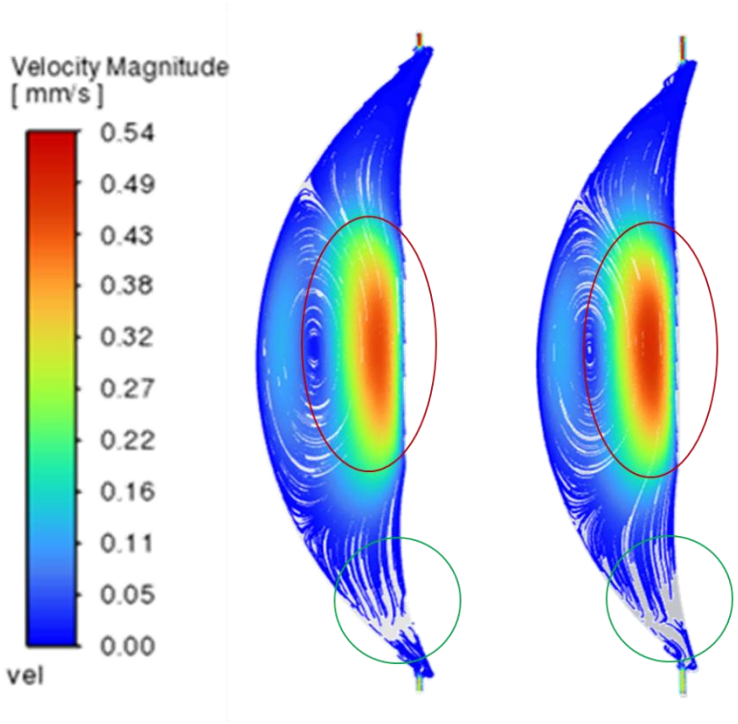


Figure 40 Velocity pathline results under normal conditions for the upright European-representative eye (left) and the upright African-representative eye (right)

Figure 41 further shows that the maximum velocity at the lens site is 0.47 mm/s for both the European model and African model although one can observe a slightly larger "red" region for the African-representative eye. As gravity introduces a vertical pressure gradient, the aqueous humour flow is redistributed toward the inferior section of the anterior chamber, making the ACD less significant compared to its effect in the supine position. At the corneal wall, the maximum flow velocity is 0.12 mm/s for both the European model and African model. The maximum outflow velocity at the collector channel outlets is 0.57 mm/s for the European model and 0.56 mm/s for the African model. The narrower ACA of the European model creates a more confined flow, which increases velocity as the pressure decreases towards the outlet. The directionality of the vectors suggests that aqueous humour flows smoothly toward the TM, which is essential for effective outflow and IOP regulation.

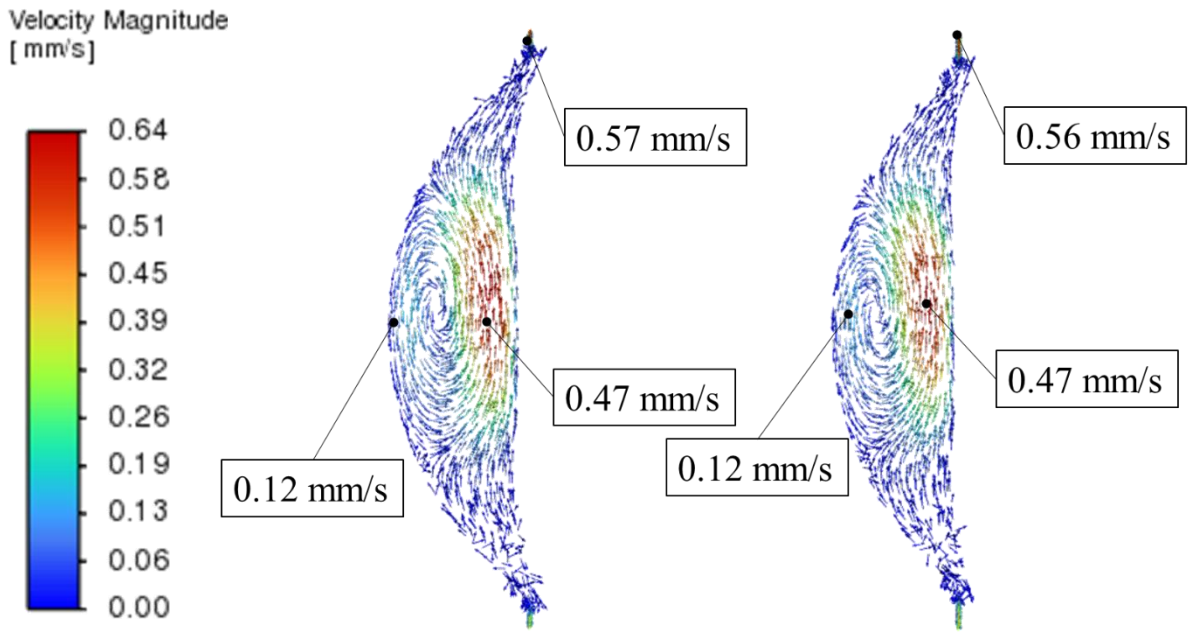


Figure 41 Velocity vector results under normal conditions for the upright European-representative eye (left) and the upright African-representative eye (right)

While the overall structures remain similar to supine conditions, several orientation-induced changes occur, which can be better observed in Figure 42. In the European model, the recirculation region exhibits a higher velocity magnitude. This is likely due to the deeper ACD, which allows the aqueous humour to circulate over a greater distance before reversing direction. Consequently, a stagnation point (indicated by the red dot) appears in the superior region on the cornea. In contrast, the African model, with its shallower ACD and wider ACA, exhibits a more compact recirculation zone, also resulting in a stagnation point location at a lower peak central velocity.

The graph provided in Figure 43 further quantifies the position of the stagnation point as a result of the velocity changes in the anterior chamber. The graph provides the average velocity on the y-axis and the normalized position of the stagnation point on the x-axis. The normalized position is a function of the y-position of the stagnation point (y_{stag}) and the length of the cornea (L_{cornea}):

$$Stag_{norm} = \frac{y_{stag}}{L_{cornea}} \tag{5.3}$$

In the European eye model, the deeper anterior chamber permits a more inferior stagnation point (lower $Stag_{norm}$), which supports stronger central flow and higher average velocity. Conversely, the African model, with its shallower ACD and wider ACA, shows a superior shift in stagnation point and reduced average velocity. Although the clinical implications of a stagnation point shift is now known, it could potentially alter nutrient exposure in the corneal periphery (based on previous studies of uneven nutrient distributions [91,95]).

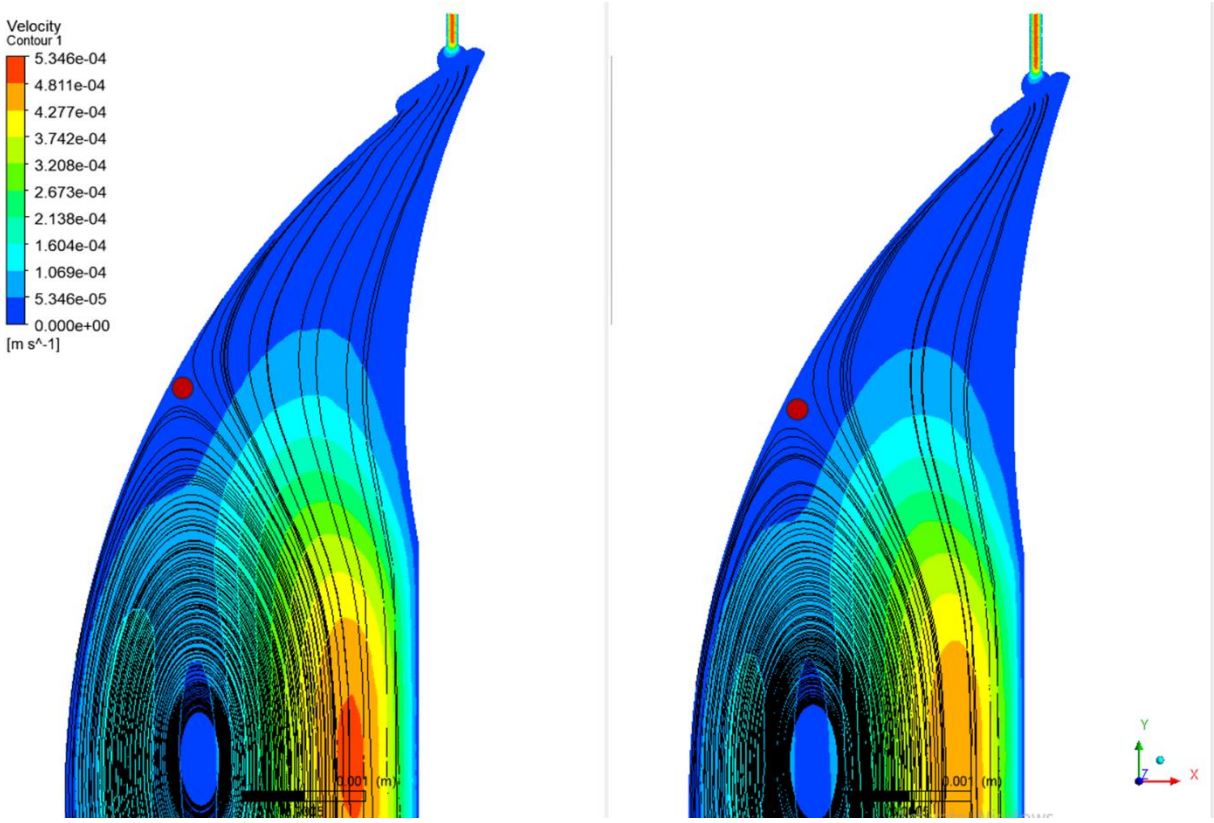


Figure 42 Velocity magnitude and streamline contours for normal upright orientation for the European model (left) and African model (right)

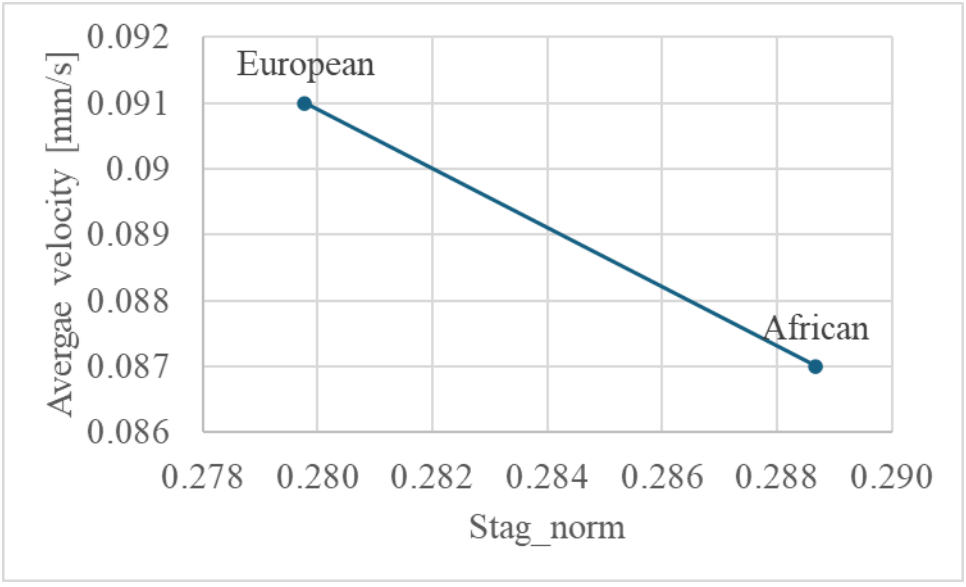


Figure 43 Normalized stagnation point position versus average anterior chamber velocity for normal upright eye models

The most pronounced vorticities were identified using the Q-criterion, which is provided for the supine and upright positions in Figure 44 and Figure 45, respectively. The highest Q-values are recognised

where the flow moves from the Schlemm's canal to the outlet channels. These vortices align with the sharp geometry changes at this point in the anterior segment. In the supine position, the maximum Q-value is 158.1 and 134.8 for the European and African eye model, respectively. In the upright position, the maximum Q-value is 175.4 and 180.7 for the European and African eye model, respectively. Vortex formation near surgical sites can lead to fibrotic scarring [101], which will be explored in the following sections.

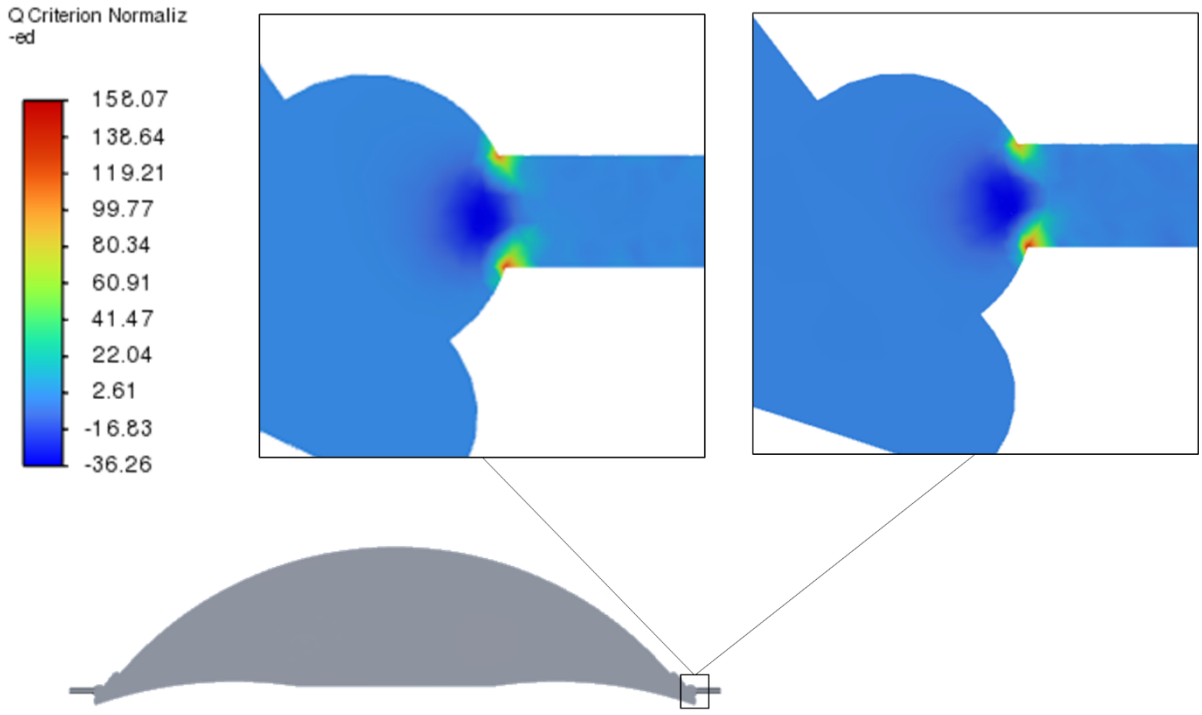


Figure 44 Q-criterion results under normal conditions for the supine European-representative eye (left) and the supine African-representative eye (right)

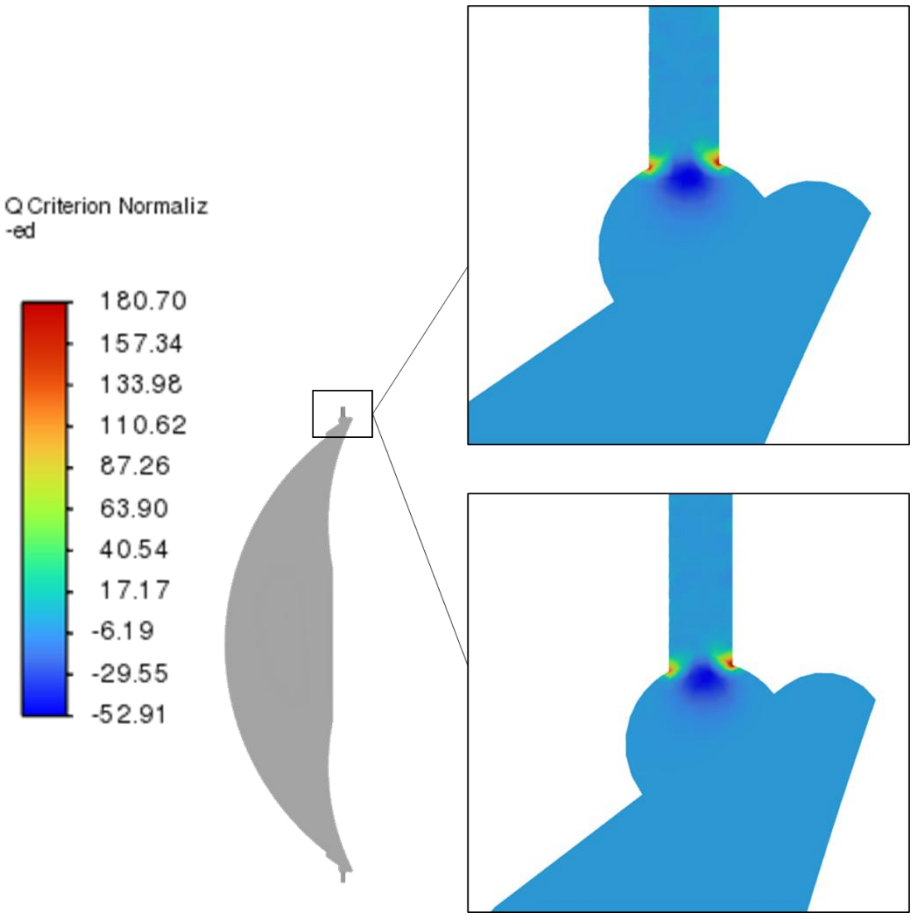


Figure 45 Q-criterion results under normal conditions for the upright European-representative eye (top) and the upright African-representative eye (bottom)

Though there are slight variances between the European and African models, both illustrate similar conditions for normal aqueous humour flow. This suggests that geometrical differences between the eye anatomies do not have a dominant effect under normal conditions. These normal eye conditions as discussed in this section will be used as a baseline comparison for healthy conditions when analysing the surgical procedures going forward.

5.4.2 Post-Surgical Flow

The following section will discuss the results of the trabeculectomy simulations and compare them to the results acquired for normal flow conditions. The IOP distributions and velocity pathlines will be analysed for both the European and African models. The results will focus on the post-sutured scenarios in both the supine and upright positions. However, some unsutured results may also be discussed. The post-sutured result parameters will reflect the sutured incision at steady-state (approximately one day post-op).

The results for the IOP distributions for unsutured and sutured trabeculectomy are provided in Figure 46 and Figure 47, respectively. In the unsutured condition, with the incision open to atmosphere, both

models show extremely low IOP values close to 0 mmHg. This is expected because the open incision allows free drainage of aqueous humour, resulting in minimal resistance and a substantial drop in IOP. These near-zero pressures reflect an acute hypotony state due to unregulated outflow, which is common immediately after trabeculectomy before suturing.

Further analysis on the unsutured results can be found in Appendix E.

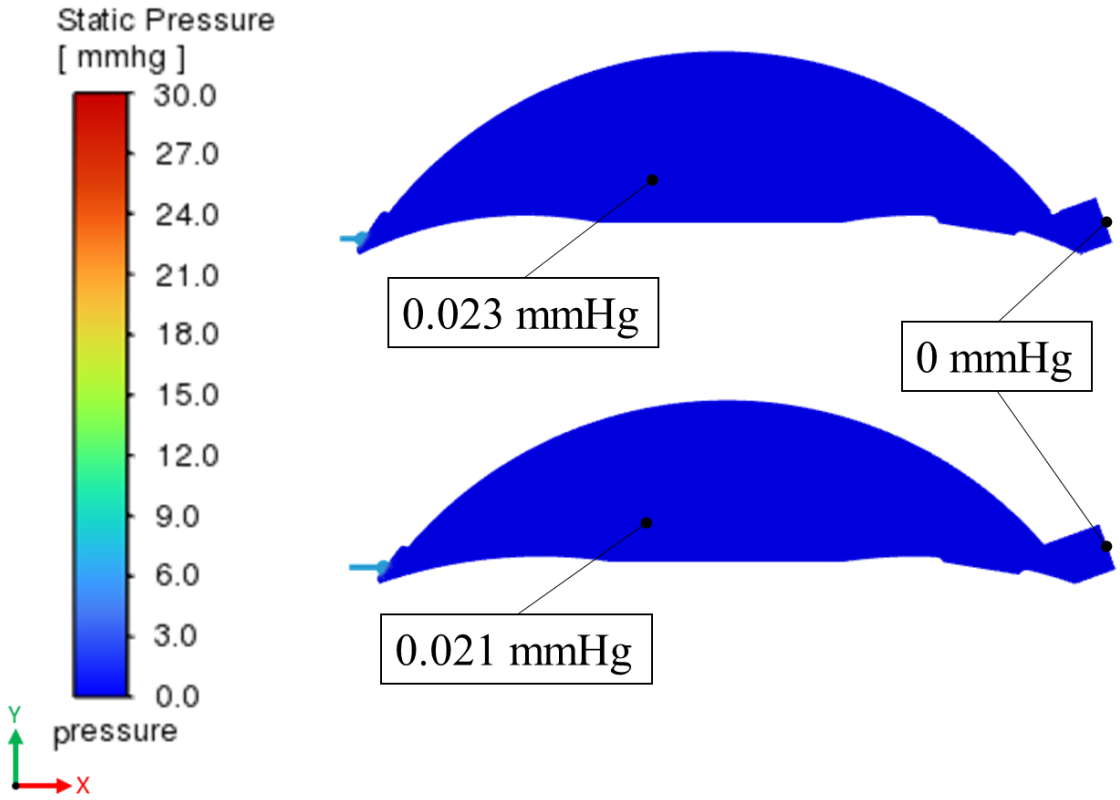


Figure 46 IOP results under trabeculectomy conditions for the supine unsutured European-representative eye (left) and supine unsutured African representative eye (right)

After suturing, both models have reached a steady-state IOP of approximately 7 mmHg, which is a controlled, moderately low pressure. This value indicates that suturing effectively restored partial resistance to the outflow, allowing the anterior chamber to maintain a stable, safer IOP. This IOP level is within an acceptable range for one day post-surgery, as it is high enough to avoid hypotony-related complications while still achieving the desired reduction in IOP for glaucoma management. Additionally, this provides sufficient margin for an eventual increase in IOP as the sutures heal over time.

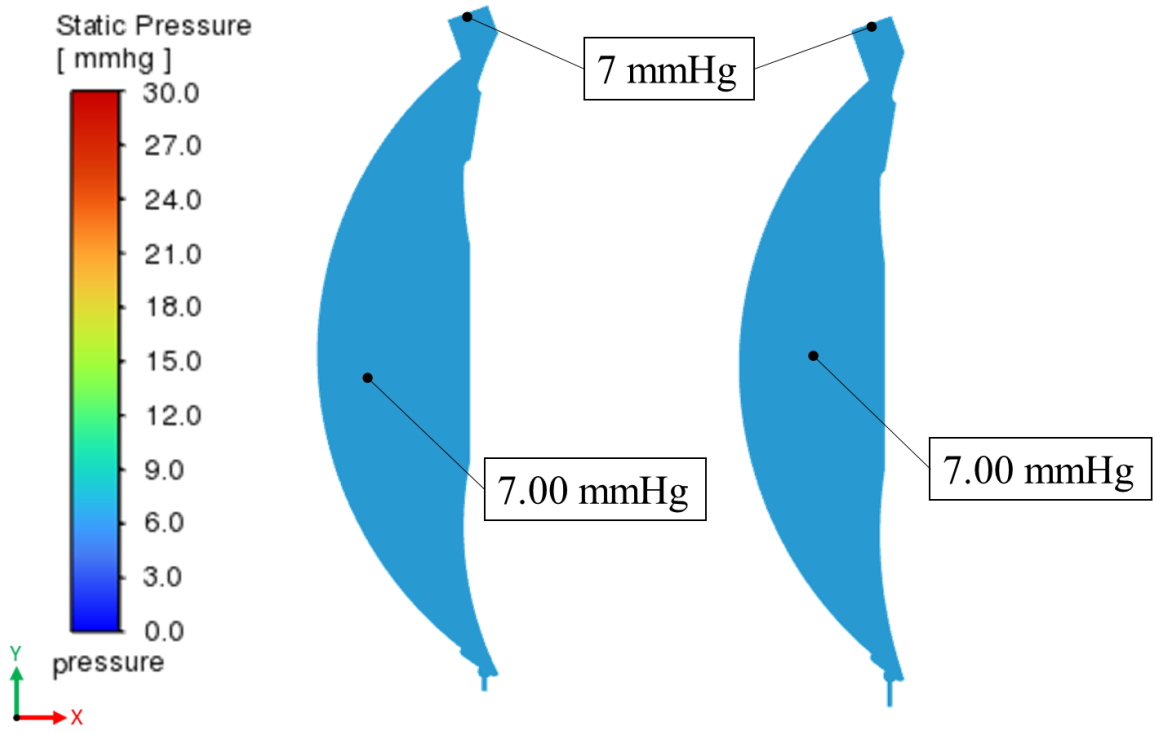


Figure 47 IOP results under trabeculectomy conditions for the upright sutured European-representative eye (left) and the upright sutured African representative eye (right)

The IOP results for unsutured and sutured NPDS are provided in Figure 48 and Figure 49, respectively. For the unsutured conditions, the European model shows a significantly lower IOP (4.60 mmHg). In contrast, the African model has a higher IOP (8.96 mmHg). This large discrepancy between the two models may be attributed to anatomical and geometric variations. Since the European model has a deeper ACD, which provides a larger fluid volume for circulation, it may allow for greater IOP decrease as the aqueous humour flow is less constrained. The shallower ACD in the African model reduces the available fluid volume, leading to higher flow resistance and a lower IOP drop. Even with the same outflow pathway geometry, the reduced space in the anterior chamber leads to a relatively higher IOP. Additionally, the shorter TML in the African model may lead to more resistance in the remaining outflow pathway, helping to maintain a higher residual IOP.

The difference between the unsutured NPDS and unsutured trabeculectomy cases are noticeable and can most likely be explained in how each procedure alters the outflow resistance and the role of anatomical differences in controlling flow dynamics. In trabeculectomy, the surgery creates a full-thickness opening in the TM, completely bypassing all natural resistance. This pathway provides an essentially unrestricted outflow. With NPDS, the outflow pathway is still partially regulated by the eye's anatomy and resistance of the unaffected TM. Thus, the differences in anatomical features seem to have a much greater influence on how effectively aqueous humour is drained in NPDS vs trabeculectomy.

Further analysis on the unsutured results can be found in Appendix E.

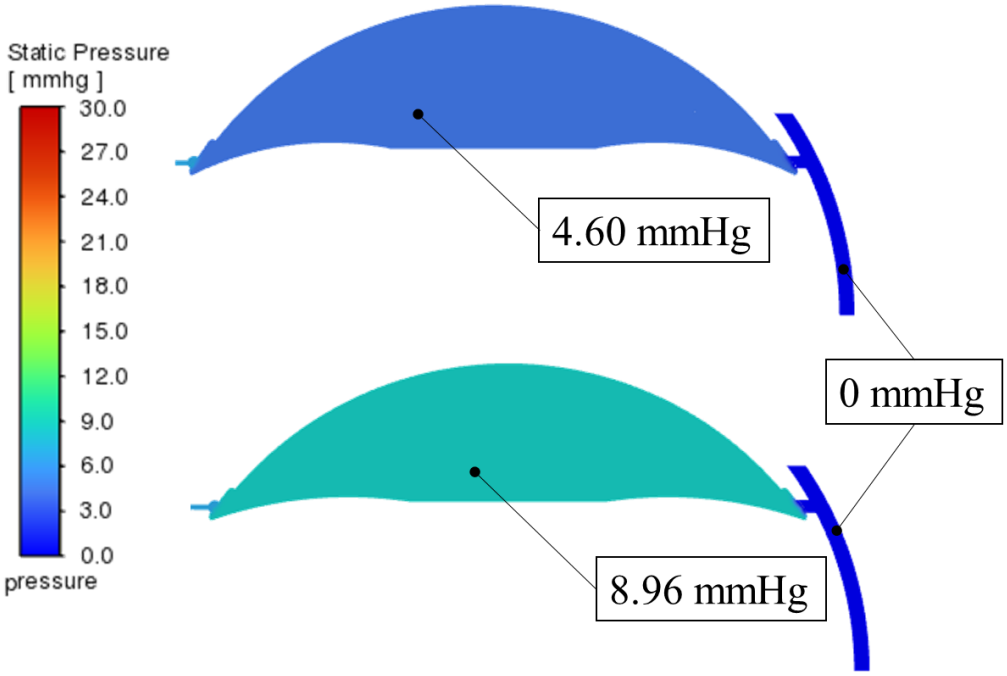


Figure 48 IOP results under NPDS conditions for the supine unsutured European-representative eye (left) and the supine unsutured African representative eye (right)

When the surgical site is sutured, the IOP rises significantly and becomes nearly identical in both models (26.78 mmHg for the European model and 26.68 mmHg for the African model). The similarity in results may indicate the dominance of the sutures in controlling outflow resistance. Suturing introduces significant resistance to the outflow pathway, effectively normalizing aqueous humour dynamics across both geometries. Regardless of anatomical differences, the sutures now dominate the flow resistance, making the surgical site the primary determinant of IOP. Both models reach IOPs post-suturing similar to pre-operative conditions, which suggests that the sutures may be too tight, requiring adjustment to allow more drainage. The same suturing conditions were defined for NPDS as for trabeculectomy, which suggests that NPDS have significantly more sensitive suturing requirements.

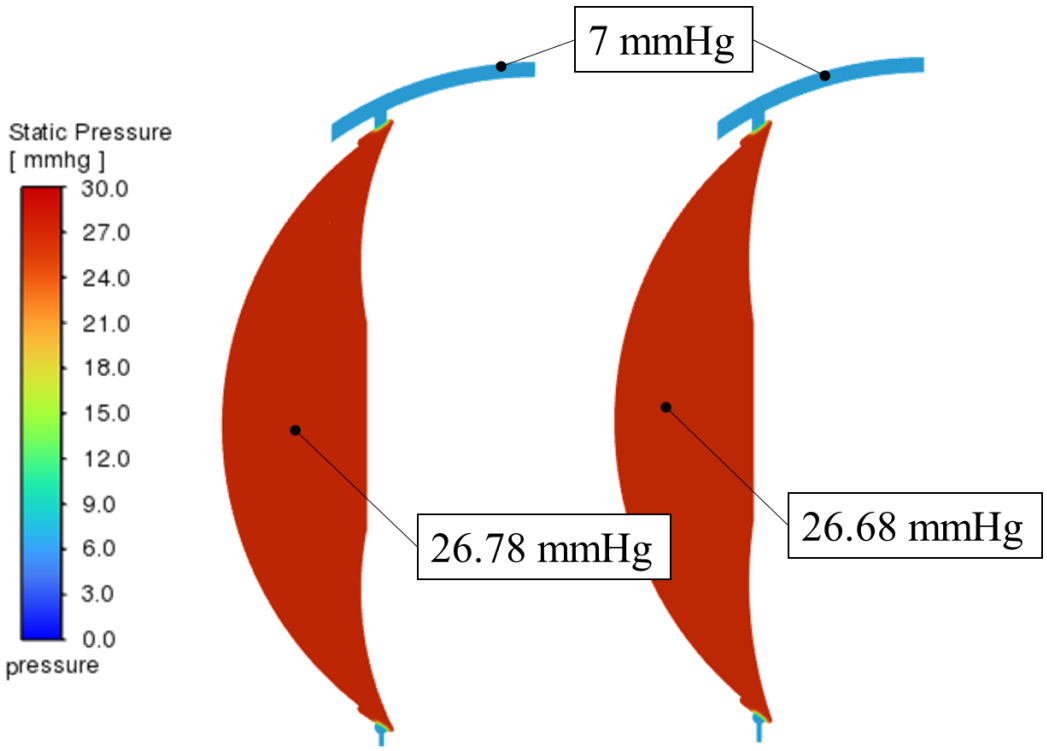


Figure 49 IOP results under NPDS conditions for the upright sutured European-representative eye (left) and the upright sutured African representative eye (right)

The IOP results for unsutured and sutured mNPDS are provided in Figure 50 and Figure 51, respectively. The unsutured results for both the European and African model show a drastic reduction in IOP as the surgical pathway's outflow resistance has been substantially reduced in the mNPDS modification. Both models approximate 0.02 mmHg, which is similar to what was achieved in the unsutured trabeculectomy models, indicating a similar reduction in TM resistance.

Further analysis on the unsutured results can be found in Appendix E.

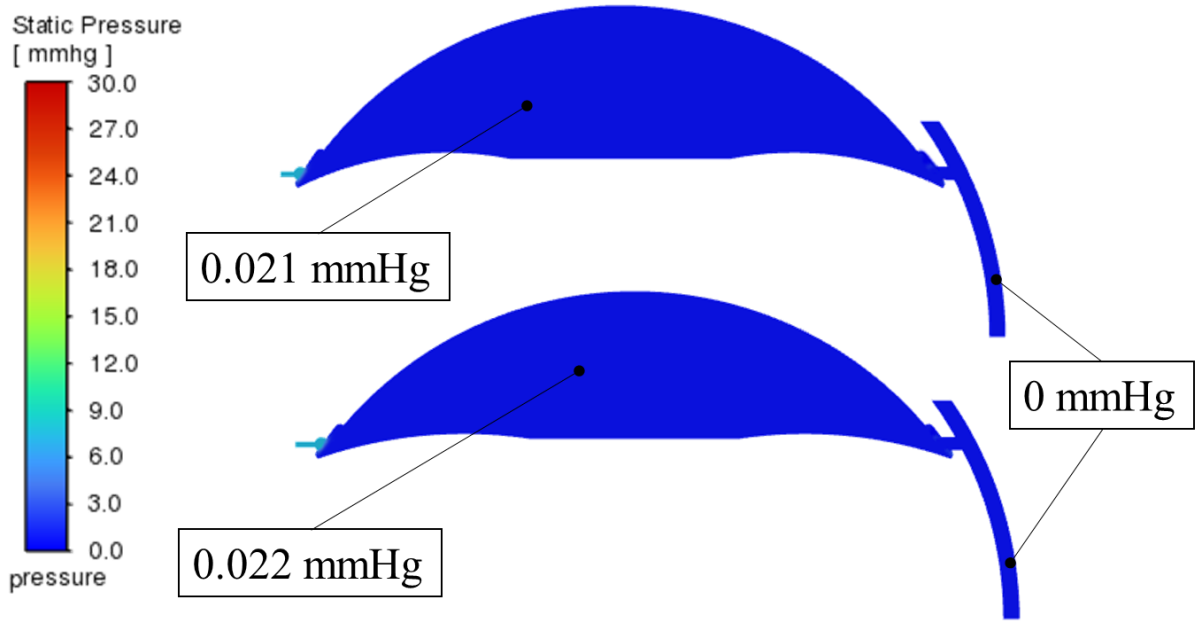


Figure 50 IOP results under mNPDS conditions for the supine unsutured European-representative eye (top) and the supine unsutured African-representative eye (bottom)

For both the European and African sutured models, the sutures effectively restore the IOP to a healthy post-operative range. Once again, the results are similar to what was achieved in the sutured trabeculectomy models, which is approximately 7 mmHg. Based on IOP alone, the mNPDS shows a similar efficacy to trabeculectomy. These results also align with what was realized in the idealised models analysed in section 4 of this thesis.

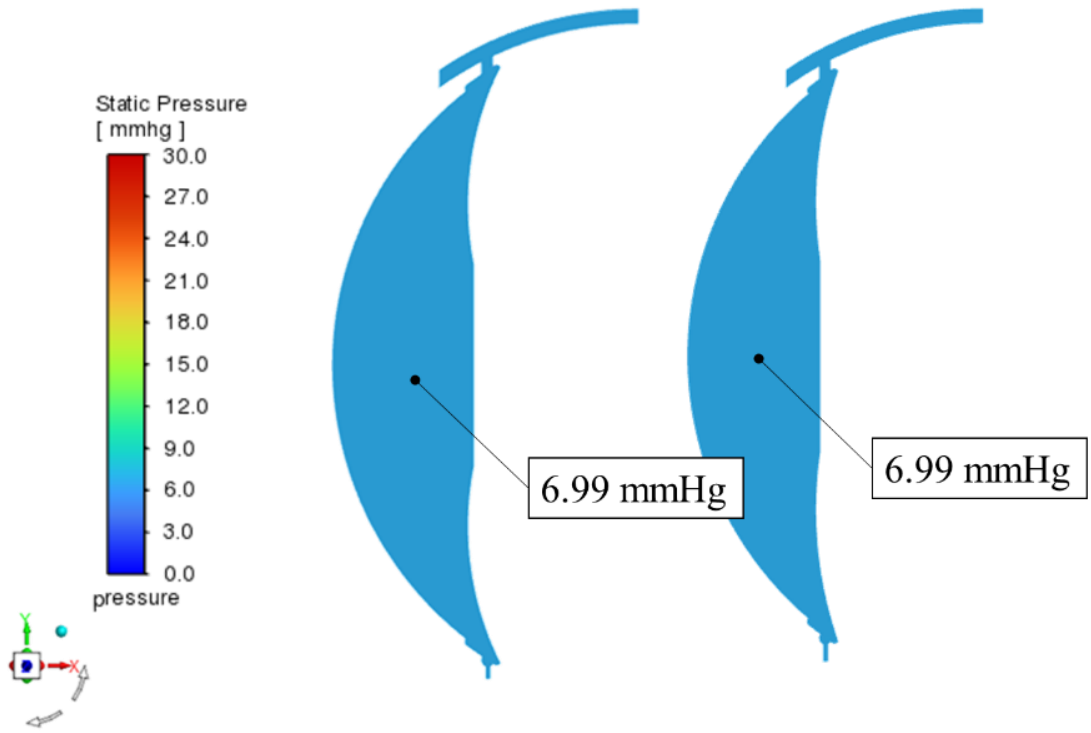


Figure 51 IOP results under mNPDS conditions for the upright sutured European-representative eye (left) and the upright sutured African-representative eye (right)

The IOP results are consistent with those observed for the idealised model in chapter 4.5. Both the trabeculectomy and mNPDS procedures successfully decrease the IOP after suturing, while the NPDS procedure returns to a glaucomic state when applying the same suture outlet pressure boundary. NPDS has the potential to decrease IOP, as demonstrated in Figure 48, depending on suturing tightness. This will be further explored in section 5.4.6.

Next, the velocity flow fields for the post-surgical simulations will be compared to those observed for normal flow conditions to identify how the flow magnitude and distribution is altered with different procedures. Though the whole anterior segment will be considered, focus will be placed on the superior ACA, as this is where the surgical site will be for all of the filtration surgeries considered. As a recapitulation of what was observed for the normal model, Figure 52 and Figure 53 is given to provide a close-up look of the superior ACA under normal flow conditions in the supine and upright conditions, respectively.

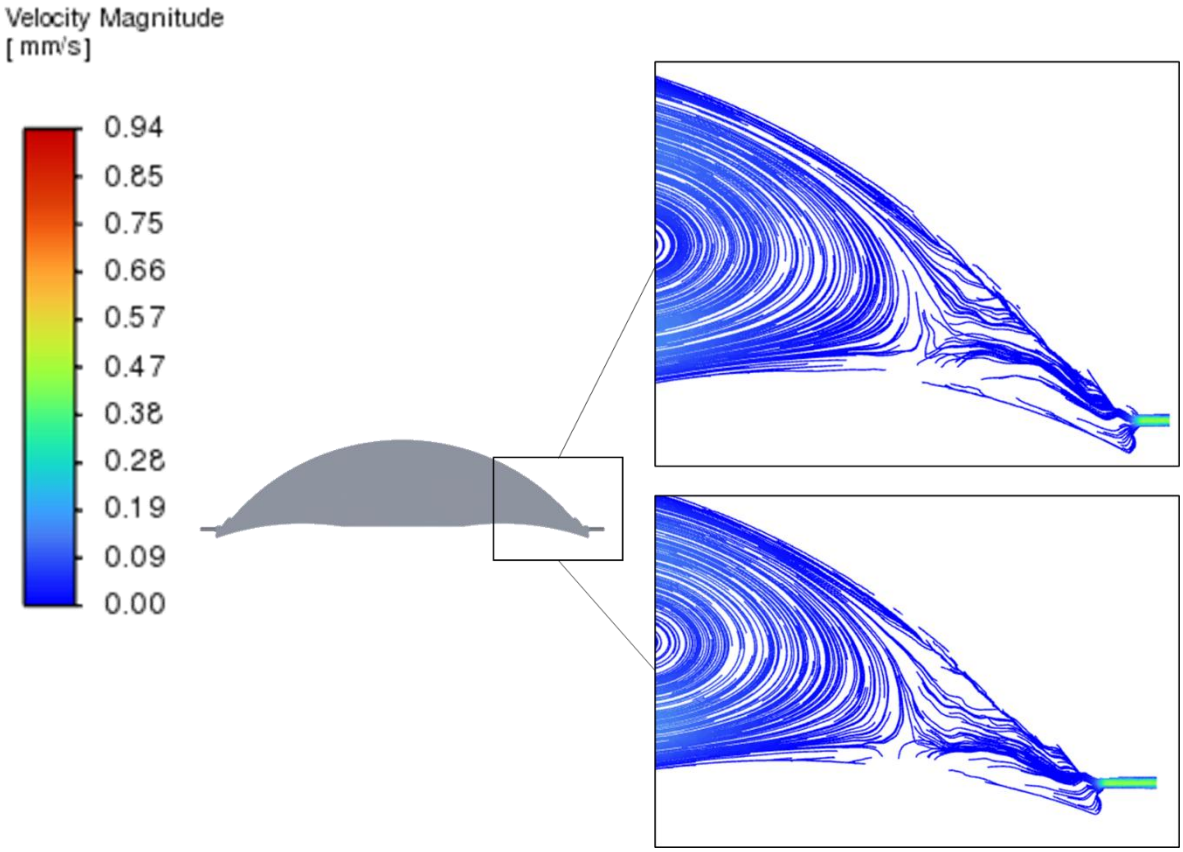


Figure 52 Inset velocity pathline results under normal for the supine sutured European-representative eye (top) and the supine sutured African representative eye (bottom)

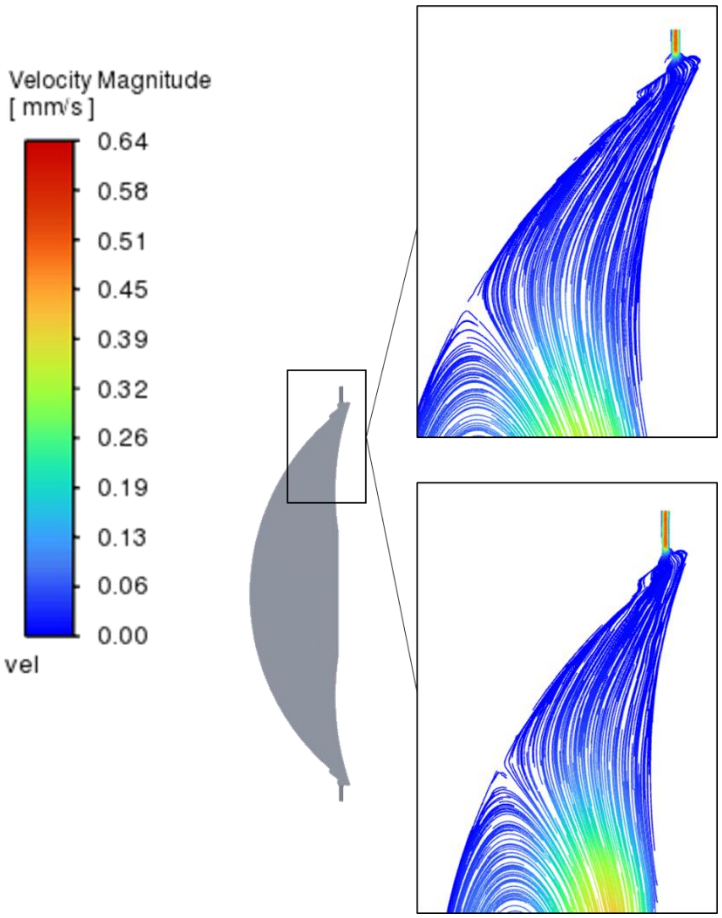


Figure 53 Inset velocity pathline results under normal for the upright sutured European-representative eye (top) and the supine sutured African representative eye (bottom)

Figure 54 shows the velocity pathline results for sutured trabeculectomy in the supine position. The central recirculation zones are still present. However, there is an increase in flow velocity at the pupil and at the corneal wall compared to normal conditions. The velocity magnitude at the surgical outlet is 0.94 mm/s for the European model and 0.93 mm/s for the African model. This is a substantial increase from the normal flow outlet velocity (0.47 mm/s), which is diverting flow away from the other outlet channels.

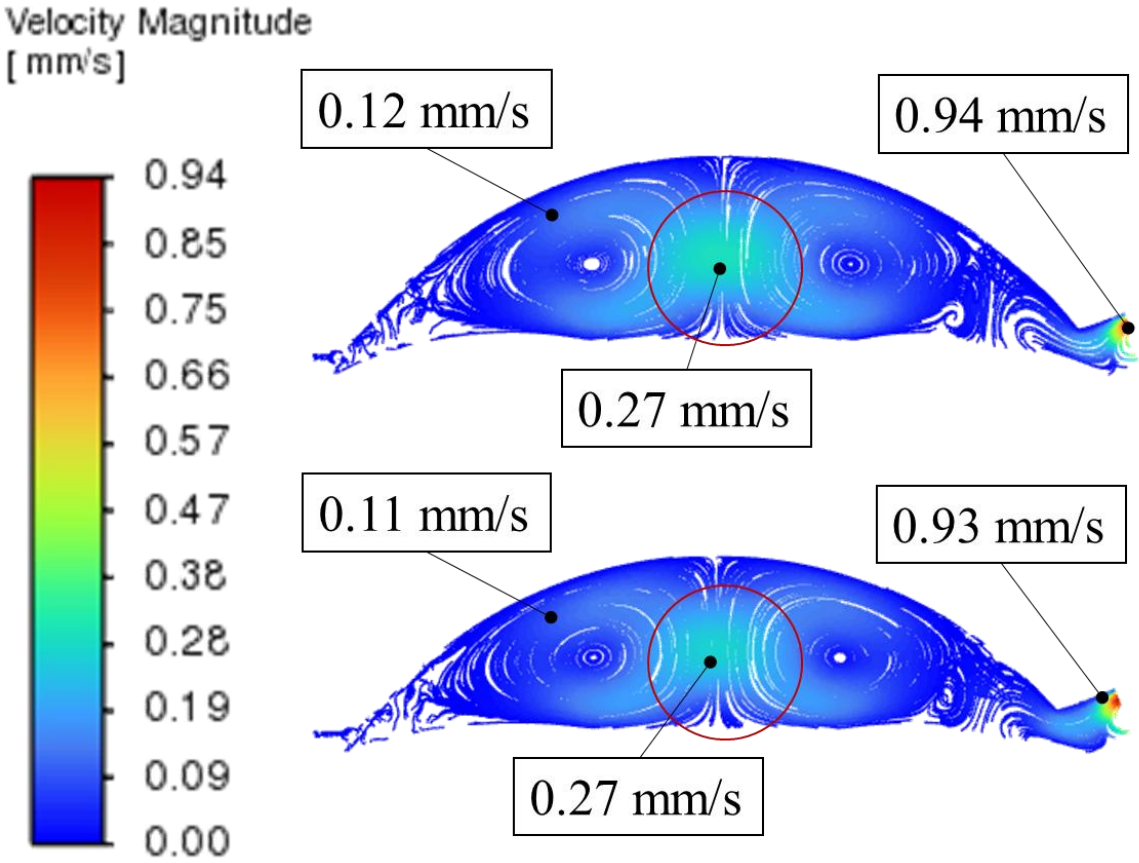


Figure 54 Velocity pathline results under trabeculectomy conditions for the supine sutured European-representative eye (top) and the supine sutured African representative eye (bottom), with the flow concentration circled in red

Comparing this flow to Figure 52, there is also a clear flow alteration at the iridectomy, which is more closely illustrated in Figure 55. The entrance flow from the iridectomy site for each model is indicated by the black arrows. The European model exhibits a more vertical entry of aqueous humour through the iridectomy site, whereas the African model shows a more angular entry. This can be attributed to the wider ACA and shallower ACD in the African model, which creates a more horizontally oriented flow path that aligns more quickly with the anterior chamber's bulk recirculation. The European model, with its narrower ACA and deeper ACD, allows the flow to enter more vertically, delaying its integration into the bulk flow stream. This suggests that anatomical differences not only affect the magnitude of flow but also its vector orientation, influencing changes in the flow field following glaucoma filtration surgery.

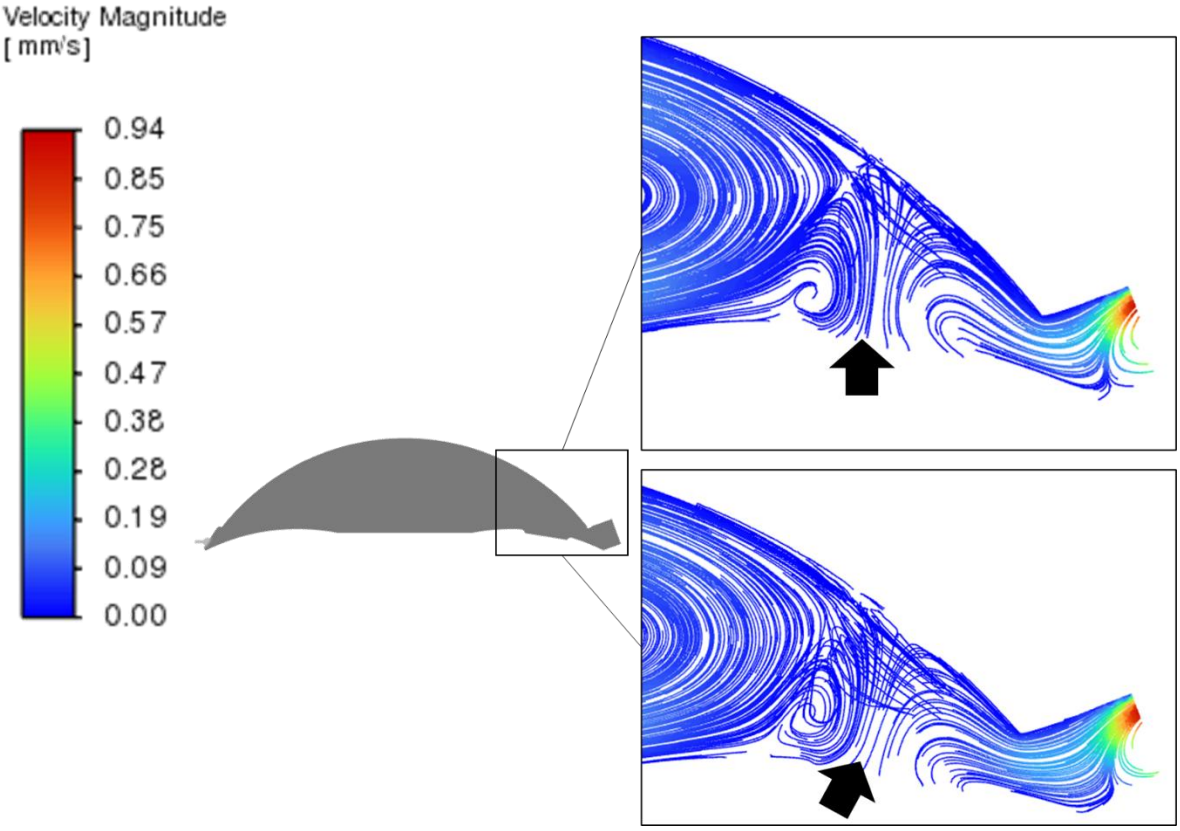


Figure 55 Inset velocity pathline results under trabeculectomy conditions for the supine sutured European-representative eye (top) and the supine sutured African representative eye (bottom), with the black arrow indicating the entrance flow from the iridectomy site

In Figure 56, it can be more clearly observed that the African model shows a longer, more extended swirl near the iridectomy, while the European model has a more confined or compact swirl, and a more vertical streamline entry into the outlet. The African model's shallower ACD compresses the available vertical space in the anterior chamber, which restricts vertical streamline movement, causing the flow to be redirected more laterally as it exits through the iridectomy. As a result, the streamlines are forced to enter the outlet at a more oblique angle. The deeper ACD in the European model provides more vertical space for recirculation and flow development. This allows the streamlines to approach the iridectomy outlet from below, more perpendicularly to the iris, resulting in shorter, tighter outlet swirls.

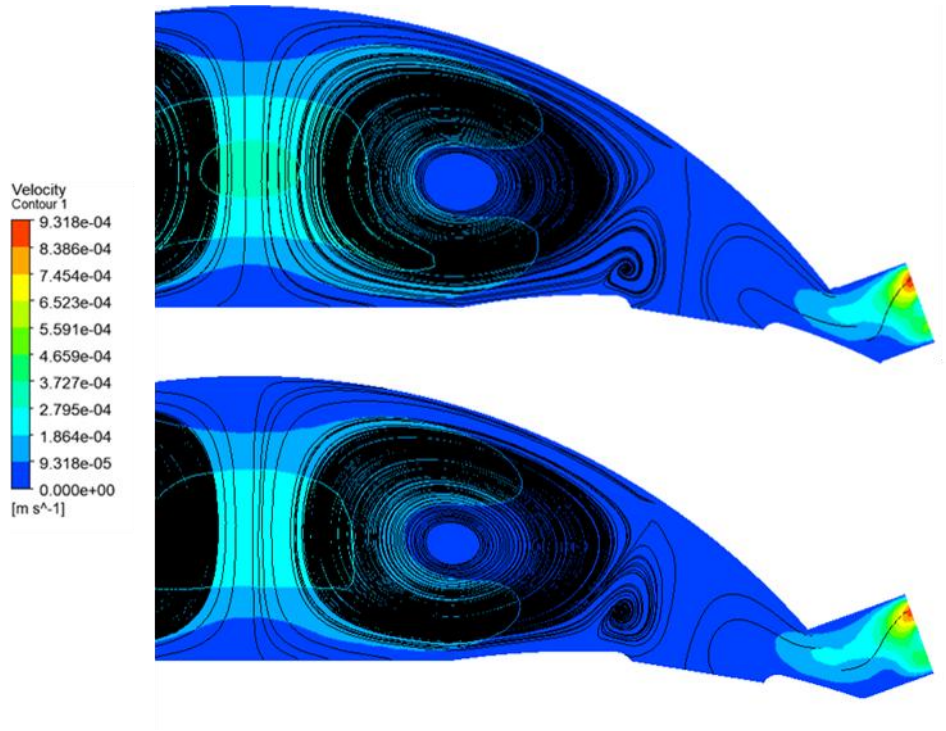


Figure 56 Velocity magnitude and streamline contours for trabeculectomy supine orientation for the European model (top) and African model (bottom)

Figure 57 shows the velocity magnitude contours at the conventional and surgical outlets for the trabeculectomy models from the top view (vertical projection view looking straight onto the sclerostomy). The maximum flow velocity is not centred with the sclerostomy punch, which is expected due to the angle at which the punch is made. In the supine position, the maximum flow velocity is offset towards the anterior, with a secondary velocity peak towards the posterior. The peak velocity of the European model is slightly higher than the African model, which aligns with Figure 54. However, anatomical differences between the European and African models do not significantly influence the core offset of the peak velocity at the surgical site.

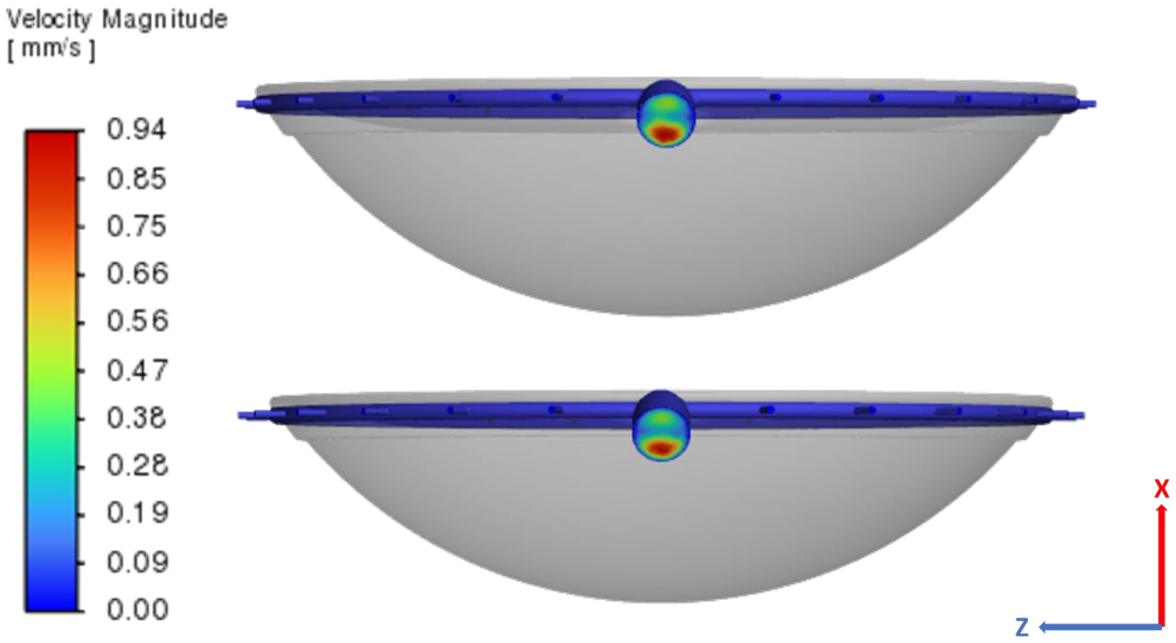


Figure 57 Sclerostomy top view of velocity magnitude contours at the outlets under trabeculectomy conditions for the supine sutured European-representative eye (top) and the supine sutured African representative eye (bottom)

Figure 58 shows the velocity pathline results for sutured trabeculectomy in the upright position. Here, the maximum velocities near the surgical incision are slightly reduced, reaching velocity values below normal conditions. Despite this decrease in magnitude, the flow to the other outlet channels is significantly diminished, which essentially changes the overall flow pattern in the anterior chamber.

In the European model, the maximum flow of 0.64 mm/s is at the pupil with stronger circulation (circled in red in Figure 58). This is a considerable increase in this area of the anterior chamber when compared to normal flow of 0.47 mm/s. The maximum flow at the corneal wall is similar to the normal model at 0.12 mm/s.

In the African model, there is weaker central flow at the pupil compared to the European model (circled in red). The maximum velocity value at this point is 0.47 mm/s, which is equivalent to the normal flow conditions. However, the flow at the corneal wall is decreased by 25% from 0.12 mm/s for normal flow conditions to 0.09 mm/s in the trabeculectomy model. This could indicate a drastic nutrient deficiency transport to the corneal wall [91,95,156].

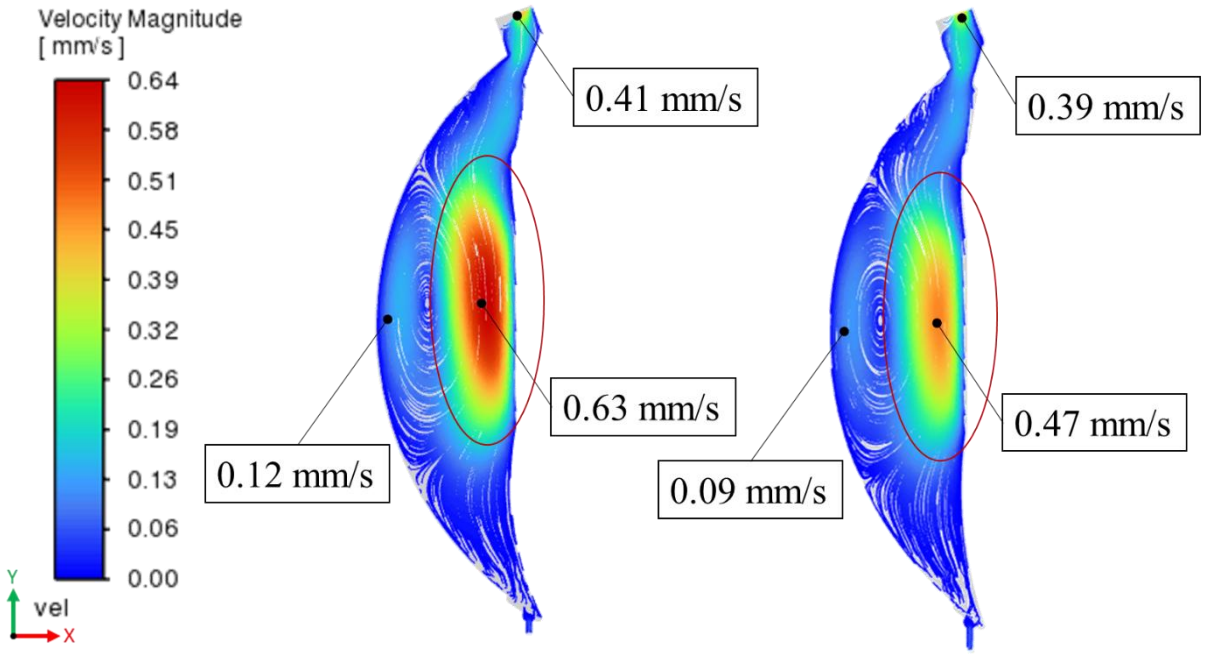


Figure 58 Velocity pathline results under trabeculectomy conditions for the upright sutured European-representative eye (left) and the upright sutured African representative eye (right), with the flow concentration circled in red

Compared to Figure 53, both sutured models further indicate an accelerated flow region near the surgical site (Figure 59), which can introduce deviations in drainage patterns. There are indications of irregular flow near the incision site, most likely due to the flow alteration caused by the iridectomy. This incision in the iris to the posterior chamber allows for an additional inlet flow that perturbs the normal vortex pattern. Furthermore, there is some out-of-plane flow (circled in red in Figure 59) which is not present under normal flow conditions. These flow alterations could result in fibrotic scarring, which could potentially cause the procedure to failure in the long term [101].

This alteration can disrupt the uniformity of aqueous humour flow, which is essential for nutrient delivery to the avascular tissues of the cornea and lens. The continued directional flow toward the incision site, even at lower velocities, may contribute to mild hypotony, especially in the African model where flow velocities are generally lower [36].

These flow alterations further support the notion that the trabeculectomy outlet pathway dominates the flow field. Thus, the pre-existing anatomical differences are no longer small contributors, but rather impacts how the flow field forms and behaves. The deeper ACD of the European model provides space for stronger recirculation. The African model's shallower ACD restricts vertical loop formation. Its wider ACA disperses the flow, making it less focused and less capable of opposing gravity.

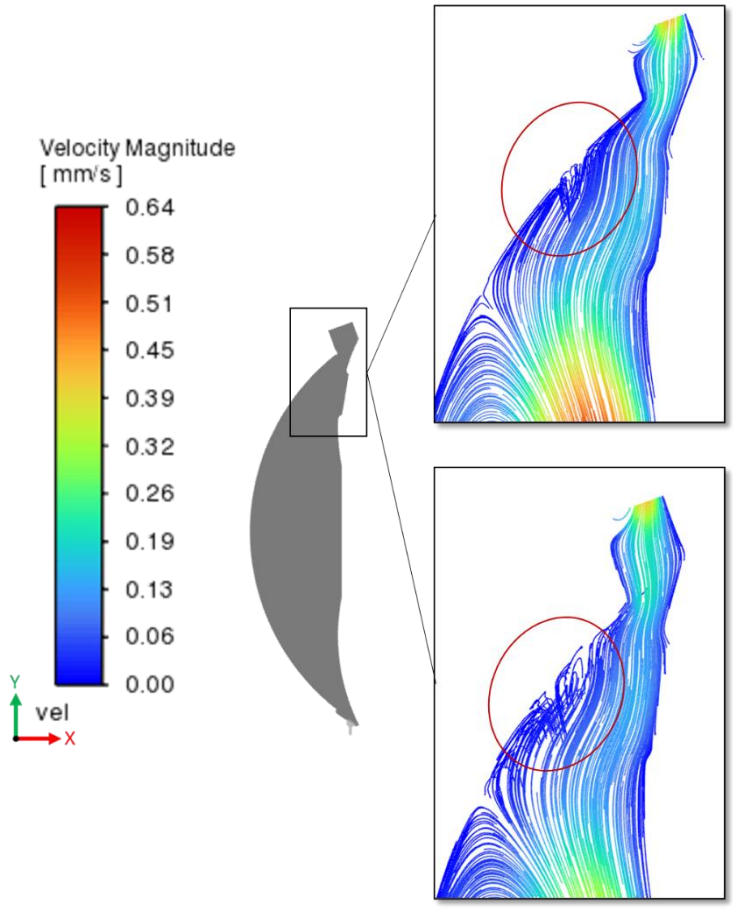


Figure 59 Inset velocity vector results under trabeculectomy conditions for the upright sutured European-representative eye (top) and the upright sutured African representative eye (bottom), with out-of-plane flow circled in red

Figure 60 illustrates that the European model exhibits a distinct velocity deflection zone near the superior corneal wall, which is affecting the out-of-plane flow behaviour and further supports the effect of anatomical differences. This feature, circled in red and characterized by upward-curving streamlines and mild rotational behaviour, is likely enabled by the deeper ACD of the European model, which provides more space for flow expansion and curvature. In contrast, the African model, with its shallower ACD, shows a more constrained flow that adheres more closely to the iris surface and exits more directly. This difference underscores how geometry not only influences outlet alignment but also permits or restricts the formation of secondary flow regions near boundary surfaces.

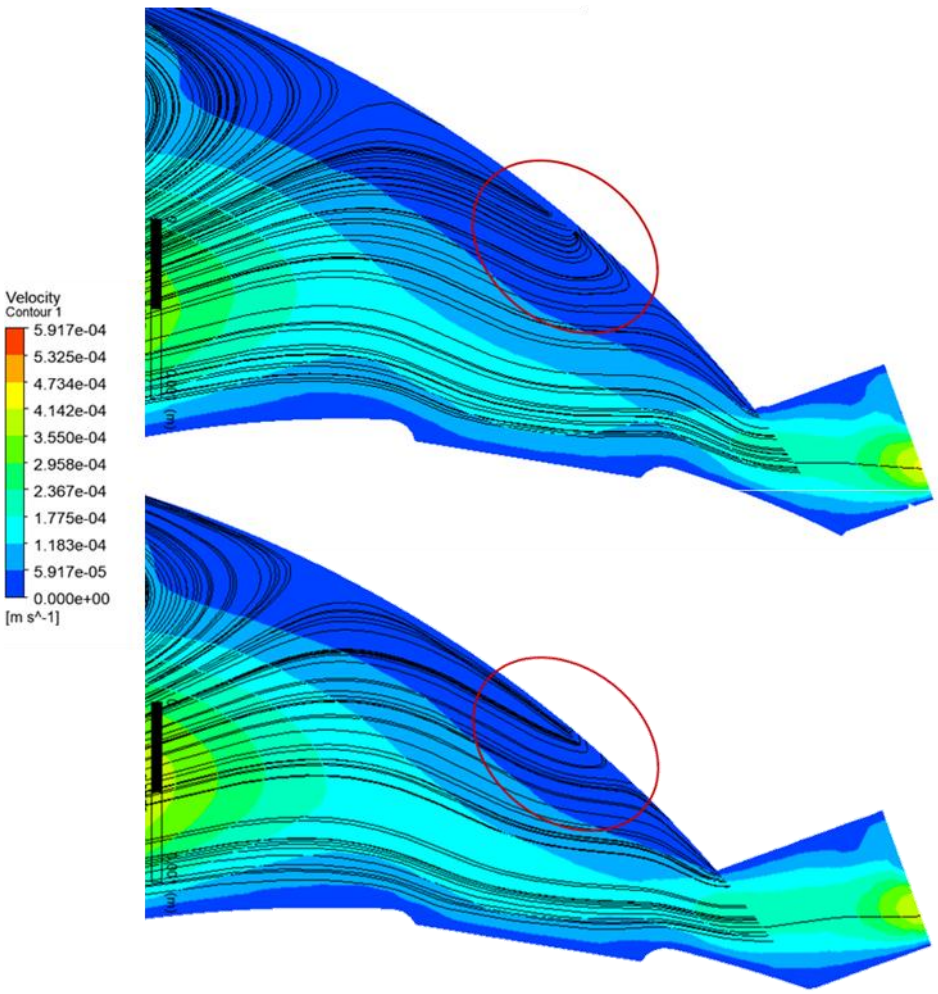


Figure 60 Velocity magnitude and streamline contours for trabeculectomy supine orientation for the European model (top) and African model (bottom)

The velocity profiles in the sutured state further show that average and peak velocities in the African model are noticeably lower than those in the European model. This difference becomes more significant considering that the additional drainage pathway created by trabeculectomy may divert flow away from the central anterior chamber, reducing the natural circulation pattern. In the normal (pre-surgical) state, aqueous humour flow ensures the delivery of essential nutrients. The trabeculectomy has altered this distribution pattern, and in the African model, the lower velocities suggest a diminished ability to circulate these nutrients effectively [45,91,95,156]. Reduced central velocities mean that nutrients may not reach all areas of the cornea and lens with sufficient frequency, especially if flow is directed predominantly toward the drainage pathway. This can result in localized nutrient deficiencies, potentially leading to complications such as corneal decompensation or delayed tissue recovery in the African model [95,101].

Figure 61 shows the velocity magnitude contours at the conventional and surgical outlets for the trabeculectomy models from the top view for the upright position. Here, the maximum flow velocity is offset towards the posterior, with a discreet secondary velocity peak towards the anterior. There is no

noticeable difference in the core offset between the two models, which further suggests that anatomical differences do not affect flow alignment in trabeculectomy.

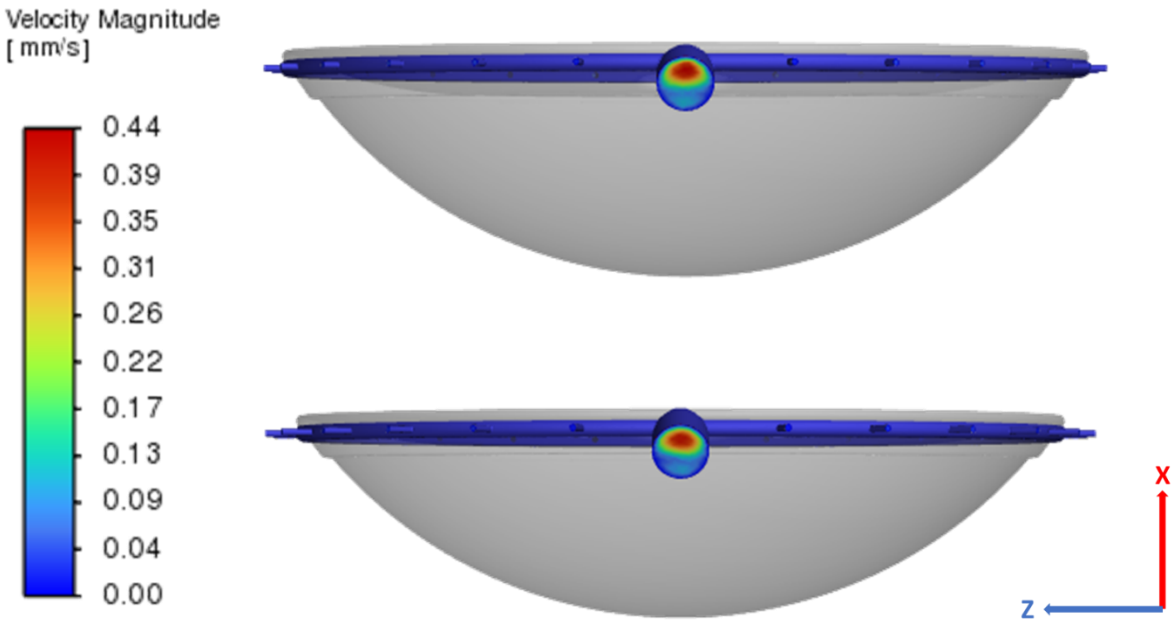


Figure 61 Top view of velocity magnitude contours at the outlets under trabeculectomy conditions for the upright sutured European-representative eye (top) and the upright sutured African-representative eye (bottom)

Figure 62 shows the velocity pathline results for sutured NPDS in the supine position. Here, the overall flows are very similar between the two ethnic models. The peak velocities near the pupil are 0.20 mm/s for the European eye model and 0.18 mm/s for the African eye model. Near the corneal wall, the velocity magnitude is 0.08 mm/s for the European eye model and 0.09 mm/s for the African eye model. These values closely align with what those of normal eye conditions, most likely because the TM remains completely intact for the NPDS procedure. As shown for the normal conditions, the deeper ACD in the European model creates greater vertical space, which can promote more fully developed recirculatory motion and increased velocity gradients. In supine orientation, buoyancy effects from temperature gradients will be better aligned with the deeper ACD geometry, enhancing flow circulation and peak velocity development centrally.

The most noticeable flow irregularities is the increased outflow from the surgical site. Specifically, there are very high velocities through the deroofing of the Schlemm's canal, which are more closely shown in Figure 63. Immediately after the TM, the flow enters a constricted region where the Schlemm's canal deroofing takes place. Hence, the flow accelerates as it exits the TM into this narrower canal. This explains the initial velocity spike observed. The flow then abruptly enters the deep scleral flap space, which has a much larger volume and cross-sectional area. Due to conservation of mass, the fluid cannot sustain high velocities throughout this expanded space. Therefore, the fluid decelerates and diffuses throughout the deep flap region.

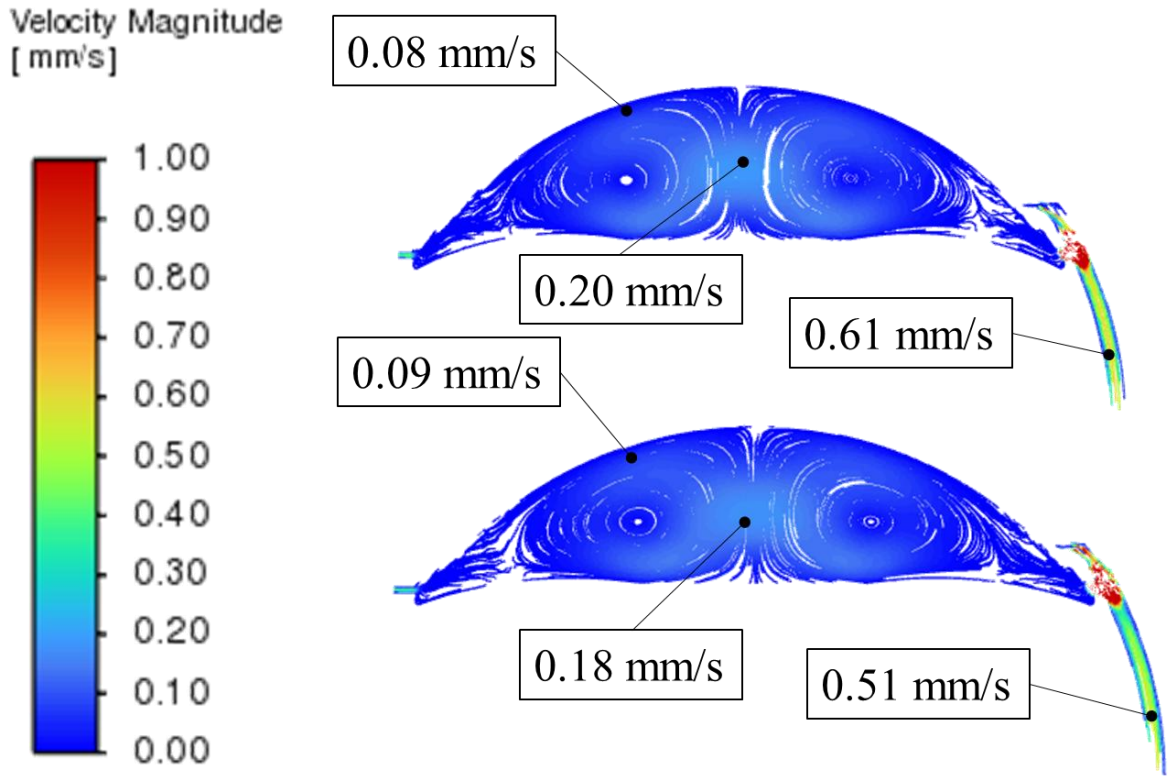


Figure 62 Velocity pathline results under NPDS conditions for the supine sutured European-representative eye (top) and the supine sutured African-representative eye (bottom)

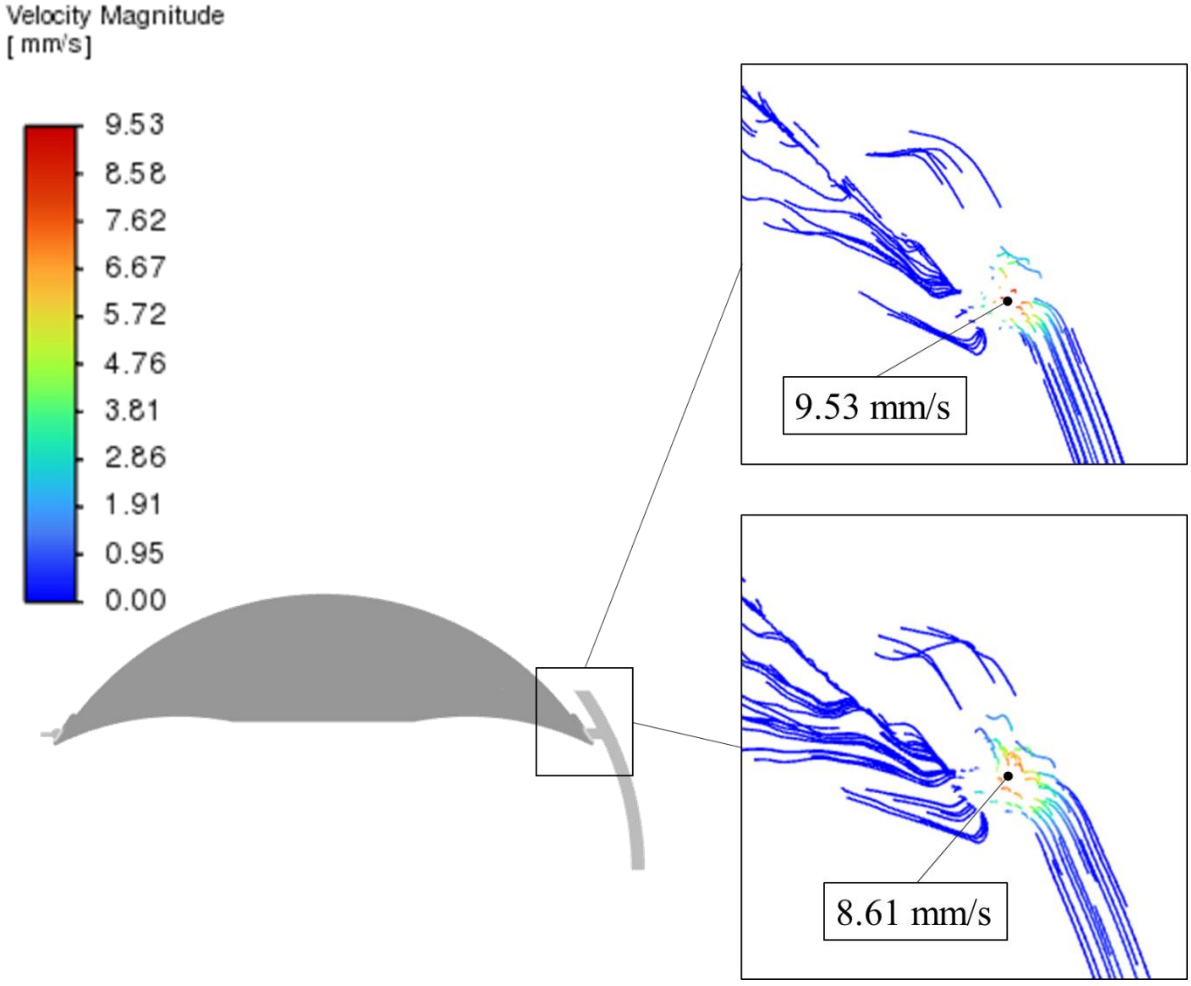


Figure 63 Inset velocity pathline results under NPDS conditions for the supine sutured European-representative eye (top) and the supine sutured African-representative eye (bottom)

Figure 64 shows the velocity pathline results for sutured NPDS in the supine position, which show similar trends to what was observed for the supine condition. The peak velocities near the pupil are 0.48 mm/s for the European eye model and 0.47 mm/s for the African eye model. These values closely align with what those of normal eye conditions. The European model further aligns well with normal conditions regarding the corneal flow at 0.11 mm/s. However, there is decreased flow near the corneal wall for the African model compared to its normal flow conditions, with a velocity magnitude of 0.08 mm/s. This could indicate a disruption in proper nutrient distribution.

Overall, the African model consistently shows an increased outflow at the surgical site, which is further illustrated in Figure 65. The wider ACA in the African model appears to allow for increased drainage near the surgical site. However, both models still align relatively closely with normal flow conditions, indicating the potential of NPDS as a safer alternative to prevent post-operative complications. However, without the proper suturing techniques, NPDS still shows to be ineffective based on its IOP reduction.

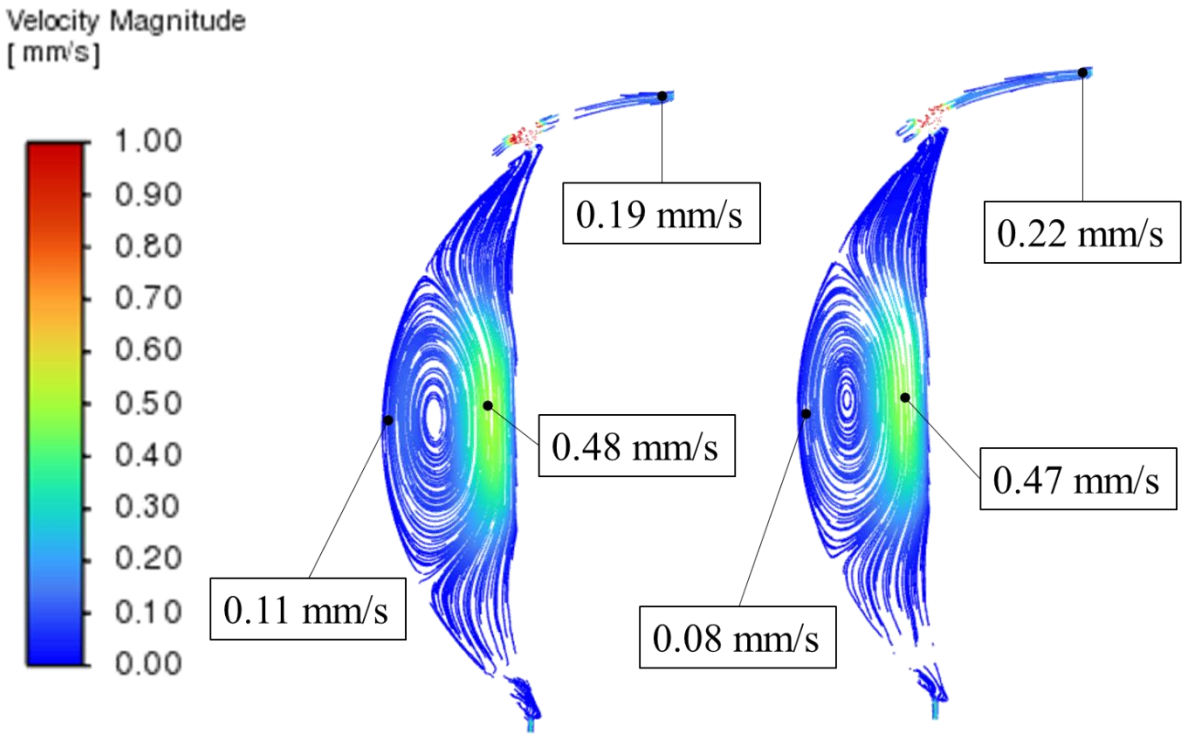


Figure 64 Velocity pathline results under NPDS conditions for the upright sutured European-representative eye (left) and the upright sutured African-representative eye (right)

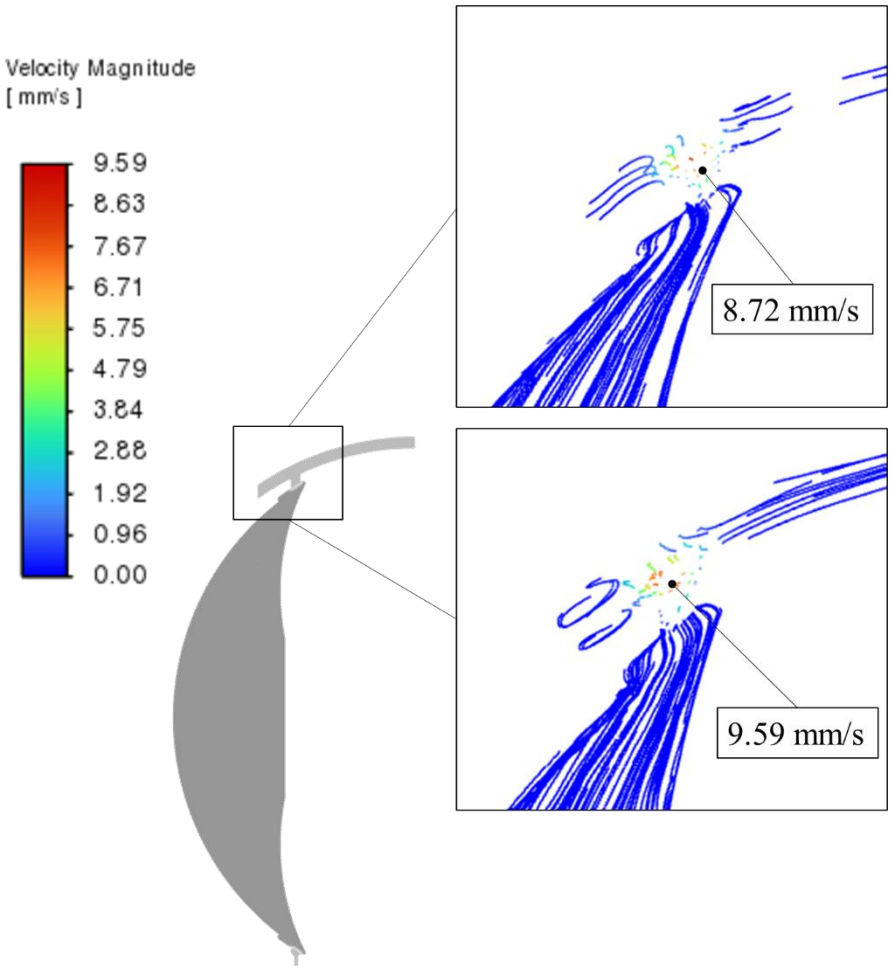


Figure 65 Inset velocity pathline results under NPDS conditions for the upright sutured European-representative eye (top) and the upright sutured African-representative eye (bottom)

Figure 66 shows the velocity pathline results for sutured mNPDS in the supine position. For both the sutured European and African models, the modelled sutures show to effectively restore a more balanced flow pattern, with greater circulation within the anterior chamber. The central vortex structure is as observed in pre-surgical conditions, indicating that flow is re-engaging with the corneal wall and lens.

In the European model, a velocity of 0.13 mm/s is observed at the corneal wall and a peak velocity of 0.30 mm/s is observed near the lens. In the African model, a velocity of 0.12 mm/s is observed at the corneal wall and a peak velocity of 0.26 mm/s is observed near the lens. There is high outflow velocity at the surgical site. However, unlike in the trabeculectomy procedure, there are no distinct flow alterations.

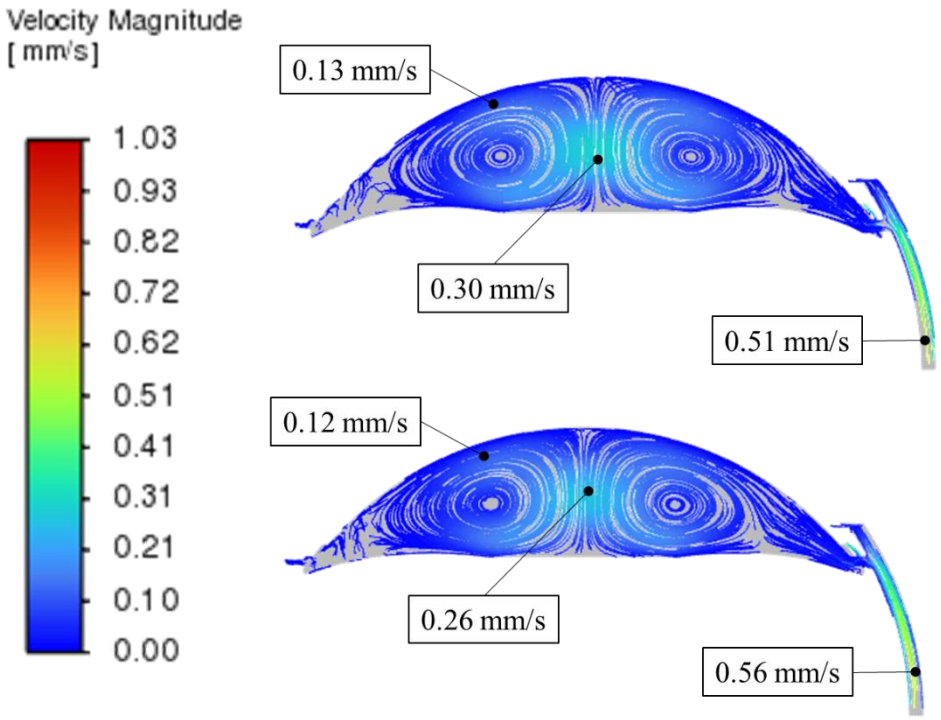


Figure 66 Velocity pathline results under mNPDS conditions for the supine sutured European-representative eye (top) and the supine sutured African-representative eye (bottom)

The European model's deeper ACD and narrower angle enable stronger central momentum in the supine orientation, as shown in Figure 67 by the tighter, more densely packed circular streamlines at the centre of the vortex and the higher velocity at the centre of the anterior chamber. In this orientation, the surgical outlet remains laterally oriented relative to gravitational force, where the influence of gravity and hence buoyancy is lower. The African model shows broader, more spaced streamlines, correlating with slightly weaker rotational momentum influenced by the shallower ACD and wider ACA, leading to earlier flow dispersion and a broader vortex core. This is further supported by the African model's displays of a tighter streamline concentration at the superior ACA, reflecting smoother entry due to its wider ACA and shallower ACD. In contrast, the European model shows more diffused streamlines, linked to deeper ACD and narrower ACA, which reduces the channelling of flow in this region.

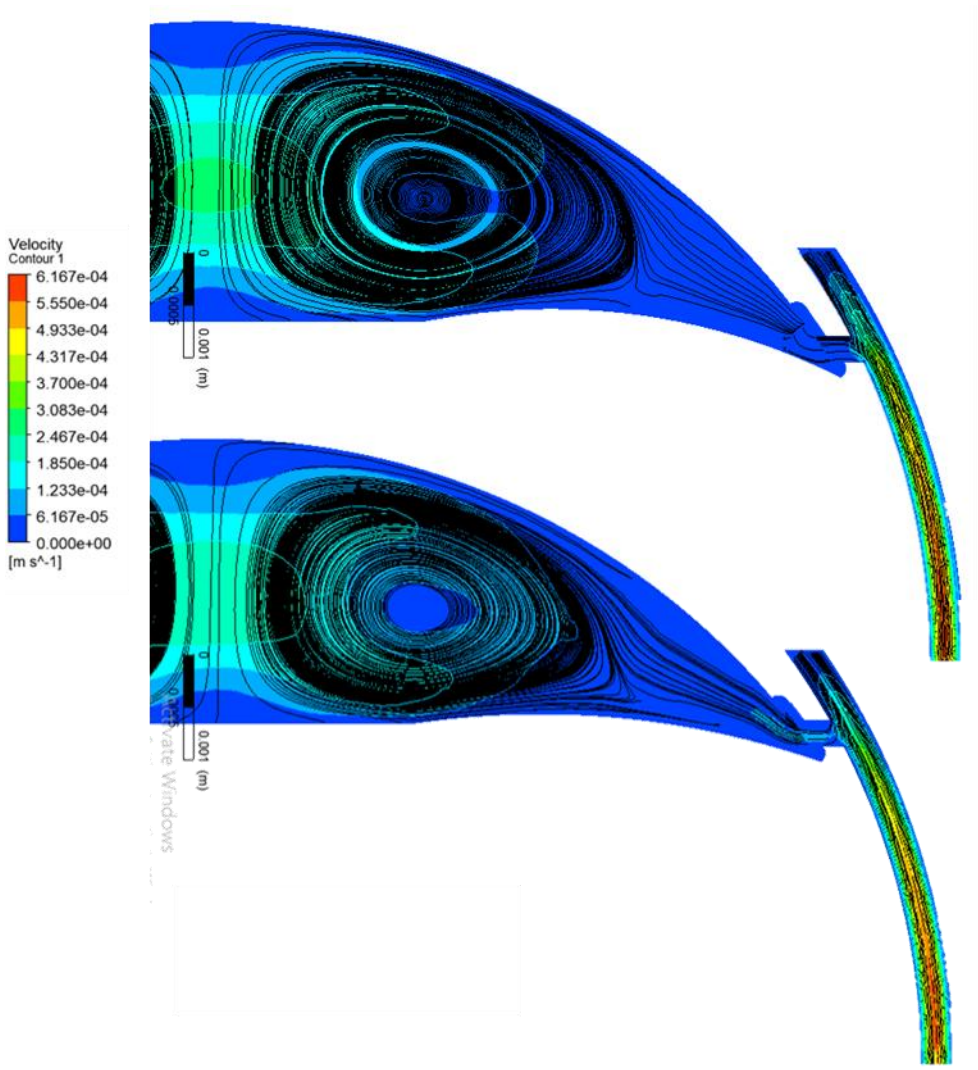


Figure 67 Velocity magnitude and streamline contours for mNPDS supine orientation for the European model (top) and African model (bottom)

Figure 68 shows the velocity pathline results for sutured mNPDS in the upright position. The velocities within the anterior chamber are restored to a healthy range, supporting nutrient delivery and pressure regulation. In the European model, a velocity of 0.11 mm/s is observed at the corneal wall and a peak velocity of 0.50 mm/s is observed near the lens. In the African model, a velocity of 0.12 mm/s is observed at the corneal wall and a peak velocity of 0.59 mm/s is observed near the lens. Unlike in the trabeculectomy procedure, there is no accelerated outflow near the surgical site, despite the removal of the TM resistance in the mNPDS procedure. This suggests that mNPDS has a lower risk of over-drainage compared to trabeculectomy.

The simulated sutures in both the sutured models restore flow symmetry within the anterior chamber, with well-defined central vortices and recirculation patterns. The flow re-engages with the corneal wall and central anterior chamber. Peak velocities are significantly reduced near the surgical site, which

indicates that the flow is now better controlled. Additionally, both sutured mNPDS models most closely represent their respective normal flow conditions compared to trabeculectomy and NPDS.

In the upright orientation with downward gravitational pull and the surgical site located above the fluid volume, the shorter vertical distance in the African model minimizes resistance to central flow. The African model's wider ACA redirects flow upward and out via the surgical drainage pathway.

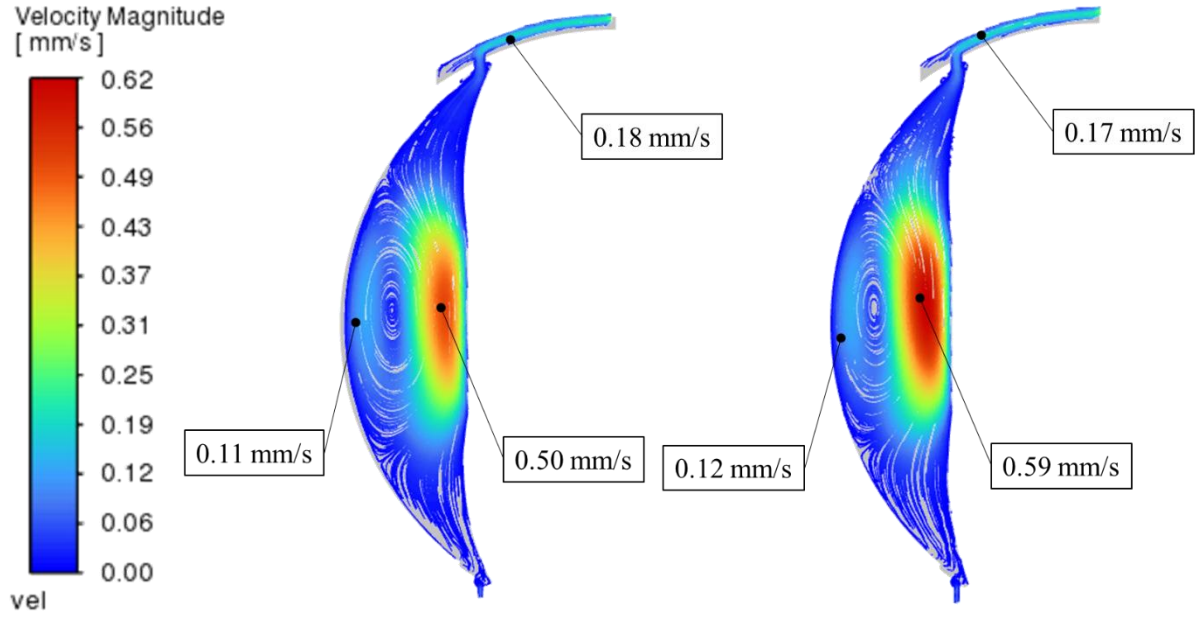


Figure 68 Velocity pathline results under mNPDS conditions for the upright sutured European-representative eye (left) and the upright sutured African-representative eye (right)

In the supine position, the European model's deeper ACD and narrower ACA allow for stronger central recirculation and more efficient pressure-driven flow toward the surgical outlet. However, in the upright orientation, the African model benefits from its shallower ACD and wider ACA, which reduce the vertical resistance and allow flow to realign upward toward the outlet. This reversal highlights how gravitational reorientation can amplify or suppress geometric advantages and underscores the importance of patient positioning and anatomical tailoring in surgical planning.

5.4.3 Wall Shear Stress

The WSS contours for the post-surgical simulations will be compared to those observed for normal flow conditions to identify whether post-surgical flow alterations result in harmful WSS. The WSS is considered harmful when it exceeds 3 Pa (0.02 mmHg), which can lead to ECD [171]. Figure 69 and Figure 70 provides an overview of the corneal WSS under normal conditions for the supine and upright orientations, respectively, for both ethnic models.

WSS is a crucial factor in understanding the mechanical interactions between the aqueous humour flow and the ocular tissues, especially after surgical interventions. Both supine models exhibit a concentric

pattern of WSS that decreases radially from the centre of the anterior chamber towards the periphery. This gradient suggests that the highest WSS is concentrated around the central corneal endothelium, while WSS diminishes closer to the central and peripheral structures. The maximum WSS values at the corneal wall is 3.3E-06 mmHg for the European model and 3.1E-06 mmHg for the African model. Although not represented on the colour scale, the maximum WSS at the outlets was determined to be 1.8E-04 mmHg for both models.

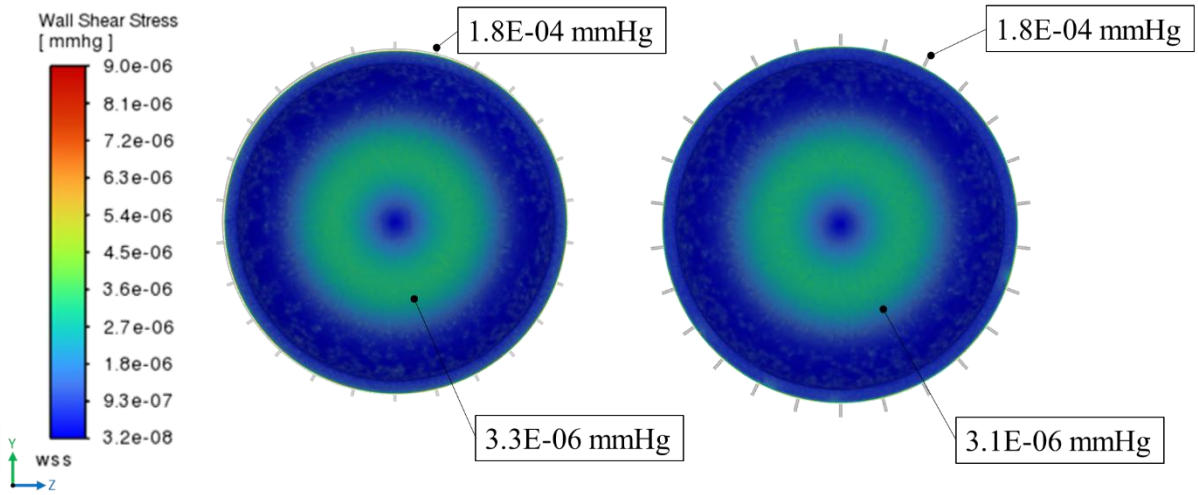


Figure 69 WSS results under normal conditions for the supine European-representative eye (left) and the supine African-representative eye (right)

In the upright position, WSS is higher in the top half of the anterior chamber for both models. This distribution is due to the gravitational settling of aqueous humour toward the inferior half, leading to a relatively higher flow velocity near the top chamber as fluid circulates upward. The maximum WSS values at the corneal wall is 5.6E-06 mmHg for the European model and 5.5E-06 mmHg for the African model. Although not represented on the colour scale, the maximum WSS at the outlets was determined to be 2.0E-04 mmHg for both models.

The WSS distribution appears similar between the two models, with comparable ranges and spatial patterns. This similarity in WSS implies that, despite anatomical differences, the fundamental flow characteristics and their impact on ocular tissues remain relatively consistent across these ethnic models under baseline conditions.

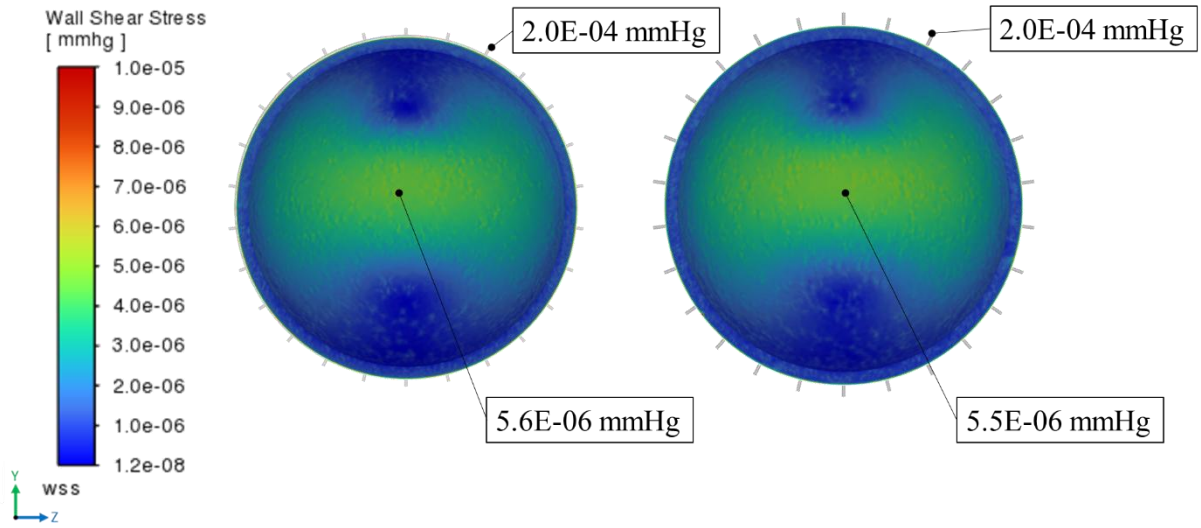


Figure 70 WSS results under normal conditions for the upright European-representative eye (left) and the upright African-representative eye (right)

Figure 71 provides an overview of the WSS unsutured trabeculectomy model for each ethnic eye. Before suturing, the WSS is predominantly low throughout the anterior chamber, but there is a distinct and intense concentration of WSS near the incision site of 0.03 mmHg in the European model and 0.02 mmHg in the African model. This is expected, given the rapid outflow of aqueous humour directed through the incision when it is open to the atmosphere. The European model has a deeper anterior chamber, which localizes the high shear stress to a smaller region around the incision, potentially concentrating stress on a narrow area of tissue. This could increase the risk of scarring specifically in this region. The wider ACA in the African model may allow for a more dispersed flow near the incision.

Furthermore, these extremely high WSS values (> 3 Pa or 0.02 mmHg) could potentially lead to ECD [171]. The WSS at the collector channels are also extremely high, which further indicate the need for prompt suturing to prevent exposing the eye tissues to high WSS over long periods of time, leading to ECD.

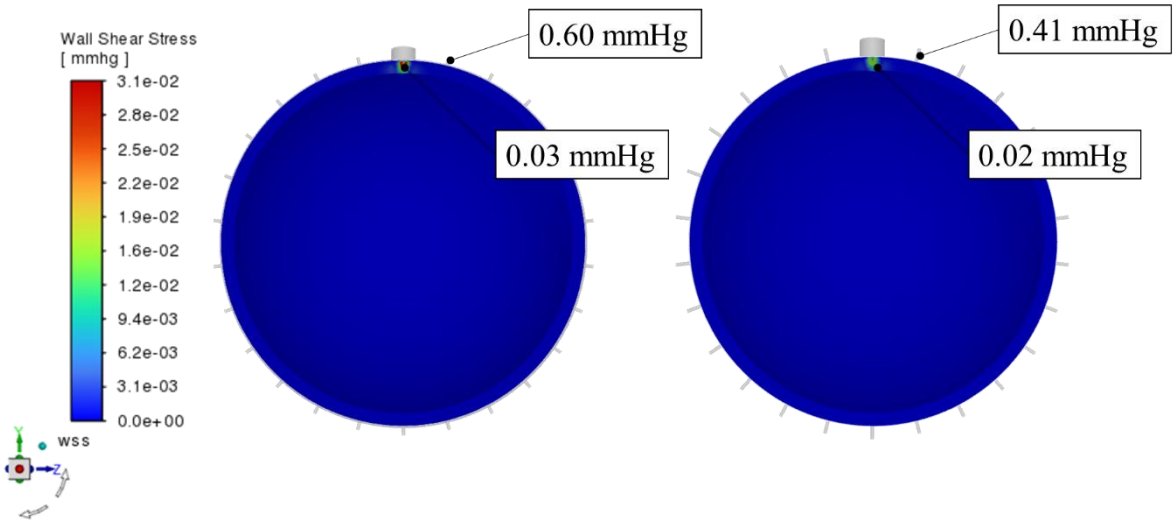


Figure 71 WSS results under trabeculectomy conditions for the upright unsutured European-representative eye (left) and the upright unsutured African representative eye (right)

Figure 72 provides an overview of the WSS for the sutured trabeculectomy models in the supine position, while Figure 73 provides an overview of the WSS for the sutured trabeculectomy model in the upright position. Both figures depict the WSS around the periphery of the anterior chamber and at the anterior chamber walls.

After suturing, the WSS at the incision is substantially lower compared to the open-incision state. This reduction indicates that the outflow is now more controlled, reducing the shear forces on surrounding tissues and minimizing the risk of mechanical damage. The WSS distribution now covers a broader area in both models, with low but measurable WSS across the corneal wall and anterior chamber. This pattern indicates that circulation has been restored, promoting a more uniform distribution of shear forces and reducing the risk of stagnant zones.

The European model's higher WSS near the central region is consistent with the higher central velocities. This distribution reduces the risk of stagnant zones and supports a more stable nutrient supply, minimizing the risk of hypotony-related complications [36]. The African model shows slightly lower WSS post-suturing, particularly in the central chamber, which could compromise flow circulation. This reduced shear may lead to chronic low IOP and nutrient deficiencies, as well as risks for structural complications like corneal decompensation and bleb failures [45,91]. This could explain the higher complication rates seen clinically in African eyes post-trabeculectomy [172].

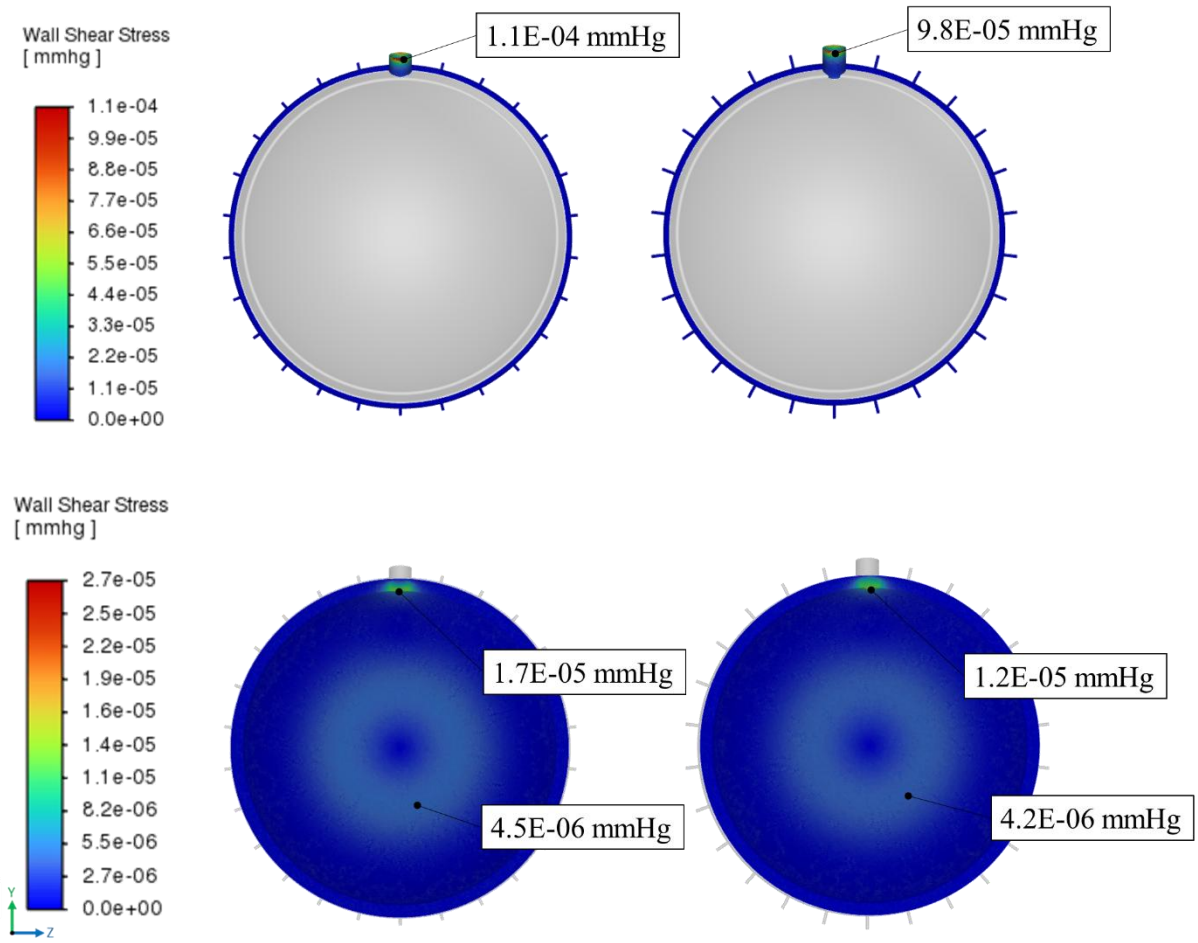


Figure 72 WSS results under trabeculectomy conditions for the supine sutured European-representative eye at the periphery (top left), supine sutured African-representative eye at the periphery (top right), supine sutured European-representative eye at the anterior chamber walls (bottom left), and the supine sutured African-representative eye at the anterior chamber walls (bottom right)

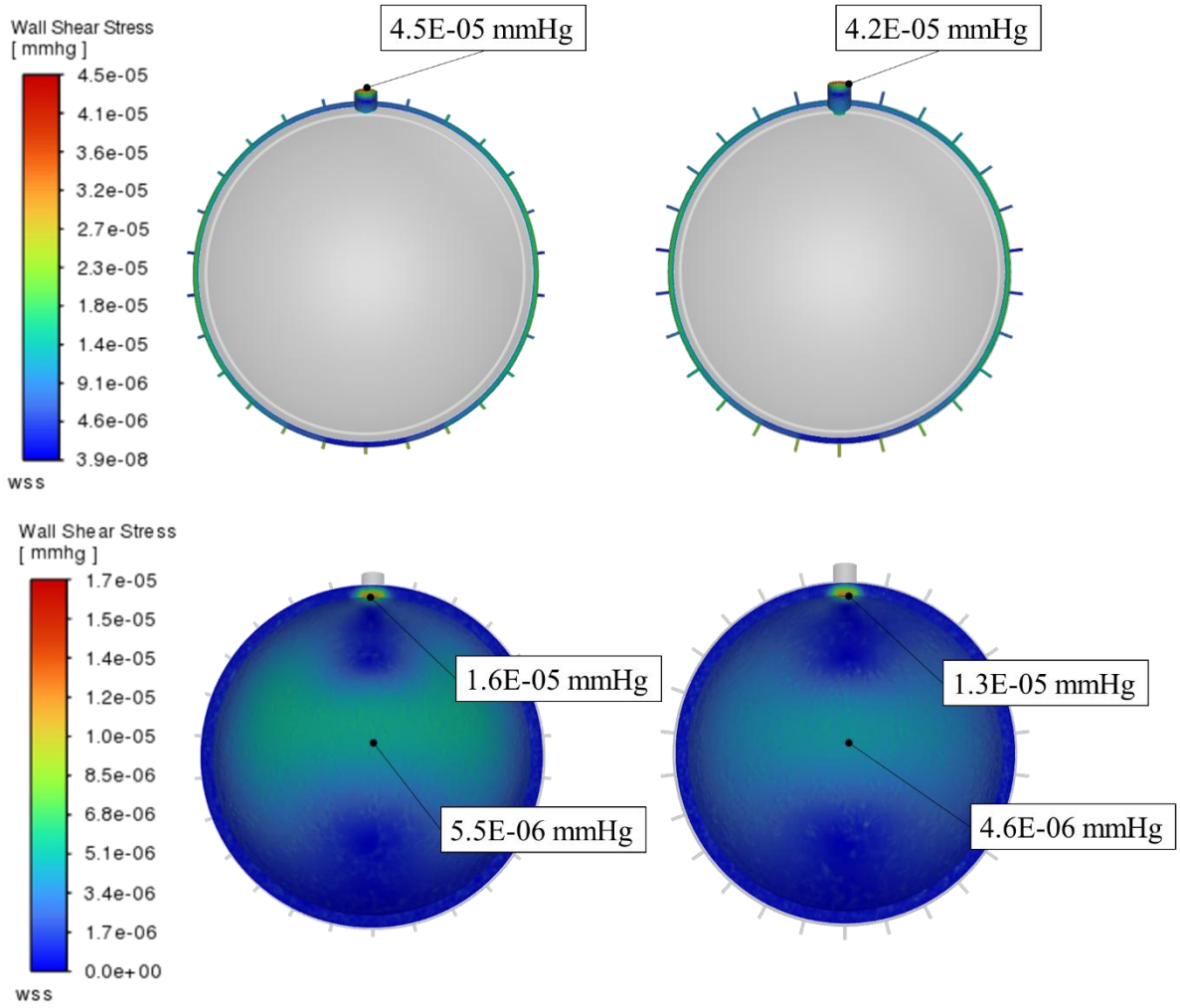


Figure 73 WSS results under trabeculectomy conditions for the upright sutured European-representative eye at the periphery (top left), upright sutured African-representative eye at the periphery (top right), upright sutured European-representative eye at the anterior chamber walls (bottom left), and the upright sutured African-representative eye at the anterior chamber walls (bottom right)

A closer look at the Kelly punch site (Figure 74) provides some additional insights. The European model does indicate higher WSS at the surgical site near the iris. However, the African model has a minor section of peak WSS on the cornea side. This is due to the size of the Kelly punch tool (0.8 mm). Since the African model has a shorter TM length, the tool would slightly punch into the cornea as well, resulting in a slight WSS elevation at this point. However, the elevation is insignificant and does not surpass the damaging value of 3 Pa.

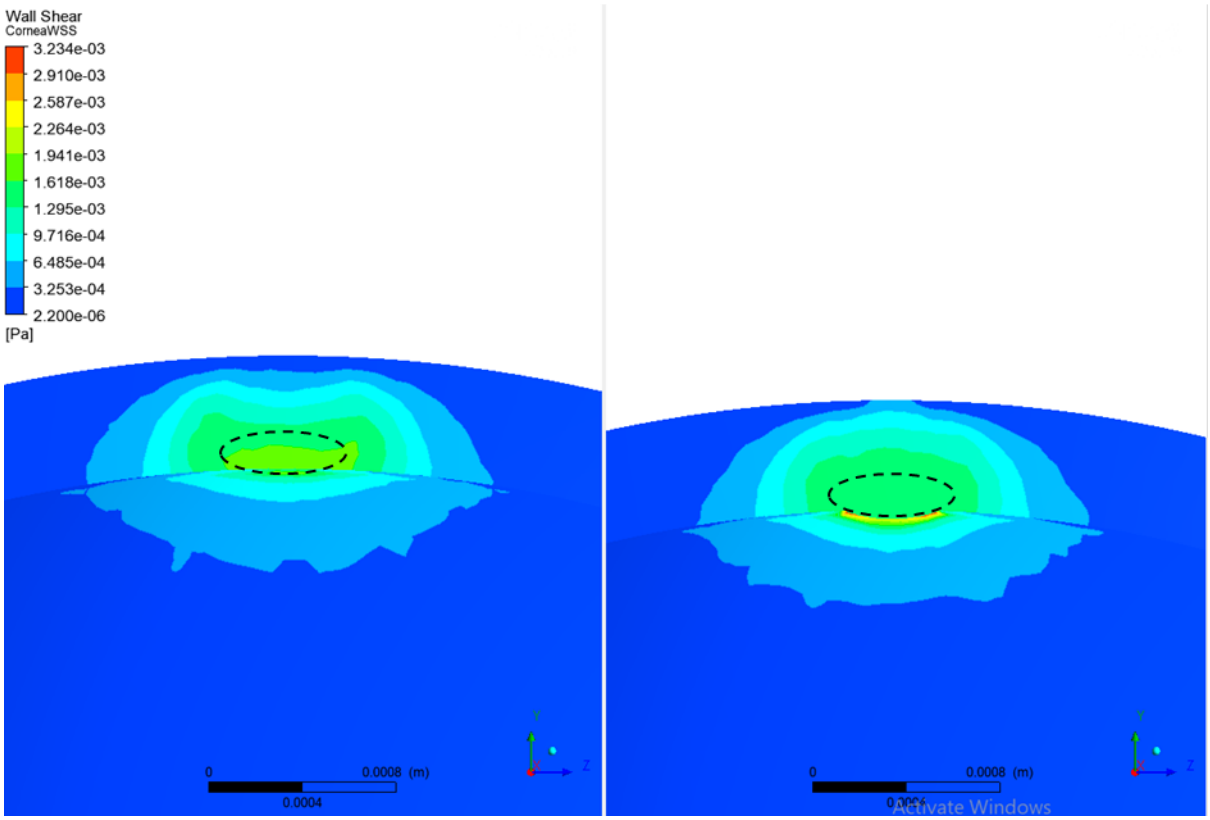


Figure 74 Close-up view of the WSS for the trabeculectomy surgical site WSS results supine sutured European-representative eye (left) and the supine sutured African-representative eye (right), with the dashed line indicating where the sclerostomy punch tool would be applied

Further adjusting the WSS magnitude scale resulted in Figure 75 to analyse whether the entry angle described in Figure 55 has any significant effect on the WSS on the cornea. The WSS resulting from the iridectomy entrance flow is circled in red. The African model WSS shows a very slight upward shift on the cornea. This is due to the parallel inflow from the iridectomy, resulting in a more curvature of flow near the cornea, whereas the European model flow follows the ACA and the curvature of the cornea more smoothly. This is supported by the view provided in Figure 76, which shows the pathlines from the iridectomy and the resulting WSS on the cornea. Overall, the WSS differences at this site is insignificant and does not exceed the harmful value of 3 Pa.

Furthermore, the average WSS on these surfaces are still similar, with 1.49E-06 mmHg (~0.0002 Pa) for the European model and 1.40E-06 mmHg (~0.0002 Pa) for the African model.

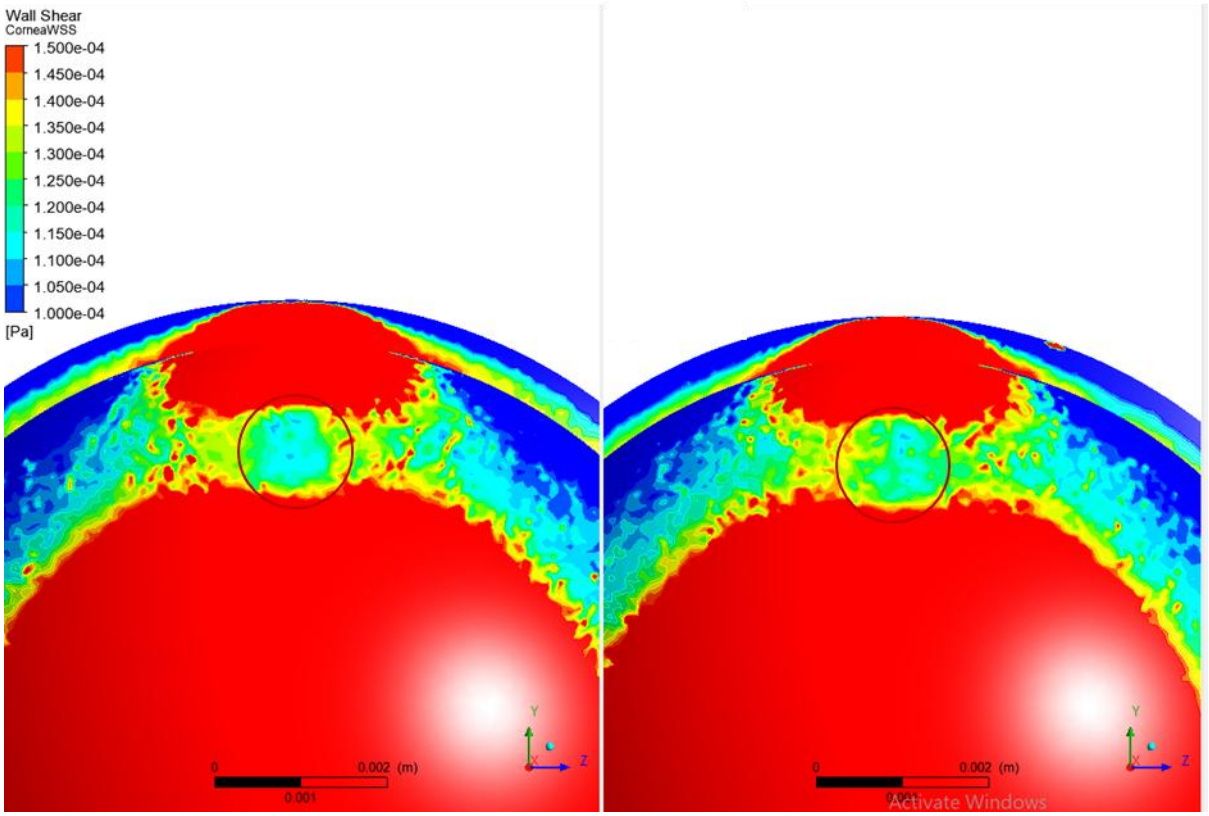


Figure 75 Close-up view of the adjusted WSS scale for the trabeculectomy surgical site WSS results supine sutured European-representative eye (left) and the supine sutured African-representative eye (right), with the WSS resulting from the iridectomy entrance flow circled in red

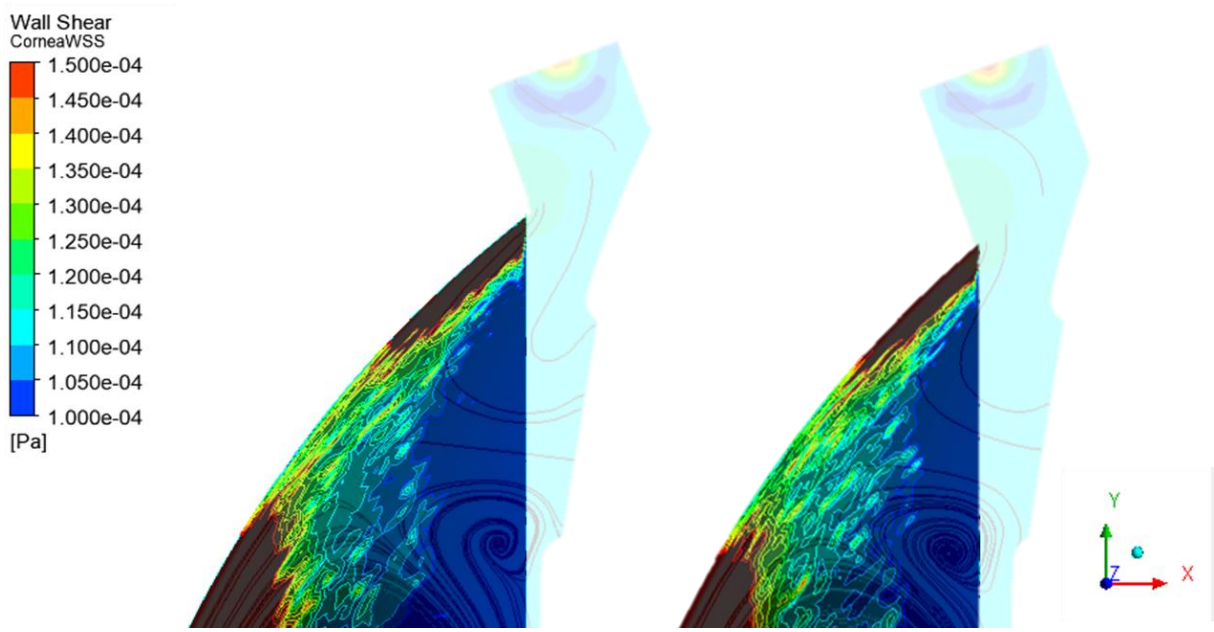


Figure 76 Side view of the adjusted WSS scale for the trabeculectomy surgical site WSS results supine sutured European-representative eye (left) and the supine sutured African-representative eye (right), along with the velocity pathlines resulting from the iridectomy inflow

Figure 77 provides an overview of the WSS for the supine sutured NPDS models, while Figure 78 provides an overview of the WSS for the upright sutured NPDS models, specifically around the periphery of the anterior chamber, with a focus on the incision site, and at the anterior chamber walls.

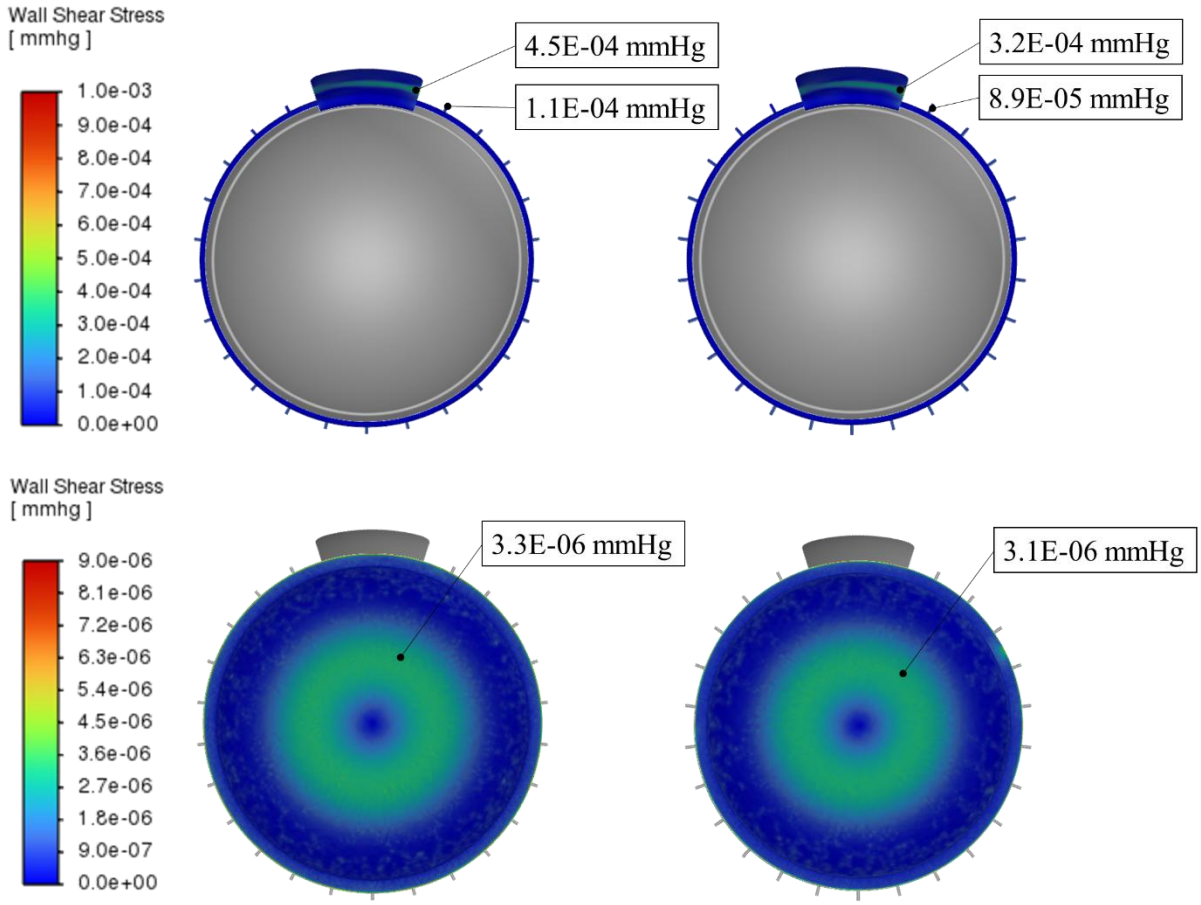


Figure 77 WSS results under NPDS conditions for the supine sutured European-representative eye around the periphery (top left), the supine sutured African-representative eye around the periphery (top right), supine sutured European-representative eye at the anterior chamber walls (bottom left), and the supine sutured African-representative eye at the anterior chamber walls (bottom right)

For the upright sutured European model, the WSS is concentrated relatively symmetrically along the corneal walls with a maximum value of 5.0E-06 mmHg. This pattern aligns closely with normal flow WSS with a maximum value of 5.6E-06, indicating effective restoration of circulation. In the sutured African model, the WSS is lower along the corneal walls at 4.7E-06 mmHg compared to the 5.5E-06 mmHg under normal conditions, indicating a slightly weaker interaction between the corneal wall and the aqueous humour.

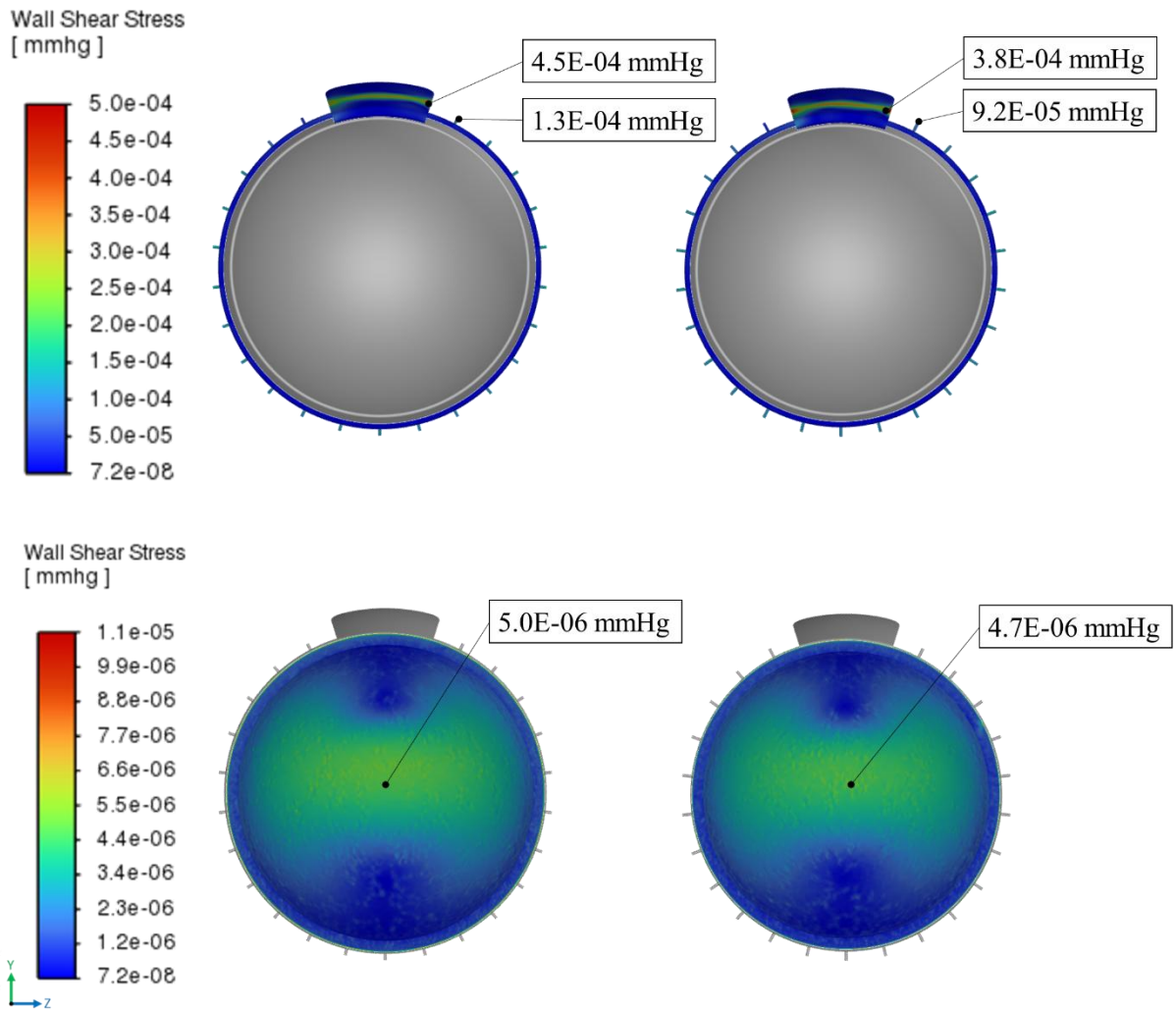


Figure 78 WSS results under NPDS conditions for the upright sutured European-representative eye around the periphery (top left), the upright sutured African-representative eye around the periphery (top right), upright sutured European-representative eye at the anterior chamber walls (bottom left), and the upright sutured African-representative eye at the anterior chamber walls (bottom right)

For both models, the WSS near the surgical site remains relatively low, consistent with the lower velocities observed in the sutured condition. Trabeculectomy models typically show elevated WSS near the surgical site, which suggests that NPDS minimizes the risk of scarring or bleb failure [101].

Figure 79 demonstrates how the increased WSS on the scleral flap is a result of the increase in velocity when the aqueous humour exits the TM, as explained in Figure 63. The increased velocity is a result of flow escaping the high resistance TM volume, before entering the narrower Schlemm's canal deroofed volume, causing an abrupt increase in velocity gradient. Thereafter, the flow enters the deep flap area, where it decreases in velocity magnitude.

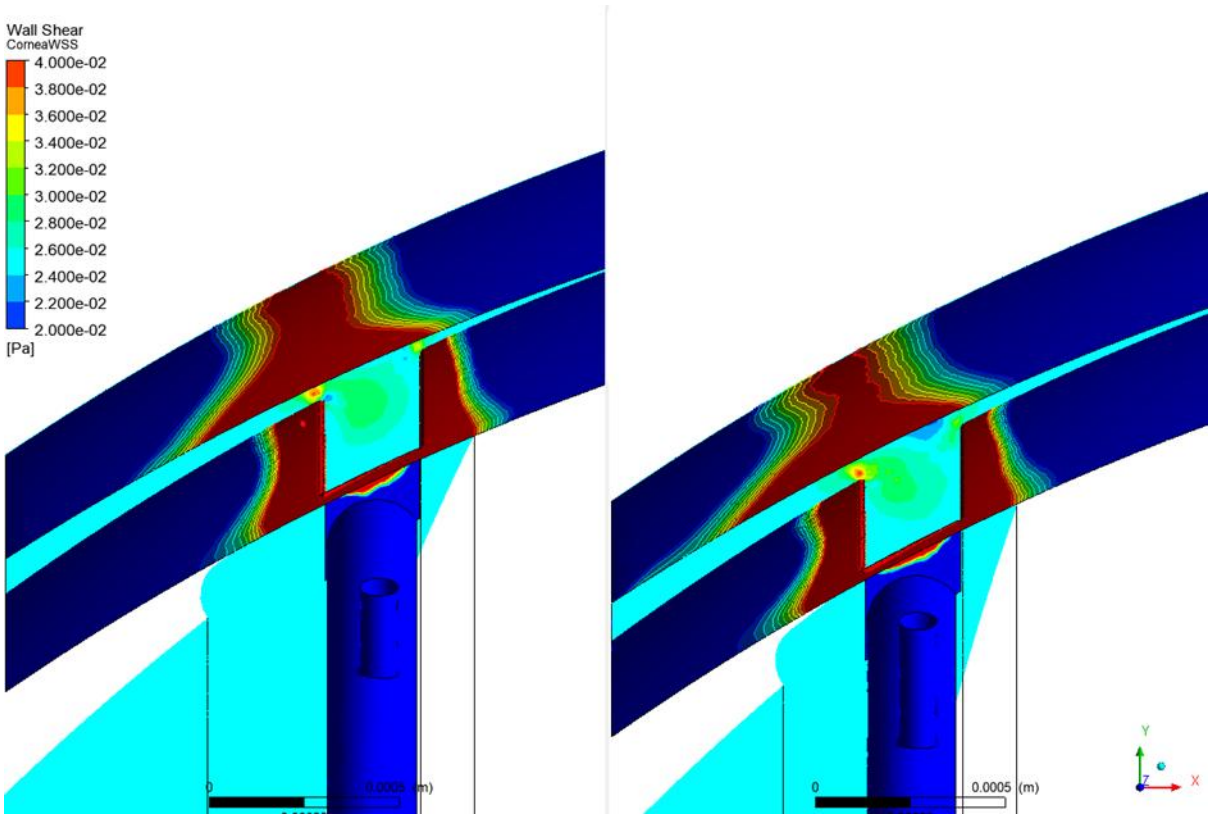


Figure 79 Side view of the adjusted scale for the NPDS surgical site WSS results for supine sutured European-representative eye (left) and the supine sutured African-representative eye (right), along with the velocity contours

Figure 80 provides an overview of the WSS for the sutured mNPDS models in the supine position, while Figure 81 provides an overview of the WSS for the sutured mNPDS models in the upright position. Both figures depict the WSS around the periphery of the anterior chamber and at the anterior chamber walls.

For all models, the WSS is concentrated relatively symmetrically along the corneal walls. Overall, the African models depict lower WSS than the European model, specifically at the surgical site.

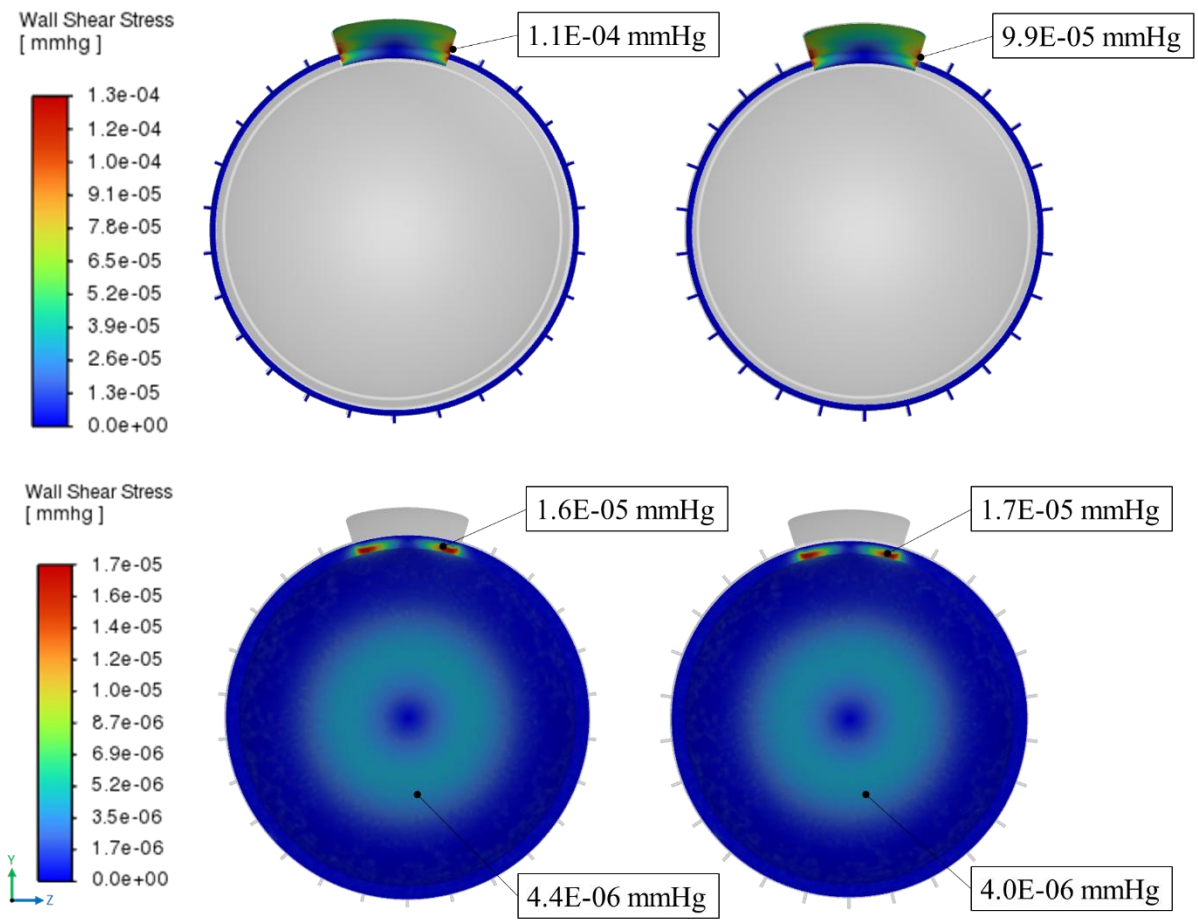


Figure 80 WSS results under mNPDS conditions for the supine sutured European-representative eye around the periphery (top left), the supine sutured African-representative eye around the periphery (top right), supine sutured European-representative eye at the anterior chamber walls (bottom left), and the supine sutured African-representative eye at the anterior chamber walls (bottom right)

Figure 81 shows that the European model's WSS at the corneal walls has a maximum value of 5.0E-06 mmHg, which closely aligns with normal flow WSS with a maximum value of 5.6E-06, indicating effective restoration of circulation. Similarly, the African model has a maximum corneal WSS of 5.1E-06 mmHg compared to the 5.5E-06 mmHg under normal conditions. These indicate that the WSS for mNPDS correlates better to normal conditions than what was seen in NPDS.

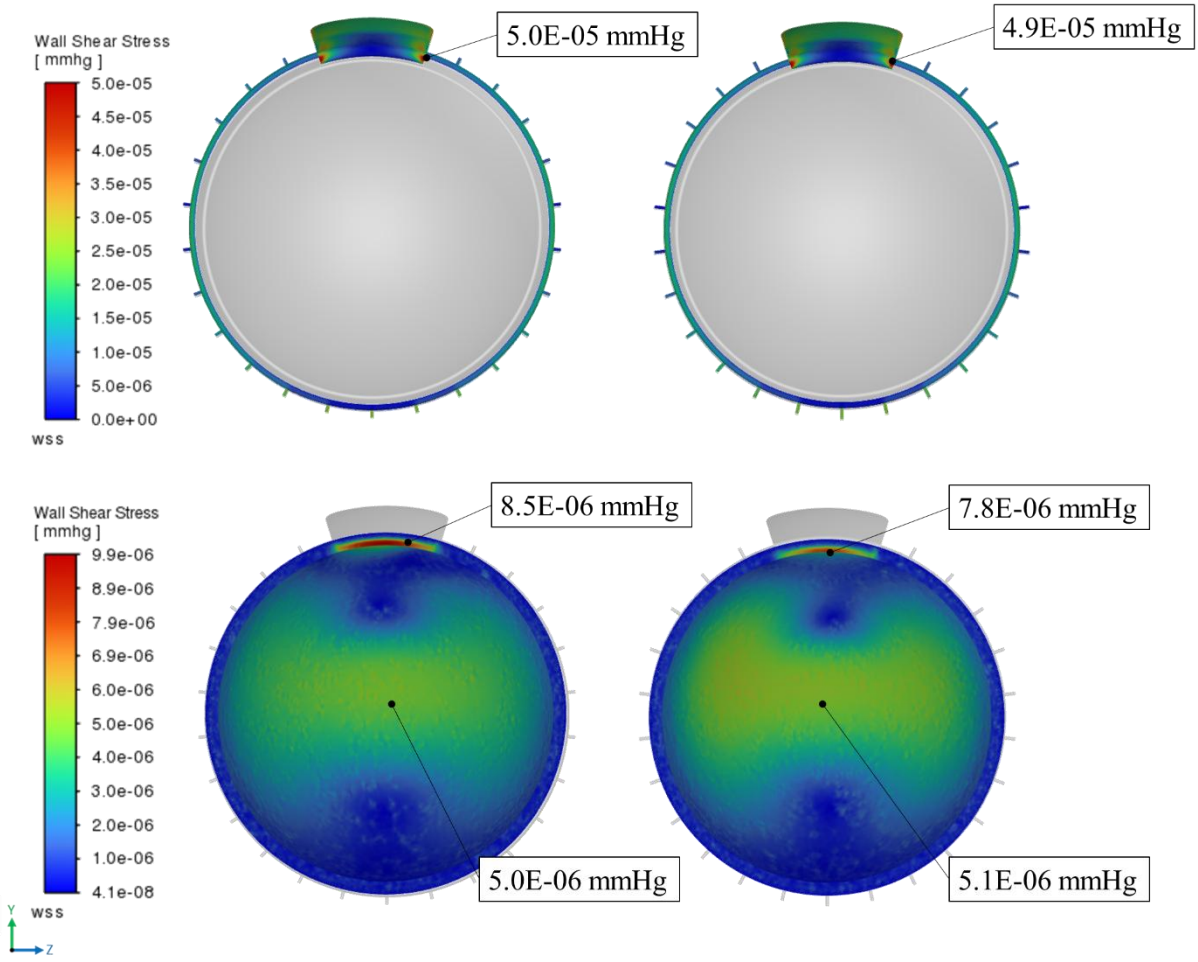


Figure 81 WSS results under mNPDS conditions for the upright sutured European-representative eye around the periphery (top left), the upright sutured African-representative eye around the periphery (top right), upright sutured European-representative eye at the anterior chamber walls (bottom left), and the upright sutured African-representative eye at the anterior chamber walls (bottom right)

Figure 82 shows a close-up view of the mNPDS deep scleral flap in the supine orientation for both models. This demonstrates how the WSS is influenced by the more gradual outflow of aqueous humour at the mNPDS surgical site compared to the NPDS surgical site (Figure 79). Since a section of the TM is removed for the mNPDS procedure, there is a significant decrease in resistance to the aqueous humour outflow. The high WSS towards the sides of the flap is due to the membrane peel underneath the flap being slightly narrower than the flap itself, causing an increased resistance to outflow towards the sides. When the aqueous humour towards the sides of the flap exits the TM, it has a slightly accelerated velocity, which, in turn, causes the increased WSS. However, this accelerated velocity does not lead to significant changes in WSS values. There is also no significant difference in WSS patterns between the European and African models.

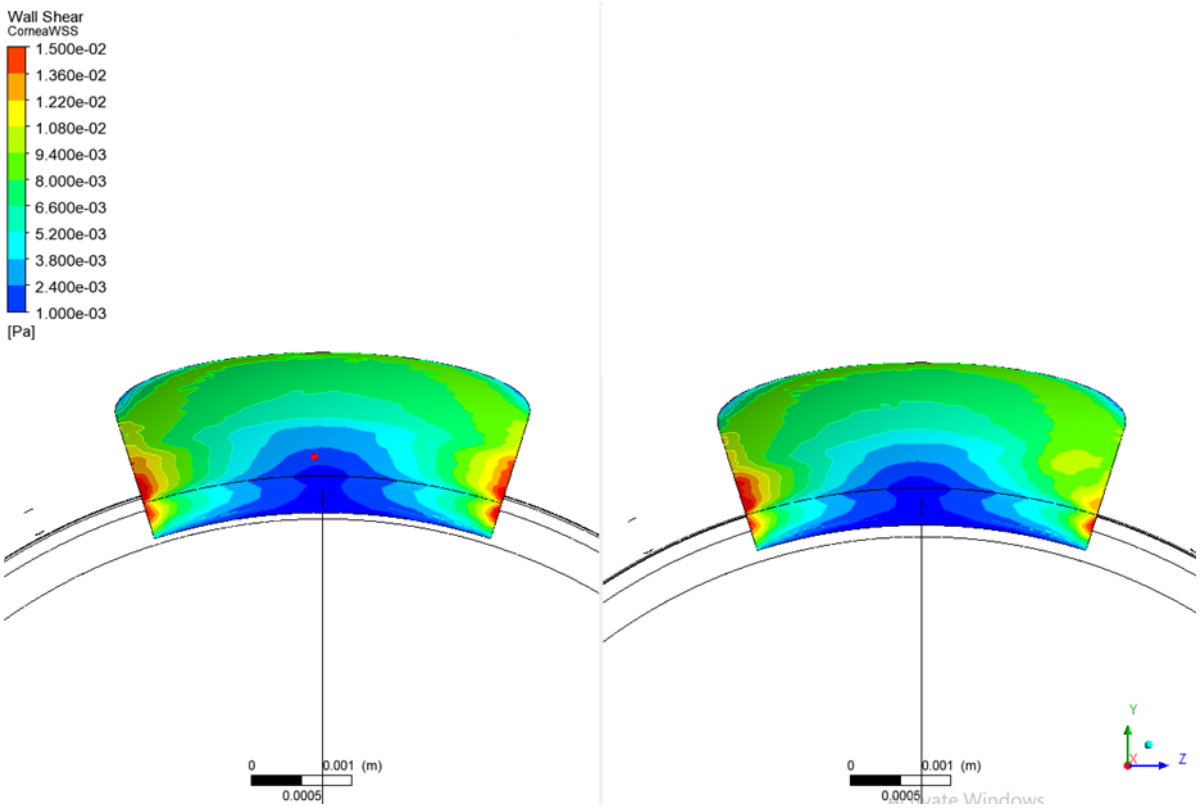


Figure 82 Adjusted scale for the mNPDS surgical site WSS results for supine sutured European-representative eye (left) and the supine sutured African-representative eye (right)

5.4.4 Vorticity & Q-Criterion

Vorticity magnitude reflects local rotational motion in the anterior chamber and can indicate alterations in aqueous humour distribution. Although major changes in vorticity are not expected across all surgical models, this section highlights key regional differences before examining the vortex core behaviour in more detail using the Q-criterion.

While vorticity magnitude highlights general rotational behaviour, it does not isolate distinct vortex structures. To more clearly identify vortex cores and flow coherence, the following section applies the Q-criterion to evaluate vortex core strength and distribution.

The Q-criterion values previously discussed for normal flow in section 5.4.1 were further scaled for $Q > 0$ to identify more specific vortex formations, which is provided in Figure 83 and Figure 84 for the supine and upright positions, respectively. For both positions and ethnicities, there are vortex formations near the central region of the anterior chamber, with the African model ($Q = 0.13$) indicating a slightly stronger recirculation than the European model ($Q = 0.12$). This aligns with the recirculation flow described in Figure 37 and Figure 40. Tiny vortices can be observed throughout the outlet channels as the aqueous drains, which aligns with the sharp geometry change from the Schlemm's canal as previously described. The maximum Q-value at the outlet in the upright position for the European model is 23.3, which is significantly larger than for the African model at only 6.5. The maximum Q-value at

the outlet in the supine position for the European model is 38.7, and 13.2 for the African model. This is most likely because of the smaller ACA of the European model, which can reduce the space through which the aqueous humour can flow. This forces the flow to converge more sharply as it approaches the outlet, increasing the local flow velocity gradients.

There are also small vortex formations ($Q \approx 0.01$) near the wall of the iris, though these are not significant. In general, there are no substantial vorticities observed except for those resulting from the recirculation flows.

The λ_2-values were also examined, and it was found that the vortex cores ($\lambda < 0$) align with the vortex-dominated regions ($Q > 0$) in this flow. This suggests that the simulations are well-resolved, that there are no unsteady effects, and that the vortex-dominated regions are coherent.

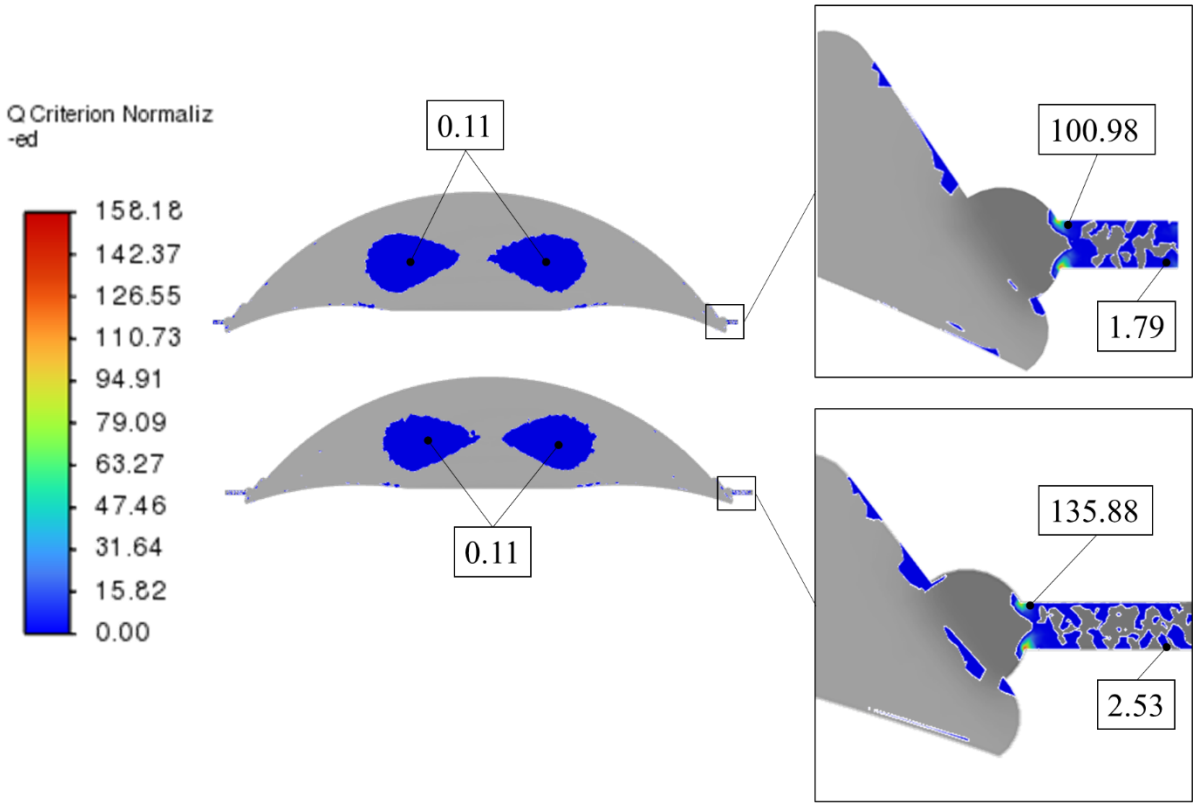


Figure 83 $Q > 0$ results under normal conditions for the supine European-representative eye (top) and the supine African-representative eye (bottom)

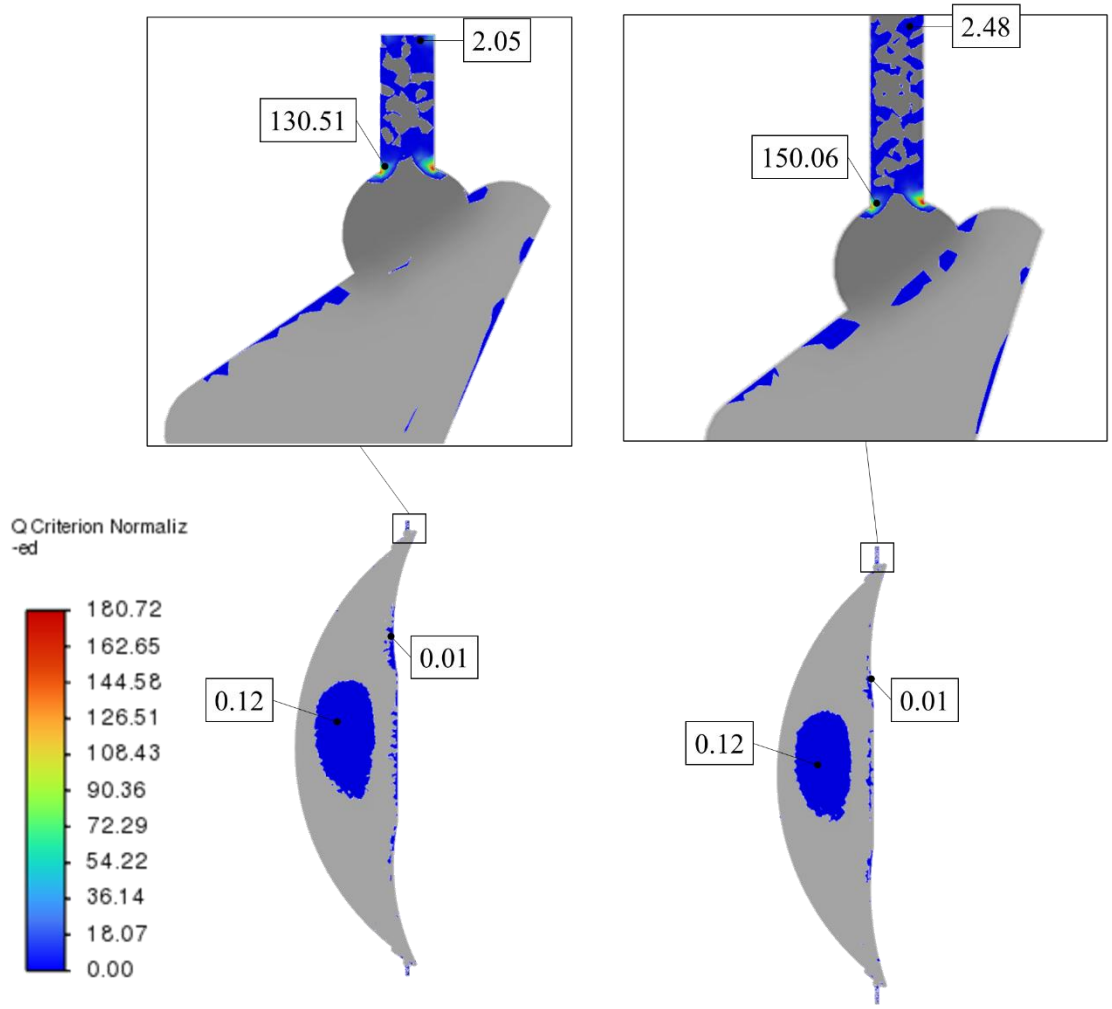


Figure 84 $Q > 0$ results under normal conditions for the upright European-representative eye (left) and the upright African-representative eye (right)

The Q-criterion for $Q > 0$ is provided in Figure 85 and Figure 86 for the supine and the upright positions, respectively. For all models, there is a clear vortex formation near the iridectomy which is not present under normal flow conditions, which is consistent with the flow alterations identified in Figure 58 and Figure 59. These vortices are strongest closest to the ACA and in the supine position, with a Q-value of 0.6 for the European model and 0.2 for the African model. Vortex formation near surgical sites may introduce tissue remodelling and result in fibrotic scarring [101].

The λ_2-values were also examined, and it was found that the vortex cores ($\lambda < 0$) align with the vortex-dominated regions ($Q > 0$) in this flow.

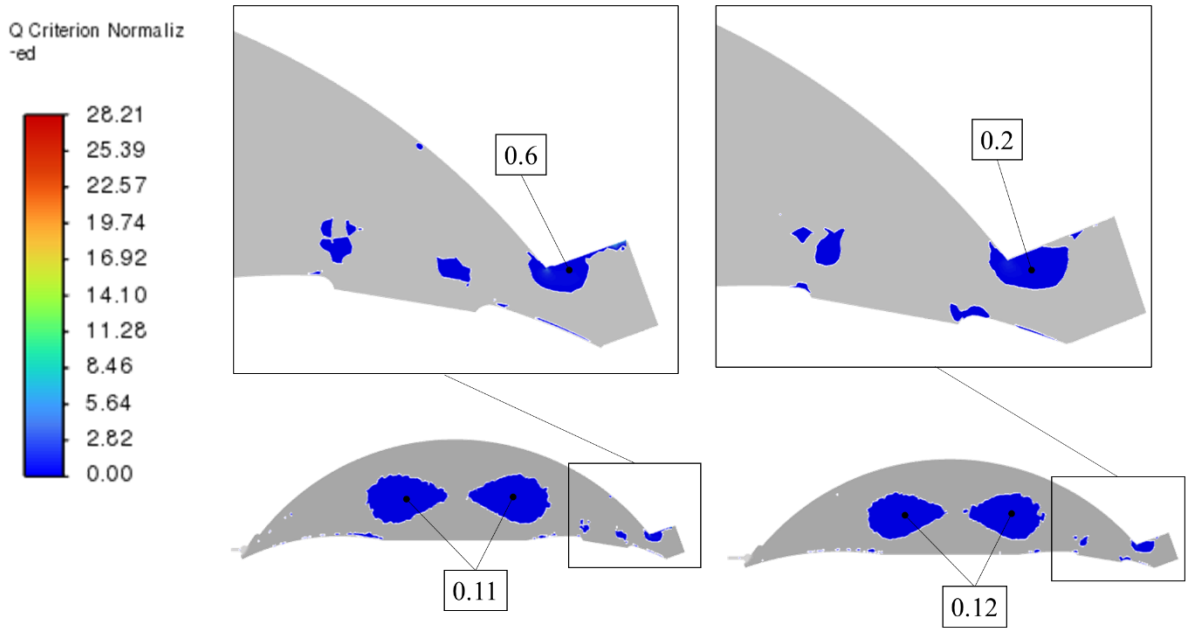


Figure 85 $Q > 0$ results under trabeculectomy conditions for the supine sutured European-representative eye (left) and the supine sutured African representative eye (right)

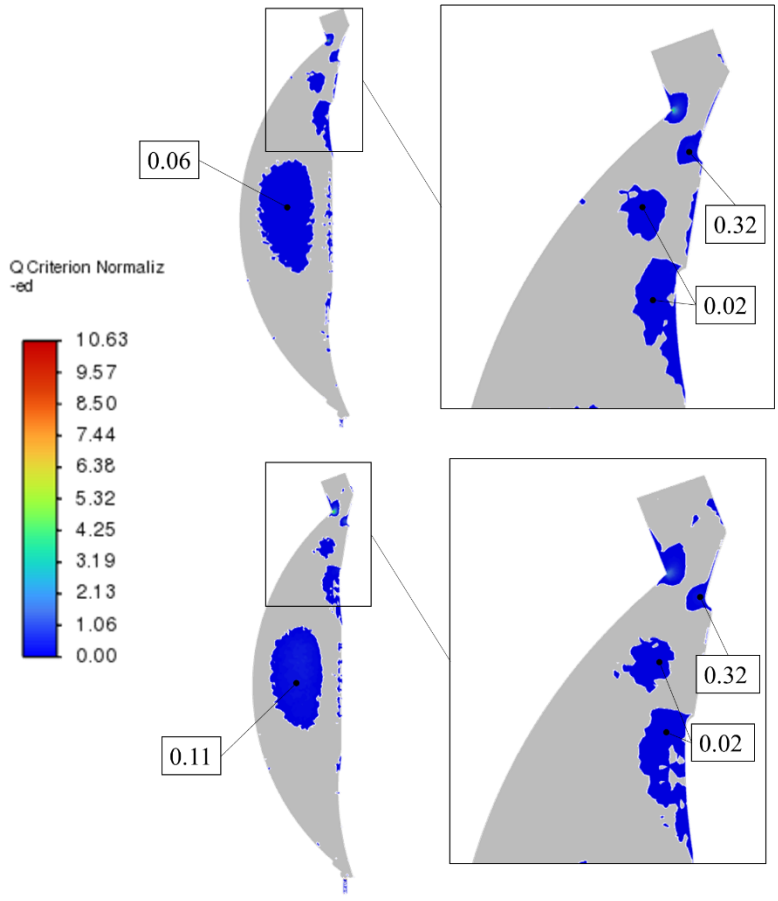


Figure 86 $Q > 0$ results under trabeculectomy conditions for the upright sutured European-representative eye (top) and the upright sutured African representative eye (bottom)

Figure 87 and Figure 88 show the Q-criterion for $Q > 0$ in the supine and upright positions, respectively. As expected, the Q-value is its highest just after the TM for all models. Due to the sudden increase in flow. Since this is not in the position where suturing takes place, it most likely would not affect the healing process. There are some vortices through the drainage pathway, similar to what is seen for the outlet channels under normal flow conditions. There are no distinct vortex formations in the anterior chamber.

The λ_2-values were also examined, and it was found that the vortex cores ($\lambda < 0$) align with the vortex-dominated regions ($Q > 0$) in this flow.

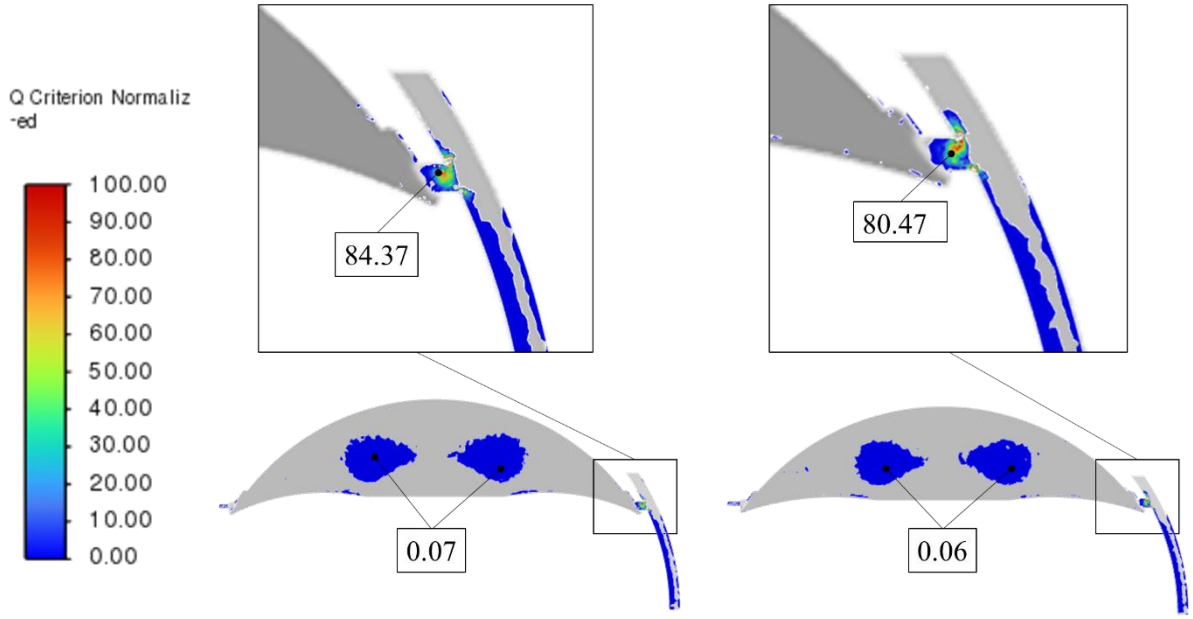


Figure 87 $Q > 0$ results under NPDS conditions for the upright supine European-representative eye (left) and the supine sutured African-representative eye (right)

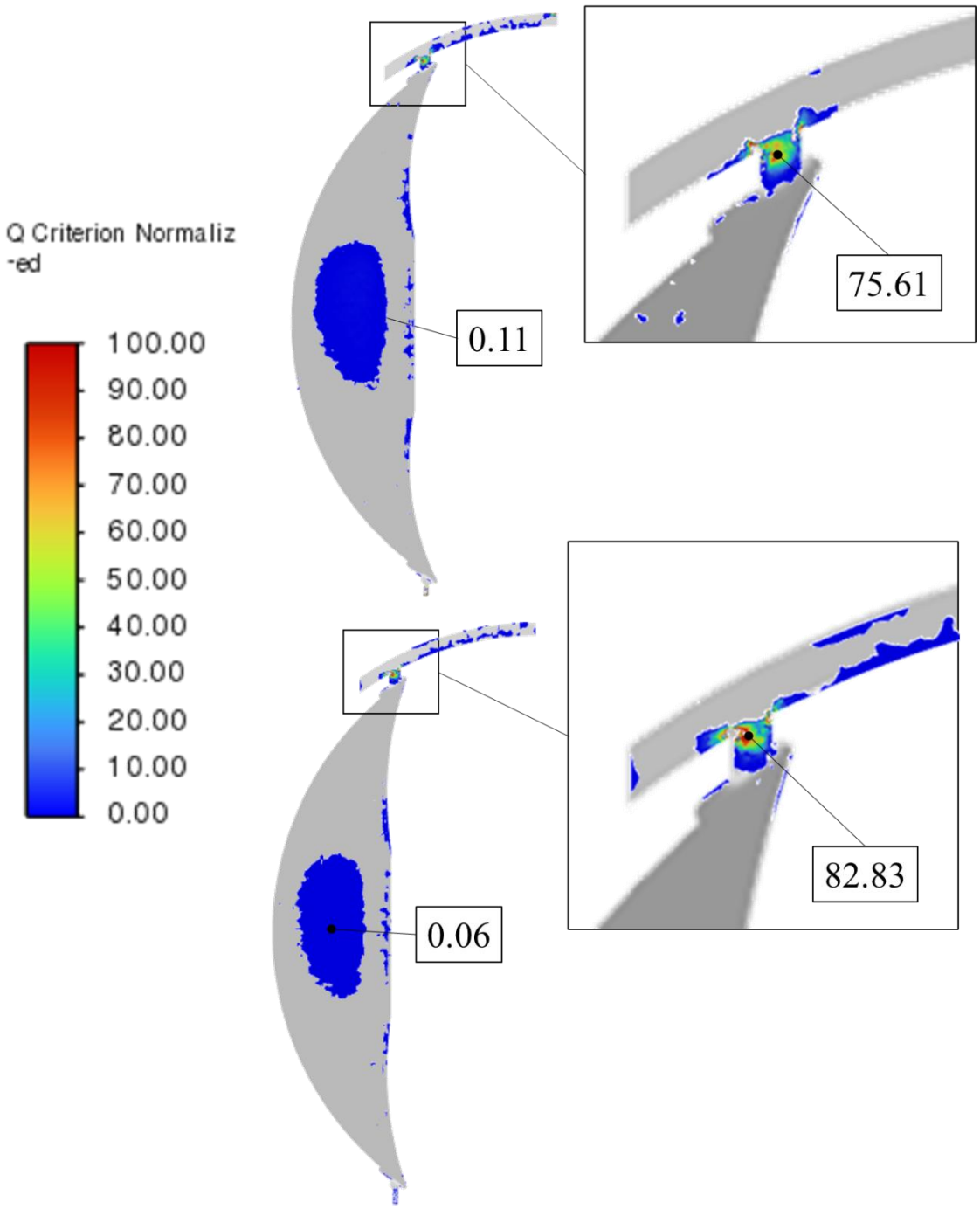


Figure 88 $Q > 0$ results under NPDS conditions for the upright sutured European-representative eye (top) and the upright sutured African-representative eye (bottom)

Figure 89 and Figure 90 shows the Q-criterion for $Q > 0$ in the supine and upright positions, respectively. Indicated on both figures is where the Q-value is the highest. In this case, it is due to the flow over a sharp geometric change. There are some vortices through the drainage pathway, similar to what is seen for the outlet channels under normal flow conditions. There are no distinct vortex formations in the anterior chamber.

The λ_2-values were also examined, and it was found that the vortex cores ($\lambda < 0$) align with the vortex-dominated regions ($Q > 0$) in this flow.

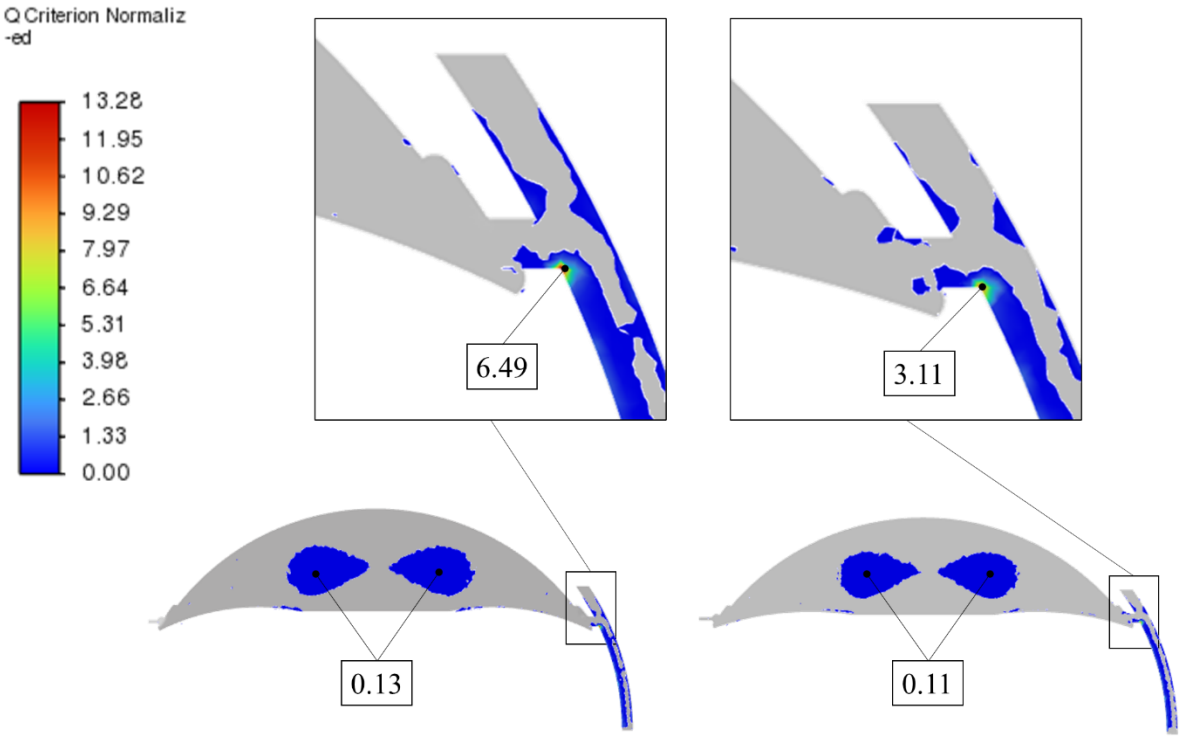


Figure 89 $Q < 0$ results under mNPDS conditions for the supine sutured European-representative eye (left) and the supine sutured African-representative eye (right)

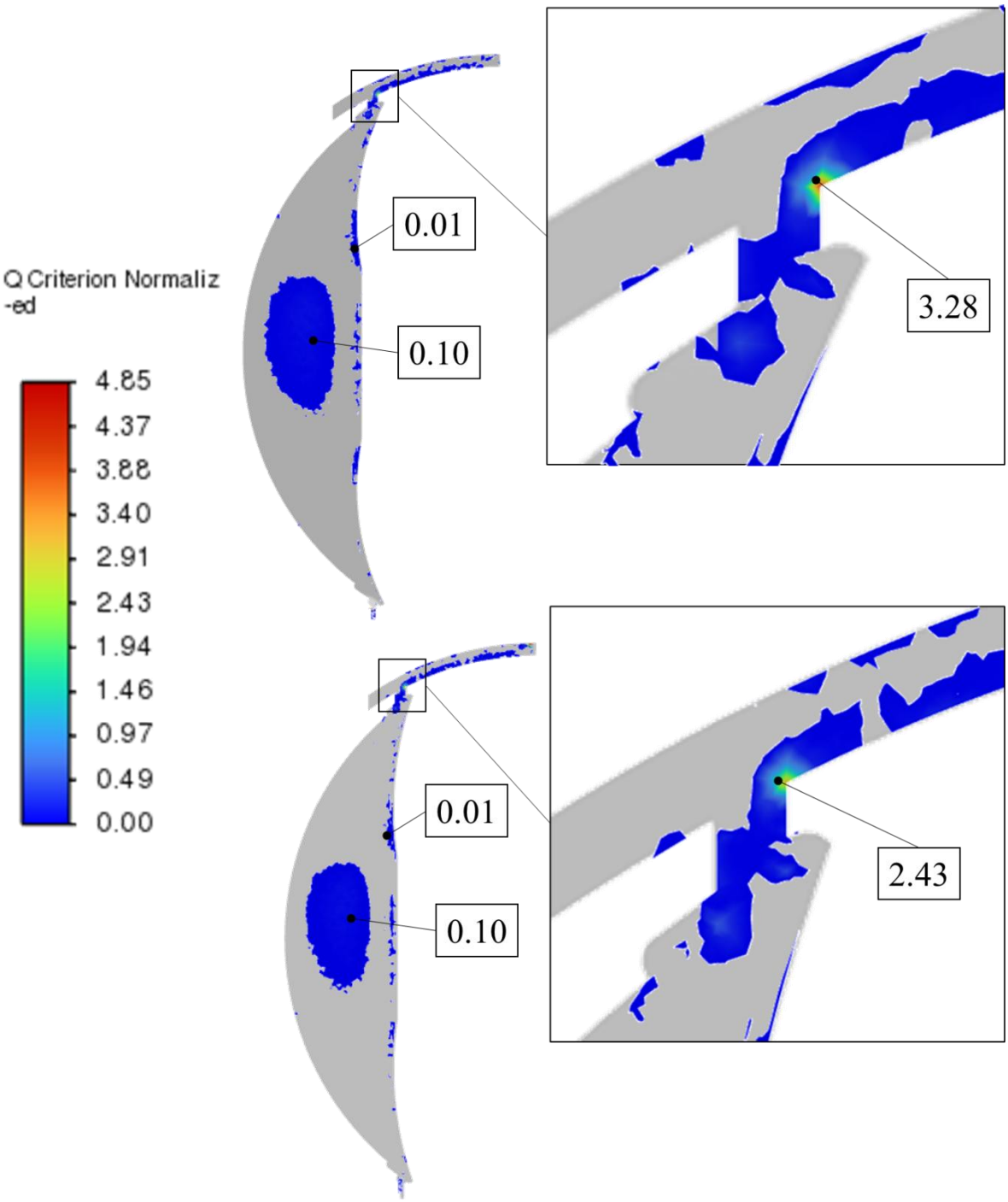


Figure 90 $Q < 0$ results under mNPDS conditions for the upright sutured European-representative eye (top) and the upright sutured African-representative eye (bottom)

5.4.5 Uniformity Index

A uniformity index (UI) was determined as a quantitative measure of how evenly distributed the outlet flow velocity flow property is for each model. The UI assists in analysing the peak velocity position and whether the highest velocity regions remain centrally located or shift asymmetrically due to surgical interventions.

To quantify the position and spread of peak velocity, the UI can be formulated as

$$UI = 1 - \frac{\sum_i |v_i - v_{avg}|}{n \cdot v_{max}} \quad 5.1$$

Where:

- v_i is the local velocity at each sample point,
- v_{avg} is the average velocity in the anterior segment,
- n is the total number of sampling points, and
- v_{max} is the maximum velocity in the anterior segment.

A UI-value of approximately 1 indicates a highly uniform velocity distribution. A UI-value approximating 0 indicates a highly non-uniform velocity distribution with large variations in peak velocity positioning.

For the goal of evaluating flow distribution pre- and post-surgery, the UI-value was directly extracted from ANSYS Fluent over the total outlet surface region. The resulting UI-values for each sutured upright model is provided in Table 12.

As expected, the normal UI-value for both ethnic-representative models are the highest (0.84 for the European model and 0.77 for the African model), suggesting a relatively uniform outflow profile over the outlet. However, gravitational forces in the upright orientation introduce a vertical asymmetry in the anterior chamber flow field. This disrupts uniform outflow distribution, leading to UI-values below unity.

Similar UI values are obtained for the trabeculectomy models (0.61 for the European model and 0.60 for the African model), displaying a decrease in the outflow uniformity compared to the normal models. The results are consistent with the focal flow concentration that occurs due to the sclerostomy surgical site created for a trabeculectomy procedure. The similarity in UI-values suggest that the geometrical differences between the European and African models are small contributors, and that the bulk flow field is dominated by the invasive alterations made to the eye models. This is consistent with the flow field analysis performed in section 5.4.2.

The largest disparity is observed for the NPDS models. Specifically, the African model shows a significant decrease in outflow uniformity. Because of the shallower ACD and wider ACA, the flow had less vertical space to spread, leading to high-velocity concentration near part of the outlet, which was illustrated in Figure 65. The African NPDS model showed tight streamlines entering a limited region of the flap, while other outlet channels were underutilized, resulting in a poor flow distribution. The European NPDS model, with its deeper ACD and narrower ACA, allows for more vertical development of flow and better distribution along the deep flap length.

The UI-values between the European and African mNPDS models are also similar in value. These are the closest to the normal UI-values, suggesting that the membrane peel improves flow symmetry at the surgical outlet. This interpretation is further supported by the full comparison of flow fields previously provided and discussed in sections 5.4.1 to 5.4.4, and will also further be summarised in section 5.5.

Table 12 UI-value calculations for all upright models

	European	**African**
Normal	0.84	0.77
Trabeculectomy	0.61	0.60
NPDS	0.69	0.43
mNPDS	0.76	0.77

The convergence in mNPDS UI-values confirms its superiority in achieving the most uniform outflow. For yet another metric, this presents mNPDS as a strong candidate for procedures aiming to maintain normal hydrodynamics while reducing IOP.

5.4.6 Parametric Study on Suturing Tightness

For all models studied in this work thus far, a suture pressure of 7 mmHg was selected for the glaucoma filtration procedures to match the typical collector channel pressure. However, as previously mentioned, the exact suture pressure resistances for these procedures are not known. To further account for this unknown parameter, a parametric study was performed on the "suture tightness" for all the models, including trabeculectomy, NPDS, and mNPDS for the European and African eye models. The purpose of this study is to determine how the post-suturing IOP changes with suture tightness between the different procedures and ethnicities.

For each model, the suture pressure was adjusted from 0 mmHg to 10 mmHg, with an increment of 1 mmHg. The results are provided on the graph in Figure 91.

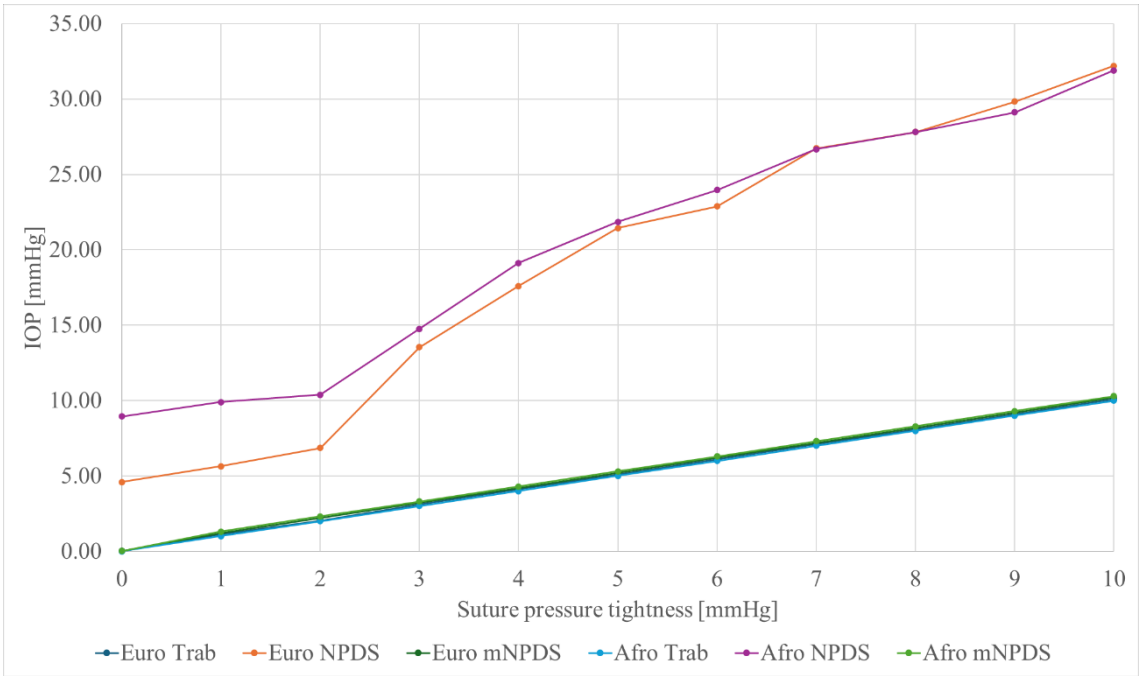


Figure 91 IOP results for all models based on suture pressure tightness, with a target IOP of 10 mmHg indicated by the dashed line

In ophthalmology, there is a concept known as the 10-10-10 target, which suggests that the ideal glaucoma filtration surgery should take less than 10 minutes to perform, achieve an IOP of <10 mmHg, and last for at least 10 years without significant post-operative complications [173]. On the graph, the ideal postoperative IOP has been indicated with the dashed line.

The graph shows that trabeculectomy and mNPDS, both for the European and African models, follow a linear trend, showing a positive relationship between the suture tightness and IOP. The mNPDS consistently show slightly higher IOP results, although these are not very significant (<1% difference). For both trabeculectomy and mNPDS, the suture tightness should approximate 10 mmHg for the postoperative IOP to achieve 10 mmHg.

The NPDS results also show a positive relationship between the suture tightness and resulting IOP. However, the trendline is biphasic. For lower suture pressures (<2.5 mmHg), The resulting IOP shows minimal changes and remains below or close to the ideal outcome of 10 mmHg. However, for higher suture pressures, the trendline shows a sharp and nearly linear increase in the resulting IOP. The IOP difference between the European and African model is also initially more pronounced, and then starts to follow a similar trendline as the suture tightness increases. The resulting IOP for each suture pressure is significantly elevated compared to the trabeculectomy and mNPDS results.

This indicates that NPDS procedures are more sensitive to suture tightness overall, most likely because the TM resistance in the case of NPDS is less affected, and the most important driver for a decrease in IOP is the enlarged outflow area created by the deep scleral flap. In this case, the suture tightness to

achieve a postoperative IOP of 10 mmHg should be ~2.5 mmHg for the European eye model and ~2.0 mmHg for the African eye model. It is also an indication that NPDS procedures are much more susceptible to anatomical variances in the anterior chamber, especially at a lower suture tightness, whereas trabeculectomy and mNPDS provide more consistent and efficient results for the same suture tightness.

5.4.7 Unsteady Considerations

The possibility of unsteady behaviour was considered and examined by using the unsutured trabeculectomy model as a case study. The unsutured trabeculectomy model represents the greatest alterations as its procedure creates the most invasive surgical opening leading to rapid outflow and steep velocity gradients. If this extreme case demonstrates steady-state behaviour, it is likely that less extreme cases (i.e., sutured conditions, NPDS, and mNPDS) will also achieve steady results. Additionally, all models use the same fundamental flow domain with minor geometric differences and consistent boundary conditions.

The k-omega model was selected due to the low Reynolds number of aqueous humour flow. After performing the simulation, the residuals indicated that the simulation reached convergence. The continuity residual steadily reduces over time along with the velocity components which show a stable convergence trend. The energy residual initially oscillates to suggest transient effects, but these are damped over time.

The mass flow rate plot in Figure 92 shows that the flow reaches steady conditions. After the initial transient phase, the mass flow rate stabilizes with minimal oscillations. Some fluctuations are observed, but these are negligibly small ($<1 \times 10^{-5}$ kg/s) and do not indicate meaningful unsteady behaviour.

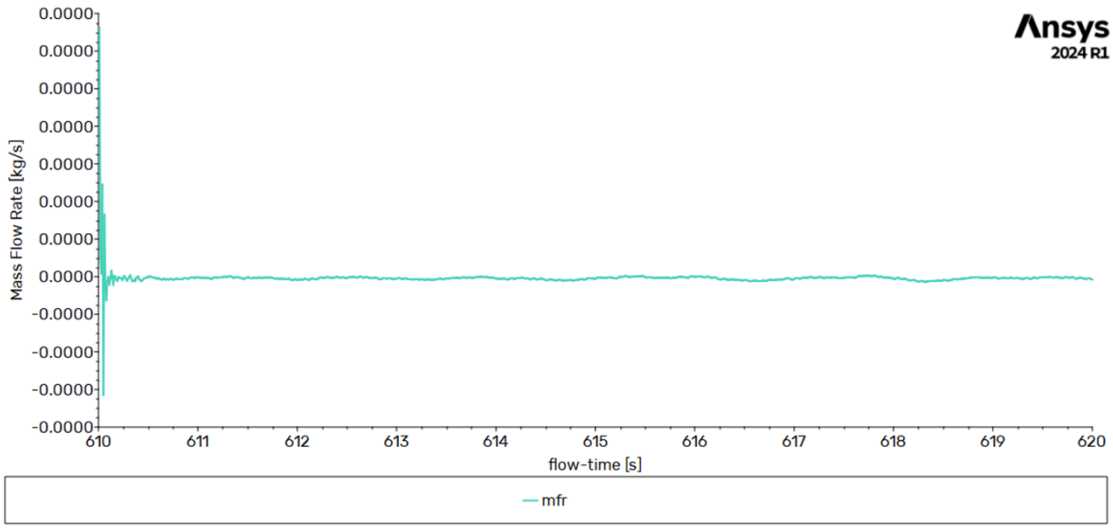


Figure 92 Mass flow rate plot results for unsteady unsutured trabeculectomy simulation

Based on these results, the unsutured trabeculectomy model exhibits steady flow behaviour after an initial transient period. The unsutured trabeculectomy model serves as a sufficient basis for concluding that all models are likely steady, given that it represents the most extreme case.

5.5 Summary

This section offers valuable insights into the post-surgical flow dynamics of aqueous humour for different surgical procedures including trabeculectomy, NPDS, and mNPDS and how these are influenced by anatomical differences between European- and African-representative eyes. A summary of the most important values extracted from the CFD simulations for the European-representative and African representative eye models are provided in Table 13 and Table 14, respectively.

Based on the literature explored in section 4.5.1, the IOP results align with clinical expectations for early post-op conditions (~1-day post-surgery). As demonstrated in section 4, trabeculectomy stabilizes the IOP as expected when sutured for both the European and African models, showing effectiveness in restoring pressure control. Sutured mNPDS also maintains stable IOP with smoother flow dynamics compared to trabeculectomy, suggesting that mNPDS may better regulate outflow. Sutured NPDS restores the IOP to glaucomatous conditions, which could be corrected with releasable sutures as demonstrated with the IOP decrease when the incision site is unsutured. However, this will be much more challenging to regulate long-term. In general, NPDS seems to be more heavily influenced by anatomical differences and may make it more difficult to control the surgical outcome long-term.

Table 13 Summary of main European-representative model results in the upright position

Model	Normal flow	Sutured trabeculectomy	Sutured NPDS	Sutured mNPDS	Key Observations
Post-suturing IOP [mmHg]	-	7.00	26.79	6.99	With identical suture tightness, trabeculectomy and mNPDS provide good IOP decrease, while NPDS requires lower tension sutures.
Top outflow [mm/s]	-	0.43	0.19	0.18	Trabeculectomy shows the highest outflow rate.
Max corneal flow [mm/s]	0.12	0.12	0.11	0.11	All surgical procedures indicate adequate flow at the corneal wall compared to normal conditions.
Max pupil flow [mm/s]	0.47	0.63	0.65	0.50	Trabeculectomy and NPDS indicate increased flow velocities at the pupil region, while mNPDS is more consistent with normal flow conditions.
Q-criterion at ACA	0.01	0.32	0.01	0.01	Trabeculectomy shows distinct vortices near the ACA compared to NPDS and mNPDS.
Q-criterion top outlet	38.70	3.40	75.61	4.85	NPDS shows high-strength vortices at the TM.
Max corneal WSS [mmHg]	5.6E-06	5.5E-06	5.0E-06	5.0E-06	Slight decrease from normal conditions for all surgical procedures.
Max top outlet WSS [mmHg]	2.0E-04	4.5E-05	4.5E-04	5.0E-05	No indications of ECD.

Table 14 Summary of main African-representative model results in the upright position

Model	Normal flow	Sutured trabeculectomy	Sutured NPDS	Sutured mNPDS	Key Observations
Post-suturing IOP [mmHg]	-	7.00	26.71	6.99	With identical suture tightness, trabeculectomy and mNPDS provide good IOP decrease, while NPDS requires lower tension sutures.
Top outflow [mm/s]	-	0.38	0.22	0.17	Trabeculectomy shows the highest outflow rate.
Max corneal flow [mm/s]	0.12	0.09	0.09	0.12	Trabeculectomy and NPDS indicate decreased flow near the corneal wall, while mNPDS is more consistent with normal flow conditions.
Max pupil flow [mm/s]	0.47	0.47	0.48	0.59	Trabeculectomy and NPDS flow at the pupil is consistent with normal flow conditions, while mNPDS shows increased flow velocities.
Q-criterion at ACA	0.01	0.32	0.01	0.01	Trabeculectomy shows distinct vortices near the ACA and surgical site compared to NPDS and mNPDS.
Max Q-criterion top outlet	13.20	1.10	82.83	4.85	NPDS shows high-strength vortices at the TM.
Max corneal WSS [mmHg]	5.5E-06	4.6E-06	4.7E-06	5.1E-06	Slight decrease from normal conditions for all surgical procedures.
Max top outlet WSS [mmHg]	2.0E-04	4.2E-05	3.8E-04	4.9E-05	No indications of ECD.

When analysing the distribution of aqueous humour flow post-operatively for all surgeries, the European eye model consistently shows sufficient flow (~0.11 mm/s) near the corneal wall compared to its normal flow conditions. This suggests that nutrient delivery to avascular tissues is generally more uniform, which is most likely due to the European model's deeper ACD that provides a larger fluid volume for circulation. In terms of nutrient distribution, any procedure would be sufficient for the European model.

Lower velocities near the corneal wall in the African eye models suggest a risk of nutrient deficiencies, especially for procedures like trabeculectomy, where the maximum flow is reduced to 0.09 mm/s compared to normal conditions (~0.12 mm/s). This may suggest reduced nutrient delivery to some regions, increasing the risk of tissue damage or delayed healing [46,90]. This suggests that mNPDS is the best option with a corneal flow velocity of 0.12 mm/s to be the best option for the African model in terms of sufficient nutrient delivery.

Elevated velocities near the surgical site in the trabeculectomy models could promote fibrosis and scarring, which may compromise long-term drainage efficiency [100,101]. The simulations demonstrate that trabeculectomy procedures, though effective in IOP reduction, may lead to uneven bleb formation due to higher velocities at the surgical site and flow alterations. Though African eyes have been identified to being more susceptible to post-operative fibrosis [70,172], the simulations do not indicate a particular predisposition for this. In fact, the higher velocities and stronger vortex formation in the European eye model would give a greater indication of risk. Additionally, the core offset of the peak velocities at the surgical site does not vary with the two models, suggesting that other factors must contribute to ethnic differences in trabeculectomy success rates, including post-operative healing responses, differences in long-term IOP regulation, and variations in bleb formation and function over time. Thus, these complications could be related to more patient-specific factors.

NPDS showed to be the least effective procedure. However, its effectiveness can be optimised by decreasing the suture tightness (introducing looser sutures). The extent of the suture tightness was shown to be heavily dependent on the anatomical variances between the European and African models. Clinically, this would make it a more challenging procedure to manage post-operatively, as the postoperative IOP is more sensitive to suture tightness changes. Looser sutures could also affect the healing process.

Overall, the European model exhibits more balanced flow patterns across all procedures. Its closer alignment with normal flow dynamics suggests a lower risk of complications like scarring, hypotony, and nutrient imbalances.

Anatomical differences between African and European eyes are partially responsible for determining the outcomes of glaucoma filtration surgeries. The procedures are more sensitive to these differences in an unsutured state, particularly in the African eye models, which show greater flow irregularity and

post-surgical risk. Suturing significantly mitigates these effects, making procedures like trabeculectomy and mNPDS the most effective and anatomically resilient choices.

The normal condition models demonstrated that a deeper ACD promotes stronger central recirculation because of the larger vertical space. A shallower ACD restricts the recirculation volume. However, these anatomical effects are also impacted by body orientation and surgical modifications. It was demonstrated that upright orientations can introduce gravitational asymmetry, which interacts with anatomical structure and surgical alterations to either assist or hinder drainage efficiency. Furthermore, each surgery alters flow resistance and redirection differently, and anatomical geometry determines how effective or disruptive that alteration becomes. The mNPDS appears to adapt and cause the least changes across anatomical and orientation differences.

None of the post-surgical models exhibited noteworthy elevations in WSS. For all models, WSS near the corneal wall remained fairly consistent compared to normal flow conditions. At the surgical site outlet, all models displayed an increase in WSS as expected due to the increased velocity outflow. However, these elevations were not high enough to give an indication of potential ECD, as these are generally four orders of magnitude less than the required 0.02 mmHg (3 Pa [171]) to cause potential damage to the cell. During surgery, WSS at the surgical outlet and surrounding outlets do tend to increase above this limit. Although only for a short period of time, this increased WSS has the potential to cause ECD, which indicates the requirement for prompt and proper suturing post-surgery.

Finally, both trabeculectomy and mNPDS demonstrate effective IOP reduction. However, mNPDS may offer a safer alternative as it appears to be the most balanced procedure for restoring aqueous humour flow while mitigating potential post-surgical risks, especially for African eyes. These findings emphasize the importance of tailoring surgical approaches to patient-specific anatomical and ethnic differences, balancing short-term effectiveness with long-term outcomes. The post-surgical flow differences suggest that surgical choices should consider individual eye geometry, not only the disease state.

6 Reconstructed OCT Model

This section describes the methodology and results for generating a 3D model of the anterior segment of a patient-specific eye. The main objective is to evaluate the accuracy and clinical relevance of reconstructed 3D anterior chamber models derived from OCT scans compared to models created using generalized 3D models based on anatomical dimensions. By conducting CFD simulations on both types of models, the study aims to determine whether the effort-intensive process of using patient-specific OCT-based reconstructions offers significant advantages over traditional, simplified models based on average anatomical data. Specifically, the analysis would focus on comparing IOP reduction patterns, bulk and localise flow patterns, and wall shear stresses in the two model types to assess the validity and reliability of general geometric assumptions in capturing key biomechanical and fluid dynamic behaviours of the anterior chamber.

This comparison would provide insights into the trade-offs between modelling accuracy and procedural efficiency, guiding future choices between individualized and generalized modelling approaches in glaucoma surgery simulations. Ultimately, the study seeks to establish whether patient-specific modelling is necessary for precise surgical outcome predictions or if simplified, literature-based models suffice for pre-surgical planning and clinical research purposes.

6.1 Methodology

The process involves data acquisition with Cylite Hyperparallel Optical Coherence Tomography (HP-OCT), image preprocessing, segmentation using ITK-SNAP, and 3D model generation. The initial step is the acquisition of high-resolution OCT images of the patient's eye using the Cylite HP-OCT system. This system has the capability of generating a full volumetric anterior and posterior imaging, capturing over 300,000 A-scans per second. The next step involved converting the Cylite HP-OCT scans from their native format (h5) to NRRD files, which are compatible with segmentation software like ITK-SNAP using a Python script (provided by Cylite). This conversion ensures the scans retain the necessary structural data for building the 3D model.

ITK-SNAP, which is a versatile open-source tool for medical image segmentation, was employed to reconstruct the OCT scans into a 3D model. The interface displays sagittal, axial, and coronal views, along with a 3D rendering panel (Figure 93). The view settings can be adjusted to optimize the visualization of the anterior segment. The next step involves setting up initial contours around the region of interest (ROI) using semi-automatic methods.

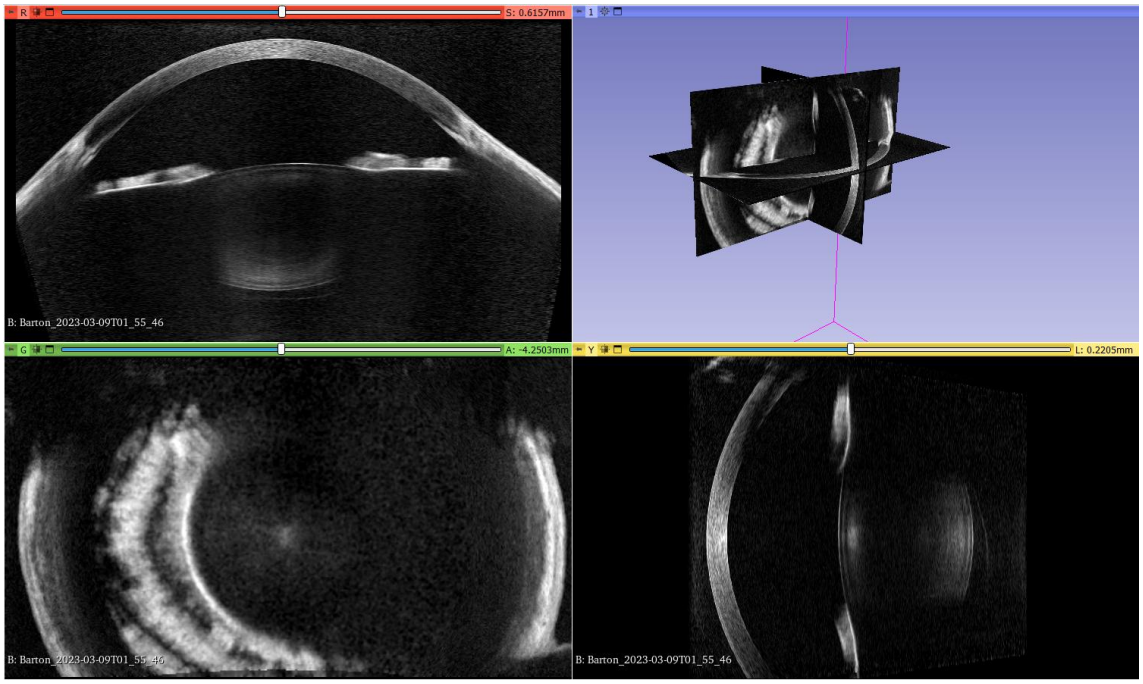


Figure 93 Visualization of the anterior segment of a patient's eye using ITK-SNAP displaying the sagittal view (top left), the axial view (bottom left), the coronal view (bottom right), and a 3D rendering of the segmented structure (top right).

The ROI was further manually refined as necessary to achieve a higher accuracy around complex anatomical structures and finally produce a 3D model of the anterior segment (Figure 94). Using the paintbrush tool, the anterior chamber and background across multiple slices in all three planes (axial, sagittal, and coronal) were manually indicated. After marking these areas, the "Grow from Seeds" tool was employed, which allowed the software to detect and delineate the full anterior chamber automatically. This step concluded with exporting the segmented model as an STL file, which provides a 3D surface representation suitable for further manipulation.

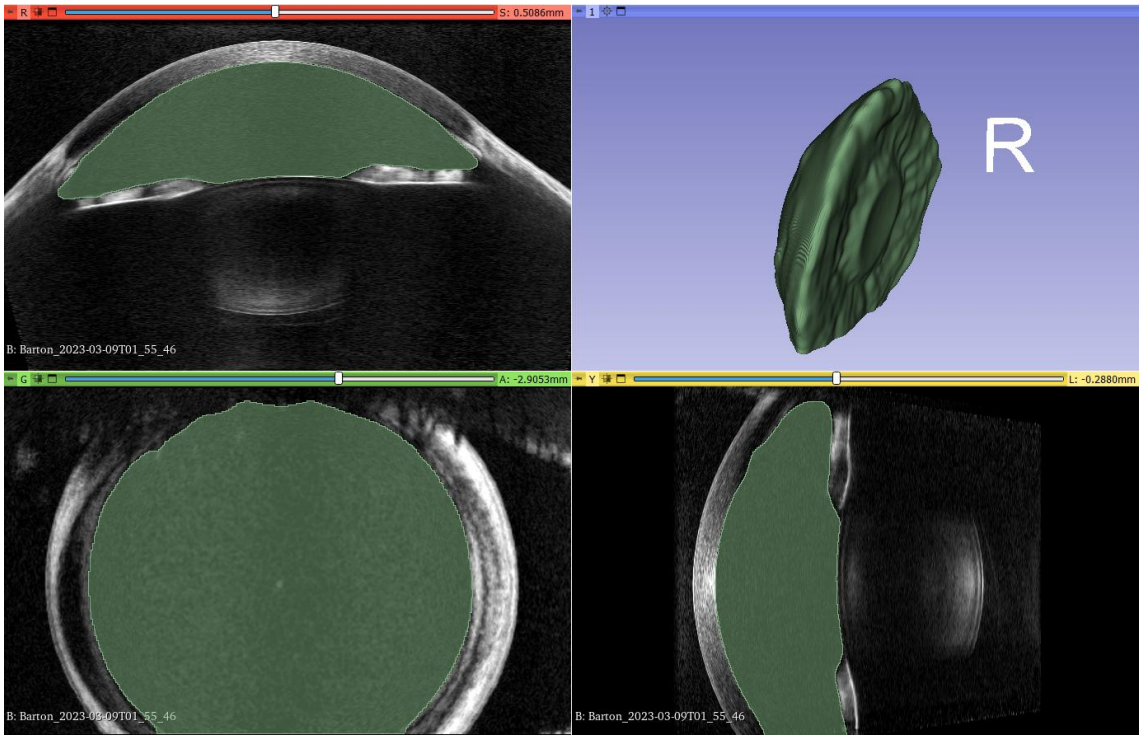


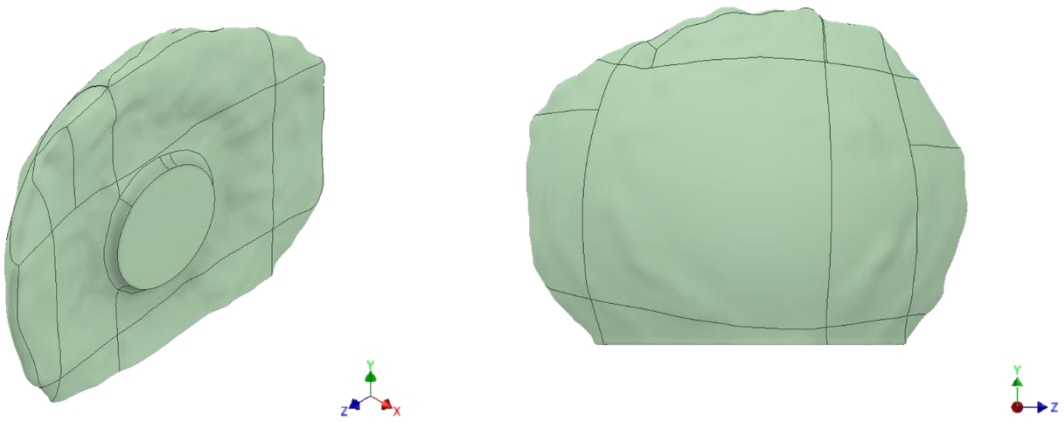
Figure 94 Segmented anterior segment of the patient's eye using ITK-SNAP with the ROI highlighted in green displaying the sagittal view (top left), the axial view (bottom left), the coronal view (bottom right), and a 3D rendering of the segmented structure (top right).

The next phase involved converting the STL surface mesh into a solid model using SpaceClaim. Solid models are essential for CAD software, as they allow for additional modifications and are better suited for simulations. The STL file was imported into SpaceClaim, and the "Autoskin" tool was used to convert the surface mesh into a solid object. This process involved selecting the facets of the anterior chamber and automatically converting them into a solid representation. Once the solid model was generated, it was exported as a STEP file, which is compatible with CAD and simulation tools like AutoDesk Inventor and Fluent.

The resulting 3D model may exhibit imperfections such as jagged edges and incomplete structures. The initial segmented model often contains small bumps and may have portions that are inaccurately cut off (Figure 95). These imperfections can hinder accurate simulations and visualizations.

Segmenting OCT scans presents several challenges compared to more traditional medical imaging modalities like MRI. OCT scans provide high-resolution images of the anterior segment but often suffer from artifacts and noise, making segmentation difficult. In contrast, MRI provides clearer images with better contrast between different tissue types, facilitating easier segmentation.

Additionally, OCT scans require precise differentiation between various layers of the cornea, sclera, and other structures, which can be challenging due to the close proximity and similar reflectivity of these layers.

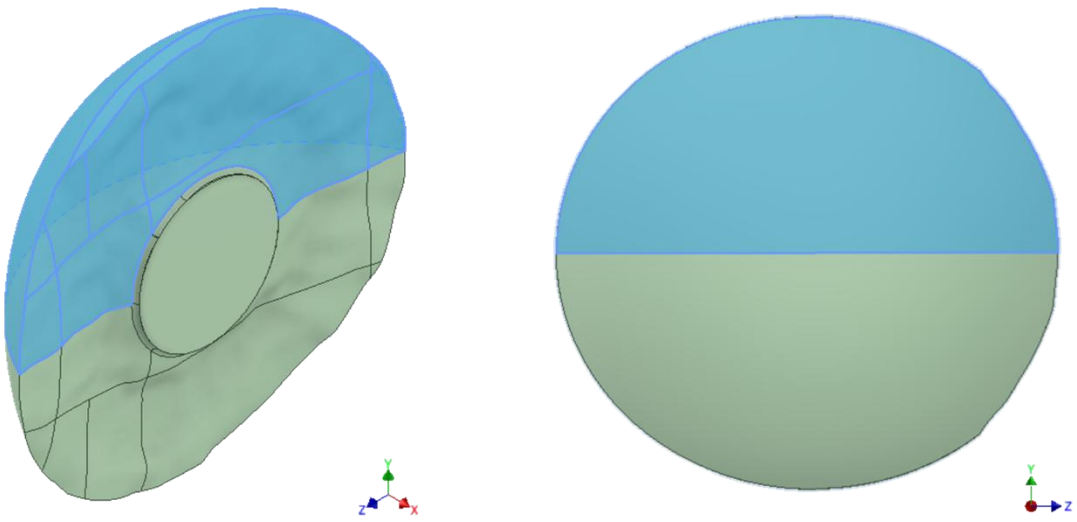


(a) (b)

Figure 95 3D model of segmented and reconstructed patient-specific eye as (a) isometric view and (b) front view.

Autodesk Inventor is employed to refine the model by addressing surface irregularities and reconstructing missing parts. The process begins by importing the STL file into Autodesk Inventor and converting the imported mesh into a solid body for editing. The "Smooth" tool was used to iteratively smooth the surface of the model, reducing the appearance of small bumps and jagged edges. The cutting tool was used to remove more pronounced bumps on the anterior surface of the model.

To correct structural anomalies such as cut-off parts of the eye, the top section (highlighted in blue in Figure 96) was mirrored around the z-axis, which constructed a symmetrical copy of the intact part of the eye and merged with the original model to restore the complete structure.



(a) (b)

Figure 96 Mirrored patient-specific model from OCT scans as (a) isometric view and (b) front view.

Additionally, the TM, Schlemm's canal, and collector channels were manually added, and some edges were filleted to ensure smooth flow simulations. The final reconstructed patient-specific model is shown in Figure 97. The reconstructed eye model is shown to be more flattened at the top and bottom. This is typical for a real eye, which is not perfectly round, but rather nearly-round or more oval-shaped. Going forward, this will be referred to as the OCT-reconstructed model.

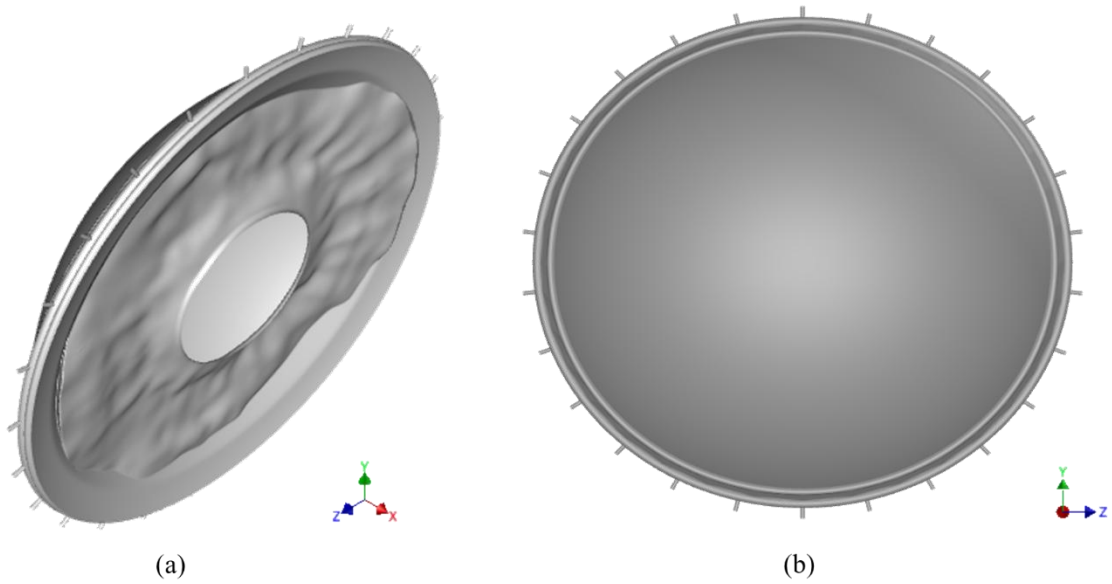
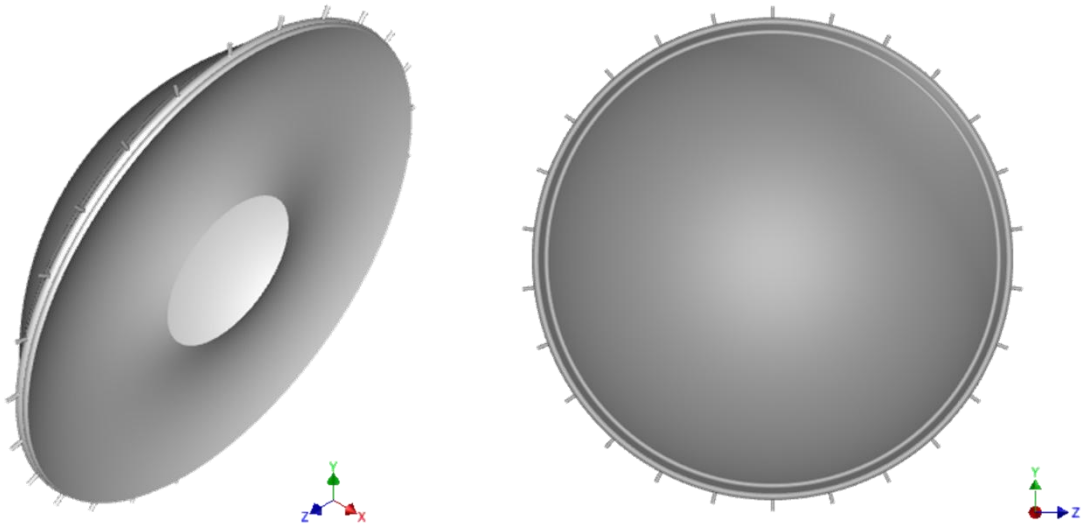


Figure 97 Final OCT-reconstructed model from OCT scans as (a) isometric view and (b) front view.

Additionally, a simplified 3D model was created in a similar manner as described in section 5.1. This geometry is based on measurements taken from the scan model based on the XY-planar profile, which are provided in Table 15, and rotated around the x-axis to create a cylindrical model, similar to the method in section 5.1. While the OCT-reconstructed model captures natural anatomical asymmetry, the cylindrical dimension-based model was constructed using average biometric parameters to provide a geometrically standardized baseline that supports reproducible, generalizable, and interpretable analysis of aqueous humour dynamics. Given the known geometric distortions in OCT imaging, particularly in axial depth and angle flattening, the cylindrical reconstruction provides a consistent, distortion-free geometry for evaluating baseline aqueous humour dynamics. Creating standardized cylindrical geometries based on a known set of parameters is easily repeatable and eliminates ambiguity in model construction. The simplified cylindrical model based on the scan dimensions is depicted in Figure 98. Going forward, this model will be referred to as the dimension-based model.

Table 15 Anterior chamber geometry parameters for dimension-based model based on OCT scan data

WTW [mm]	13.2
ACD [mm]	3.8
ACA [deg]	36
LV [mm]	0.1
PD [mm]	4.2



(a) (b)

Figure 98 Final dimension-based model based on OCT scan parameters as (a) isometric view and (b) front view.

The Fluent setup for both the OCT-reconstructed model and the dimension-based model was completed in an identical manner as the method described in section 5.2. The permeability parameters and calculated results are provided in Table 16.

Table 16 Permeability parameter and calculation results for OCT-reconstructed and dimension-based models

Parameter description	Symbol	Unit	Normal flow	Glaucomatous flow
Boundary conditions				
Target IOP	IOP	mmHg	13.5	27.0
Outlet pressure	p_o	mmHg	7.00	7.00
Change in pressure	Δp	mmHg	-6.50	-20.0
Inlet mass flow rate	$\dot{m}$	kg/s	5.00E-08	5.00E-08
Porous region properties				
Superficial velocity	v	Pa·s	1.56E-06	1.56E-06
Porous zone area	A	m^2	3.21E-05	3.21E-05
Equivalent TM height	Δm	m	2.26E-04	2.26E-04
Power law coefficients				
Source term = dp/dx	S_i	Pa/m	-3.83E+06	-1.18E+07
Pressure jump coefficient	C_0	-	2.46E+12	7.58E+12
Flow coefficient	C_1	-	1	1
TM permeability	α	m^2	4.06E-16	1.32E-16
Viscous resistance	C	m^{-2}	2.46E+15	7.58E+15

6.2 Results & Discussion

The initial pre-surgical flow conditions were simulated for each model to determine whether the detailed iris structure and oval shape of the OCT-reconstructed model significantly influences the aqueous humour dynamic results when compared to the dimension-based version of the model. Figure 99 provides the velocity pathline results for each model in both the supine and upright positions.

Both the OCT-reconstructed model and the dimension-based model exhibit flow patterns as expected based on the previous models from sections 4 and 5. However, there are some slight variations in terms of velocity magnitudes. While both models have identical maximum velocities at the outlet (0.47 mm/s in the supine position and 0.57 mm/s in the upright position), the central peak velocities differ.

In the supine position, the central peak velocity is 0.26 mm/s and 0.28 mm/s for the OCT-reconstructed model and dimension-based model, respectively. In the upright position, the central peak velocity is 0.52 mm/s and 0.55 mm/s for the OCT-reconstructed model and dimension-based model, respectively. Thus, the OCT-reconstructed model consistently shows a decreased peak central velocity. Since the

OCT-reconstructed model has a slightly oblong shape, its overall volume is also larger. This increased volume allows for a broader flow path, which increases the flow area and, consequently, reduces the flow velocity to maintain the same volumetric flow rate imposed by the boundary conditions. The detailed iris structure on the OCT-reconstructed model does not seem to have an effect on the overall flow patterns.

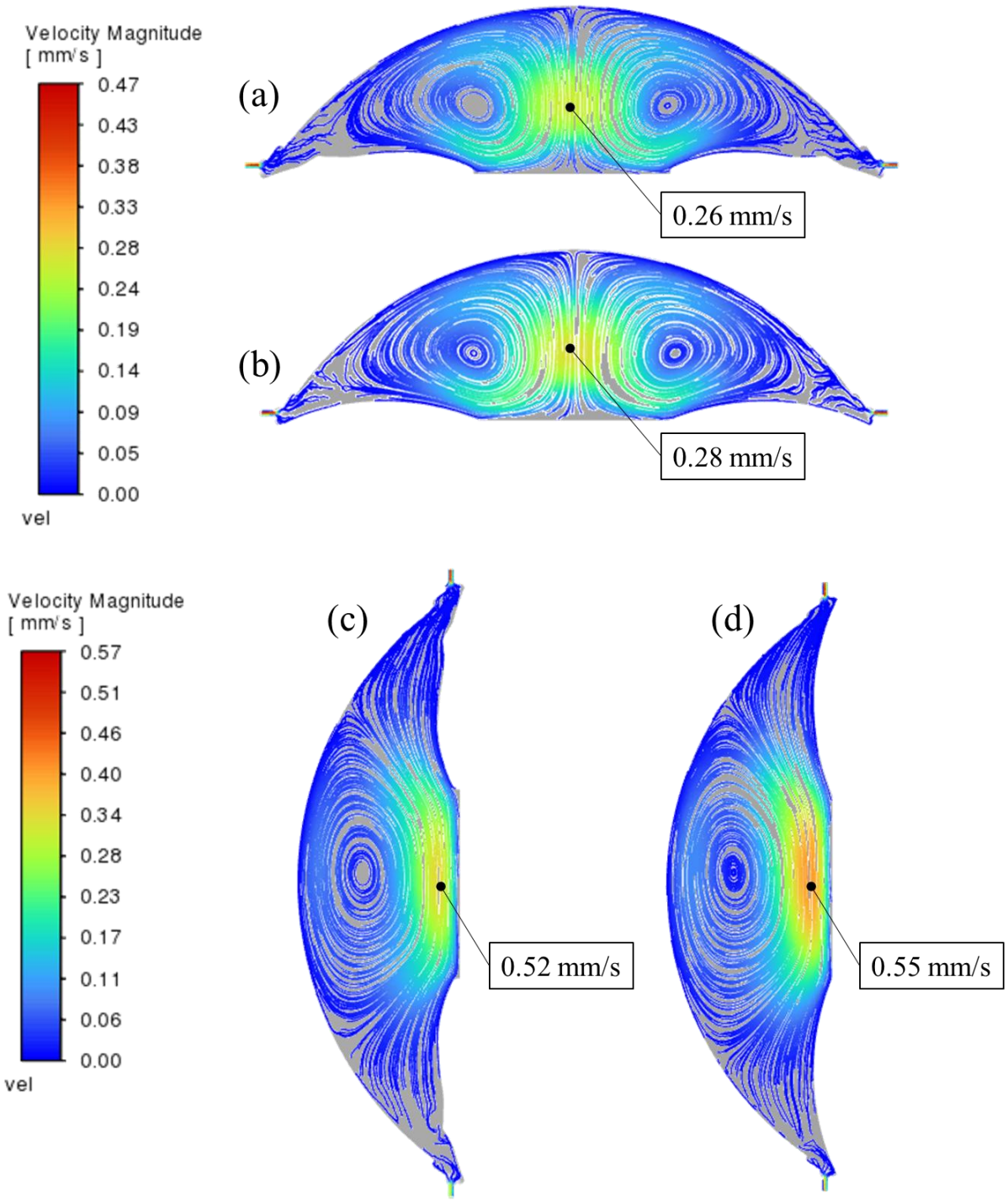


Figure 99 Pre-surgical velocity pathline results for (a) OCT-reconstructed model in supine position, (b) dimension-based model in supine positions, (c) OCT-reconstructed model in upright position, and (d) dimension-based model in upright positions.

Localized flow differences can be observed specifically near the iris wall between the two models. This can be seen in Figure 100, which shows the WSS contour results of the iris region in the supine position. In this figure, the OCT-reconstructed model includes only the segment of the iris captured in the OCT

scan, as the adjacent geometry could not be reliably reconstructed, and is, therefore, limited due to its physiological accuracy. Future work should focus on enhancing the anatomical precision of OCT reconstructions by capturing the full extent of patient-specific anterior chamber structures.

Nevertheless, the OCT-reconstructed model captures the undulations and ridges at the iris wall, resulting in a more irregular distribution of the WSS contours. The dimension-based model has a smooth, continuous geometry, resulting in a uniform distribution of WSS. While the OCT-based model does show a larger variation in WSS magnitudes between the undulations, these observed differences are marginal and do not indicate a meaningful deviation (between 1.1 and 2.1 mmHg).

Despite these textural differences, the radial extent and thickness of the high-WSS band near the central cornea remain similar in both models, indicating comparable shear gradients and flow behaviour in this critical region. This suggests that while there are there are indications of localized fluid dynamic differences, the overall shear load distribution remains consistent between the two geometries. Thus, the global results show how the dimension-based model is a good representation of the results that would be achieved in a patient-specific model.

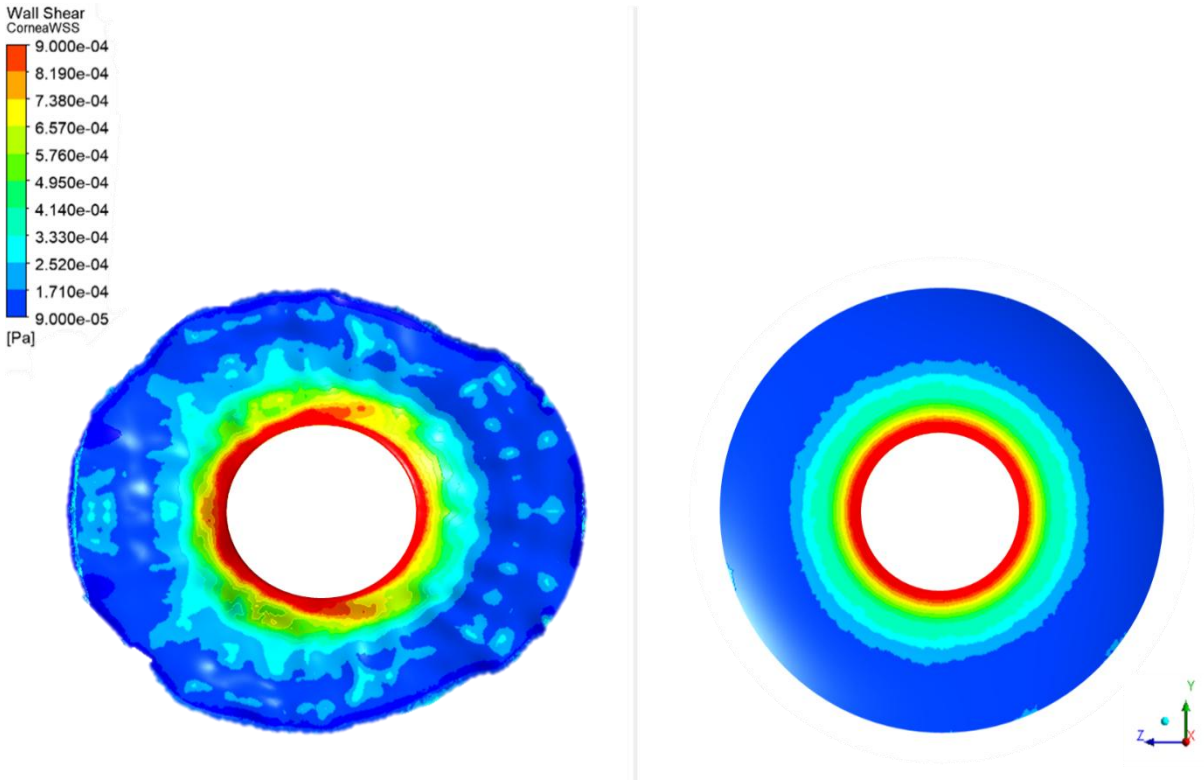


Figure 100 WSS contour results on the iris for the OCT-reconstructed model (left) and dimension-based model (right) in the supine orientation

For the upright position, there is an indication of out-of-plane flow near the corneal wall of the OCT-reconstructed model (circled in red in Figure 101). This is not seen in the dimension-based model due to its smooth, continuous geometry of the anterior chamber. However, for both orientations, there is no

obvious difference in the global flow between the OCT-reconstructed model and the dimension-based models. The flow patterns are similar and also correspond with the normal flow conditions seen in previous chapters. Overall, the flow differences under normal flow conditions remain minimal.

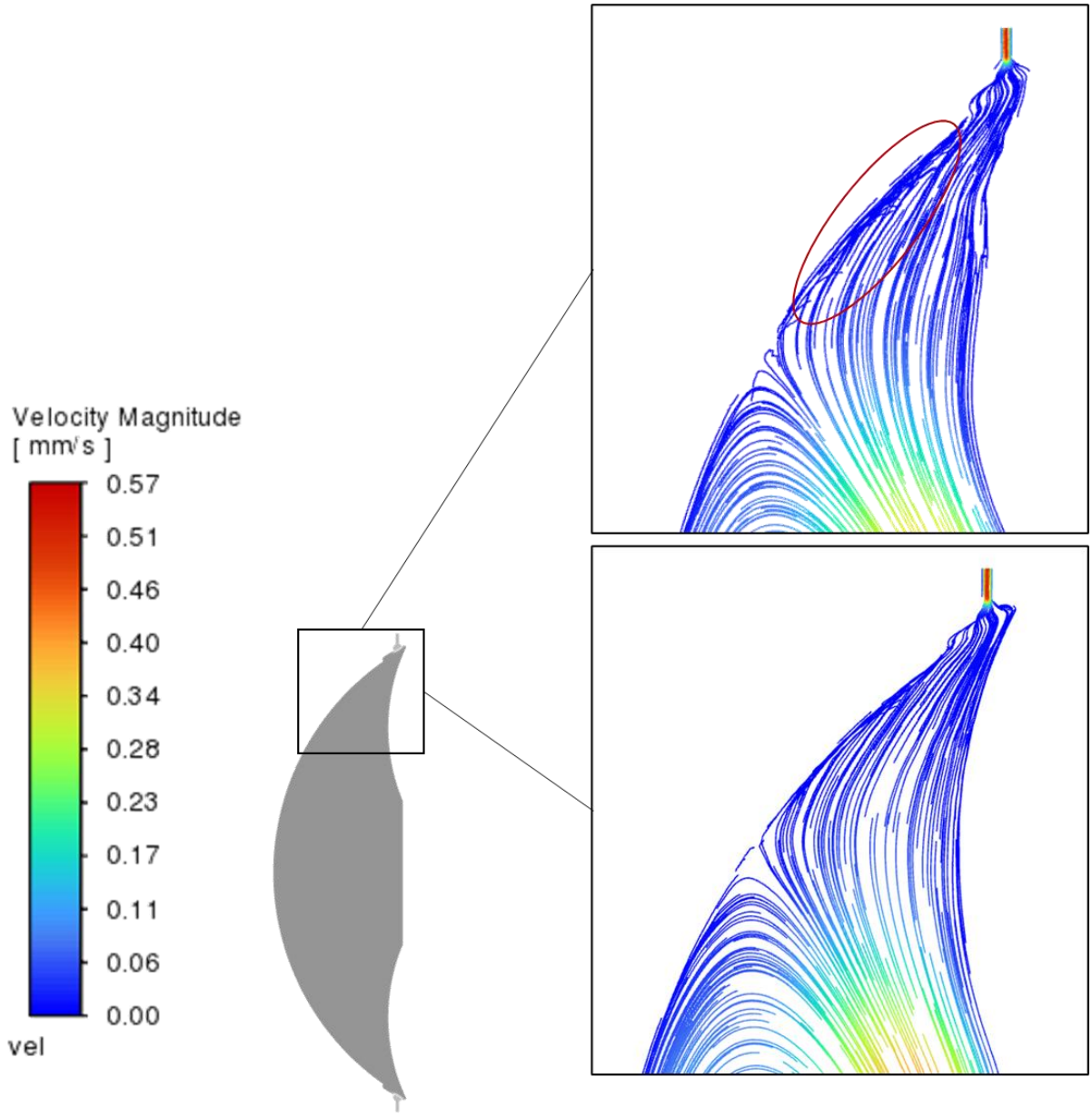


Figure 101 Inset pre-surgical velocity pathline results for OCT-reconstructed model in upright position (top) and dimension-based model in upright position (bottom), with the out-of-plane flow circled in red

Additionally, both models were reconfigured to further simulate the trabeculectomy procedure as described in section 5.2. This was done to further analyse whether there are differences in the aqueous humour dynamic results when the models are no longer axisymmetric. The velocity pathline results for each model in both the supine and upright positions are provided in Figure 102.

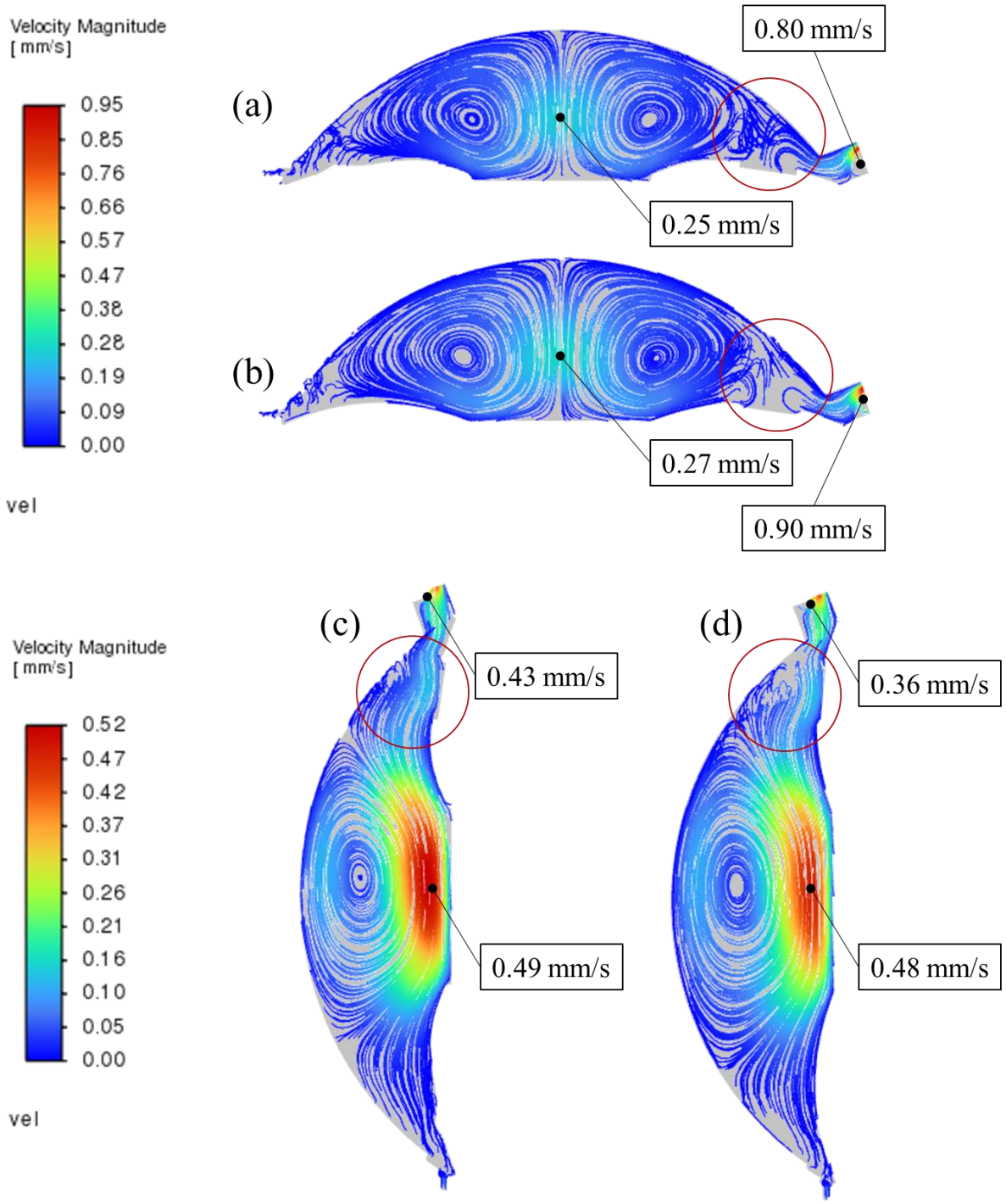


Figure 102 Post-trabeculectomy velocity pathline results for (a) OCT-reconstructed model in supine position, (b) dimension-based model in supine positions, (c) OCT-reconstructed model in upright position, and (d) dimension-based model in upright positions, with the flow disturbances circled in red

In the case of trabeculectomy, the central peak velocities show very minor discrepancies. In the supine position, the central peak velocity is 0.25 mm/s and 0.27 mm/s for the OCT-reconstructed model and dimension-based model, respectively. In the upright position, the central peak velocity is 0.49 mm/s and 0.48 mm/s for the OCT-reconstructed model and dimension-based model, respectively. Comparing this to the pre-surgical models, the peak central velocities of all models were only slightly decreased,

with the largest decrease being 0.07 mm/s in the upright dimension-based model. This suggests that there are no significant differences regarding central flow between the OCT-reconstructed model and the dimension-based model. Slight differences may occur due to volume differences.

However, a more significant difference can be observed at the surgical outlet and iridectomy sites (circled in red in Figure 102). For the OCT-reconstructed model in both the supine and upright positions, the pathlines are more densely packed, indicating stronger variations in out-of-plane flow. This is most likely due to the surface irregularity of the more complex iris structure in the dimension-based model which can create localized flow disturbances.

The zoomed-in views of these flow disturbances are provided in Figure 103 and Figure 104 for the supine and upright positions, respectively. This leads to a noticeable difference in the velocity magnitude at the surgical outlet, which is approximately 0.1 mm/s between the OCT-reconstructed and dimension-based models.

However, Figure 105 shows that, despite the differences in peak flow velocities between the OCT-reconstructed and dimension-based models, these variations do not significantly impact the WSS distribution at the outlet. The WSS peak regions at the sclerostomy outlet show slight differences in their angular position. This could be due to the slight geometric variations between the models. However, the magnitudes and general WSS distribution are highly comparable. This indicates that the peak velocity magnitude differences between the two models does not significantly affect the shear force exerted on the wall.

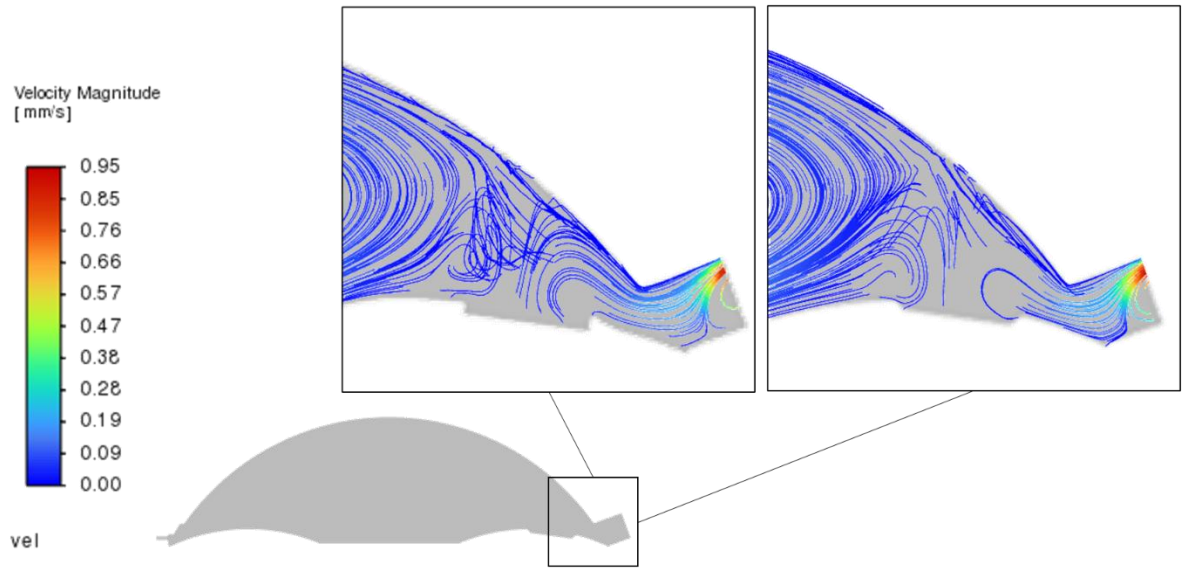


Figure 103 Inset post-trabeculectomy velocity pathline results for OCT-reconstructed model in supine position, (left) and the dimension-based model in supine position (right)

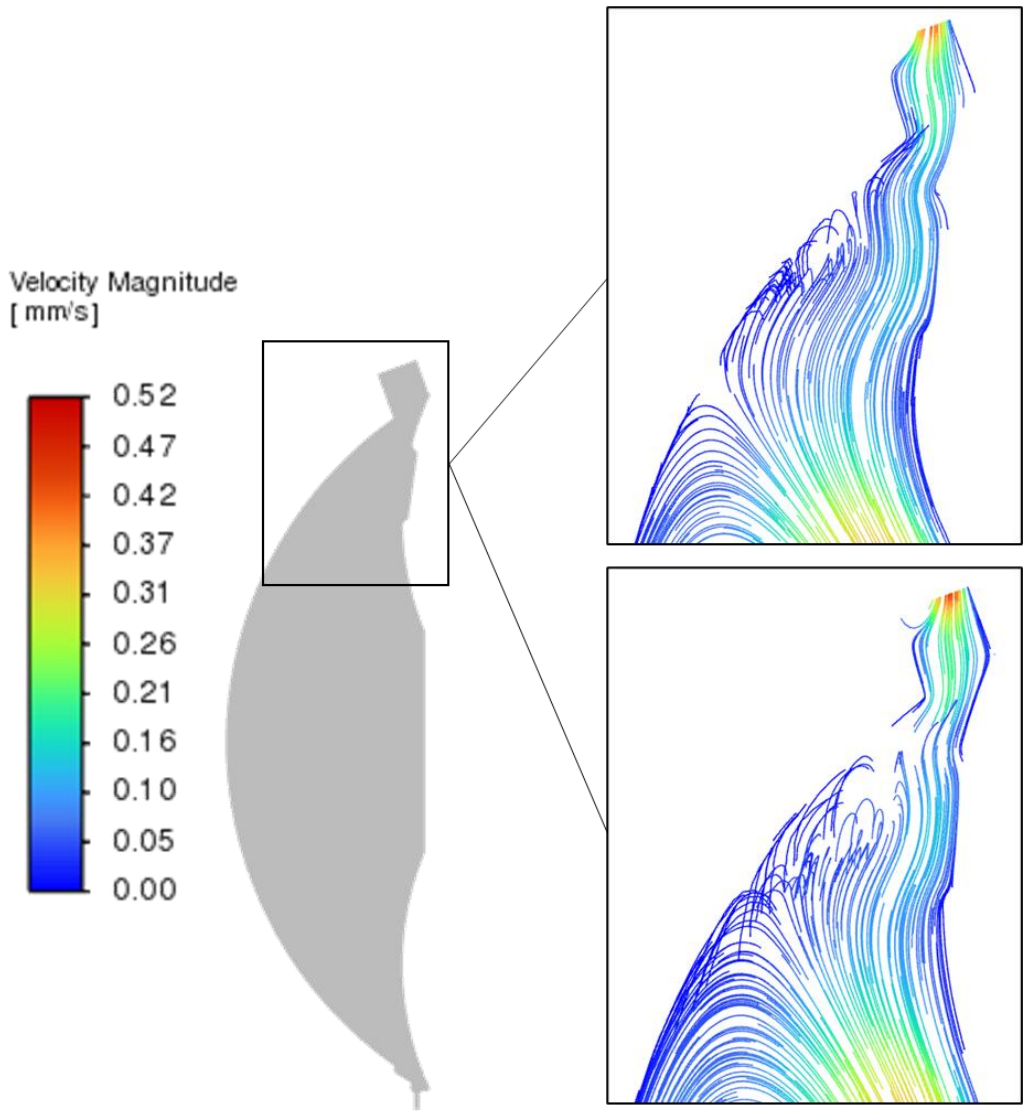


Figure 104 Inset post-trabeculectomy velocity pathline results for OCT-reconstructed model in upright position (top) and the dimension-based model in upright position (bottom)

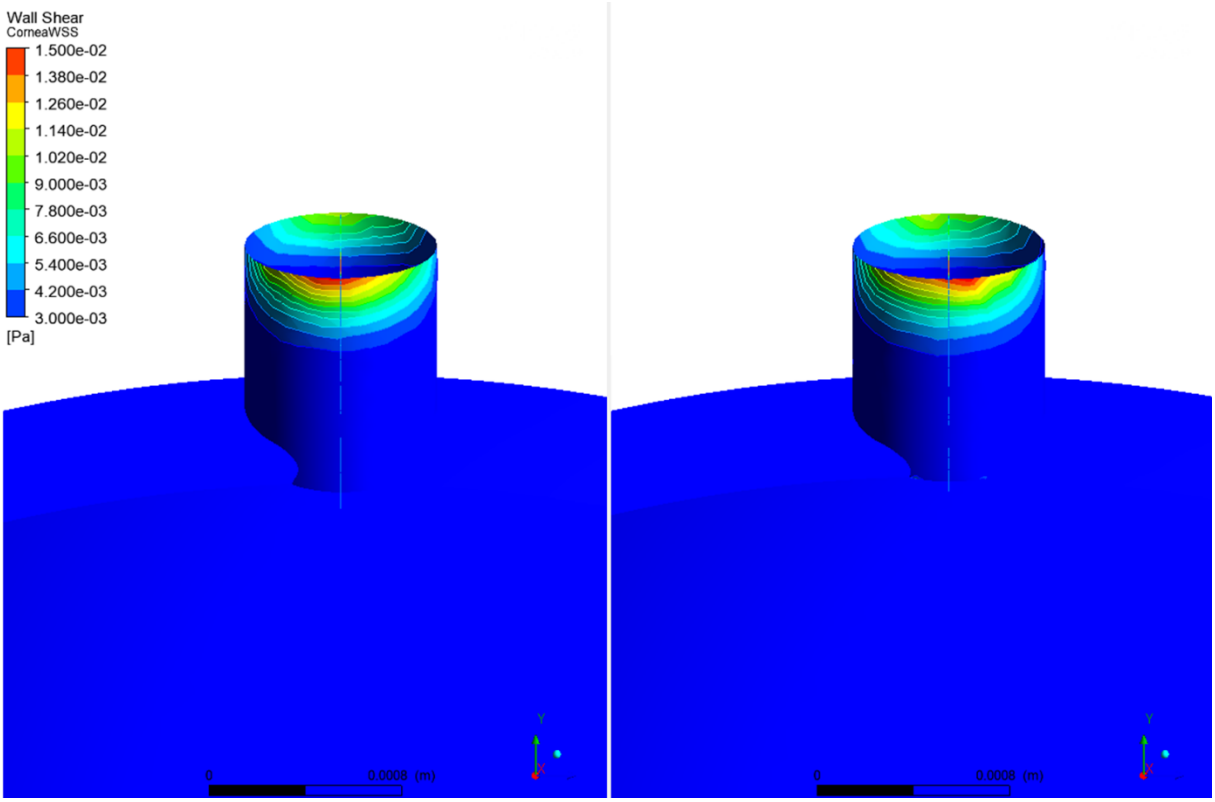


Figure 105 Comparison on WSS contours under supine trabeculectomy conditions for the OCT-reconstructed model (left) and the dimension-based model (right)

To further analyse the local flow field differences, a more detailed flow field is shown in Figure 106 for the supine conditions. The OCT-reconstructed model (left) shows a more irregular flow pattern near the iris wall (circled in red). Since the iris surface is not perfectly smooth, the flow can separate and reattach in a less consistent manner, causing local flow disturbances.

In contrast, the dimension-based model (right) has a smooth iris wall, resulting in a more streamlined flow with two swirls on either side of the iridectomy, unlike the OCT-reconstructed model, which only shows one swirl on the left side of the iridectomy. This is because the smoother geometry reduces tiny local friction effects that would otherwise dampen smaller vortices. In the OCT model, the irregular surface geometry of the iris could cause micro-disturbances, slightly disrupting these swirl formations.

However, these localized wall disturbances in the OCT-reconstructed model do not significantly affect the overall flow dynamics. The global flow field remains nearly identical between the two models, suggesting that the increased complexity of the OCT model primarily affects local flow characteristics without significantly altering the overall flow dynamics.

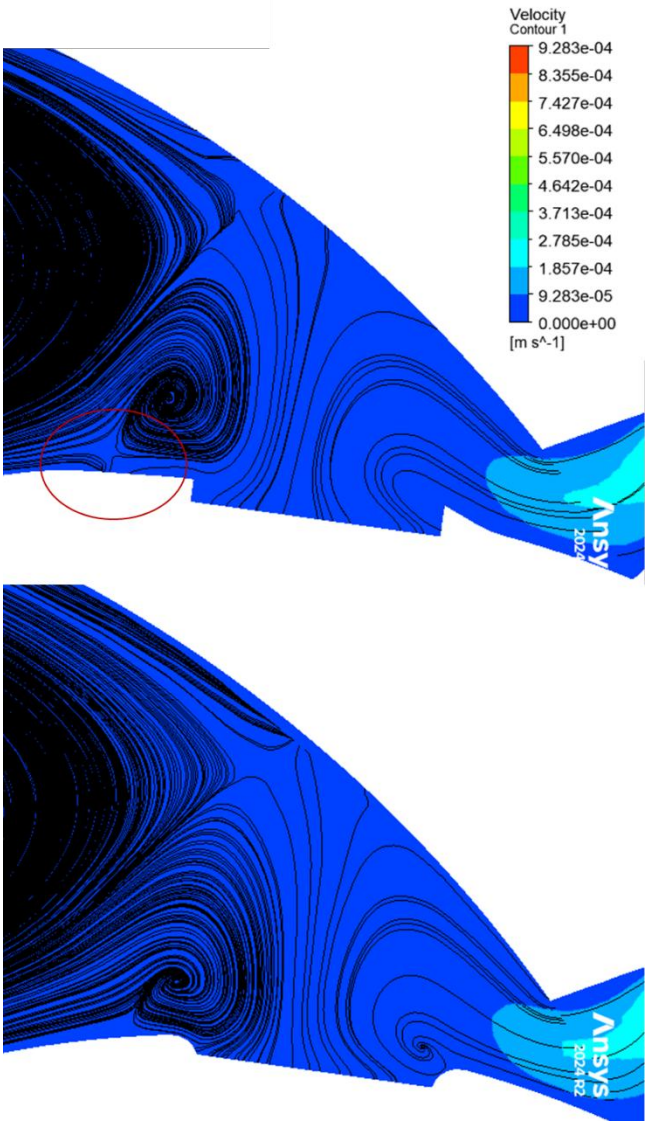


Figure 106 Comparison on velocity contours and streamlines under supine trabeculectomy conditions for the OCT-reconstructed model (top) and the dimension-based model (bottom)

Table 17 summarizes the central velocity results for all conditions and provides a basic error analysis as an overview of the main deviations between the OCT-reconstructed and dimension-based models.

Table 17 Error analysis of central rotational flow magnitudes based on maximum central velocity

Max central velocity [mm/s]	**OCT-reconstructed**	**Dimension-based**	**Error%**
Normal supine	0.26	0.28	7.1%
Normal upright	0.52	0.55	5.5%
Trabeculectomy supine	0.25	0.27	7.4%
Trabeculectomy upright	0.49	0.48	2.1%

Across all conditions, error margins remained under 7.5%, with the largest deviation being only 0.02 mm/s in absolute terms. These differences are within the expected computational tolerance and are unlikely to significantly influence surgical outcome predictions such as IOP reduction or outflow profile.

Furthermore, the oval shape of the OCT-reconstructed model removes the axisymmetric conditions displayed in the dimension-based model. Additionally, the introduction of the sclerostomy and the iridectomy in the trabeculectomy models further affect the overall symmetry of the models. Therefore, to further understand the impact of geometric asymmetry on flow distribution, the UI-values were calculated over the total outlet region for all models. The results are provided in Table 18.

Table 18 UI-values and error% results for all OCT-reconstructed and dimension-based models

	OCT-reconstructed	**Dimension-based**	**Error%**
Normal supine	0.78	0.77	1.9%
Normal upright	0.77	0.76	1.4%
Trabeculectomy supine	0.62	0.61	2.8%
Trabeculectomy upright	0.61	0.62	2.8%

As expected, the normal models have the highest UI-values, suggesting the most uniform outflow distribution. The trabeculectomy models show a decrease in UI-values due to the asymmetry introduced by the sclerostomy and iridectomy modifications. This is consistent with the results found in section 5.4.5.

The results show insignificant differences (<3%) in outflow distribution between the OCT-reconstructed and dimension-based models for every scenario. This suggests that the dimension-based model is accurate in terms of flow uniformity, despite the asymmetry introduced due to the oval-shape of the OCT-reconstructed model. Even though the OCT-reconstructed model has a more complex shape, it does not introduce significant variations in outflow distribution.

Overall, the findings in this section suggest that the computational effort required for OCT-reconstructed models may not be justified for studies focused on overall outflow characteristics. The dimension-based model offers a more practical alternative while maintaining similar accuracy.

6.3 Summary

This section investigates the potential differences between dimension-based models and OCT-reconstructed models that lends itself to more anatomical complexity. Specifically, the oblong eye shape and iris structure was considered for the OCT-reconstructed model.

The results show that there is no significant difference between the two models when simulating pre-surgical conditions. However, more noticeable disparities occur for post-surgical models that are no longer axisymmetric. These disparities are apparent regarding the rotational motion at the surgical site and the outlet velocity magnitude. While the post-surgical models are able to give a good indication of potential flow disturbances, as well as the increase or decrease in velocities at the surgical outlet, patient-specific OCT-reconstructed models may represent the prospective aqueous humour dynamic changes more meticulously.

Conversely, these OCT-reconstructed models are much more resource intensive to produce. Additionally, due to most of the current technology being unable to capture smaller detail in the eye, as well as the loss of detail that occurs during the model reconstruction process, even these more anatomically complex models may not fully represent the exact patient-specific structures. Moreover, a typical biometric scanner will not be able to capture details like the iris composition but will only be able to provide generic geometric details like those that have been studied in this thesis (i.e., WTW, ACA, ACD, etc.). Since it has been demonstrated that an idealised eye can give a good indication of the potential post-surgical changes in aqueous humour flow, it can be considered for further studies going forward.

7 Conclusion & Recommendations

7.1 Conclusions

The main objective of this study was to evaluate the immediate post-operative outcomes of different glaucoma filtration surgeries using CFD. Various 3D eye models were developed to simulate three types of surgeries: trabeculectomy, NPDS, and mNPDS. The resulting IOP values immediately after surgery (incisions open to atmosphere) and after suturing were provided. Additionally, changes in velocity patterns, vertices, and WSS was analysed and compared to qualitative clinical and experimental studies.

Initially, a single idealised model geometry was used. The correlation between simulation and clinical results underscores CFD's potential as a reliable tool for predicting surgical outcomes, offering a cost-effective and time-efficient method to assess the effectiveness of glaucoma procedures before conducting clinical trials. Thus, CFD can help improve our understanding of potential surgical outcomes by simulating their effect on aqueous humour flow dynamics.

This comparative study using CFD has yielded important insights into the immediate post-operative outcomes of trabeculectomy, NPDS, and mNPDS. The simulations effectively evaluated IOP and the rate of post-operative reduction for each surgery. Trabeculectomy and mNPDS were shown to be effective in achieving appropriate post-IOP levels, while NPDS was less successful. Although NPDS without the membrane peel is no longer standard practice, the decision to use it remains at the surgeon's discretion. This study emphasizes the success of the membrane peel in mNPDS, which is more commonly used today.

One key limitation of the idealised model is that it uses the same geometry for all cases, whereas clinical research involves diverse eye geometries. Differences in anterior chamber parameters among patients could lead to discrepancies between simulated results and actual clinical outcomes. Therefore, an attempt was made to represent European- and African-representative eyes based on available biometric data.

The African model consistently showed lower velocities in regions like the corneal wall, which could indicate a higher risk of nutrient deficiencies. This provides new knowledge on how average African eye geometry is contributing to higher failure rates of glaucoma surgical treatments. These differences are also indicative of the importance of considering ethnicity-specific anatomy when choosing surgical techniques, as procedures may not have uniform safety across populations.

In normal flow conditions, anatomical differences between the European and African models only modestly influence aqueous humour dynamics within the anterior chamber, since the system remains largely symmetric and governed by conventional outflow resistance. However, following trabeculectomy, the creation of a dominant new flow pathway via the iridectomy amplifies geometric

differences. This leads to greater differences in central and outlet flow velocities post-surgery, compared to normal physiological conditions. In the mNPDS models, flow performance shifts significantly between orientations due to the interplay between anatomical geometry and gravitational direction.

The distribution of aqueous humour flow in post-operative models is governed by a dynamic interaction between anatomical structure, surgical modification, and gravitational orientation. The ACD and ACA play critical roles in determining flow coherence and efficiency, but their effects are nonlinear and dependent on both the direction of gravity and the surgical pathway imposed. While trabeculectomy disrupts flow most dramatically and amplifies anatomical differences, mNPDS maintains a more physiological flow profile and is more adaptable across geometries and positions. These findings underscore the need for personalized surgical planning that accounts for patient anatomy, posture, and procedure-specific flow mechanics.

Overall, trabeculectomy consistently showed to be effective at decreasing IOP. However, its post-operative flow profile does not align with normal flow conditions. This suggests that trabeculectomy presents a higher risk of nutrient deficiencies and complications such as corneal decompensation or fibrosis due to altered flow dynamics. NPDS was the most ineffective solution for reducing IOP and showed to be the most sensitive to suturing tightness. Conversely, mNPDS more often demonstrated a post-operative flow profile that most closely aligned with normal flow conditions. This suggests that mNPDS may be more effective in maintaining a physiologically balanced aqueous humour flow while still effectively decreasing IOP. The unsutured conditions across all procedures produced significant irregularities, indicating the importance of proper suturing in restoring IOP.

Additionally, the clinical relevance of an OCT-reconstructed 3D anterior chamber model was compared to a generalized dimension-based model. Although the OCT-reconstructed model and the dimension-based model exhibit minor percentage differences in peak velocities, the absolute differences are minimal, and the overall flow characteristics remain consistent. This suggests that the increased complexity of generating OCT-based models may not justify the minor gains in accuracy, particularly for studies requiring multiple models. Dimension-based models, by contrast, offer a scalable, reproducible, and generalizable approach to aqueous humour flow simulation, allowing for the consistent application of average biometric parameters across populations. Given the strong agreement in flow patterns between the two approaches, the dimension-based model is recommended for large-scale comparative studies and surgical assessments.

While CFD is a powerful tool for guiding surgical decisions, it has inherent limitations compared to clinical studies. Biometric parameters are influenced by numerous factors, including measurement techniques and inter-individual variability. The confounding effects of these variables could skew the precision of the modelled geometries. Age is a particularly significant factor in ACD. Given that

glaucoma tends to occur earlier in African patients, their ACDs at the time of surgery may be higher than those of European patients, who typically undergo surgery later in life with a naturally shallower ACD. Additionally, the TM resistance parameters used in the model might not perfectly match clinical conditions, affecting the accuracy of the simulations. Corneal thickness was not considered, as the present CFD framework only resolves the aqueous humour flow domain and not the structural mechanics of surrounding tissues. Its influence could be assessed in future studies using a coupled fluid-structure interaction (FSI) approach.

Suturing tightness is another critical parameter that can introduce errors, as suture pressure is often not measured during surgery. Without precise measurements, the suture pressure in the simulations remains an estimate, adding uncertainty. However, the ability to adjust suture pressure during simulations allows for better control over aqueous outflow, enhancing the flexibility of the CFD model. These limitations highlight the importance of interpreting CFD results carefully and using clinical studies to validate and refine the models for a more accurate understanding of glaucoma surgeries.

Since the ethnic-representative models are based on statistical averages, the overall results regarding flow and vorticity are not particularly pronounced, even though clear differences can be observed. However, individual eye geometries do differ even more drastically than the geometries discussed in this thesis. Thus, more prominent differences may be observed. This is especially true when observing the drastic differences in parameters discussed in section 2.2. This indicates that a more patient-specific approach to glaucoma treatment may be necessary, rather than a broader ethnic-specific approach. However, a detailed patient specific model based on a full reconstruction from OCT scans may not be necessary. The results in chapter 6 shows that, while patient-specific OCT-reconstructed models provide a high level of anatomical detail, the marginal improvements in flow prediction do not outweigh the significant resource-intensiveness associated with their use. Dimension-based models, when derived from accurate biometry, offer a reliable alternative for evaluating aqueous humour dynamics and guiding surgical planning.

The key advantage of this CFD study is its ability to compare surgical outcomes without the variability introduced by individual patient differences. The models successfully replicated results similar to those expected in clinical procedures, demonstrating CFD's potential as a virtual tool for evaluating and comparing glaucoma surgeries. CFD models could serve as "digital twins" with greater clinical relevance by incorporating patient-specific or demographically representative geometries. Additionally, combining CFD with finite element analysis could improve the understanding of corneal biomechanics and the effects of post-operative scarring, leading to more accurate simulations. Despite its limitations, this study highlights CFD's potential as a preliminary tool for assessing glaucoma surgery outcomes, warranting further exploration through collaboration with clinical trials and continued refinement of the model.

In conclusion, this study makes the following novel contributions:

1. This is the first study to simulate and compare glaucoma surgical treatments using CFD.
2. This is the first study to construct and compare across different ethnic-representative anterior chamber models based on available biometric data.
3. This is the first study to attempt a comparative CFD aqueous humour flow analysis based on ethnic biometry data.

This detailed CFD-based flow analysis enhances our understanding of how different surgical interventions influence aqueous humour dynamics. The results provide a basis for optimizing surgical techniques to balance effective IOP reduction with minimizing risks such as hypotony, fibrosis, and nutrient deprivation, ultimately improving patient outcomes.

7.2 Recommendations for Future Research

The following recommendations for future work are made based on the limitations discussed and the additional parameters to be investigated that will further contribute to this work.

Future studies should include simulations based on glaucoma severity (low, moderate, and high pre-surgical IOP to evaluate how the disease stage impacts post-operative flow dynamics. Glaucoma severity is closely linked to IOP, with more advanced disease stages typically presenting with higher IOPs [174]. The current study assumes a uniform pre-operative IOP and anatomical baseline across all models. However, simulating different glaucoma severities would allow for a more nuanced evaluation of how disease progression influences the effectiveness of surgical procedures.

The current study also evaluated anatomical differences in the context of representative European and African eye geometries. While this offers insight into population-level trends, the interplay between multiple geometric parameters makes it difficult to isolate the effect of each individual feature on fluid dynamics. A systematic parametric study would allow for the independent varying of key anterior chamber parameters, such as ACD, ACA, and TML, while keeping all other variables constant.

While this study focuses on trabeculectomy, NPDS, and mNPDS, many glaucoma treatment options exist, including minimally invasive glaucoma surgeries, Ahmed and Baerveldt shunts, and Xen implants, similar to the study described in section 4.4 [148]. Each of these introduces different pathways for aqueous humour drainage, which also differ in the location of aqueous drainage, drainage control mechanisms (valved vs. non-valved), and surgical trauma, and could be included in future simulations. Such extensions would not only improve pre-surgical planning but could inform device manufacturers, surgeons, and regulators on the biomechanical implications of novel glaucoma therapies.

Furthermore, the current study treats the anterior chamber and its walls (including the cornea and trabecular meshwork) as rigid structures, which is a reasonable assumption for early-stage CFD analysis. However, in reality, ocular tissues are viscoelastic and deform under fluctuating IOP and

surgical modifications. By incorporating FSI models in the future to simulate the coupled interaction between fluid dynamics and tissue mechanics, the coupled behaviour between aqueous humour flow dynamics and tissue mechanics can be studied, similar to some hemodynamic studies [175,176]. A preliminary FSI study conducted by a student [177] indicated that wall compliance becomes significant primarily under high IOP conditions, particularly in the context of GDD's and endothelial shear stress. Since filtration surgeries markedly lower IOP in the early post-operative period, the rigid-wall CFD approach adopted here remains appropriate, though future extensions incorporating FSI could provide further insights.

While CFD provides powerful insights into post-surgical flow behaviour under controlled and isolated conditions, experimental validation remains crucial for verifying and improving model realism. Further developing experimental setups that include transparent physical eye models with varied geometries to replicate individual anatomical features, like those discussed in section 4.3.2 [127,128], would offer a complementary platform to cross-validate simulation results.

The current study successfully highlights how anatomical differences between European- and African-representative eyes can affect aqueous humour flow patterns and surgical outcomes. However, these two groups represent only part of the global population. Many other ethnic and demographic groups exhibit distinct biometric profiles that could influence glaucoma pathophysiology and post-operative dynamics in different ways. For example, existing literature already indicates that East Asians, for instance, have a higher prevalence of PACG and tend to have shallower anterior chambers and narrower angles than other populations [178–180]. Including a broader range of ethnic and demographic groups in biometry studies would help generalize findings across diverse populations.

Based on the data acquired in section 5.1, future models should stratify patients based on age groups to account for the natural progression of ACD changes over time and their impact on surgical outcomes. Such an extension would provide a more accurate representation of post-surgical flow behaviour, account for natural biometric evolution such as ACD shallowing, and improve the predictive clinical relevance of glaucoma surgical planning across diverse patient populations.

Finally, it is common for glaucoma patients, especially older adults, to undergo cataract surgery either before, alongside, or after glaucoma surgery, which can significantly alter anterior segment anatomy [69,181]. Future CFD studies should incorporate cataract-induced changes to anterior chamber anatomy to more comprehensively model aqueous humour dynamics following combined surgical interventions. Accounting for lens removal and structural remodelling would enhance the clinical relevance of simulations, improve risk prediction for combined procedures, and support personalized surgical decision-making in glaucoma management.

8 References

[1] Vision and eye health. Eye Anatomy and How the Eye Works. Vision and Eye Health n.d. http://www.vision-and-eye-health.com/eye-anatomy.html (accessed August 11, 2020).

[2] Aqueous Humor - an overview n.d. https://www.sciencedirect.com/topics/medicine-and-dentistry/aqueous-humor (accessed July 16, 2020).

[3] Ento Key. Production and Flow of Aqueous Humor n.d. https://entokey.com/production-and-flow-of-aqueous-humor/ (accessed August 11, 2020).

[4] Nolan W, Yip J. Glaucoma in the World n.d.

[5] Anderson DR. Collaborative normal tension glaucoma study. Curr Opin Ophthalmol 2003;14:86–90. https://doi.org/10.1097/00055735-200304000-00006.

[6] Leske MC, Heijl A, Hyman L, Bengtsson B. Early Manifest Glaucoma Trial: design and baseline data. Ophthalmology 1999;106:2144–53. https://doi.org/10.1016/S0161-6420(99)90497-9.

[7] Musch DC, Lichter PR, Guire KE, Standardi CL. The Collaborative Initial Glaucoma Treatment Study: study design, methods, and baseline characteristics of enrolled patients. Ophthalmology 1999;106:653–62. https://doi.org/10.1016/S0161-6420(99)90147-1.

[8] Kass MA, Heuer DK, Higginbotham EJ, Johnson CA, Keltner JL, Philip Miller J, et al. The Ocular Hypertension Treatment Study: a randomized trial determines that topical ocular hypotensive medication delays or prevents the onset of primary open-angle glaucoma. Arch Ophthalmol 2002;120:701–13. https://doi.org/10.1001/ARCHOPHT.120.6.701.

[9] Esporcatte BLB, Tavares IM. Normal-tension glaucoma: an update. Arq Bras Oftalmol 2016;79:270–6. https://doi.org/10.5935/0004-2749.20160077.

[10] Primary Open-Angle Glaucoma - EyeWiki n.d. https://eyewiki.aao.org/Primary_Open-Angle_Glaucoma (accessed August 1, 2024).

[11] Glaucoma Research Foundation. Are You at Risk For Glaucoma? Glaucoma Research Foundation 2019. https://www.glaucoma.org/glaucoma/are-you-at-risk-for-glaucoma.php (accessed August 12, 2020).

[12] Katz J, Friedman DS. African Americans and Glaucoma. Glaucoma Research Foundation 2017. https://www.glaucoma.org/glaucoma/african-americans-and-glaucoma.php (accessed August 12, 2020).

[13] Bagus T, Alberto K, Muteba M, Makgotloe A. Analysis of corneal biometry in a black South African population. African Vision and Eye Health 2019;78. https://doi.org/10.4102/aveh.v78i1.495.

[14] Hui MM, Clement CI. Evaluation of the early to mid-term efficacy and safety of deep sclerectomy without an intrascleral spacer for open-angle glaucoma in an Australian population. J Curr Glaucoma Pract 2018;12:107–12. https://doi.org/10.5005/jp-journals-10078-1233.

[15] Wei X, Cho KS, Thee EF, Jager MJ, Chen DF. Neuroinflammation and microglia in glaucoma: time for a paradigm shift. J Neurosci Res 2019;97:70–6. https://doi.org/10.1002/jnr.24256.

[16] Huang AS, Camp A, Xu BY, Penteado RC, Weinreb RN. Aqueous Angiography: Aqueous Humor Outflow Imaging in Live Human Subjects. Ophthalmology 2017;124:1249–51. https://doi.org/10.1016/j.ophtha.2017.03.058.

[17] Cairns JE. Trabeculectomy. Preliminary report of a new method. Am J Ophthalmol 1968;66:673–9. https://doi.org/10.1016/0002-9394(68)91288-9.

[18] In Defense of Trabeculectomy n.d. https://www.reviewofophthalmology.com/article/in-defense-of-trabeculectomy (accessed August 1, 2024).

[19] Landers J, Martin K, Sarkies N, Bourne R, Watson P. A twenty-year follow-up study of trabeculectomy: Risk factors and outcomes. Ophthalmology 2012;119:694–702. https://doi.org/10.1016/j.ophtha.2011.09.043.

[20] S.A. Gandolfi; L. Quaranta; N. Ungaro; L. Cimino; C. Sangermani; M. Tardini; S. Bettelli. Deep Sclerectomy vs Trabeculectomy in Open Angle Glaucoma. 7–Year Prospective Randomised Clinical Trial. Invest Ophthalmol Vis Sci 2005;46:1217.

[21] Eldaly MA, Bunce C, ElSheikha OZ WR. Comparison of two surgical techniques for the control of eye pressure in people with glaucoma. Cochrane 2014. https://www.cochrane.org/CD007059/EYES_comparison-of-two-surgical-techniques-for-the-control-of-eye-pressure-in-people-with-glaucoma (accessed August 11, 2020).

[22] Rulli E, Biagioli E, Riva I, Gambirasio G, De Simone I, Floriani I, et al. Efficacy and safety of trabeculectomy vs nonpenetrating surgical procedures: A systematic review and meta-analysis. JAMA Ophthalmol 2013;131:1573–82. https://doi.org/10.1001/jamaophthalmol.2013.5059.

[23] Elewa L, Hamid M. Deep sclerectomy versus subscleral trabeculectomy in glaucomatous eyes with advanced visual field loss. Journal of the Egyptian Ophthalmological Society 2014;107:277. https://doi.org/10.4103/2090-0686.150690.

[24] Sheheitli H, Tirpack AR, Parrish RK. Which patients would most likely to benefit: MIGs or MeGs, which one is it? Asia-Pacific Journal of Ophthalmology 2019;8:436–40. https://doi.org/10.1097/APO.0000000000000260.

[25] Elhofi A, Helaly HA. Non-penetrating deep sclerectomy versus trabeculectomy in primary congenital glaucoma. Clinical Ophthalmology 2020;14:1277–85. https://doi.org/10.2147/OPTH.S253689.

[26] Bouillot A, Pierru A, Blumen-Ohana E, Brasnu E, Baudouin C, Labbé A. Changes in choroidal thickness and optic nerve head morphology after filtering surgery: nonpenetrating deep sclerectomy versus trabeculectomy. BMC Ophthalmol 2019;19. https://doi.org/10.1186/s12886-019-1031-3.

[27] Sharifipour F, Yazdani S, Asadi M, Saki A, Nouri-Mahdavi K. Modified deep sclerectomy for the surgical treatment of glaucoma. J Ophthalmic Vis Res 2019;14:144–50. https://doi.org/10.4103/jovr.jovr_228_17.

[28] Suominen SMA, Harju MP, Vesti ET. Deep sclerectomy in primary open-angle glaucoma and exfoliative glaucoma. Eur J Ophthalmol 2016;26:568–74. https://doi.org/10.5301/EJO.5000762.

[29] Elhofi A, Helaly HA. Non-penetrating deep sclerectomy versus trabeculectomy in primary congenital glaucoma. Clinical Ophthalmology 2020;14:1277–85. https://doi.org/10.2147/OPTH.S253689.

[30] Mokbel TH, Ghanem AA, Moawad AI, Nafie EM, Nematallah EH. Comparative study of phacoemulsification-subscleral trabeculectomy versus phacoemulsification-deep sclerectomy. Saudi Journal of Ophthalmology 2009;23:189–96. https://doi.org/10.1016/j.sjopt.2009.10.008.

[31] Cillino S, Di Pace F, Casuccio A, Calvaruso L, Morreale D, Vadalà M, et al. Deep sclerectomy versus punch trabeculectomy with or without phacoemulsification: A randomized clinical trial. J Glaucoma 2004;13:500–6. https://doi.org/10.1097/01.ijg.0000137869.18156.81.

[32] Jiang N, Zhao GQ, Lin J, Hu LT, Che CY, Wang Q, et al. Meta-analysis of the efficacy and safety of combined surgery in the management of eyes with coexisting cataract and open angle glaucoma. Int J Ophthalmol 2018;11:279–86. https://doi.org/10.18240/ijo.2018.02.17.

[33] Khairy HA, Green FD, Nassar MK, Azuara-Blanco A. Control of intraocular pressure after deep sclerectomy. Eye 2006;20:336–40. https://doi.org/10.1038/sj.eye.6701878.

[34] Wadhwa SD, Higginbotham EJ. Ethnic differences in glaucoma: prevalence, management, and outcome. Curr Opin Ophthalmol 2005;16:101–6. https://doi.org/10.1097/01.icu.0000156137.28193.48.

[35] van Setten GB. Survival of the best? – Why some surgical techniques such as deep sclerectomy 'fail.' Acta Ophthalmol 2020:1–2. https://doi.org/10.1111/aos.14383.

[36] Okonkwo ON, Tripathy K. Ocular Hypotony. Journal of Knowledge Globalization 2023;1:43–59.

[37] Muñoz-Negrete FJ, Arnalich-Montiel F, Casado A, Rebolleda G. Nonpenetrating deep sclerectomy for glaucoma after Descemet stripping automated endothelial keratoplasty: Three consecutive case reports. Medicine (United States) 2015;94:e543. https://doi.org/10.1097/MD.0000000000000543.

[38] Abdelrahman AM, Eltanamly R, Sabry M. Sutureless Deep Sclerectomy: A Preliminary Report. J Glaucoma 2017;26:e255–6. https://doi.org/10.1097/IJG.0000000000000778.

[39] Samsudin A, Eames I, Brocchini S, Khaw PT. The Influence of Scleral Flap Thickness, Shape, and Sutures on Intraocular Pressure (IOP) and Aqueous Humor Flow Direction in a Trabeculectomy Model. J Glaucoma 2016;25:e704–12. https://doi.org/10.1097/IJG.0000000000000360.

[40] Hau S, Barton K. Corneal complications of glaucoma surgery. Curr Opin Ophthalmol 2009;20:131–6. https://doi.org/10.1097/ICU.0b013e328325a54b.

[41] Trabeculectomy - EyeWiki n.d. https://eyewiki.org/Trabeculectomy (accessed November 27, 2024).

[42] Vijaya L, Manish P, Ronnie G, Shantha B. Management of complications in glaucoma surgery. Indian J Ophthalmol 2011;59:S131. https://doi.org/10.4103/0301-4738.73689.

[43] Diagnosis and Management of Malignant Glaucoma - American Academy of Ophthalmology n.d. https://www.aao.org/eyenet/article/diagnosis-management-of-malignant-glaucoma (accessed November 7, 2024).

[44] Krix-Jachym K, Zarnowski T, Rękas M. Risk Factors of Malignant Glaucoma Occurrence after Glaucoma Surgery. J Ophthalmol 2017;2017:9616738. https://doi.org/10.1155/2017/9616738.

[45] Goel M. Aqueous Humor Dynamics: A Review. Open Ophthalmol J 2010;4:52–9. https://doi.org/10.2174/1874364101004010052.

[46] Fitt AD, Gonzalez G. Fluid mechanics of the human eye: Aqueous humour flow in the anterior chamber. Bull Math Biol 2006;68:53–71. https://doi.org/10.1007/s11538-005-9015-2.

[47] Zhang F, Chen H, Huang Y. Computer modeling of drug delivery in the anterior human eye after subconjunctival and episcleral implantation. Comput Biol Med 2017;89:162–9. https://doi.org/10.1016/j.compbiomed.2017.07.016.

[48] Murgoitio-Esandi J, Xu BY, Song BJ, Zhou Q, Oberai AA. A Mechanistic Model of Aqueous Humor Flow to Study Effects of Angle Closure on Intraocular Pressure. Transl Vis Sci Technol 2023;12. https://doi.org/10.1167/tvst.12.1.16.

[49] Naghipoor J, Jafary N, Rabczuk T. Mathematical and computational modeling of drug release from an ocular iontophoretic drug delivery device. Int J Heat Mass Transf 2018;123:1035–49. https://doi.org/10.1016/j.ijheatmasstransfer.2018.03.021.

[50] Fernández-Vigo JI, Macarro-Merino A, Fernández-Francos J, De-Pablo-Gómez-de-Liaño L, Martínez-de-la-Casa JM, García-Feijóo J, et al. Computational study of aqueous humor dynamics assessing the vault and the pupil diameter in two posterior-chamber phakic lenses. Invest Ophthalmol Vis Sci 2016;57:4625–31. https://doi.org/10.1167/iovs.16-19900.

[51] Izadi T. Computational Modeling of Fluid Flow and Intraocular Pressure following Glaucoma Surgery. Bina Journal of Ophthalmology 2014;20:46–60.

[52] Abu Bakar N, Mydin RBSMN, Yusop N, Matmin J, Ghazalli NF. Understanding the ideal wound healing mechanistic behavior using in silico modelling perspectives: A review. J Tissue Viability 2024;33:104–15. https://doi.org/10.1016/J.JTV.2023.11.001.

[53] Lusthaus JA. Imaging of aqueous outflow in health and glaucoma. Justifying the re-direction of aqueous. Eye 2024 2024:1–7. https://doi.org/10.1038/s41433-024-02968-8.

[54] Toris CB, Gagrani M, Ghate D. Current methods and new approaches to assess aqueous humor dynamics. Expert Rev Ophthalmol 2021;16:139–60. https://doi.org/10.1080/17469899.2021.1902308.

[55] Gupta D, Moore D, Bojikian K, Slabaugh M. Relationship between eye shape and the risk for glaucoma. Invest Ophthalmol Vis Sci 2013;54:3524–3524.

[56] Kuzin AA, Varma R, Reddy HS, Torres M, Azen SP. Ocular Biometry and Open Angle Glaucoma: The Los Angeles Latino Eye Study. Ophthalmology 2010;117:1713. https://doi.org/10.1016/J.OPHTHA.2010.01.035.

[57] Taubenslag KJ, Kammer JA. Outcomes Disparities between Black and White Populations in the Surgical Management of Glaucoma. Semin Ophthalmol 2016;31:385–93. https://doi.org/10.3109/08820538.2016.1154163.

[58] Mamidipaka A, Shi A, Addis V, He J, Lee R, Di Rosa I, et al. Outcomes of Trabeculectomy and Predictors of Success in Patients of African Ancestry with Primary Open Angle Glaucoma. J Glaucoma 2024. https://doi.org/10.1097/IJG.0000000000002503.

[59] Julia Salinas RS, Aishat Mohammed NHF, Warren JZ. Primary Open-Angle Glaucoma in Individuals of African Descent: A Review of Risk Factors. J Clin Exp Ophthalmol 2015;06. https://doi.org/10.4172/2155-9570.1000450.

[60] Restrepo NA, Cooke Bailey JN. Primary Open-Angle Glaucoma Genetics in African Americans. Curr Genet Med Rep 2017;5:167–74. https://doi.org/10.1007/s40142-017-0131-8.

[61] Verma SS, Gudiseva H V., Chavali VRM, Salowe RJ, Bradford Y, Guare L, et al. A multi-cohort genome-wide association study in African ancestry individuals reveals risk loci for primary open-angle glaucoma. Cell 2024;187:464-480.e10. https://doi.org/10.1016/J.CELL.2023.12.006.

[62] Williams SEI, Carmichael TR, Allingham RR, Hauser M, Ramsay M. The genetics of POAG in black South Africans: A candidate gene association study. Sci Rep 2015;5:8378. https://doi.org/10.1038/srep08378.

[63] Bonnemaijer PWM, Cook C, Nag A, Hammond CJ, Van Duijn CM, Lemij HG, et al. Genetic African ancestry is associated with central corneal thickness and intraocular pressure in primary open-angle glaucoma. Invest Ophthalmol Vis Sci 2017;58:3172–80. https://doi.org/10.1167/iovs.17-21716.

[64] Bonnemaijer PWM, Lo Faro V, Sanyiwa AJ, Hassan HG, Cook C, Van de Laar S, et al. Differences in clinical presentation of primary open-angle glaucoma between African and European populations. Acta Ophthalmol 2021;99:e1118. https://doi.org/10.1111/AOS.14772.

[65] Girkin CA, McGwin G, McNeal SF, DeLeon-Ortega J. Racial differences in the association between optic disc topography and early glaucoma. Invest Ophthalmol Vis Sci 2003;44:3382–7. https://doi.org/10.1167/iovs.02-0792.

[66] Chen RI, Barbosa DT, Hsu CH, Porco TC, Lin SC. Ethnic differences in trabecular meshwork height by optical coherence tomography. JAMA Ophthalmol 2015;133:437–41. https://doi.org/10.1001/jamaophthalmol.2014.5864.

[67] Liu L. Anatomical Changes of the Anterior Chamber Angle With Anterior-Segment Optical Coherence Tomography. Archives of Ophthalmology 2008;126:1682–6. https://doi.org/10.1001/ARCHOPHT.126.12.1682.

[68] Wang Y, Guo Y, Zhang Y, Huang S, Zhong Y. Differences and Similarities Between Primary Open Angle Glaucoma and Primary Angle-Closure Glaucoma. Eye Brain 2024;16:39–54. https://doi.org/10.2147/EB.S472920.

[69] Kouroupaki AI, Triantafyllopoulos GI, Pateras E, Karabatsas CH, Plakitsi A. Anterior Segment Changes in Patients With Glaucoma Following Cataract Surgery. Cureus 2024;16. https://doi.org/10.7759/CUREUS.58703.

[70] Nagar AM, Maghsoudlou P, Wormald R, Barton K, Hysi P, Lim KS. Differences in the Surgical Outcomes of Glaucoma Surgery in Patients of African Caribbean Descent. Curr Eye Res 2022;47:1567–77. https://doi.org/10.1080/02713683.2022.2126859.

[71] Cheng JW, Cheng SW, Cai JP, Li Y, Wei RL. Systematic overview of the efficacy of non penetrating glaucoma surgery in the treatment of open angle glaucoma. Medical Science Monitor 2011;17:RA155. https://doi.org/10.12659/MSM.881840.

[72] Klemm M. Tiefe Sklerektomie: Eine Alternative zur Trabekulektomie. Ophthalmologe 2015;112:313–8. https://doi.org/10.1007/s00347-014-3161-6.

[73] Correia Barbosa R, Gonçalves R, Bastos R, Alves Pereira S, Basto R, Viana AR, et al. Trabeculectomy Vs Non‐penetrating Deep Sclerectomy for the Surgical Treatment of Open-Angle Glaucoma: A Long-Term Report of 201 Eyes. Clinical Ophthalmology 2023;17:1619–27. https://doi.org/10.2147/OPTH.S405837.

[74] Correia Barbosa R, Gonçalves R, Bastos R, Alves Pereira S, Basto R, Viana AR, et al. Trabeculectomy Vs Non-penetrating Deep Sclerectomy for the Surgical Treatment of Open-Angle Glaucoma: A Long-Term Report of 201 Eyes. Clin Ophthalmol 2023;17:1619. https://doi.org/10.2147/OPTH.S405837.

[75] Chiselita D. Non-penetrating deep sclerectomy versus trabeculectomy in primary open-angle glaucoma surgery. Eye 2001;15:197–201. https://doi.org/10.1038/EYE.2001.60,.

[76] Kozobolis V, Panos GD, Konstantinidis A, Teus M, Labiris G. Modified deep sclerectomy combined with Ex-PRESS filtration device versus trabeculectomy for primary open angle glaucoma. Int J Ophthalmol 2017;10:728–32. https://doi.org/10.18240/ijo.2017.05.11.

[77] Gabai A, Cimarosti R, Battistella C, Isola M, Lanzetta P. Efficacy and Safety of Trabeculectomy Versus Nonpenetrating Surgeries in Open-Angle Glaucoma: A Meta-Analysis. J Glaucoma 2019;28:823–33. https://doi.org/10.1097/IJG.0000000000001323.

[78] Kitsos G, Aspiotis M, Alamanos Y, Psilas K. A modified deep sclerectomy with or without external trabeculectomy: A comparative study. Clinical Ophthalmology 2010;4:557–64. https://doi.org/10.2147/opth.s10350.

[79] Walkden A, Mercieca K, Perumal D, Anand N. Primary glaucoma surgery in Fuchs' heterochromic uveitis: a comparison of trabeculectomy versus deep sclerectomy. Ther Adv Ophthalmol 2019;11:251584141986976. https://doi.org/10.1177/2515841419869761.

[80] Elhofi A, Helaly HA. Non-penetrating deep sclerectomy versus trabeculectomy in primary congenital glaucoma. Clinical Ophthalmology 2020;14:1277–85. https://doi.org/10.2147/OPTH.S253689.

[81] Sangtam T, Roy S, Mermoud A. Outcome and complications of combined modified deep sclerectomy and trabeculectomy for surgical management of glaucoma: A pilot study. Clinical Ophthalmology 2020;14:795–803. https://doi.org/10.2147/OPTH.S244945.

[82] Sousa DC, Pinto LA. Trabeculectomy – Prevention and Management of Complications. European Ophthalmic Review 2018;12:98. https://doi.org/10.17925/EOR.2018.12.2.98.

[83] Birchall W, Wells AP. The effect of scleral flap edge apposition on intraocular pressure control in experimental trabeculectomy. Clin Exp Ophthalmol 2008;36:353–7. https://doi.org/10.1111/j.1442-9071.2008.001738.x.

[84] Kotliar KE, Kozlova T V., Lanzl IM. Postoperative aqueous outflow in the human eye after glaucoma filtration surgery: Biofluidmechanical considerations. Biomedizinische Technik 2009;54:14–22. https://doi.org/10.1515/BMT.2009.003.

[85] Birchall W, Bedggood A, Wells AP. Do scleral flap dimensions influence reliability of intraocular pressure control in experimental trabeculectomy? Eye 2007;21:402–7. https://doi.org/10.1038/SJ.EYE.6702253;KWRD=MEDICINE.

[86] Dhingra S, Eames I, Nicolle A, Taban V, Brocchini S, Khaw PT. The Effect Of Scleral Flap Shape And Size On Aqueous Flow And Pressure Following Trabeculectomy: Implications From Mathematical And Physical Modelling. Invest Ophthalmol Vis Sci 2011;52:651.

[87] Tse KM, Lee HP, Shabana N, Loon SC, Watson PG, Thean SYLH. Do shapes and dimensions of scleral flap and sclerostomy influence aqueous outflow in trabeculectomy? A finite element simulation approach. British Journal of Ophthalmology 2012;96:432–7. https://doi.org/10.1136/bjophthalmol-2011-300228.

[88] Rowlands MA, Maharaj ASR. A Review of Scleral Flap Shape on Trabeculectomy Outcomes. Vision Pan-America 2016;15:70–4. https://doi.org/10.15234/vpa.v15i3.345.

[89] Downes SM, Misson GP, Jones HJ, O'neill EC. The predictive value of post-operative intraocular pressures following trabeculectomy. Eye 1994 8:4 1994;8:394–7. https://doi.org/10.1038/eye.1994.93.

[90] Sukhija J, Jain AK. Early vs late intraocular pressure following trabeculectomy with releasable suture in advanced glaucoma. Ann Ophthalmol 2006;38:127–30. https://doi.org/10.1385/AO:38:2:127/METRICS.

[91] Sears ML, Sarrafpour S, Teng CC. Aqueous Humor and the Dynamics of Its Flow: Formation of Aqueous Humor. Albert and Jakobiec's Principles and Practice of Ophthalmology 2020:1–35. https://doi.org/10.1007/978-3-319-90495-5_184-1.

[92] Roy TK, Secomb TW. Effects of impaired microvascular flow regulation on metabolism-perfusion matching and organ function. Microcirculation 2021;28:e12673. https://doi.org/10.1111/MICC.12673.

[93] Matienzo D, Bordoni B. Anatomy, Blood Flow. StatPearls 2023.

[94] Rivers RJ, Meininger CJ. The Tissue Response to Hypoxia: How Therapeutic Carbon Dioxide Moves the Response toward Homeostasis and Away from Instability. International Journal of Molecular Sciences 2023, Vol 24, Page 5181 2023;24:5181. https://doi.org/10.3390/IJMS24065181.

[95] Coroneo MT, Graterol-Nisi G, Maver E, Gillies RM. Aqueous Humor Circulation in the Era of Minimally Invasive Surgery for Glaucoma. Ann Biomed Eng 2023:1–10. https://doi.org/10.1007/S10439-023-03427-3/TABLES/2.

[96] Bansal A, Amin H, Rekha R. Correlation of aqueous humor electrolytes with serum electrolytes in cataract patients. Indian J Ophthalmol 2021;69:2675. https://doi.org/10.4103/IJO.IJO_20_21.

[97] Micun Z, Falkowska M, Młynarczyk M, Kochanowicz J, Socha K, Konopińska J. Levels of Trace Elements in the Lens, Aqueous Humour, and Plasma of Cataractous Patients—A Narrative Review. Int J Environ Res Public Health 2022;19:10376. https://doi.org/10.3390/IJERPH191610376.

[98] Mercieca K, Perumal D, Darcy K, Anand N. Cataract extraction after deep sclerectomy and its effect on intraocular pressure control. Eye 2018;33:557. https://doi.org/10.1038/S41433-018-0262-5.

[99] Dwivedi R, Somerville T, Cheeseman R, Rogers C, Batterbury M, Choudhary A. Deep sclerectomy and trabeculectomy augmented with Mitomycin C: 2-year post-operative outcomes. Graefe's Archive for Clinical and Experimental Ophthalmology 2021;259:1965. https://doi.org/10.1007/S00417-021-05144-W.

[100] Schlunck G, Meyer-ter-Vehn T, Klink T, Grehn F. Conjunctival fibrosis following filtering glaucoma surgery. Exp Eye Res 2016;142:76–82. https://doi.org/10.1016/J.EXER.2015.03.021.

[101] Battista NA, Douglas DR, Lane AN, Samsa LA, Liu J, Miller LA. Vortex Dynamics in Trabeculated Embryonic Ventricles. J Cardiovasc Dev Dis 2019;6:6. https://doi.org/10.3390/JCDD6010006.

[102] Wiedenmann CJ, Gottwald C, Zeqiri K, Frömmichen J, Bungert E, Gläser M, et al. Slow Interstitial Fluid Flow Activates TGF-β Signaling and Drives Fibrotic Responses in Human Tenon Fibroblasts. Cells 2023;12:2205. https://doi.org/10.3390/CELLS12172205/S1.

[103] Pedersen JA, Lichter S, Swartz MA. Cells in 3D matrices under interstitial flow: Effects of extracellular matrix alignment on cell shear stress and drag forces. J Biomech 2010;43:900–5. https://doi.org/10.1016/J.JBIOMECH.2009.11.007.

[104] Siggers JH, Ethier CR. Fluid Mechanics of the Eye. Annu Rev Fluid Mech 2012;44:347–72. https://doi.org/10.1146/annurev-fluid-120710-101058.

[105] Colombo M, Bologna M, Garbey M, Berceli S, He Y, Rodriguez Matas JF, et al. Computing patient-specific hemodynamics in stented femoral artery models obtained from computed tomography using a validated 3D reconstruction method. Med Eng Phys 2020;75:23–35. https://doi.org/10.1016/j.medengphy.2019.10.005.

[106] Collection SE. Computational Fluid Dynamics Simulations of Blood Flow 2018:2–5.

[107] Xu L, Zhao B, Liu X, Liang F. Computational methods applied to analyze the hemodynamic effects of flow-diverter devices in the treatment of cerebral aneurysms: Current status and future directions. Med Nov Technol Devices 2019;3:100018. https://doi.org/10.1016/j.medntd.2019.100018.

[108] Ngoepe MN, Ventikos Y. Computational modelling of clot development in patient-specific cerebral aneurysm cases. Journal of Thrombosis and Haemostasis 2016;14:262–72. https://doi.org/10.1111/jth.13220.

[109] Abouali O, Modareszadeh A, Ghaffarieh A, Tu J. Investigation of saccadic eye movement effects on the fluid dynamic in the anterior chamber. J Biomech Eng 2012;134. https://doi.org/10.1115/1.4005762.

[110] Chen H, Zhang F, Huang Y, Wu J. Numerical investigation of topical drug transport in the anterior human eye. Int J Heat Mass Transf 2015;85:356–66. https://doi.org/10.1016/j.ijheatmasstransfer.2015.01.142.

[111] Modarreszadeh SA, Abouali O, Ghaffarieh A, Ahmadi G. Physiology of aqueous humor dynamic in the anterior chamber due to rapid eye movement. Physiol Behav 2014;135:112–8. https://doi.org/10.1016/j.physbeh.2014.05.017.

[112] Dzierka M, Jurczak P. Review of applied mathematical models for describing the behaviour of aqueous humor in eye structures. International Journal of Applied Mechanics and Engineering 2015;20:757–72. https://doi.org/10.1515/ijame-2015-0049.

[113] Abu-Hassan DW, Acott TS, Kelley MJ. The Trabecular Meshwork: A Basic Review of Form and Function. J Ocul Biol 2014;2. https://doi.org/10.13188/2334-2838.1000017.

[114] Martínez Sánchez GJ, Escobar del Pozo C, Rocha Medina JA. Numerical model of aqueous humor drainage: effects of collector channel position. Med Eng Phys 2019;65:24–30. https://doi.org/10.1016/j.medengphy.2018.12.022.

[115] Martínez Sánchez GJ, Escobar del Pozo C, Rocha Medina JA, Naude J, Brambila Solorzano A. Numerical simulation of the aqueous humor flow in the eye drainage system; a healthy and pathological condition comparison. Med Eng Phys 2020;83:82–92. https://doi.org/10.1016/j.medengphy.2020.07.010.

[116] Mauro A, Massarotti N, Salahudeen M, Romano MR, Romano V, Nithiarasu P. A generalised porous medium approach to study thermo-fluid dynamics in human eyes. Med Biol Eng Comput 2018;56:1823–39. https://doi.org/10.1007/s11517-018-1813-4.

[117] Niederer P, Fankhauser F, Kwasniewska S. Fluiddynamik des Kammerwassers beim chronischen einfachen Glaukom: Mechanismen der Drucknormalisierung durch ein künstliches Abflusssystem. Ophthalmologe 2012;109:30–6. https://doi.org/10.1007/s00347-011-2478-7.

[118] Gardiner BS, Smith DW, Coote M, Crowston JG. Computational modeling of fluid flow and intra-ocular pressure following glaucoma surgery. PLoS One 2010;5. https://doi.org/10.1371/journal.pone.0013178.

[119] Hunter KS, Fjield T, Heitzmann H, Shandas R, Kahook MY. Characterization of micro-invasive trabecular bypass stents by ex vivo perfusion and computational flow modeling. Clinical Ophthalmology 2014;8:499–506. https://doi.org/10.2147/OPTH.S56245.

[120] Fernández-Vigo JI, Marcos AC, Agujetas R, Montanero JM, Sánchez-Guillén I, García-Feijóo J, et al. Computational simulation of aqueous humour dynamics in the presence of a posterior-chamber versus iris-fixed phakic intraocular lens. PLoS One 2018;13:e0202128. https://doi.org/10.1371/journal.pone.0202128.

[121] Schaumburg F, Guarnieri FA. Assessment of thermal effects in a model of the human head implanted with a wireless active microvalve for the treatment of glaucoma creating a filtering bleb. Phys Med Biol 2017;62:N191–203. https://doi.org/10.1088/1361-6560/aa5dae.

[122] Nasrollahi A, Rizzo P. Modeling a new dynamic approach to measure intraocular pressure with solitary waves. J Mech Behav Biomed Mater 2020;103:103534. https://doi.org/10.1016/j.jmbbm.2019.103534.

[123] Kara E, Kutlar AI. CFD analysis of the Ahmed glaucoma valve and design of an alternative device. Comput Methods Biomech Biomed Engin 2010;13:655–62. https://doi.org/10.1080/10255841003717616.

[124] Villamarin A, Roy S, Hasballa R, Vardoulis O, Reymond P, Stergiopulos N. 3D simulation of the aqueous flow in the human eye. Med Eng Phys 2012;34:1462–70. https://doi.org/10.1016/j.medengphy.2012.02.007.

[125] Wang W, Qian X, Song H, Zhang M, Liu Z. Fluid and structure coupling analysis of the interaction between aqueous humor and iris. Biomed Eng Online 2016;15. https://doi.org/10.1186/s12938-016-0261-3.

[126] Khan MA. Numerical study on human cornea and modified multiparametric correction equation for Goldmann applanation tonometer. J Mech Behav Biomed Mater 2014;30:91–102. https://doi.org/10.1016/j.jmbbm.2013.10.002.

[127] Yang H, Song H, Mei X, Li L, Fu X, Zhang M, et al. Experimental research on intraocular aqueous flow by PIV method. Biomed Eng Online 2013;12:1–8. https://doi.org/10.1186/1475-925X-12-108.

[128] Wang W, Qian X, Li Q, Zhang G, Zhao H, Li T, et al. Experimental study of aqueous humor flow in a transparent anterior segment phantom by using PIV technique. MCB Molecular and Cellular Biomechanics 2019;16:59–74. https://doi.org/10.32604/mcb.2019.06393.

[129] Villamarin A, Roy S, Hasballa R, Vardoulis O, Reymond P, Stergiopulos N. 3D simulation of the aqueous flow in the human eye. Med Eng Phys 2012;34:1462–70. https://doi.org/10.1016/j.medengphy.2012.02.007.

[130] Avtar R, Srivastava R. Modelling the flow of aqueous humor in anterior chamber of the eye. Appl Math Comput 2006;181:1336–48. https://doi.org/10.1016/J.AMC.2006.03.002.

[131] Lam K, Lawlor M. Anatomy of the Aqueous Outflow Drainage Pathways. Minimally Invasive Glaucoma Surgery 2020:11–9. https://doi.org/10.1007/978-981-15-5632-6_2/FIGURES/1.

[132] Abu-Hassan DW, Acott TS, Kelley MJ. The Trabecular Meshwork: A Basic Review of Form and Function. J Ocul Biol 2014;2. https://doi.org/10.13188/2334-2838.1000017.

[133] Karimi A, Razaghi R, Stanik A, Daniel D'costa S, Mirafzal I, Kelley MJ, et al. High-resolution modeling of aqueous humor dynamics in the conventional outflow pathway of a normal human donor eye. Comput Methods Programs Biomed 2025;260:108538. https://doi.org/10.1016/J.CMPB.2024.108538.

[134] ANSYS FLUENT 12.0 User's Guide - 7.2.3 Porous Media Conditions n.d. https://www.afs.enea.it/project/neptunius/docs/fluent/html/ug/node233.htm (accessed May 9, 2024).

[135] Kumar S, Acharya S, Beuerman R, Palkama A. Numerical solution of ocular fluid dynamics in a rabbit eye: Parametric effects. Ann Biomed Eng 2006;34:530–44. https://doi.org/10.1007/s10439-005-9048-6.

[136] Heys JJ, Barocas VH. A boussinesq model of natural convection in the human eye and the formation of Krukenberg's spindle. Ann Biomed Eng 2002;30:392–401. https://doi.org/10.1114/1.1477447.

[137] Alimahomed F. CFD SIMULATION OF THE AQUEOUS HUMOR FLOW IN THE EYE. Aston University, 2020.

[138] Wang W, Qian X, Song H, Zhang M, Liu Z. Fluid and structure coupling analysis of the interaction between aqueous humor and iris. Biomed Eng Online 2016;15:569–86. https://doi.org/10.1186/s12938-016-0261-3.

[139] Critical richardson number - Glossary of Meteorology n.d. https://glossary.ametsoc.org/wiki/Critical_richardson_number (accessed December 15, 2024).

[140] Wang W, Qian X, Li Q, Zhang G, Zhao H, Li T, et al. Experimental Study of Aqueous Humor Flow in a Transparent Anterior Segment Phantom by Using PIV Technique. Molecular & Cellular Biomechanics 1970;16:59–74. https://doi.org/10.32604/MCB.2019.06393.

[141] ANSYS FLUENT 12.0 User's Guide - 26.3.1 Choosing the Pressure-Velocity Coupling Method n.d. https://www.afs.enea.it/project/neptunius/docs/fluent/html/ug/node785.htm (accessed January 14, 2025).

[142] Spierer O, Cavuoto KM, Suwannaraj S, McKeown CA, Chang TC. Outcome of optical iridectomy in Peters anomaly. Graefe's Archive for Clinical and Experimental Ophthalmology 2018;256:1679–83. https://doi.org/10.1007/S00417-018-4000-2/TABLES/2.

[143] Keller KE, Acott TS. The Juxtacanalicular Region of Ocular Trabecular Meshwork: A Tissue with a Unique Extracellular Matrix and Specialized Function. J Ocul Biol 2013;1:3. https://doi.org/10.13188/2334-2838.1000003.

[144] ANSYS FLUENT 12.0 User's Guide - 6.1.3 Choosing the Appropriate Mesh Type n.d. https://www.afs.enea.it/project/neptunius/docs/fluent/html/ug/node164.htm (accessed January 22, 2022).

[145] ANSYS FLUENT 12.0 User's Guide - 6.2.2 Mesh Quality n.d. https://www.afs.enea.it/project/neptunius/docs/fluent/html/ug/node167.htm (accessed January 22, 2022).

[146] Vinne EJH Van Der, Basson N. Validating CFD Models of Aqueous Humour Dynamics with In-Vitro Temperature Gradients n.d.

[147] Francis BA, Singh K, Lin SC, Hodapp E, Jampel HD, Samples JR, et al. Novel glaucoma procedures: a report by the American Academy of Ophthalmology. Ophthalmology 2011;118:1466–80. https://doi.org/10.1016/J.OPHTHA.2011.03.028.

[148] Basson N, Peng CHS, Geoghegan P, van der Lecq T, Steven D, Williams S, et al. A computational fluid dynamics investigation of endothelial cell damage from glaucoma drainage devices. Scientific Reports 2024 14:1 2024;14:1–8. https://doi.org/10.1038/s41598-023-50491-9.

[149] Vallabh NA, Kennedy S, Vinciguerra R, McLean K, Levis H, Borroni D, et al. Corneal Endothelial Cell Loss in Glaucoma and Glaucoma Surgery and the Utility of Management with Descemet Membrane Endothelial Keratoplasty (DMEK). J Ophthalmol 2022;2022. https://doi.org/10.1155/2022/1315299.

[150] Lee JS, Park S, Seong GJ, Kim CY, Lee SY, Choi W, et al. Long-term Intraocular Pressure Fluctuation Is a Risk Factor for Visual Field Progression in Advanced Glaucoma. J Glaucoma 2022;31:310–6. https://doi.org/10.1097/IJG.0000000000002011.

[151] Hau S, Bunce C, Barton K. Corneal Endothelial Cell Loss after Baerveldt Glaucoma Implant Surgery. Ophthalmol Glaucoma 2021;4:20–31. https://doi.org/10.1016/J.OGLA.2020.06.012.

[152] Kim MS, Kim KN, Kim CS. Changes in Corneal Endothelial Cell after Ahmed Glaucoma Valve Implantation and Trabeculectomy: 1-Year Follow-up. Korean J Ophthalmol 2016;30:416. https://doi.org/10.3341/KJO.2016.30.6.416.

[153] Koo EB, Hou J, Han Y, Keenan JD, Stamper RL, Jeng BH. Effect of glaucoma tube shunt parameters on cornea endothelial cells in patients with Ahmed valve implants. Cornea 2015;34:37–41. https://doi.org/10.1097/ICO.0000000000000301.

[154] Tan AN, Webers CAB, Berendschot TTJM, de Brabander J, de Witte PM, Nuijts RMMA, et al. Corneal endothelial cell loss after Baerveldt glaucoma drainage device implantation in the anterior chamber. Acta Ophthalmol 2017;95:91–6. https://doi.org/10.1111/AOS.13161.

[155] Basson N, Alimahomed F, Geoghegan PH, Williams SE, Ho WH. An aqueous humour fluid dynamic study for normal and glaucomatous eye conditions. 2022 44th Annual International Conference of the IEEE Engineering in Medicine & Biology Society (EMBC), IEEE; 2022, p. 3963–6. https://doi.org/10.1109/EMBC48229.2022.9871009.

[156] Lim LS, Ho CL, Ang LPK, Aung T, Tan DTH. Inferior Corneal Decompensation Following Laser Peripheral Iridotomy in the Superior Iris. Am J Ophthalmol 2006;142:166–8. https://doi.org/10.1016/j.ajo.2006.01.070.

[157] Heinz C, Koch JM, Heiligenhaus A. Trabeculectomy or modified deep sclerectomy in juvenile uveitic glaucoma. J Ophthalmic Inflamm Infect 2011;1:165–70. https://doi.org/10.1007/s12348-011-0039-5.

[158] Pantalon A, Feraru C, Tarcoveanu F, Chiselita D. Success of Primary Trabeculectomy in Advanced Open Angle Glaucoma. Clin Ophthalmol 2021;15:2219. https://doi.org/10.2147/OPTH.S308228.

[159] Lusthaus JA, Khatib TZ, Meyer PAR, McCluskey P, Martin KR. Aqueous outflow imaging techniques and what they tell us about intraocular pressure regulation. Eye 2020 35:1 2020;35:216–35. https://doi.org/10.1038/s41433-020-01136-y.

[160] Lucas-Sánchez M, Serradell JM, Comas D. Population history of North Africa based on modern and ancient genomes. Hum Mol Genet 2021;30:R17–23. https://doi.org/10.1093/HMG/DDAA261.

[161] Sun M, Höllhumer R. White-to-white corneal diameter: normal values in the adult black African population obtained with an optical biometer. South African Ophthalmology Journal 2022;17:29–32.

[162] Mashige K-P. Corneal parameters and their correlations with refractive error, axial length, anterior chamber depth and lens thickness in black South Africans. International Eye Science 2017;17:597–603. https://doi.org/10.3980/J.ISSN.1672-5123.2017.4.03.

[163] Rozema JJ. Refractive development I: Biometric changes during emmetropisation. Ophthalmic and Physiological Optics 2023;43:347–67. https://doi.org/10.1111/OPO.13094.

[164] Rampersad N, Hansraj R. Distribution of anterior chamber angle measurements in South African young adults: an optical coherence tomography study. Int Ophthalmol 2022;42:1697–709. https://doi.org/10.1007/S10792-021-02164-7/TABLES/2.

[165] Lee RY, Chon BH, Lin SC, He M, Lin SC. Association of Ocular Conditions With Narrow Angles in Different Ethnicities. Am J Ophthalmol 2015;160:506-515.e1. https://doi.org/10.1016/J.AJO.2015.06.002.

[166] Lee RY, Huang G, Cui QN, He M, Porco TC, Lin SC. Association of Lens Vault with Narrow Angles among Different Ethnic Groups. Curr Eye Res 2012;37:486–91. https://doi.org/10.3109/02713683.2012.669006.

[167] Olsen T, Arnarsson A, Sasaki H, Sasaki K, Jonasson F. On the ocular refractive components: the Reykjavik Eye Study. Acta Ophthalmol Scand 2007;85:361–6. https://doi.org/10.1111/J.1600-0420.2006.00847.X.

[168] Muzhambi VT, Ho WH, Bason Word N. Analysis of biometry data from major population (ethnic) groups on the anterior chamber of the human eye and its implication on Glaucoma. Unpublished. University of Cape Town, 2024.

[169] Loth E, Ahmad J, Chatham C, López B, Carter B, Crawley D, et al. The meaning of significant mean group differences for biomarker discovery. PLoS Comput Biol 2021;17:e1009477. https://doi.org/10.1371/JOURNAL.PCBI.1009477.

[170] Buhrmann RR, Quigley HA, Barron Y, West SK, Oliva MS, Mmbaga BBO. Prevalence of Glaucoma in a Rural East African Population. n.d.

[171] Dolan JM, Kolega J, Meng H. High Wall Shear Stress and Spatial Gradients in Vascular Pathology: A Review. Ann Biomed Eng 2012;41:1411. https://doi.org/10.1007/S10439-012-0695-0.

[172] Nguyen AH, Fatehi N, Romero P, Miraftabi A, Kim E, Morales E, et al. Observational Outcomes of Initial Trabeculectomy With Mitomycin C in Patients of African Descent vs Patients of European Descent: Five-Year Results. JAMA Ophthalmol 2018;136:1106. https://doi.org/10.1001/JAMAOPHTHALMOL.2018.2897.

[173] Khaw PT, Chiang M, Shah P, Sii F, Lockwood A, Khalili A. Enhanced Trabeculectomy – The Moorfields Safer Surgery System. Dev Ophthalmol 2012;50:1–28. https://doi.org/10.1159/000334776.

[174] Sihota R, Angmo D, Ramaswamy D, Dada T. Simplifying "target" intraocular pressure for different stages of primary open-angle glaucoma and primary angle-closure glaucoma. Indian J Ophthalmol 2018;66:495. https://doi.org/10.4103/IJO.IJO_1130_17.

[175] Lopes D, Puga H, Teixeira JC, Teixeira SF. Influence of arterial mechanical properties on carotid blood flow: Comparison of CFD and FSI studies. Int J Mech Sci 2019;160:209–18. https://doi.org/10.1016/j.ijmecsci.2019.06.029.

[176] Mendez V, Di Giuseppe M, Pasta S. Comparison of hemodynamic and structural indices of ascending thoracic aortic aneurysm as predicted by 2-way FSI, CFD rigid wall simulation and patient-specific displacement-based FEA. Comput Biol Med 2018;100:221–9. https://doi.org/10.1016/j.compbiomed.2018.07.013.

[177] Mulu-Sumbi JS. Development of a fluid-structure-interaction model for aqueous humour flow in the anterior chamber of the human eye. Unpublished. University Of Cape Town, 2024.

[178] Lim LS, Saw SM, Jeganathan VSE, Tay WT, Aung T, Tong L, et al. Distribution and determinants of ocular biometric parameters in an asian population: The Singapore malay eye study. Invest Ophthalmol Vis Sci 2010;51:103–9. https://doi.org/10.1167/iovs.09-3553.

[179] Tham YC, Li X, Wong TY, Quigley HA, Aung T, Cheng CY. Global prevalence of glaucoma and projections of glaucoma burden through 2040: A systematic review and meta-analysis. Ophthalmology 2014;121:2081–90. https://doi.org/10.1016/j.ophtha.2014.05.013.

[180] Tan GS, He M, Zhao W, Sakata LM, Li J, Nongpiur ME, et al. Determinants of Lens Vault and Association With Narrow Angles in Patients From Singapore. Am J Ophthalmol 2012;154:39–46. https://doi.org/10.1016/J.AJO.2012.01.015.

[181] Baykara M, Poroy C, Erseven C. Surgical outcomes of combined gonioscopy-assisted transluminal trabeculotomy and cataract surgery. Indian J Ophthalmol 2019;67:505–8. https://doi.org/10.4103/ijo.IJO_1007_18.

[182] Lee HM, Kim KN, Park KS, Lee NH, Lee SB, Kim CS. Relationship between Tube Parameters and Corneal Endothelial Cell Damage after Ahmed Glaucoma Valve Implantation: A Comparative Study. J Clin Med 2020;9:1–11. https://doi.org/10.3390/JCM9082546.

[183] Kaji Y, Oshika T, Usui T, Sakakibara J. Effect of shear stress on attachment of corneal endothelial cells in association with corneal endothelial cell loss after laser iridotomy. Cornea 2005;24. https://doi.org/10.1097/01.ICO.0000178735.27674.52.

[184] Tseng VL, Kim CH, Romero PT, Yu F, Robertson-Brown KW, Phung L, et al. Risk Factors and Long-Term Outcomes in Patients with Low Intraocular Pressure after Trabeculectomy. Ophthalmology 2017;124:1457–65. https://doi.org/10.1016/j.ophtha.2017.05.014.

[185] Choudhari NS, Badakere SV, Richhariya A, Chittajallu SNSH, Senthil S, Garudadri CS. Is Ahmed Glaucoma Valve Consistent in Performance? Transl Vis Sci Technol 2018;7. https://doi.org/10.1167/TVST.7.3.19.

[186] Nouri-Mahdavi K, Caprioli J. Evaluation of the hypertensive phase after insertion of the Ahmed Glaucoma Valve. Am J Ophthalmol 2003;136:1001–8. https://doi.org/10.1016/S0002-9394(03)00630-5.

[187] Kim JY, Lee JS, Lee T, Seo D, Choi W, Bae HW, et al. Corneal endothelial cell changes and surgical results after Ahmed glaucoma valve implantation: ciliary sulcus versus anterior chamber tube placement. Scientific Reports 2021 11:1 2021;11:1–9. https://doi.org/10.1038/s41598-021-92420-8.

[188] Mashige K-P. Corneal parameters and their correlations with refractive error, axial length, anterior chamber depth and lens thickness in black South Africans. International Eye Science 2017;17:597–603. https://doi.org/10.3980/J.ISSN.1672-5123.2017.4.03.

[189] Chen MJ, Liu YT, Tsai CC, Chen YC, Chou CK, Lee SM. Relationship between central corneal thickness, refractive error, corneal curvature, anterior chamber depth and axial length. Journal of the Chinese Medical Association 2009;72:133–7. https://doi.org/10.1016/S1726-4901(09)70038-3.

[190] Liu S, Yu M, Ye C, Lam DSC, Leung CKS. Anterior Chamber Angle Imaging with Swept-Source Optical Coherence Tomography: An Investigation on Variability of Angle Measurement. Invest Ophthalmol Vis Sci 2011;52:8598–603. https://doi.org/10.1167/IOVS.11-7507.

[191] Rampersad N, Hansraj R. Distribution of anterior chamber angle measurements in South African young adults: an optical coherence tomography study. Int Ophthalmol 2022;42:1697–709. https://doi.org/10.1007/S10792-021-02164-7/METRICS.

[192] Lee RY, Huang G, Cui QN, He M, Porco TC, Lin SC. Association of Lens Vault with Narrow Angles among Different Ethnic Groups. Curr Eye Res 2012;37:486–91. https://doi.org/10.3109/02713683.2012.669006.

[193] Lim LS, Saw SM, Jeganathan VSE, Tay WT, Aung T, Tong L, et al. Distribution and Determinants of Ocular Biometric Parameters in an Asian Population: The Singapore Malay Eye Study. Invest Ophthalmol Vis Sci 2010;51:103–9. https://doi.org/10.1167/IOVS.09-3553.

[194] Olsen T, Arnarsson A, Sasaki H, Sasaki K, Jonasson F. On the ocular refractive components: the Reykjavik Eye Study. Acta Ophthalmol Scand 2007;85:361–6. https://doi.org/10.1111/J.1600-0420.2006.00847.X.

[195] Foster PJ, Alsbirk PH, Baasanhu J, Munkhbayar D, Uranchimeg D, Johnson GJ. Anterior chamber depth in Mongolians: Variation with age, sex, and method of measurement. Am J Ophthalmol 1997;124:53–60. https://doi.org/10.1016/S0002-9394(14)71644-7.

[196] Sanchis-Gimeno JA, Sanchez-Zuriaga D, Martinez-Soriano F. White-to-white corneal diameter, pupil diameter, central corneal thickness and thinnest corneal thickness values of emmetropic subjects. Surgical and Radiologic Anatomy 2012;34:167–70. https://doi.org/10.1007/S00276-011-0889-4/METRICS.

[197] Rüfer F, Schröder A, Erb C. White-to-white corneal diameter: Normal values in healthy humans obtained with the Orbscan II topography system. Cornea 2005;24:259–61. https://doi.org/10.1097/01.ICO.0000148312.01805.53.

[198] Domínguez-Vicent A, Monsálvez-Romín D, Del águila-Carrasco AJ, García-Lázaro S, Montés-Micó R. Measurements of anterior chamber depth, white-to-white distance, anterior chamber angle, and pupil diameter using two Scheimpflug imaging devices. Arq Bras Oftalmol 2014;77:233–7. https://doi.org/10.5935/0004-2749.20140060.

[199] Wei L, He W, Meng J, Qian D, Lu Y, Zhu X. Evaluation of the White-to-White Distance in 39,986 Chinese Cataractous Eyes. Invest Ophthalmol Vis Sci 2021;62:7–7. https://doi.org/10.1167/IOVS.62.1.7.

[200] Xu G, Wu G, Du Z, Zhu S, Guo Y, Yu H, et al. Distribution of White-to-White Corneal Diameter and Anterior Chamber Depth in Chinese Myopic Patients. Front Med (Lausanne) 2021;8:732719. https://doi.org/10.3389/FMED.2021.732719/BIBTEX.

[201] Miao A, Tang Y, Zhu X, Qian D, Zheng T, Lu Y. Associations between anterior segment biometry and high axial myopia in 3438 cataractous eyes in the Chinese population. BMC Ophthalmol 2022;22:1–12. https://doi.org/10.1186/S12886-022-02300-6/FIGURES/2.

[202] Lee RY, Chon BH, Lin SC, He M, Lin SC. Association of Ocular Conditions With Narrow Angles in Different Ethnicities. Am J Ophthalmol 2015;160:506-515.e1. https://doi.org/10.1016/J.AJO.2015.06.002.

[203] Friedman DS, Gazzard G, Min CB, Broman AT, Quigley H, Tielsch J, et al. Age and sex variation in angle findings among normal Chinese subjects: A comparison of UBM, Scheimpflug, and gonioscopic assessment of the anterior chamber angle. J Glaucoma 2008;17:5–10. https://doi.org/10.1097/IJG.0B013E31806AB327.

[204] Schuster AK, Pfeiffer N, Nickels S, Schulz A, Höhn R, Wild PS, et al. Distribution of Anterior Chamber Angle Width and Correlation With Age, Refraction, and Anterior Chamber Depth—The Gutenberg Health Study. Invest Ophthalmol Vis Sci 2016;57:3740–6. https://doi.org/10.1167/IOVS.16-19600.

[205] Xu L, Cao WF, Wang YX, Chen CX, Jonas JB. Anterior Chamber Depth and Chamber Angle and Their Associations with Ocular and General Parameters: The Beijing Eye Study. Am J Ophthalmol 2008;145:929-936.e1. https://doi.org/10.1016/J.AJO.2008.01.004.

[206] Sun JH, Sung KR, Yun SC, Cheon MH, Tchah HW, Kim MJ, et al. Factors Associated with Anterior Chamber Narrowing with Age: An Optical Coherence Tomography Study. Invest Ophthalmol Vis Sci 2012;53:2607–10. https://doi.org/10.1167/IOVS.11-9359.

Appendix A. In-Vitro Experimental Setup

This section details the development of a foundational in-vitro setup for studying aqueous humour hydrodynamics as validation for the CFD models. This setup aimed to replicate physiological conditions within the eye, providing accurate validation data for CFD simulations.

A 3D-printed flow phantom was used to simulate the anterior segment of the eye. The phantom was based on the idealised geometry described in section 4 and scaled up by a factor of five to enhance visualization and ensure detailed observation of flow patterns. The flow phantom and inlet adaptor were fabricated using a Formlabs 3D printer with Clear Resin V4. Post-printing, the model was washed with isopropanol (IPA) and cured in a UV oven at 60°C for 15 minutes. The outer surface was then sanded with 2000p and 4000p sandpaper to smoothen the surface and coated with mineral oil to enhance optical clarity.

The schematic diagram of the setup (Figure 107) consists of the following numbered components:

1. Dye feeder: A 3 mL syringe with a 0.9 mm outer diameter hypodermic needle is used to introduce dye into the flow for visualization.
2. Syringe pump: An NE300 Single Channel syringe pump models the constant production rate of aqueous humour, ensuring a steady flow.
3. Additional syringe: A 50 mL syringe is used to pre-fill the system with glycerine, facilitating the initial setup of the experiment.
4. Reservoir: This collects the outflow of the working fluid, ensuring a continuous flow circuit.
5. Valves: These are used to close the system during pre-filling, preventing leaks and ensuring accurate flow conditions.
6. Flow phantom: The 3D-printed model representing the human anterior chamber, scaled up for better visualization and detailed study.
7. Clear silicone tubing: Tubing with a 6 mm inner diameter connects various components of the setup, ensuring smooth fluid transfer.
8. Inlet adaptor: Connects the flow phantom to the tubing, ensuring a secure and leak-proof connection.
9. Camera and lamp: An iPhone 11 Pro rear camera and LED lamp are used to capture and illuminate the flow, respectively, providing high-quality visualization of the dye and particles within the flow phantom.

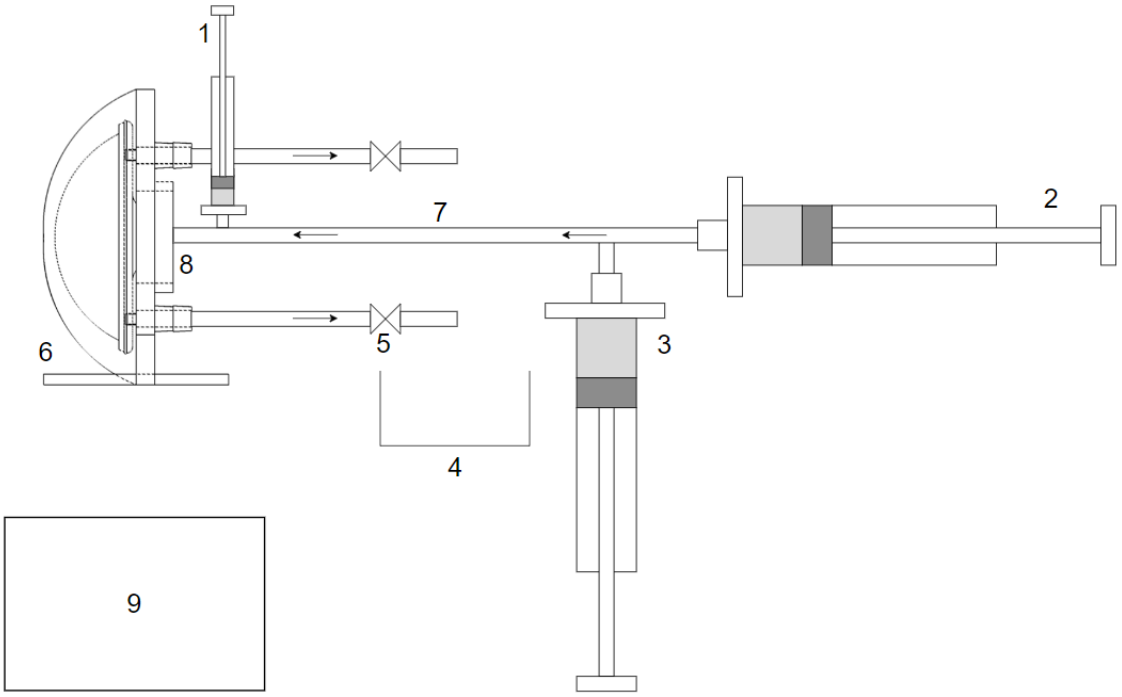


Figure 107 Schematic representation of the in-vitro flow setup, showing the key components and flow paths [146].

8.1.1 Dye Injection Setup

Dye injection techniques were used to observe qualitative flow patterns. A green dye, which matches the specific gravity of the working fluid, was injected into the flow to visualize the aqueous humour dynamics. The experiments were conducted with and without temperature gradients to evaluate their effect on the flow, which showed significant differences in flow behaviour, highlighting the impact of thermal effects on aqueous humour dynamics. The experimental results with temperature gradients closely matched the CFD simulations, validating the importance of incorporating temperature effects in the models.

Figure 108 illustartes a comparison between the CFD simulation without a temperature gradient and the in-vitro dye injection setup. The CFD simulation indicated a smooth and symmetrical flow, faster in the central region and slower near the edges. The dye dispersion showed a similar behavior, with central flow and outward dispersion. However, the dye flow path indicated asymmetrical dispersion, particularly in the front of the model, where the flow did not split into two streams as expected.

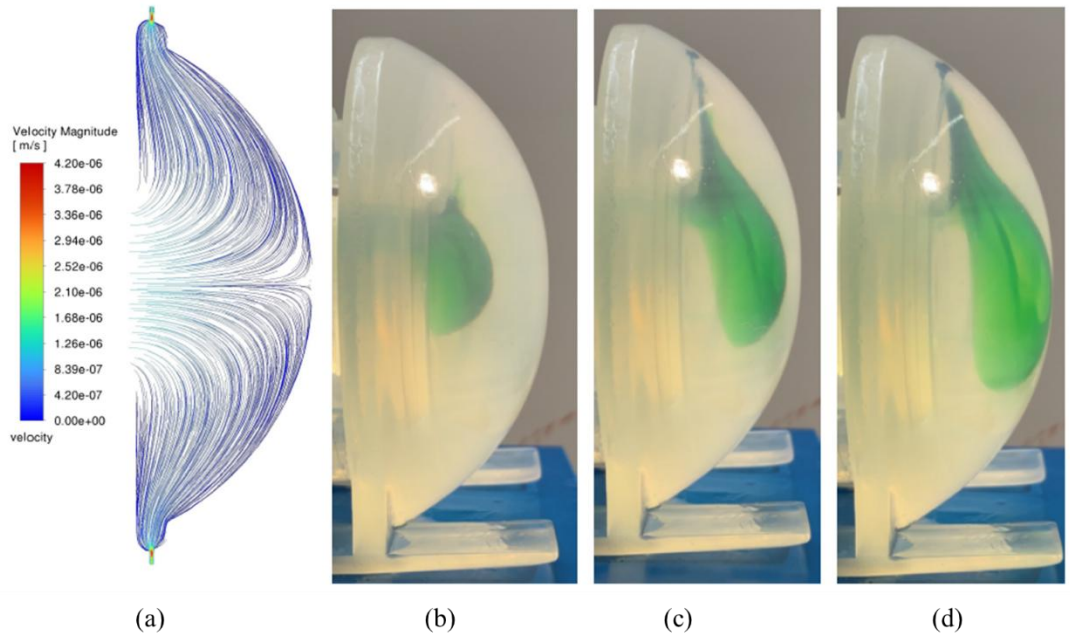


Figure 108 (a) CFD simulation on the xy-plane comparison for experimental dye visualization without temperature gradient at (b) 30 seconds, (c) 60 seconds, (d) 90 seconds [146].

Figure 109 illustrates a comparison between the CFD simulation with a temperature gradient and the in-vitro dye injection setup. The experimental setup incorporated temperature gradients to simulate buoyancy-driven flow within the eye. The cornea was maintained at 34°C, while the iris was kept at 37°C. Glycerine was used as the working fluid due to its higher refractive index, which enhances the clarity of the flow region of interest. The glycerine was heated to approximately 3°C above the measured room temperature on a heating plate before being inserted into the syringe pump. The syringe was insulated to maintain its temperature throughout the experiment. Thermocouples were placed at strategic locations to measure the temperature of the glycerine during the experiment.

The CFD simulation exhibited a circulate flow near the front of the eye, induced by the temperature gradient. The warmer fluid, being less dense, rose while the cooler fluid descended, creating a continuous circulation. The dye visualization showed that the inserted fluid floated on top of the ambient fluid, consistent with the simulation, suggesting initial higher velocity upwards due to the buoyancy effect.

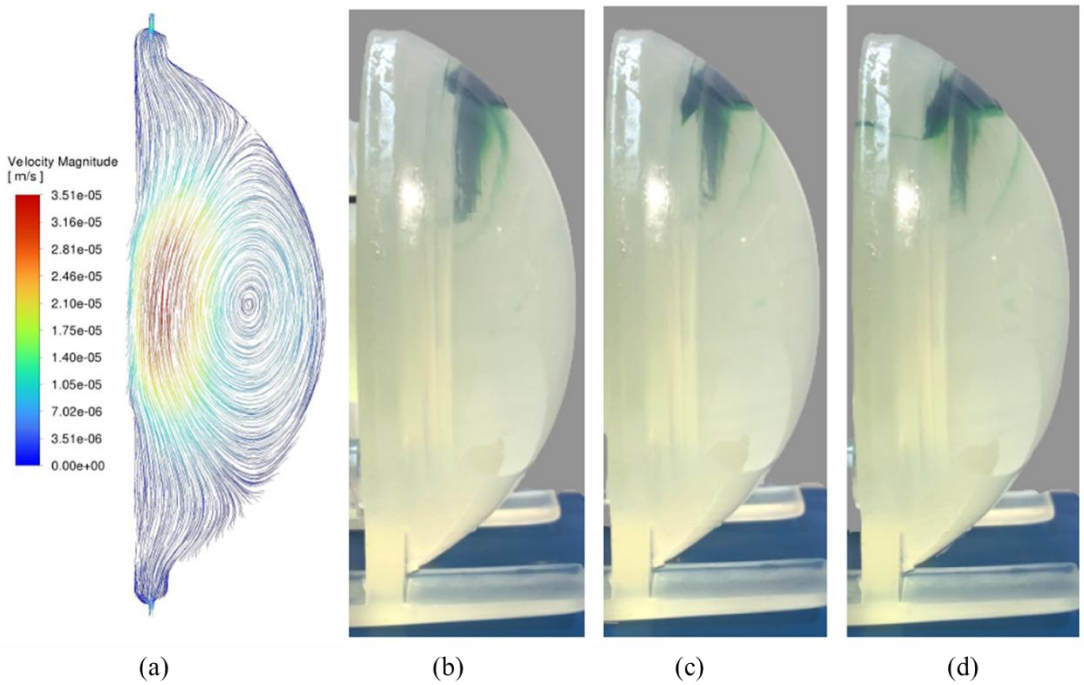


Figure 109 (a) CFD simulation on the xy-plane comparison for experimental dye visualization with temperature gradient at (b) 30 seconds, (c) 60 seconds, (d) 90 seconds [146].

One potential reason for discrepancies between dye visualization and CFD simulations could be the mixing behaviour of the dye with glycerine. If the dye does not perfectly match the density and viscosity of the glycerine, it could affect the flow paths and mixing behaviour, leading to deviations from the simulated flow. Inaccuracies in representing buoyancy effects in the dye visualization could also contribute to differences. The dye might not exhibit the same buoyancy-driven behaviour as the glycerine, particularly if there are slight differences in temperature gradients or fluid properties. Other experimental limitations, such as the precision of dye injection and the resolution of the imaging system, could also affect the observed flow patterns. Slight variations in the setup or measurements can lead to differences from the idealised conditions assumed in the simulations. Despite these differences, the qualitative trends observed in the dye visualization generally matched the CFD simulations, confirming the overall flow behaviour and validating the models' qualitative accuracy.

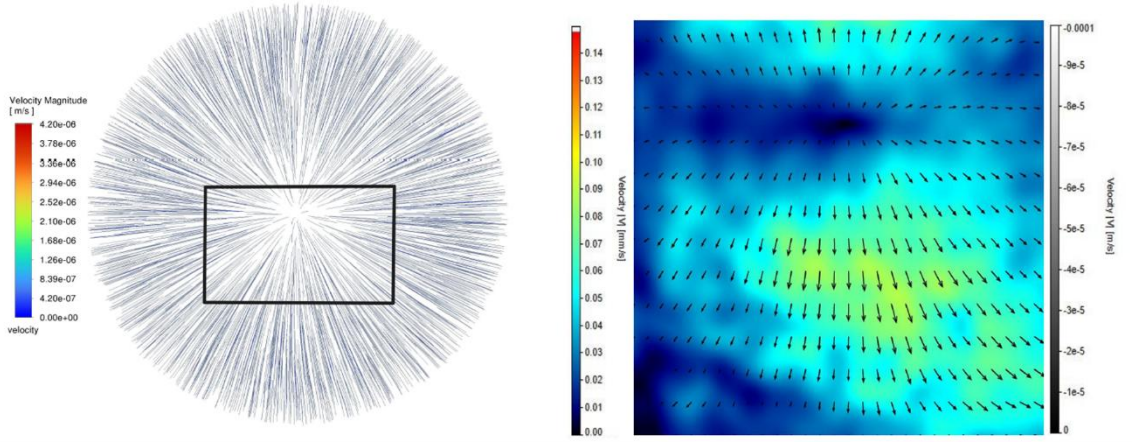
8.1.2 Particle Image Velocimetry Setup

Particle Image Velocimetry (PIV) was used for quantitative analysis of the flow. The glycerine was seeded with 55 µm polyamide particles, and an LED sheet illuminated the flow. A LaVision camera (Imager SX 9M) recorded the motion of the particles, and Davis 10.2.1 imaging software processed the data to provide quantitative information about velocity and flow structure. PIV is a well-established technique in fluid dynamics research due to its ability to provide detailed and accurate measurements of flow velocity fields. By capturing the movement of seed particles within the fluid, PIV offers a high-resolution, non-intrusive method for visualizing and quantifying flow patterns. The high frame rate of

the LaVision camera (Imager SX 9M) and the advanced processing capabilities of Davis 10.2.1 imaging software ensure that the data collected is precise and reliable.

The analysis was confined to a small window on the yz-plane (front view of the anterior chamber) due to lighting issues and the need for high-resolution data. Focusing on a smaller region allowed for detailed and accurate measurements. This approach ensured that the most relevant and precise data were obtained within the available timeframe.

Figure 110 depicts the comparison of the CFD model simulation without a temperature gradient with the PIV setup. The CFD simulation depicted a uniform and symmetrical flow pattern, with velocity vectors showing a smooth flow from the inlet to the outlet, faster in the central region and slower near the edges. The PIV results showed the flow's direction through vectors and the velocity magnitude by colour gradient. The overall velocity magnitude observed in the PIV experiments was slightly higher than that predicted by the CFD simulation, and the flow direction exhibited a slight rightward deflection.



(a) (b)

Figure 110 (a) CFD simulation on the yz-plane (PIV window outlined in black) comparison for (b) particle visualization without temperature gradient [146].

The qualitative flow patterns observed in the PIV experiments were similar to those predicted by the CFD simulations. Both methods showed a central region of higher velocity and slower flow near the edges, indicating that the general behaviour of the aqueous humour dynamics was accurately captured by the simulations.

Figure 111 depicts the comparison of the CFD model simulation with a temperature gradient with the PIV setup. The CFD simulation anticipated a high-velocity region around the inlet and two symmetrical vortices on both sides, driven by the temperature gradient causing buoyancy effects. The PIV results indicated a high-velocity region near the top of the plot, situated above the inlet. The observed flow showed a predominant downward flow spreading outwards, rather than the expected symmetrical vortices.

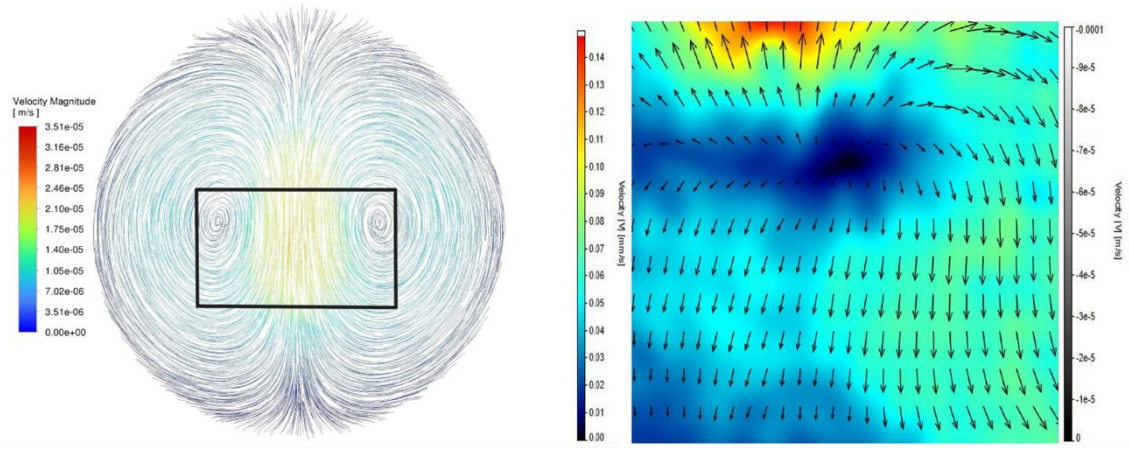


Figure 111 (a) CFD simulation on the yz-plane (PIV window outlined in black) comparison for (b) particle visualization with temperature gradient [146].

The overall flow patterns observed in the PIV experiments were generally similar to those predicted by the CFD simulations. Both methods identified a high-velocity region near the inlet, although the exact flow structures differed.

The velocities observed in the PIV experiments were in the same order of magnitude as those predicted by the CFD simulations. This agreement indicates that the simulations accurately captured the overall speed of the flow, even though some differences in flow structures were observed.

The resolution of the PIV system and the precision of particle seeding can impact the accuracy of the measurements. High-resolution imaging and precise particle seeding are critical for capturing detailed flow patterns. Any limitations in these aspects can lead to discrepancies between the observed and simulated flow structures. Despite these limitations, the qualitative trends and velocity magnitudes observed in the PIV experiments generally matched the CFD simulations, providing robust validation for the models. The agreement in flow patterns and velocities indicates that the CFD models reliably predict the key dynamics of aqueous humour flow, while acknowledging that experimental limitations can lead to some differences in the observed flow structures.

Appendix B. GDD as Glaucoma Treatment Study

GDD insertion involves three geometric parameters: tube-cornea angle (TCA), tube-cornea distance (TCD), and tube length (TL), as illustrated in Figure 112. The TCA is the angle between the GDD and the corneal wall, the TCD is the shortest distance from the GDD tip to the corneal wall, and the TL is the inserted tube length. These parameters are interrelated and define the insertion orientation. Clinical studies show that smaller TCAs and TCDs increase ECD risk [154,182].

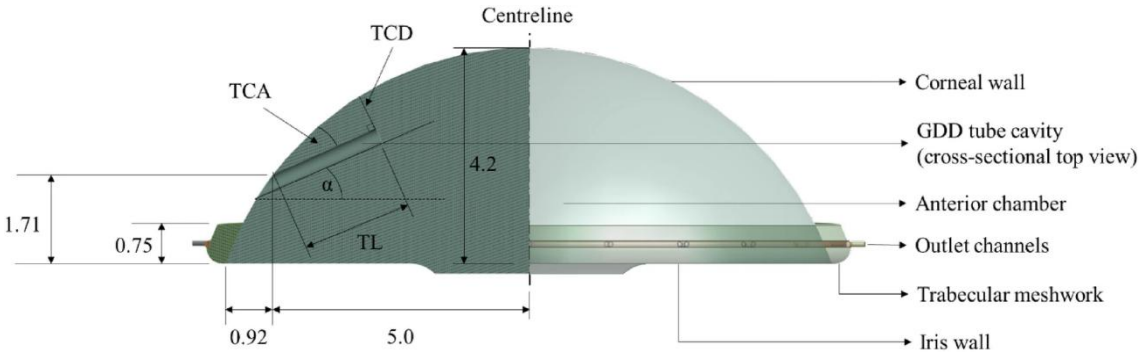


Figure 112 Diagram illustrating measurements in mm of the idealised anterior chamber of the eye, showing the placement of a glaucoma drainage device (published in [148]*).*

For this investigation, the Ahmed Glaucoma Valve (AGV) was selected, utilizing the idealised 3D model of the anterior chamber to reflect typical clinical insertion angles and positions. All of the conditions and boundaries remained the same, with the addition of the GDD modelled as a mass flow outlet at 3E-8 kg/s [120].

The ranges of TCA and TCD were selected based on clinical studies [154,182], ranging from 25.17° to 45.36° and 0.54 mm to 1.27 mm, respectively. TL was constant at 2.21 mm.

This section will briefly describe the results of the student project that was based on the overall study of this thesis, which aimed to study the ECD effects of GDD's using the methodology of the idealised eye simulations.

Kaji et al. [183] proposed ECD is likely when the WSS on the cornea exceeds 1 Pa. This analysis highlights how the size of the ECD region changes with different TCD. Notably, as the TCD increases, there is a clear and steady decrease in the percentage of the cornea classified as the ECD region, which aligns with the conclusions drawn by previous studies [151,154,182].

In relation to the mechanical behaviour of the tube used in the (GDD), calculations indicate that the deflection remains extremely small compared to the tube's inner diameter. This minor deflection suggests that the tube experiences minimal deformation, significantly lowering the likelihood of bending or flutter, which could affect fluid dynamics. As a result, deformation of the tube is considered negligible in further analyses of fluid flow patterns in the anterior chamber.

The corneal regions where WSS exceeds 1 Pa, identified as the “ECD regions”, are typically located near the insertion site of the GDD tube and the tube’s outlet. These findings align with clinical observations, which report higher rates of ECD in areas adjacent to the GDD insertion point. For cases with a smaller TCD, the ECD region tends to extend from the insertion site towards the inferior nasal region, forming what can be described as a "tail." This observation is of interest since Koo et al. [153] have reported higher levels of ECD in the inferior nasal area, though a direct comparison is difficult due to the lack of information regarding their specific insertion angles. As the TCD increases, the overall size of the ECD region decreases, and this "tail" disappears at higher TCD values. Once the TCD surpasses approximately 1.27 mm, no discernible ECD region remains.

Dynamic simulations conducted over time revealed fluctuations in the aqueous humour flow. For the case with the smallest TCD, the flow exhibited periodic fluctuations with a cycle time of approximately 1 second. As the TCD increased, the fluctuation cycle lengthened, reaching 4 seconds for the next size, and eventually the fluctuations ceased entirely beyond a certain TCD threshold. Interestingly, the “tail” of the ECD region showed a wave-like movement, fluttering in a pseudo-steady manner. The fluid streamlines close to the cornea’s surface also showed swirls around the ECD region, deviating from the more regular and steady flow patterns observed in the absence of a GDD.

These fluctuations in flow led to minor variations in IOP of approximately 1.5 mmHg. While small relative to the total IOP, these fluctuations are unlikely to cause noticeable symptoms such as palpitations. However, variations in IOP, particularly over extended periods, have been associated with the progression of glaucoma in various clinical trials [150,184].

Aside from the small IOP fluctuations caused by changes in flow, this model assumes consistent outflow of fluid through the AGV, resulting in stable post-IOP levels. However, both laboratory and clinical evidence indicate that AGV function can be inconsistent [185]. Additionally, it is common for patients to experience a ‘hypertensive phase’ approximately three to six weeks after surgery, thought to be caused by encapsulation of the bleb [186]. Acute IOP spikes during this phase are recognized as a potential cause of ECD, likely resulting from increased WSS. This analysis did not specifically evaluate the impact of post-IOP spikes on WSS, though it can be assumed that any such spikes would contribute to ECD. This means that even in cases where the tube is placed optimally, there is still a risk of ECD due to transient increases in WSS.

Research conducted by [187] further supports these findings, showing that ECD near the tube becomes statistically significant only from six months after surgery. Their study, which measured ECD at intervals of one month, six months, and one year, found that ECD levels only began to diverge significantly from non-operated control eyes after the six-month mark. This suggests that temporary IOP increases following surgery may not have as great an effect on long-term ECD development as previously thought.

The fluctuating flow behaviour and its effect on WSS were significant at certain time points but diminished after a certain period. This implies that careful adjustment of TCD and insertion angles could help reduce the risk of ECD over time. In conclusion, these findings underline the importance of optimizing the placement of GDDs to minimize corneal damage and control IOP fluctuations, thereby improving outcomes for glaucoma patients in the long term.

Appendix C. Anterior Chamber Raw Parameter Data

Source	Ethnicity	Sex	Age Group	n	WTW (mm)	ACD (mm)	ACA (deg)	LV (µm)	PD (mm)
[161]	African	Both	40-90	680	11.58 ± 1.12				
	European	Both	40-90	359	11.88				
[188]	African	Both	28.15±13	600	11.77 ± 0.32				
[189]	East-Asian	Male	40-80	226		3.0 ± 0.5			
		Female		274		2.9 ± 0.5			
[163]	African	Both	20-29	305		3.35			
			30-39			3.34			
			40-49			2.7			
			50-59			2.59			
			60+			2.44			
[190]	East-Asian	Both	24-69	30		2.9 ± 0.4	31.03 ± 19.69		4.77 ± 0.88
[191]	African	Both	17-29	349			37.02		
[192]	East-Asian	Both				2.81 ± 0.32		0.265 ± 0.288	4.08
	African	Both				2.91 ± 0.34		0.200 ± 0.237	3.9

	European	Both				2.86 ± 0.38		0.431 ± 0.248	3.92
[193]	East-Asian	Male	40-49	361		3.34 ± 0.02			
			50-59	398		3.19 ± 0.02			
			60-69	310		3.05 ± 0.02			
			70-80	264		2.93 ± 0.02			
		Female	40-49	416		3.27 ± 0.02			
			50-59	488		3.11 ± 0.02			
			60-69	330		2.88 ± 0.02			
			70-80	221		2.84 ± 0.02			
[193]	East-Asian	Both	40-79	951		2.9 ± 0.09			
[194]	European	Male	Mean 67.9	325		3.2 ± 0.32			
		Female	Mean 68.1	398		3.08 ± 0.34			
[195]	East-Asian	Male	20-29			3.01 ± 0.26			
			30-39			2.89 ± 0.28			
			40-49			2.69 ± 0.27			
			50-59			2.54 ± 0.29			
			60-69			2.45 ± 0.27			
			70+			2.34 ± 0.22			
		Female	20-29			2.84 ± 0.25			
			30-39			2.81 ± 0.3			

			40-49			2.59 ± 0.31			
			50-59			2.37 ± 0.29			
			60-69			2.3 ± 0.26			
			70+			2.27 ± 0.21			
[196]	Multiple	Male		198	11.9 ± 0.2				3.5 ± 0.3
		Female		181	11.8 ± 0.2				3.8 ± 0.5
[197]	European	Male	10-80	242	11.77 ± 0.37				
		Female	10-80	148	11.64 ± 0.47				
[198]	European	Both	20-40	80	11.87 ± 0.38	3.16 ± 0.24	36.78 ± 2.86		3.22 ± 0.55
[199]	East-Asian	Male	<40	457	12 ± 0.45				
			40-49	960	11.93 ± 0.44				
			50-59	1648	11.86 ± 0.43				
			60-69	2539	11.8 ± 0.44				
			70-79	1957	11.71 ± 0.43				
			>80	746	11.71 ± 0.42				
		Female	<40	315	11.8 ± 0.5				
			40-49	761	11.72 ± 0.45				
			50-59	2124	11.64 ± 0.42				
			60-69	4377	11.5 ± 0.41				
			70-79	2836	11.52 ± 0.38				
			>80	951	11.57 ± 0.43				
[200]	East-Asian	Both	24–26		11.63 ± 0.36	3.25 ± 0.25			

			27–29		11.60 ± 0.37	3.21 ± 0.26			
			30–32		11.55 ± 0.37	3.16 ± 0.25			
			33–35		11.55 ± 0.35	3.13 ± 0.25			
			36–38		11.58 ± 0.39	3.11 ± 0.27			
			39–40		11.55 ± 0.38	3.02 ± 0.23			
[201]	East-Asian	Male	<=59	554	11.56 ± 0.42	3.05 ± 0.48			
			60-69	558	11.48 ± 0.43	2.93 ± 0.43			
			>=70	388	11.5 ± 0.44	2.91 ± 0.49			
		Female	<=59	670	11.4 ± 0.4	2.9 ± 0.46			
			60-69	840	11.32 ± 0.41	2.87 ± 0.55			
			>=70	428	11.3 ± 0.37	2.79 ± 0.5			
[202]	European	Both	66.3 ± 13.0	166				0.54 ± 0.31	3.9 ± 1.3
	East-Asian	Both	64.6 ± 16.2	132				0.41 ± 0.35	4.1 ± 1.3
	African	Both	62.7 ± 13.0	90				0.36 ± 0.30	3.9 ± 1.0
	European	Both	40-50	30	12.3 ± 0.47	3.05 ± 0.37		0.28 ± 0.25	4.63 ± 0.81
			50-60	30	12.4 ± 0.45	3.03 ± 0.28		0.31 ± 0.24	4.60 ± 0.88
			60-70	31	12.2 ± 0.44	2.82 ± 0.49		0.45 ± 0.33	4.25 ± 0.79
			>70	30	12. 3 ± 0.32	2.8 ± 0.4		0.52 ± 0.28	4.08 ± 0.85
	East-Asian	Both	40-50	30	11.8 ± 0.43	2.84 ± 0.31		0.29 ± 0.3	4.71 ± 0.63
			50-60	32	11.8 ± 0.46	2.73 ± 0.33		0.39 ± 0.21	4.41 ± 0.95
			60-70	31	11.8 ± 0.43	2.75 ± 0.4		0.4 ± 0.34	4.51 ± 0.93
			>70	31	11.6 ± 0.39	2.51 ± 0.35		0.59 ± 0.32	4.12 ± 0.68
[203]	East-Asian	Male	65.1 ± 8.1	133			20.63 ± 6.17		
		Female		135			20.17 ± 5.47		

[204]	European	Male	59.1 ± 10.5	1554			31.95 ± 6.82		
		Female	58.1 ± 10.3	1460			30.88 ± 6.85		
[205]	East-Asian	Both	>45	1180		2.52 ± 0.31	42.97 ± 16.25		
			46-55	846		2.39 ± 0.34	36.38 ± 15.75		
			56-65	752		2.33 ± 0.34	34.72 ± 15.43		
			66-75	207		2.25 ± 0.33	32.69 ± 14.51		
[206]	East-Asian	Both	<50	41		3.337 ± 0.363		0.170 ± 0.212	
			50-60	49		2.936 ± 0.416		0.349 ± 0.310	
			60-70	140		2.849 ± 0.507		0.432 ± 0.372	
			70-80	118		2.693 ± 0.495		0.561 ± 0.375	
			80+	40		2.554 ± 0.535		0.684 ± 0.378	
[180]	East-Asian	Male	50–59	245				0.329 ± 0.257	
			60–69	264				0.454 ± 0.292	
			≥70	163				0.576 ± 0.291	
		Female	50–59	367				0.426 ± 0.275	
			60–69	297				0.528 ± 0.274	
			≥70	128				0.628 ± 0.241	

N

A

Appendix D. Extract from Statistical Analysis Study

Figure 113 and Figure 114 are extracts from a research project report as part of a bachelor's degree conducted by Andani Muzhambi at the University of Cape Town [168].

		S.A vs M.E	S.A vs E.D	S.A vs E.A	M.E vs E.D	M.E vs E.A	E.D vs E.A
ACD	N	13690	7872	22939	14918	25341	24167
	Cohen's D	1.956	0.395	1.224	1.852	0.349	0.145

		S.A vs M.E	S.A vs E.D	S.A vs E.A	M.E vs E.D	M.E vs E.A	E.D vs E.A
AL	N	3313	8042	5467	8895	6320	11049
	Cohen's D	0.386	0.344	0.438	0.219	0.249	0.061

		S.A vs M.E	S.A vs E.D	S.A vs E.A	M.E vs E.D	M.E vs E.A	E.D vs E.A
WTW	N	3472	3217	29558	3411	29752	28491
	Cohen's D	0.002	0.341	0.217	0.359	0.222	0.658

		S.A vs M.E	S.A vs E.D	S.A vs E.A	M.E vs E.D	M.E vs E.A	E.D vs E.A
CCT	N	5782	-	5233	-	1695	-
	Cohen's D	1.314	-	1.368	-	0.068	-

		S.A vs M.E	S.A vs E.D	S.A vs E.A	M.E vs E.D	M.E vs E.A	E.D vs E.A
LT	N	7262	-	-	-	-	-
	Cohen's D	1.542	-	-	-	-	-

		S.A vs M.E	S.A vs E.D	S.A vs E.A	M.E vs E.D	M.E vs E.A	E.D vs E.A
PD	N	-	-	-	-	-	1492
	Cohen's D	-	-	-	-	-	0.315

		S.A vs M.E	S.A vs E.D	S.A vs E.A	M.E vs E.D	M.E vs E.A	E.D vs E.A
ACA	N	5313	9131	8126	4222	3217	7035
	Cohen's D	0.322	0.507	0.150	0.758	0.035	0.446

Figure 113 Results of Cohen's D analysis [168]

Sub-Saharan Ethnicity comparison							
	ACD	ACA	AL	WTW	CCT	LT	PD
Middle Eastern	1.956	0.322	0.386	0.002	1.314	1.542	-
European Descent	0.237	0.507	0.344	0.341	-	-	-
East Asian	0.377	0.150	0.438	0.217	1.368	-	-

Middle Eastern Ethnicity comparison							
	ACD	ACA	AL	WTW	CCT	LT	PD
sub-Saharan	2.902	0.322	0.386	0.002	1.314	1.542	-
European Descent	1.852	0.758	0.219	0.359	-	-	-
East Asian	0.349	0.035	0.249	0.222	0.068	-	-

European Descent Ethnicity comparison							
	ACD	ACA	AL	WTW	CCT	LT	PD
Middle Eastern	1.852	0.758	0.219	0.359	-	-	-
sub-Saharan	0.237	0.507	0.344	0.359	-	-	
East Asian	0.145	0.446	0.061	0.658	-	-	0.315

East Asian Ethnicity comparison							
	ACD	ACA	AL	WTW	CCT	LT	PD
Middle Eastern	0.349	0.035	0.249	0.222	-	-	-
European Descent	0.145	0.446	0.061	0.658	-	-	0.315
sub-Saharan	0.377	0.150	0.438	0.217	-	-	-

Figure 114 Cohen's D effect arranged per ethnicity [168]

C

Appendix E. Unsutured Surgical Results

The results for the velocity pathlines for unsutured trabeculectomy in the supine position are provided in Figure 115. Before suturing, both models show peak velocities near the incision site, which is due to the open incision allowing unrestricted outflow to the atmosphere, creating a rapid flow through the Kelly punch incision. The anterior chamber shows almost negligible flow velocities (< 1 mm/s) away from the incision site. The low velocity throughout most of the anterior chamber indicates that the bulk of the aqueous humour is quickly directed toward the drainage pathway, bypassing the normal circulation pattern. There is also highly irregular flow near the incision site. This flow pattern highlights the importance of restoring a balanced flow through the chamber. Both models exhibit similar flow patterns. Anatomical differences do not seem to significantly impact flow in this open-incision state, as the unrestricted outflow pathway dominates the dynamics.

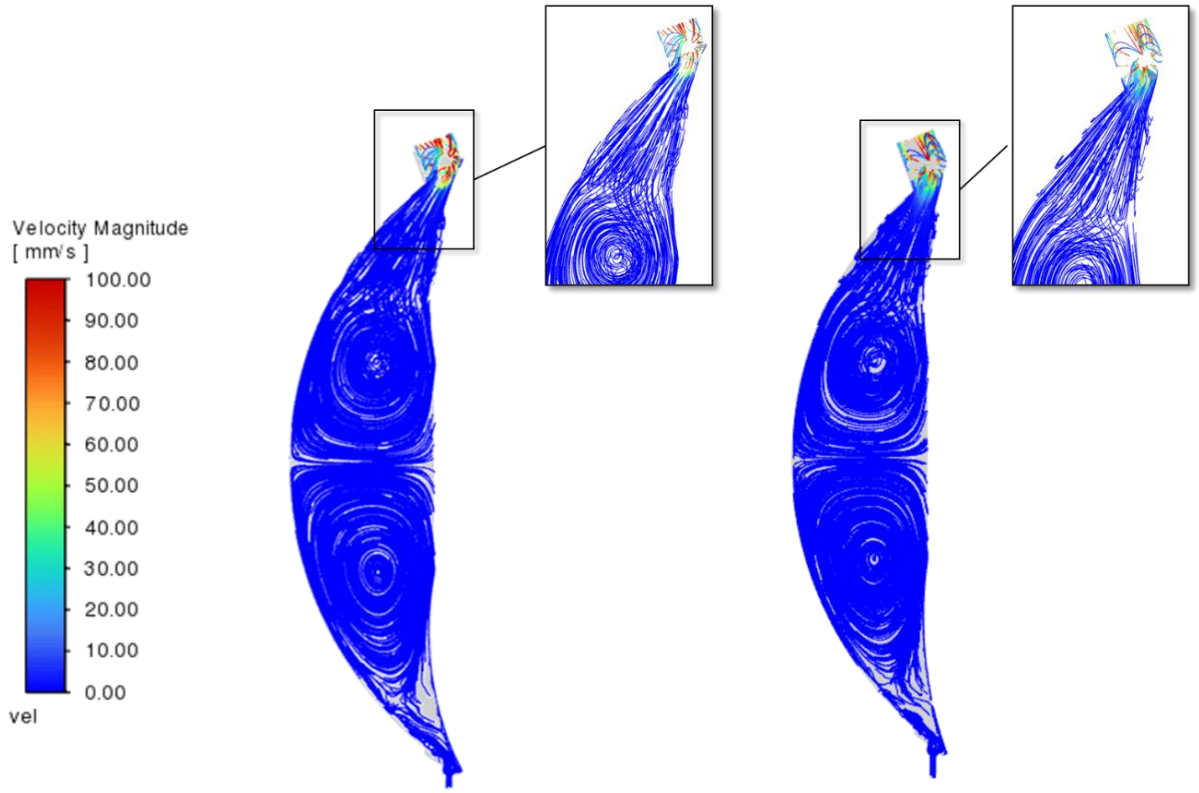


Figure 115 Velocity pathline results under trabeculectomy conditions for the supine unsutured European-representative eye (left) and the supine unsutured African representative eye (right)

The results for the velocity vectors for unsutured trabeculectomy are provided in Figure 116. Before suturing, the vectors show extremely high velocities at the incision site, where aqueous humour flows rapidly out of the anterior chamber due to the open connection to the atmosphere. These vectors confirm an accelerated flow exiting through the incision. The vectors near the incisions site also indicate reverse flow consistent with the drastically decreased IOP.

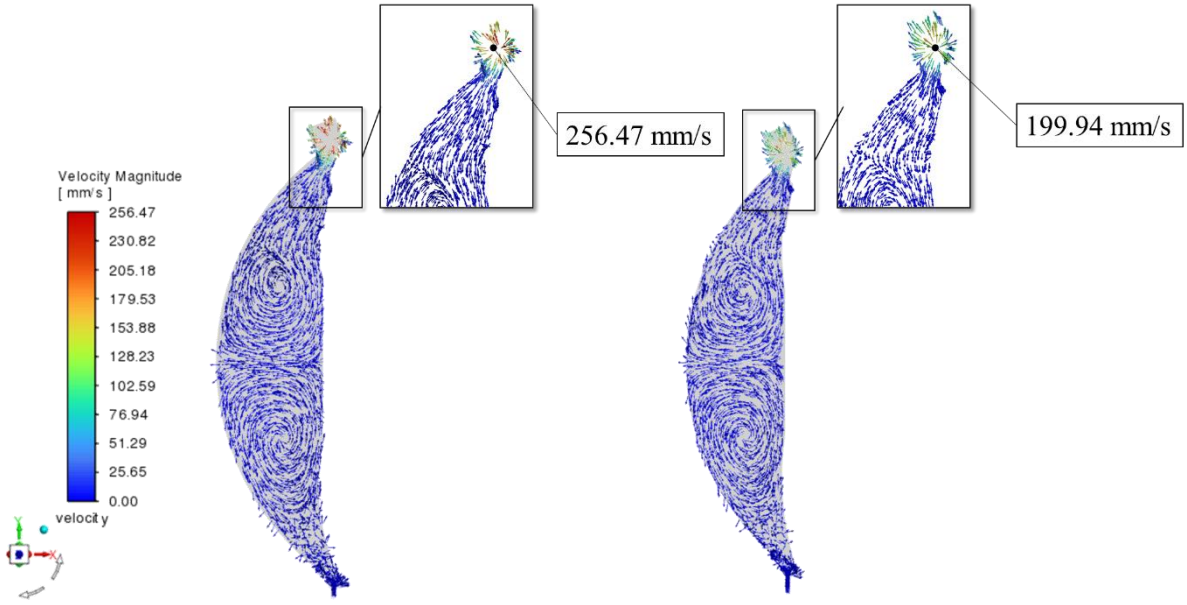


Figure 116 Velocity vector results under trabeculectomy conditions for the supine unsutured European-representative eye (left) and the supine unsutured African representative eye (right)

The velocity pathline results for unsutured NPDS are provided in Figure 117. For the unsutured conditions, both models show a strong outflow at the surgical site. The pathlines in the African model are more evenly distributed across the ACA compared to the European model. This is consistent with the wider ACA in the African model, which allows for more distributed outflow.

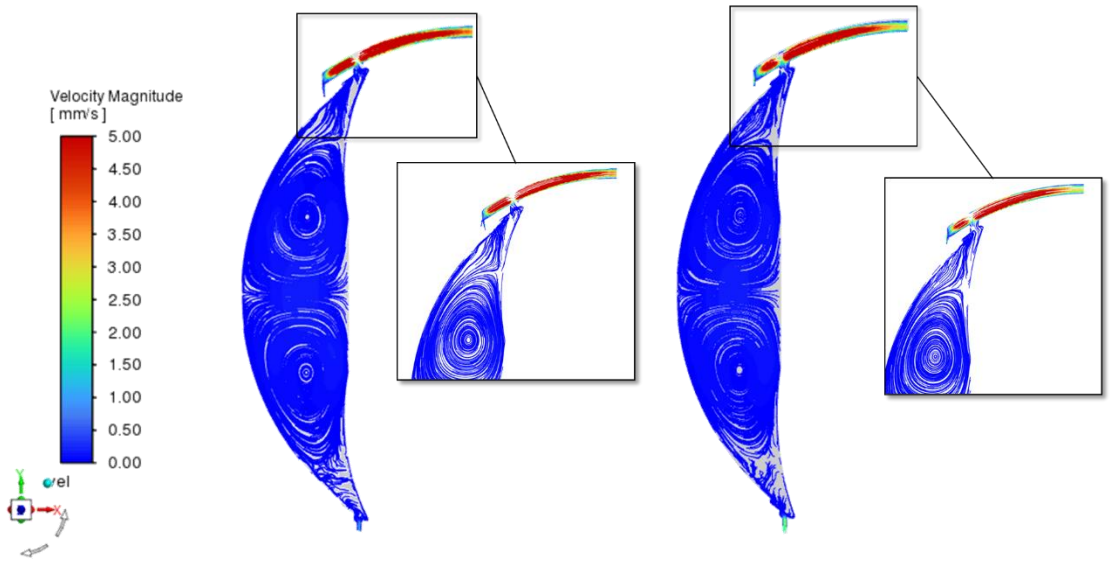


Figure 117 Velocity pathline results under NPDS conditions for the supine unsutured European-representative eye (left) and the supine unsutured African-representative eye (right)

The velocity pathline results for unsutured NPDS are provided in Figure 118. For both unsutured models, the flow is directed predominantly outward toward the surgical site, showing high velocities near the filtration site. Aligning with what was noted in the velocity pathline results, there is evidence

of vortex alteration at the ACA of the European model. In the African mode, the flow is more evenly distributed at the outflow near the surgical site.

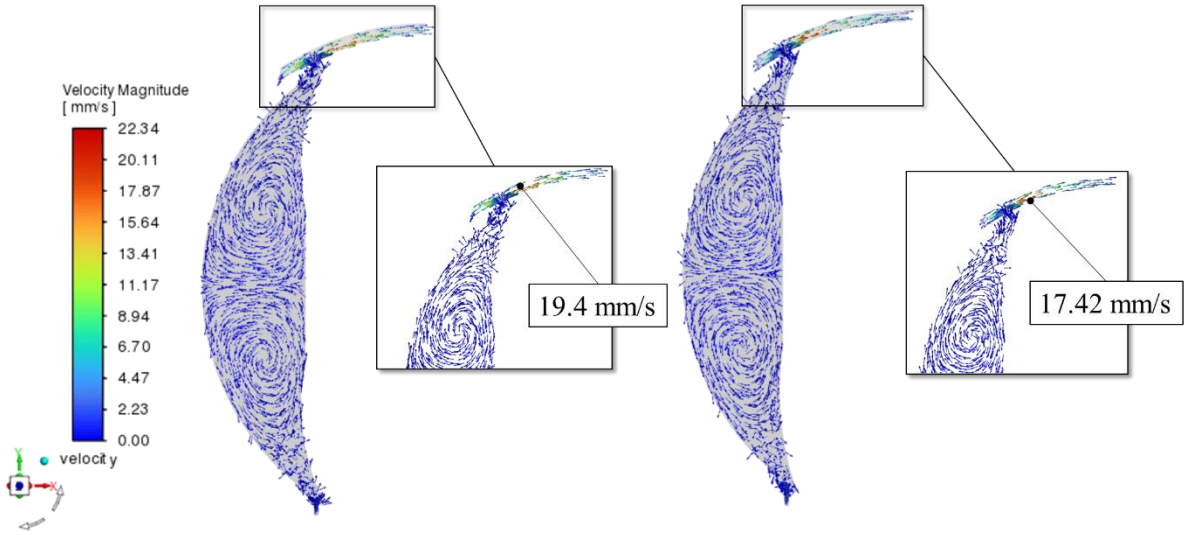


Figure 118 Velocity vector results under NPDS conditions for the supine unsutured European-representative eye (left) and the supine unsutured African representative eye (right)

The velocity pathline results for unsutured mNPDS models are provided in Figure 119. In both the unsutured models, the high velocities at the surgical site corresponds to the drastic IOP reduction seen in Figure 50. The flow seems to be heavily dominated by the surgical pathway, with most of the aqueous humour exiting quickly through the surgical site. This quick outflow results in minimal circulation in the top half of the anterior chamber, leading to in a direct and smooth outflow of aqueous humour. In contrast to the unsutured trabeculectomy models, there is less flow alteration in the top half of the anterior chamber. While this type of flow is better for preventing fibrosis, it could result in flow stagnation, leading to eventual nutrient deficiency. Therefore, proper suturing should soon follow the incision to restore sufficient flow.

The unsutured African model seems to show a slightly larger velocity outflow, most likely due to the wider ACA, while the unsutured European model suggest that its narrower ACA could introduce some outflow restriction.

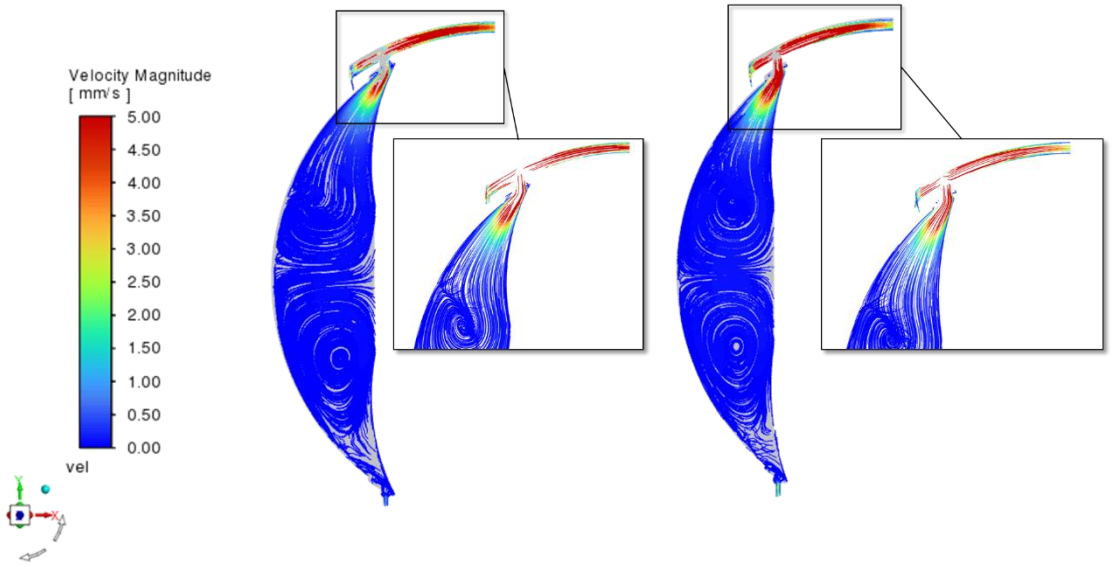


Figure 119 Velocity pathline results under mNPDS conditions for the supine unsutured European-representative eye (left) and the supine unsutured African-representative eye (right)

The velocity vectors results for unsutured mNPDS models are provided in Figure 120. For the unsutured models, the vectors indicate reverse flow in the top half of the anterior chamber consistent with the drastically reduced IOP and the associated fluid dynamics in an over-draining system with little recirculation within the top half of the anterior chamber. The reverse flow in the unsutured mNPDS models resembles that of unsutured trabeculectomy because since both surgical pathways create an almost unrestricted outflow of aqueous humour.

A large portion of the flow exits directly through the surgical opening. Peak velocities are observed at the surgical site, which are consistent with the pathlines. The peak velocities in the African model are slightly higher than in the European model, again reflecting the effects of a wider ACA consistent with the African eye geometry. Within the anterior chamber, the velocities are much lower. The African model has a noticeably higher recirculation pattern.

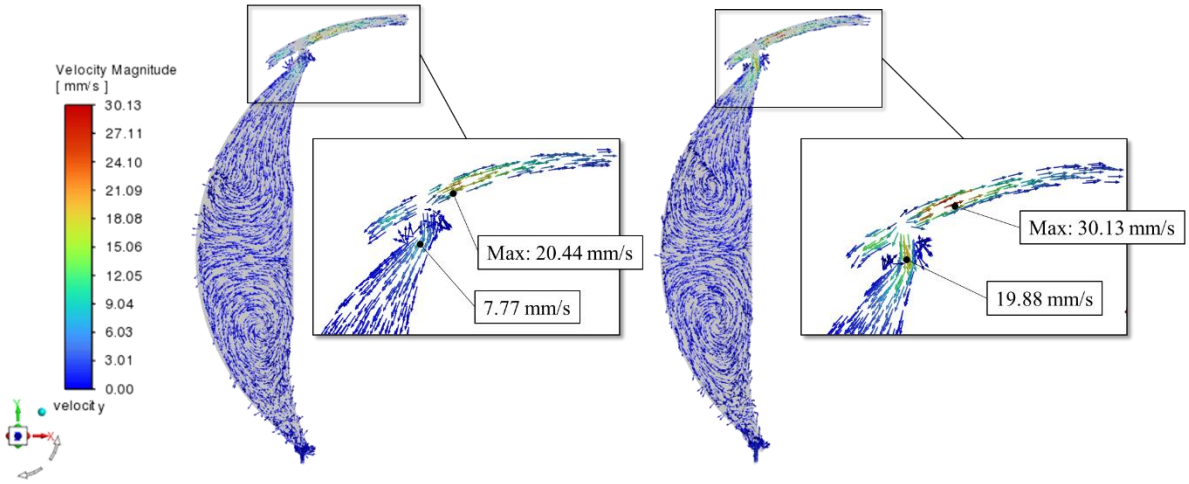


Figure 120 Velocity vector results under mNPDS conditions for the supine unsutured European-representative eye (left) and the supine unsutured African representative eye (right)